Charles University in Prague
Faculty of Mathematics and Physics

DOCTORAL THESIS

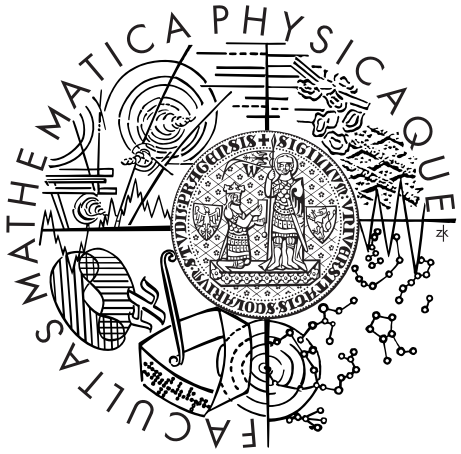

Zdeněk Matěj

Structure of Submicrocrystalline Materials studied by X-Ray Diffraction

Department of Condensed Matter Physics

Supervisor: doc. RNDr. Radomír Kužel, CSc.

Study programme: Physics

Specialisation: F3 — Physics of condensed matter and material research

Prague 2011

Acknowledgements

In the first place, I am very grateful to my supervisor doc. Dr. Radomír Kužel, for introducing me into the field of x-ray structure analysis, for his continuous support of my work, his enthusiasm and his great patience.

Beside him I would like to express my thanks to all my former and present colleagues from the Department of Condensed Matter Physics. I thank prof. Dr. Václav Holý for introducing me to many fields of physics. Scientific discussions with him were great pleasure and benefit for me. I thank my colleagues doc. Dr. Stanislav Daniš and Jan Matlák for valuable helps with experiments and the first one also for his advice concerning computers and many other tiny but important hints.

I was greatly pleased with fruitful discussions and all common experiences with my collegues, namely Dr. Milan Dopita, Dr. Daniel Šimek, Lea Chlanová and Lukáš Horák.

For many useful scientific hints and help with some experiments I would like to thank Jan Drahokoupil. My research would not be possible also without collaboration with many other people. I want to express my thanks to all of them.

Last I would like to give special thanks to my family, whose support was of great importance for me. My sister Lenka has contributed to this work also scientifically as she kindly synthesised a part of samples studied here.

This work was supported by the Doctoral Grant no. 202/05/H003 and by the Grant Agency of Charles University (258200).

I hereby declare that this thesis is a presentation of my original research work. Information derived from the published and unpublished work of others has been acknowledged in the text and a list of references is given in the bibliography.

I understand that my work relates to the rights and obligations under the Act No. 121/2000 Coll., the Copyright Act, as amended, in particular the fact that the Charles University in Prague has the right to conclude a license agreement on the use of this work as a school work pursuant to Section 60 paragraph 1 of the Copyright Act.

Prague, July 2011.

.....
Zdeněk Matěj

Název práce: Studium struktury submikrokrystalických materiálů pomocí rentgenové difrakce

Autor: Zdeněk Matěj

Katedra: Katedra fyziky kondenzovaných látek

Vedoucí disertační práce: doc. RNDr. Radomír Kužel, CSc., Katedra fyziky kondenzovaných látek

Abstrakt: Rentgenovou práškovou difrakcí byla studována struktura submikrokrystalických materiálů. Pro analýzu byla použita především metoda využívající modelování šířek a tvarů difrakčních profilů. Zkoumány byly koloidní nanočástice zlata, měděné vzorky deformované protlačováním a nanočástice oxidu titaničitého připravené různými chemickými metodami. Z charakteristické anisotropie rozšíření difrakčních profilů byly ve vzorcích mědi a zlata rozpoznány dislokace a růstové vrstevné chyby. Z difrakčních dat bylo možné určit hustoty defektů. Možnosti a omezení určování rozdělení velikostí částic pomocí difrakčních metod byly testovány na vzorcích oxidu titaničitého. Částice o velikosti 3–25 nm bylo možné charakterizovat velmi dobře, problémy se projevily pouze v případě, když vzorky obsahovaly zároveň částice velmi rozdílných velikostí. Byly vyvinuty a otestovány difrakční metody a vytvořen počítačový program, které lze používat i k analýze tenkých vrstev.

Klíčová slova: rentgenová difrakce, modelování difrakčních profilů, mřížové poruchy, rozdělení velikostí krystalitů

Title: Structure of submicrocrystalline materials studied by X-ray diffraction

Author: Zdeněk Matěj

Department: Department of Condensed Matter Physics

Supervisor: doc. RNDr. Radomír Kužel, CSc., Department of Condensed Matter Physics

Abstract: Structure of submicrocrystalline materials was investigated by X-ray powder diffraction, mainly by modelling of widths and shapes of diffraction profiles. The diffraction method was applied to colloid gold nanoparticles, copper samples deformed by equal channel angular pressing and titanium dioxide nanoparticles prepared by various chemical routes. Dislocations and twin faults were identified in the metallic samples from characteristic broadening of diffraction lines. Densities of lattice defects were estimated from the diffraction data. Possibilities and limits of the diffraction method for characterisation of a crystallite size distribution were tested on the titanium dioxide samples. Crystallites of size in the range 3–25 nm could be well characterised. The problems were encountered only for samples with extremely broad size dispersion. Diffraction methods and a computer program were developed and tested, which can be applied also for the analysis of thin films.

Keywords: X-ray diffraction, diffraction profile modelling, lattice defects, crystallite size distribution

Contents

Chapter 1

Introduction

1.1 General introduction

Nanomaterials of different kind are of great interest for materials science nowadays. Artificial creation of new structures as well as tailoring their properties and also fundamental understanding of them are highly required. By definition, nanocrystalline materials have grain sizes less than 100 nm. Materials of grain size of a few hundreds of nanometers are often called submicrocrystalline. The nanomaterials include advanced artificial molecular structures as molecular motors, atom patterns at the solid surface, semiconductor nanostructures used in microelectronics and photovoltaics, thin films, various nanotubes, single nanoparticles or also bulk nanoporous structures and ultra-fine grained (UFG) metal structures, whose treatment influences their structure at submicro or even nanoscale.

Small size usually brings specific properties of the nanomaterials, which imply their wide applicability. For example strength/hardness ductility, elastic moduli, diffusivity, specific heat, electrical, optical properties etc. For example, even such a simple system as standalone colloid nanoparticles of simple metals, as gold, founds many applications in biochemical and medical sensing, detection, diagnostics, as cellular and biological imaging agents etc. This is partially due to their strongly surface enhanced absorption and scattering of visible light, which can be in addition tuned by the particles size.

Small size of nanoparticles implies their large surface to volume ratio, which is a fundamental parameter, both from the point of view of their physical properties and their applications. Very large surface per unit mass predestines their use in chemical catalysis and in degradation of environmentally unfriendly pollutants. To achieve the large surface to volume ratio it is important to form a well defined porous microstructure, but also the phase composition of the pore walls can play an important role.

In the field of physics and engineering of metals and alloys ultra-fine grained (UFG) materials of size of few tens of nanometres can be prepared by e.g. ball milling or inner gas condensation. Since compact materials are required for applications mainly in aerospace, automotive industry or e.g. also for dental implants, subsequent consolidation is necessary. This is often related to the reduction of tensile ductility. Contrary, materials showing both enhanced strength and good ductility can be prepared by severe plastic deformation (SPD) techniques. Such

materials have usually a grain size in a submicron range (200–300 nm) but their mechanical properties are strongly influenced by microstructure of their grain boundaries at nanoscale. High fraction and nonequilibrium character of grain boundaries are specific for the SPD materials [1].

For physical, chemical and other properties of materials often not only chemical composition is of interest but their structural and microstructural features play an important and often even the most decisive role. The plasmon resonance frequency in gold nanoparticles depends on their size [2, 3]. Photocatalytic properties of titania (TiO_2) depend largely also on its crystalline state [4]. In SPD materials the yield strength and strength behaviour does no depend only on the mean grain size but it is strongly influenced also by the defect structure of grain boundaries and high density of defects within them [1].

In this connection, X-ray scattering techniques are very appropriate for characterisation as non-destructive and containing rich information on - phase composition, crystallite size, shape and distribution, microstrain, stresses, preferred grain orientation, sometimes also the lattice defects contents like dislocation density and types. As indirect techniques, they should always be complemented by other techniques, first of all by imaging methods. Nevertheless, further development and use of X-ray techniques themselves is also of interest.

Since small size of crystalline particles causes significant broadening of powder diffraction lines, the diffraction is in particular suitable for the determination of crystallite size in the range from a few nanometers to hundreds of nanometers. Lattice defects can also influence the diffraction pattern significantly. Contrary to the microscopic techniques it is often less laborious to get quantitative results from the diffraction analysis. However, a proper microstructure model is required, which is often a critical point. Therefore, microscopic methods are always helpful in particular for the qualitative analysis.

In the past, different approaches [5, 6] usually based on phenomenological models and procedures consisting in several steps were applied in the analysis of powder diffraction data. This can be illustrated for the crystallite size determination. In the first approach, a width of diffraction lines is extracted from measured data, corrected for the instrumental broadening and the crystallite size is then determined by using e.g. the well-known Scherrer formula. In the second approach, a similar quantity is evaluated from the Fourier coefficients. The methods suffer from the necessity of instrumental effects deconvolution, but the main problem is actually in completely absent feedback between the evaluated size value and the experimental data, which allows propagation of systematic errors. This has been corrected in the classical Rietveld approach [7], where the crystallite size value is considered as a model parameter and on its basis widths of diffraction lines is calculated. Diffraction lines profiles are then approximated using analytical profile functions, which are fitted to the measured data. The problem of deconvolution of the instrumental broadening is converted to a convolution problem that is better defined, and there is a direct comparison between calculated and measured pattern. Such calculations are computationally very fast and were accessible on personal computers even before a decade.

The most famous are Rietveld type programs like FullProf (Rodríguez-Carvajal [8]) or GSAS (Larson and Von Dreele [9]) or several commercial programs. They

are mainly dedicated for crystal structure determination and they are also used for quantitative phase analysis. Microstructural features are usually included by phenomenological description of anisotropic line broadening and the programs can be used for estimation of crystallite size and microstrain.

It is worth to note, that in this classical approach there is still an intermediate step between the microstructural model and the diffraction pattern. Usually some indirect parameters as e.g. volume weighted crystallite size or microstrain are the basic quantities, because diffraction profiles width can easily be evaluated from them. Hence, this method also still suffers from two drawbacks. The first is the use of parameters without straightforward meaning and the second problem are approximations connected with the use of analytical profile functions. This has been a subject of a criticism [10].

At the approximately beginning of the last decade (2000) the both problems were treated by the introduction of a method called by the authors of [11] the *whole powder pattern modelling* (WPPM). In this approach, a particular microstructure model is assumed, e.g. it is assumed that crystallites have a specific shape and that their size is distributed according to a particular size distribution. Then, the powder diffraction pattern is calculated and compared with the measured data. Finally, the parameters of the crystallite size distribution or even the whole size distribution histogram are refined from the experimental data by a numerical optimisation procedure [11, 12]. No analytical profile functions are used to describe the physical aspects of the diffraction line broadening. Basic models describing diffraction effects from planar defects [11, 13, 14] or dislocations [15] have been created. Their parameters have direct meaning as e.g. stacking fault probability or dislocation density. The models describe complex broadening anisotropy [16, 17] and shape and account for correlations in the defect arrangement [18–20]. The method is suitable for diffraction analysis of nanocrystalline and highly defected UFG materials. Despite the fact that the number of approximations introduced by this method is reduced to minimum, a different method based on the Debye formula [6, 21] is even more justified for the modelling of the diffraction pattern from very small nanostructures. In this method, the diffraction pattern is directly calculated from the atomic positions in the considered nanostructure. Unfortunately, the method is still quite computationally demanding and suitable only for structures up to approximately 20 nm size. Anyway, some successful attempts of modelling dislocations structures and grain boundaries at an atomistic scale in submicrometer blocks have appeared [22].

Nowadays, about three computer programs implementing the WPPM method on different levels are available. The one focused on the lattice defect analysis in UFG materials has been writen in Budapest by G. Ribárik — *(eC)MWP-fit* [23], another quite general one including for example the effect of different crystallite size distributions, surface relaxation, dislocations and stacking faults was created in Trento by Leoni and Scardi — *PM2k* [24]. The most flexible one including the effects of texture and residual stresses, suitable also for thin film analysis is *MAUD* [25] written by L. Lutterotti. However, this does not include models of lattice defects.

1.2 Aims of investigations

The main *aim of this work* is to critically review and improve the XRD methods mainly the *whole powder pattern modelling* method based on physically realistic models and apply them to several different nanocrystalline or submicrocrystalline materials of a high technological interest. The materials selected were in a form of powders, thin films and bulk materials.

The materials selected in particular for this thesis were the following:

- colloid Au nanoparticles with size in the range 5–100 nm for biological labelling and dynamic light scattering experiments,
- UFG pure Cu and Cu with a small addition of Zr prepared by equal channel angular pressing (ECAP) deformation,
- highly porous TiO_2 — anatase — nanopowders prepared by different chemical routes for applications in photocatalysis.

In all the systems the goal of diffraction analysis was quantitative determination of crystallite size, defects type and density.

- For the colloid Au nanoparticles the main aim was to compare crystallite size obtained by XRD with the particls size determined by transmission electron microscopy (TEM).
- In SPD Cu samples the goal was mainly the determination of dislocations character and density and the test of the applicability of the Krivoglaz-Wilkens [18–20] model of dislocation correlation to the study of these materials.
- For TiO_2 nanopowders, the basic task was the determination of phase composition and crystallite size distribution, which are the parameters crucial from the technological point of view. Comparison with other technologically important parameters as e.g. specific surface area should be desirable. Reliability and limits of XRD determination of the crystallite size distribution should be tested.

The result of the XRD analysis and models considered should be discussed also in connection with other techniques as for example TEM, EBSD or positron annihilation spectroscopy.

Since none of the available programs is capable of the analysis of wide scale of materials (powders, thin films, bulk materials) and none of them include simultaneously all the necessary models and corrections, a new modular software should be created on the basis of the total powder pattern fitting or modelling. This should be tested for the analysis of different nanocrystalline materials mentioned above.

Practical significance of results archived should consist in

- Quantitative characterisation of microstructural properties of studied samples: particles size, defects type and density.

- Assistance in the preparation and tailoring properties of materials e.g.
  - for application in other research areas as biochemical or medical sensing, markers in microscopy or imaging agents,
  - for catalytic applications for ecological disposal of environmentally unfriendly contaminants,
  - for advanced engineering applications,

  and understanding relation between their properties and microstructure.
- Development and testing of XRD methods and software for material analysis, especially also for analysis of thin films.

1.3 Structure of the work

The first part, chapter 2, widely describes defect induced diffraction line broadening, mostly from the correlated dislocations — the problem that has not been still completely solved. It is a purely theoretical chapter. The book of Krivoglaz [20] and papers of Wilkens [18, 19] are the primary sources, which are completed by recent findings of other authors. All this is complemented by comments and remarks of the present author. The aim of the chapter was not only to introduce experimental part but also to give a compact overview of these two theoretical approaches, most often used in powder diffraction analysis of dislocation induced broadening.

The author suppose that it can be used as a reference and starting point for future simulations and model developments.

The next parts of the thesis contains mostly the own work of the present author. In chapter 3, the diffraction profile analysis and the WPPM method are applied to the submicrocrystalline metals, namely colloid Au nanoparticles and SPD treated Cu samples. The chapter is mainly interested in the defect analysis. Contrary, chapter 4 describes the size analysis of TiO_2 nanopowders in quite a comprehensive way. The practical results of this work are summarised and some conclusions are given in chapter 5. The appendix A contains brief description of the program MSTRUCT, developed by the present author and used for the most of the XRD analyses in this work.

Chapter 2

Some Advanced Theory of Diffraction Profile Broadening

2.1 Introduction

In this section a brief overview of the theory of diffraction line broadening due to various crystal defects is given. The aim is to calculate the whole shape of the diffraction profile. However, if the problem is too complex, the theoretical introduction here is limited to considerations about characteristic effects, such as broadening anisotropy, or only to a qualitative description.

Defects considered are mainly various dislocations structures in cubic or hexagonal metals. Influence of faults in the stacking sequences of close packed structures (fcc and hcp) is mentioned as well. The theory here should serve as a basis for the analysis of samples of submicrocrystalline metals studied in chapter 3. No attention is given in this chapter to the size broadening effects. The crystallites size in the specimens studied in chapter 3 is about 100 nm. In such a case the size broadening effect is comparable with the instrumental resolution. The influence of both these effects on diffraction profiles is small as compared to the broadening due to the lattice defects. This is especially true for the high angle diffractions. Both the size and instrumental broadening effects have been described in detail in the author's diploma thesis (Matěj [26], in Czech), whereas the description of the strain broadening was limited only to final results for dislocations models used, without a proper discussion on the origin, approximations and limits of the models. These items are discussed here.

Crystallite size broadening is discussed in the chapter 4 in connection with the studies of nanocrystalline powders of TiO_2 with the crystallite size of $5 - 20$ nm. In this case the size broadening is the dominant effect.

Traditional LPA methods as the Warren-Averbach method (WA) [27] or the well known Sherrer equation (SchE) [28] and the Willimason-Hall plot (WH-plot) method [29] are not described here in detail. They can again be referred to e.g. the classical books Klug and Alexander [5], Warren [6], Valvoda et al. [30] (in Czech), or the thesis [26, 31]. In the second part of this chapter rather the method of total patter fitting (TPF) or the whole profile modelling method (WPPM) is briefly described. This method developed originally by Scardi and Leoni [11] and Ribárik, Ungár, and Gubicza [23] was also described in Matěj [26] but some

improvements of the method and updated references are worth mentioning here. Actually, the WPPM is the most often used method of XRD analysis in this work.

Recently, the Debye function method [32] has become more and more popular especially for modelling of nanocrystalline materials (Cervellino et al. 33) but also complex dislocation structures (Derlet et al. 22). The Debye equation approach is described here briefly and some results from the literature are mentioned at the end of the chapter.

The most of the theory introduced here is based on the book of Krivoglaz [20] and papers of Wilkens [18, 19]. This is completed by comments of the present author. The theory does not represent the original findings of the author if it is not specified explicitly.

2.2 Basic approximations

2.2.1 Kinematical approximation

Theory of scattering of x-rays or neutrons by crystalline matter is a broad topic since various types of materials can be studied in many different experimental arrangements. Generally the Maxwell's equations for x-rays or the Schrödinger equation with the appropriate boundary conditions have to be solved. In this work the nanocrystalline systems and highly imperfect crystals are studied by XRD. In this case coherently scattering domains are small enough that multiple scattering does not occur and the *kinematical approximation* can be used.

Unlike the thesis (Matěj [26]) where the formalism of the classical powder diffraction textbooks (Klug and Alexander [5], Warren [6], Valvoda et al. [30]) was adopted the theoretical introduction in this work follows the formalism of Krivoglaz [20] or Holý et al. [34].

In the scattering experiment intensity I of particles coming from the direction $\boldsymbol{K}_i$ and scattered in the direction $\mathbf{K}_f$ is a function of the diffraction vector $\boldsymbol{Q} = \boldsymbol{K}_f - \boldsymbol{K}_i$ and in the kinematical approximation can be expressed by the well known equation [20, eq. 1.2.4]

$$I(\boldsymbol{Q}) = \left| \sum_{s=1}^{N_0} f_s e^{i\boldsymbol{Q}(\boldsymbol{R}_s + \boldsymbol{u}_s)} \right|^2, \tag{2.1}$$

where it is summed over all atoms sites $\boldsymbol{R}_s$ of the ideal (or averaged) crystal, f_s is the scattering factor of the atom at the $s-th$ site and $\boldsymbol{u}_s$ is the displacement of the atom from its ideal position $\boldsymbol{R}_s$ due to the lattice imperfections.

The kinematical approximation is valid only if the path l of the particles through the object giving raise to a coherent scattering is much larger than the radiation wavelength λ and smaller than the *extinction length* L_e [20, eq. 1.2.1]

$$\lambda \ll l \ll L_e.$$

Explicit expressions for L_e in the case of neutron and x-ray diffraction are derived

in the literature [20, 35]. For x-rays we can write [20, eq. 1.2.31][1]

$$L_e \approx \frac{v}{\lambda r_e f}, \tag{2.2}$$

where v is the volume of the unit cell, $r_e \doteq 2.8\ 10^{-5}$ Å is the free electron radius and f is the structure amplitude for the perfect crystal. With typical values $v = 10$ Å^3, $\lambda = 1$ Å and $f = 30$ this gives the extinction length for x-rays $L_e \approx 1\ \mu m$ and approximately $10\times$ more for neutrons.

2.2.2 Powder orientation averaging

In this thesis solely polycrystalline materials are studied. Generally it is assumed that in an ideal polycrystalline sample (*ideal powder*) there is a statistically large number of grains and all the grains are randomly oriented. Equation 2.1 describes intensity scattered by a single crystallite. In the case of powder the scattered intensity is averaged over all possible crystallite orientations. As proposed e.g. in Krivoglaz [20] the averaging over all crystal orientation can be replaced by the averaging over various directions of the diffraction vector $\boldsymbol{Q}$ (of a given length) for a fixed orientation of the crystal [20, eq. 1.2.10]

$$I_D(Q) = 1/(4\pi Q^2) \int_S \langle I(\boldsymbol{Q}) \rangle dS, \tag{2.3}$$

where integration is taken over the surface S of the sphere of the radius Q [20, eq. 1.2.11]

$$Q = \frac{4\pi}{\lambda} \sin\theta. \tag{2.4}$$

Diffracted intensity in the powder pattern is then a function $I_D(Q)$ of the length of diffraction vector $|\boldsymbol{Q}|$ and hence also a function of the diffraction angle 2θ.

In the literature more related mainly with powder diffraction (Klug and Alexander [5], Warren [6], Valvoda et al. [30]) a slightly different formalism is used. The 2π factor is not included in the diffraction vector and for the diffraction vector length the symbol s is often used

$$s = Q/(2\pi) = \frac{2\sin\theta}{\lambda}.$$

The *powder orientation averaging* approximation expressed by eq. 2.3 is valid well in the case of *ideal powder* materials showing no preferred orientation, but is clearly wrong for strongly textured materials. Practically this approximation is more or less a theoretical concept and by using of another approximation (Powder Pattern Power Theorem, section: 2.2.3) the theory can be easily applied also for textured materials.

[1] In [35] the equation 2.2 for the extinction length is derived from a simple idea that a change of the wave phase of the radiation traveling a path l through the scattering object must be small: $|n-1|k_0 l \ll 1$, where $k_0 = 2\pi/\lambda$, the index of refraction $n \approx 1+\chi_0/2$ and $\chi_0 = -r_e\lambda^2/\pi f(0)/v$.

2.2.3 Powder pattern power theorem

If the profile of a diffraction line in a powder diffractogram have to be calculated, in the first step the intensity dependence $I(\boldsymbol{Q})$ is calculated for a single crystallite according to eq. 2.1 and then it is averaged over all crystallite orientation, i.e. the integral in the eq. 2.3 is evaluated. In many cases this is quite laborious even if the first step can be done. However, there is a simplification widely used in the powder diffraction theory. In the literature (Klug and Alexander [5], Warren [6], Valvoda et al. [30]) it is usually a tricky calculation of intensity profile $I_D(2\theta)$ directly from eq. 2.1 without the integration in eq. 2.3. In the Warren [6] it is called the *powder pattern power theorem*. It will be not described in detail here. It was done already in the thesis (Matěj [26]). Just an idea of the approximation should be discussed.

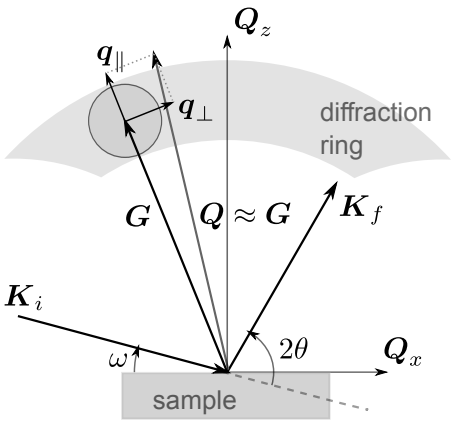

Figure 2.1: Sketch of a simple coplanar diffraction experiment. Radiation impinging the sample surface in the direction $\boldsymbol{K}_i$ at the incidence angle ω is scattered in the direction $\boldsymbol{K}_f$. Diffraction angle is denoted 2θ. Intensity $I(\boldsymbol{Q})$ in the close vicinity ($\boldsymbol{Q}$) of the diffraction maximum ($\boldsymbol{G}$) of the given crystallite is studied. Decomposition of a variation of $\boldsymbol{Q}$ from $\boldsymbol{G}$ into the components parallel ($\boldsymbol{q}_\parallel$) and perpendicular ($\boldsymbol{q}_\perp$) to $\boldsymbol{G}$ is depicted.

In the figure 2.1 a simple diffraction experiment is depicted. Diffracted intensity from the given crystallite or an ensemble of crystallites with the given orientation is studied. The idea of the powder patten power theorem approximation is that the curvature of diffraction circle in the vicinity ($\boldsymbol{Q}$) of the diffraction maximum ($\boldsymbol{G}$) of the given crystallite can be neglected and the sphere (circle in the picture) can be approximated by the tangent plane. If a variation $\boldsymbol{q}$ of the diffraction vector $\boldsymbol{Q}$ from the reciprocal lattice point $\boldsymbol{G}$ of the crystallite

$$\boldsymbol{q} = \boldsymbol{Q} - \boldsymbol{G}$$

is decomposed in the components parallel ($\boldsymbol{q}_\parallel$) and perpendicular ($\boldsymbol{q}_\perp$) to $\boldsymbol{G}$

$$\boldsymbol{q} = \boldsymbol{q}_\parallel + \boldsymbol{q}_\perp,$$

the integration in the eq. 2.3 can be replaced by the integration over the tangent plane, i.e. over $\boldsymbol{q}_\perp$,

$$I_D(Q) = \int I(\boldsymbol{Q})\ d^2\boldsymbol{q}_\perp. \tag{2.5}$$

If we substitute for $I(\boldsymbol{Q})$ from eq. 2.1 and add $\langle\rangle$ for averaging over the ensemble of crystallites with the given orientation (with different crystal shape, defect configuration, etc.)

$$I_D(Q) = \int d^2\boldsymbol{q}_\perp \left\langle \left| \sum_{s=1}^{N_0} f_s e^{i\boldsymbol{Q}(\boldsymbol{R}_s+\boldsymbol{u}_s)} \right|^2 \right\rangle$$

$$= \int d^2\boldsymbol{q}_\perp \left\langle \sum_s f_s e^{i(\boldsymbol{G}+\boldsymbol{q})(\boldsymbol{R}_s+\boldsymbol{u}_s)} \sum_{s'} f^*_{s'} e^{-i(\boldsymbol{G}+\boldsymbol{q})(\boldsymbol{R}_{s'}+\boldsymbol{u}_{s'})} \right\rangle,$$

using $\boldsymbol{G}\boldsymbol{R}_s = 0$ and neglecting $\boldsymbol{q}\boldsymbol{u}_s$[1]

$$= \int d^2\boldsymbol{q}_\perp \left\langle \sum_{s,s'} f_s f^*_{s'} e^{i\boldsymbol{q}(\boldsymbol{R}_s-\boldsymbol{R}_{s'})} e^{i\boldsymbol{G}(\boldsymbol{u}_s-\boldsymbol{u}_{s'})} \right\rangle,$$

substituting $\boldsymbol{\rho}_{s,s'} = (\boldsymbol{R}_s - \boldsymbol{R}_{s'})$, reordering summation, averaging and integration and decomposing $\boldsymbol{\rho} = \boldsymbol{\rho}_\parallel + \boldsymbol{\rho}_\perp$ we arrive to the expression[2]

$$= \sum_{\boldsymbol{\rho}_\parallel, \boldsymbol{\rho}_\perp} e^{i\boldsymbol{q}_\parallel \boldsymbol{\rho}_\parallel} \left\langle \sum_s f_s f^*_{s-\boldsymbol{\rho}} \; e^{i\boldsymbol{G}(\boldsymbol{u}_s-\boldsymbol{u}_{s-\boldsymbol{\rho}})} \right\rangle \int d^2\boldsymbol{q}_\perp \; e^{i\boldsymbol{q}_\perp \boldsymbol{\rho}_\perp}.$$

In the above equation only the last term is a function of $\boldsymbol{q}_\perp$. The integration is taken formally over the whole plane and hence it produces the 2D delta function $\delta^{(2)}(\boldsymbol{\rho}_\perp = 0)$ and this delta function cancels out the summation over $\boldsymbol{\rho}_\perp$. In this way, the final equation is obtained where the diffracted intensity is a function of a single variable ($q_\parallel = 4\pi(\sin\theta - \sin\theta_0)/\lambda$)

$$I_D(q_\parallel) = \sum_{\rho_\parallel} e^{iq_\parallel \rho_\parallel} \left\langle \sum_s f_s f^*_{s-\rho_\parallel} \; e^{i\boldsymbol{G}(\boldsymbol{u}_s-\boldsymbol{u}_{s-\rho_\parallel})} \right\rangle \tag{2.6}$$

and it has the form of the 1D Fourier transformation of the expression in the brackets $\langle\rangle$, which can be identified with the *Fourier coefficients*. An important consequence of the result is that in the powder diffraction we are interested only in the difference (correlation) of atom displacements between the points ($\boldsymbol{R}_s$ and $\boldsymbol{R}_s - \boldsymbol{\rho}_\parallel$) along the direction of the diffraction vector. In the literature (Krivoglaz [20]), usually the expression in the brackets $\langle\rangle$ is evaluated generally as a function of $\boldsymbol{\rho}$ and equation 2.6 shows that in the powder diffraction we can focus only in the dependence in the direction $\boldsymbol{\rho} = \boldsymbol{\rho}_\parallel$ parallel to the diffraction vector $\boldsymbol{G}$. This simplification is widely used, for example in Klimanek and Kužel [17].

Another advantage of the the powder pattern power theorem is that the calculation of the intensity at the diffraction ring is treated more "locally". The shape, position and intensity of diffraction lines are computed separately and it is easier to include also effects as texture, residual stress and absorption etc.

Limits of the approximation are worth to mention. It is clear that for the correctness of the approximation it is necessary that the diffraction line should be narrow in the reciprocal space as compared by the curvature of the diffraction ring (figure 2.1). Krivoglaz [20] in the chapter 1.3.2 (p. 29) sets the limit of validity to approximately 100 lattice parameters. This means that the approximation can

[1] In literature e.g. [6, ch. 13.4, p. 265, Fig. 13.6] this is usually commented as it is sufficient to use instead of $\boldsymbol{Q}$ an average value $\boldsymbol{G}$ in a scalar product $\boldsymbol{Q}(\boldsymbol{u}_s - \boldsymbol{u}_{s'})$. In Krivoglaz [20] $\boldsymbol{Q}$ is kept formally in the scalar product, but in cases considered here it is in fact always replaced by $\boldsymbol{G}$ in the final expressions. All calculations are more complicated if $\boldsymbol{Q}$ is not replaced and also a whole diffraction conception based on a Fourier transformation is broken if crystals with defects are considered.

[2] Site indexes s and real space lattice vectors $\boldsymbol{\rho}$ are used together in subscripts in the equations. This is formally incorrect, but hopefully the meaning is clear.

be inaccurate for crystals smaller than $L \approx 50\ nm$ (assuming lattice parameter 5 Å). Contrary in the [36] they compared the whole diffraction modeling method (WPPM, chapter 2.4) and the Debye formula method (chapter 2.5), The first method utilize the theorem heavily, whereas the second one does not include the powder pattern power theorem approximation at all. They calculated diffraction patterns for crystallites of size $3-10\ nm$ and found that WPPM works fine also for crystallites of size around 5 nm. Hence it looks that the approximation is valid up to such small crystallites and broad diffraction lines.

2.3 XRD line broadening due to the lattice defects

In this section, the theory of the diffraction line broadening due to various defects (mainly dislocations and stacking faults etc.) is summarized.

2.3.1 Krivoglaz theory - classification of defects

Equation 2.6 is a basic formula for calculating powder diffraction profiles. However, it is still too much general equation for a theoretical analysis of influence of a particular configuration of defects. Krivoglaz [20] used a further derivation of eq. 2.6 to simplify this task. The derivation done by Krivoglaz [20, chapter 1.5.2] is introduced here with some additional simplifications.

Displacement $\boldsymbol{u}_s$ of an atom at the site $\boldsymbol{R}_s$ is a sum of displacements $\boldsymbol{u}_{s,t}$ caused by the defects placed at sites $\boldsymbol{R}_t$. If the defects cause a phase change $\varphi_{s,t}$ of a scattered wave this must be considered too, as follows

$$\begin{aligned} \boldsymbol{u}_s &= \sum_t c_t\ \boldsymbol{u}_{s,t}\ , \\ f_s &= f + \sum_t c_t\ \varphi_{s,t}\ , \end{aligned} \tag{2.7}$$

where c_t is an occupation number equal to one if the defect is at the position $\boldsymbol{R}_t$ or zero if not. The lattice defects connected with the phase change, such as stacking or twinning faults, will be described later (chapter 2.3.8). Here, the derivation will be restricted to the case ($\varphi_{s,t} = 0$).

It is assumed that defects are positioned randomly without correlations and equation 2.6 then gives

$$I_D(q_\parallel) = |f|^2 \sum_{\rho_\parallel} e^{iq_\parallel \rho_\parallel} \sum_s \left\langle \exp\left[i \sum_t c_t \boldsymbol{G}(\boldsymbol{u}_{s,t} - \boldsymbol{u}_{s-\rho_\parallel,t})\right] \right\rangle , \tag{2.8}$$

$$I_D(q_\parallel) = |f|^2 \sum_{\rho_\parallel} e^{iq_\parallel \rho_\parallel} \sum_s \prod_t \left\langle \exp\left[i c_t \boldsymbol{G}(\boldsymbol{u}_{s,t} - \boldsymbol{u}_{s-\rho_\parallel,t})\right] \right\rangle . \tag{2.9}$$

Averaging over all defect configurations can be done for each term of the product

$$\left\langle e^{ic_t \boldsymbol{G}(\boldsymbol{u}_{s,t} - \boldsymbol{u}_{s-\rho_\parallel,t})} \right\rangle = c\ e^{i\boldsymbol{G}(\boldsymbol{u}_{s,t} - \boldsymbol{u}_{s-\rho_\parallel,t})} + (1-c)\ ,$$

where c is the probability of finding a defect on the site $\boldsymbol{R}_t$ and $(1-c)$ is the probability that there is no defect there.

By rewriting the product of in the equation for $I_D(q_\parallel)$ as

$$\prod_t [\ldots] = \exp \sum_t \ln[\ldots] \equiv \exp(-T)$$

a quantity $T(\boldsymbol{R}_s, \boldsymbol{\rho}_\parallel)$ is defined

$$T(\boldsymbol{R}_s, \boldsymbol{\rho}_\parallel) \equiv - \sum_t \ln[1 + c(e^{i\boldsymbol{G}(\boldsymbol{u}_{s,t} - \boldsymbol{u}_{s-\rho_\parallel,t})} - 1)] \ .$$

Usually the defect concentration c is very small ($c \ll 1$) and the expression for T can be expanded which gives the usually used equation for T (Krivoglaz [20, eq. 1.5.9], Daniš and Holý [37], Kaganer and Sabelfeld [38])

$$T(\boldsymbol{R}_s, \boldsymbol{\rho}_\parallel) = c \ \sum_t \left[1 - e^{i\boldsymbol{G}(\boldsymbol{u}_{s,t} - \boldsymbol{u}_{s-\rho_\parallel,t})}\right] \ . \tag{2.10}$$

Intensity of a powder diffraction line is then expressed using T as [20, eq. 5.1.2]

$$I_D(q_\parallel) = |f|^2 \sum_{\rho_\parallel} e^{iq_\parallel \rho_\parallel} \sum_s e^{-T(\boldsymbol{R}_s, \boldsymbol{\rho}_\parallel)} \ . \tag{2.11}$$

If a homogenous configuration of defects in a large crystal is considered then it can be assumed that T in equation 2.10 does not depend on the position $\boldsymbol{R}_s$ in the crystal and the sum over $\boldsymbol{R}_s$ in eq. 2.11 can be replaced by $Ne^{-T(\rho_\parallel)}$, where N is a number of lattice cells in the crystal. Scattered intensity is then the Fourier transformation of e^{-T}. In order to distinguish between regular and diffuse scattering from defective samples Krivoglaz[20, ch. 1.5.2] studied asymptotic behavior of T the in the limit of large values of the real space length $\rho_\parallel$. If e^{-T} behaves as a bell shaped function of the real space variable $\rho_\parallel$ then its Fourier transformation gives a bell shape diffraction intensity distribution typical for a *diffuse* scattering. If e^{-T} does not converge to zero for $\rho_\parallel \to \infty$ the Fourier transformation (in the limit of an infinite crystal) raises a delta function (sharp) intensity maximum. Krivoglaz denotes [20, eq. 1.5.15-16] limits of a real and an imaginary part of T as

$$2M \equiv \mathrm{Re}\, T_\infty \equiv c \lim_{\rho_\parallel \to \infty} \sum_t \left\{1 - \cos[\boldsymbol{G}(\boldsymbol{u}_{s,t} - \boldsymbol{u}_{s-\rho_\parallel,t})]\right\} \ , \tag{2.12}$$

$$-\,\mathrm{Im}\, T_\infty \equiv c\ \boldsymbol{G}\hat{\alpha}\boldsymbol{\rho}_\parallel \equiv -\delta G \rho_\parallel \equiv \lim_{\rho_\parallel \to \infty} \sin[\boldsymbol{G}(\boldsymbol{u}_{s,t} - \boldsymbol{u}_{s-\rho_\parallel,t})] \ . \tag{2.13}$$

Since e^{-T} converges to e^{-2M} for large $\rho_\parallel$ the delta maximum is weighted by this value. The imaginary part of T_∞ is on the other hand connected with a shift $\delta\boldsymbol{G}$ of the maximum as it can be included in the Fourier term $\exp(iq_\parallel \rho_\parallel)$. It accounts for an average deformation of the crystal lattice due to the defects. If the reciprocal space length parameter $q_\parallel$ is redefined to refer to this averaged deformed lattice $q_\parallel = Q_\parallel - (G_\parallel + \delta G_\parallel)$ the *regular* scattering part I_0 of the scattered intensity can be formally written as (Krivoglaz [20, eq. 1.5.20])

$$I_0 = N|f|^2 2\pi\delta(q_\parallel)e^{-2M} \ . \tag{2.14}$$

The remaining part of the overall intensity scattered I_D (eq. 2.11) is then according to Krivoglaz [20] a *diffuse* scattering I_1

$$I_1 = I_D - I_0 \ . \tag{2.15}$$

The above analysis forms a basis of the Krivoglaz [20, ch. 1.5.3] classification of defects. Krivoglaz basicaly distinguishes lattice defects of two classes.

In case of the 1st class defects the value $2M$ (eq. 2.12) converges in a limit of an infinite crystal to a finite number. Scattering from crystals containing *the first class defects* is characteristic with sharp spots of diffraction maxima weakened by the factor e^{-2M} and shifted according to eq. 2.13. Point defects with the displacement field decreasing as $u_{st} \sim 1/r_{st}^2$ are typical examples of such defects.

For the *the second class defects* the value of $2M$ approaches infinity and there are no delta-function like terms in formulae for the scattered intensity. Smooth bell shaped broadened peaks characterize the scattering from crystals containing these defects. Dislocations are typical examples. The displacement field of a straight-line dislocation decrease slowly with a distance from the dislocation line (as $u_{st} \sim 1/r_{st}$) and it can be shown then ([20]) that $2M$ (eq. 2.12) does not converge to a finite value.

If a crystal of finite size L is considered a character of scattering from the defects can change. For the second class defects $2M$ becomes finite, but in many cases it is quite huge. Krivoglaz [20] shows that it is approximately proportional to the number of defects in the crystal N_d. In this work defects in SPD materials with dislocations densities about $1 - 10\ 10^{15}$ 1/m^2 are studied. The crystalline size in SPD materials is about 100 nm which gives up to 100 dislocations in a single slip system of one crystallite.

The first-class defects in a finite crystal can sometimes behave as the defects of the second class. Krivoglaz [20] has showed that the factor $2M$ for a crystal containing dislocation loops or dislocation dipoles is proportional to the logarithm $\ln(L)$ of crystal size. If a defect density is high and the crystal size is large as compared with a characteristic defect size $2M$ can be large enough and the the diffuse scattering can dominate the scattered intensity.

Finally it must be mentioned that the Krivoglaz classification of defects is quite formal. In a real case beside the finite size of coherently scattering crystal domains, also fluctuations and a distribution of density of defects in a studied sample must be considered [20]. This results in smearing of sharp regular peaks. Instrumental broadening effects act similarly in this point. Hence it can be difficult to distinguish correctly between regular maxima and the diffuse scattering in a particular case.[1]

An extensive analysis of many defect types can be found in the book of Krivoglaz [20]. One reference in Czech is the thesis of Kužel [31]. Here in next sections the Krivoglaz theories of scattering from non-correlated dislocations (chapter 2.3.2) and dislocation dipoles (chapter 2.3.3) are briefly described

[1] It is especially true in case of powder diffraction and it can be a reason why in powder diffraction it is not to much common to distinguish between what Krivoglaz calls in his book [20] *regular lines* and diffuse *pseudolines*. This work is focused on defects of the second class and terms: *diffraction line, reflection, diffraction maximum* are used as synonyms of the Krivoglaz's *pseudoline*.

to illustrate the issue. Next the case of correlation in the dislocation arrangement is described (chapter 2.3.4) to get comparison with a model of Wilkens (1970) [19] (chapter 2.3.5).

2.3.2 Non-correlated dislocations

In this section a method of calculation of diffraction profiles from randomly distributed straight line dislocations in the crystal is briefly described. The method was originally introduced by Krivoglaz [20, ch. 5.1]. A brief well written introduction to the Krivoglaz theory can also be found in the recent (2010) paper of Kaganer Kaganer and Sabelfeld [38].

Calculation of the diffraction profile will be illustrated here on a set of straight screw dislocations intersecting the plane to which the dislocations lines are perpendicular, in random points. It is assumed that in average there no bending of the crystal, i.e. there is the same number of dislocations with opposite signs and elastically isotropic crystal is considered. Generalization to other types of dislocations (edge) and anisotropic crystals will be discussed later.

Except the dislocation core there is no phase shift $\phi_{s,t}$ related to dislocations in the crystal. Eq. 2.10 for T is a basis of the calculation. T must be evaluated as a function of the real space distance $\rho_{\parallel}$. Aftewards, its limit $2M$ (eq. 2.12) in the case $\rho_{\parallel} \to \infty$ should afterwards be analyzed to show that dislocations are defects of the second class.

In the first step an expression for a displacement $\boldsymbol{u}_{s,t}$ of an atom at the site $\boldsymbol{R}_s$ from a dislocation in the position $\boldsymbol{R}_s$ is needed. If we assume a screw dislocation with the Burgers vector $\boldsymbol{b}$ parallel to the z-axis and to the dislocation line intersecting the xy-plane in the origin (figure 2.2) then only the displacement u_z is nonzero [20, 30, 39]

$$u_z = b/(2\pi)\ \vartheta = b/(2\pi)\arctan(y/x)\ . \tag{2.16}$$

The above equation is valid for a screw dislocation in elastically isotropic medium of infinite dimensions. If boundary conditions have to be fulfilled on a surface of the crystal of finite dimensions, an additional term appears in the expression for $\boldsymbol{u}_{s,t}$ [20, 39]. This is connected to the image forces from virtual image defects. Displacements $\boldsymbol{u}^{img}_{s,t}$ from these image defects at points deep within the crystal are smaller than u_z in eq. 2.16 if the crystal is large and vary smoothly if also the dislocation line is far from the crystal surface. Hence the difference of displacements $(\boldsymbol{u}^{img}_{s,t} - \boldsymbol{u}^{img}_{s-\rho_{\parallel},t})$ due to the image forces is neglected [20].

The difference in vector fields $(\boldsymbol{u}_{s,t} - \boldsymbol{u}_{s-\rho_{\parallel},t})$ in eq. 2.10 for T is in the first step expanded in a linear term in $\rho_{\parallel}$[1]

$$(\boldsymbol{u}_{s,t} - \boldsymbol{u}_{s-\rho_{\parallel},t}) \approx (\nabla \otimes \boldsymbol{u}_{s,t}) \cdot \boldsymbol{\rho}_{\parallel}\ . \tag{2.17}$$

In the scalar product $\boldsymbol{G}(\boldsymbol{u}_{s,t} - \boldsymbol{u}_{s-\rho_{\parallel},t})$ in the expression for T the diffraction vector length G and the real space length $\rho_{\parallel}$ can be set apart if we consider that

[1] The dyadic product $(\nabla \otimes \boldsymbol{u}_{s,t})$ is actually equivalent to the Jacobian matrix of the displacement field with respect to space.

$\boldsymbol{G} = \boldsymbol{\gamma} G$ and $\boldsymbol{\rho}_{\parallel} = \boldsymbol{\gamma}\rho_{\parallel}$ where $\boldsymbol{\gamma}$ is an unit vector of directional cosines of the diffraction vector $\boldsymbol{G}$

$$\boldsymbol{G}(\boldsymbol{u}_{s,t} - \boldsymbol{u}_{s-\rho_{\parallel},t}) \approx G\big[\boldsymbol{\gamma} \cdot (\nabla \otimes \boldsymbol{u}_{s,t}) \cdot \boldsymbol{\gamma}\big]\rho_{\parallel} \ .$$

From figs. 2.2 and 2.3 it should be clear that derivatives of the displacement

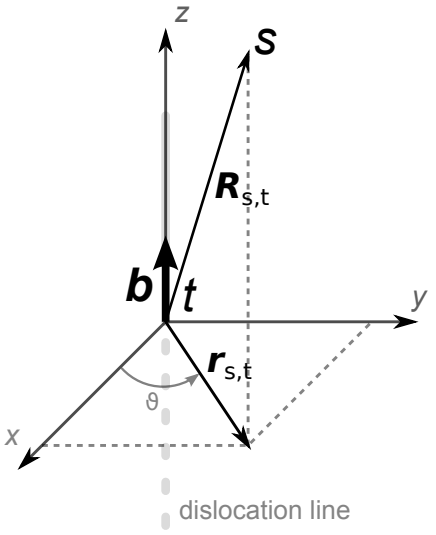

Figure 2.2: Basic scheme used in calculation of diffraction profile from a screw dislocation. The dislocation is situated at site $\boldsymbol{R}_t$ – the center of a reference system. The Burgers vector $\boldsymbol{b}$ is parallel to the z-axis. Displacement at site $\boldsymbol{R}_s$ is examined.

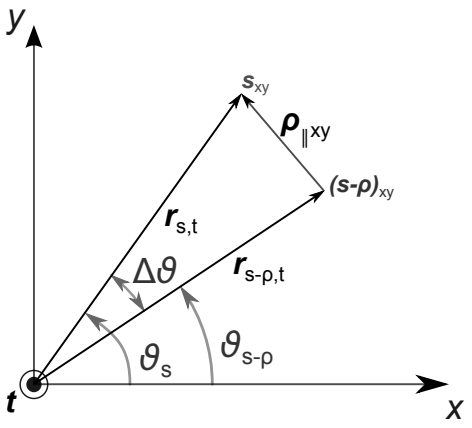

Figure 2.3: xy-plane from the schema in figure 2.2. Here a difference of displacements at two sites $\boldsymbol{R}_s$ and $\boldsymbol{R}_{s-\rho_{\parallel}}$ from a screw dislocation at site $\boldsymbol{R}_t$ is examined. It is visible that for large $r_{s,t}$ the difference of displacements $\Delta u_z \sim \Delta\vartheta \approx \rho_{\parallel}/r_{s,t}\ \tilde{\Psi}$, where $\tilde{\Psi}$ includes some directional factors. This is a basis for an approximate equation 2.18.

field (deformation) in the point $\boldsymbol{R}_s$ from a dislocation at the site $\boldsymbol{R}_t$ decrease as $1/r_{s,t}$ with the distance $r_{s,t}$ from the dislocation line. Hence finaly the whole scalar product in eq. 2.10 for T can be formally written as a linear function of (Gb), $(\rho_{\parallel}/r_{s,t})$ and Ψ

$$\boldsymbol{G}(\boldsymbol{u}_{s,t} - \boldsymbol{u}_{s-\rho_{\parallel},t}) \approx (Gb)/(2\pi)\ \frac{\rho_{\parallel}}{r_{s,t}}\ \Psi \ , \tag{2.18}$$

$$\Psi = (2\pi)/b\ r_{s,t}\ \big[\boldsymbol{\gamma} \cdot (\nabla \otimes \boldsymbol{u}_{s,t}) \cdot \boldsymbol{\gamma}\big] \approx 1 \ , \tag{2.19}$$

where $r_{s,t}$ is a length of the projection of the vector $\boldsymbol{R}_{s,t}$ into the plane perpendicular to the dislocation line (fig. 2.2) and Ψ is an orientation factor of the order of unity accounting for a relative orientation of the diffraction vector and the slip system of the dislocation.

Summation over all possible defect positions $\boldsymbol{R}_t$ is required in eq. 2.10. This summation is usually [20] replaced by an integration over the whole xy-plane (fig. 2.2) perpendicular to the dislocation line. It is assumed that there is an area S_0 per defect position $\boldsymbol{r}_t$ and dislocations are continuously distributed with the area density $n = c/S_0$. In addition, it was stated earlier that there is the same number

of dislocations of opposite signs $n_+ = n_- = n/2$. If the scattering from a crystal containing different types of defects (e.g. dislocations of different Burgers vector signs, dislocations in different slip systems etc.) must be calculated then T in eq. 2.10 is a sum of T_α corresponding to all lattice defect types [20]

$$\begin{aligned} T(\boldsymbol{R}_s, \boldsymbol{\rho}_\parallel) &= \sum_\alpha T_\alpha \\ &= \sum_\alpha c_\alpha \sum_t \left[1 - e^{i\boldsymbol{G}(\boldsymbol{u}_{s,t,\alpha} - \boldsymbol{u}_{s-\rho_\parallel,t,\alpha})}\right] \\ &= \sum_\alpha n_\alpha \int d^2\boldsymbol{r}_t \, \left[1 - e^{i\boldsymbol{G}(\boldsymbol{u}_{s,t,\alpha} - \boldsymbol{u}_{s-\rho_\parallel,t,\alpha})}\right] . \end{aligned} \tag{2.20}$$

The effects from different defects are considered to be independent and the sum can be understood as a formal convolution of them.

If the argument in the exponent in eq. 2.20 is small the exponent can be expanded into a power series. Considering the dislocations of opposite signs in a single slip system α we can find that the odd terms in the expansion will cancel out and T is real. Retaining only the second order term and substituting for the argument in the exponent from eq. 2.18 we obtain for T_α the relation

$$\begin{aligned} T_\alpha &= (n_{\alpha+} + n_{\alpha-}) \int d^2\boldsymbol{r}_t \, \left\{1 - \cos\left[\boldsymbol{G}(\boldsymbol{u}_{s,t,\alpha} - \boldsymbol{u}_{s-\rho_\parallel,t,\alpha})\right]\right\} \\ &\approx (n_{\alpha+} + n_{\alpha-}) \int d^2\boldsymbol{r}_t \, 1/2\left[\boldsymbol{G}(\boldsymbol{u}_{s,t,\alpha} - \boldsymbol{u}_{s-\rho_\parallel,t,\alpha})\right]^2 \\ &\approx \frac{(Gb)^2}{8\pi^2} \, n_\alpha \, \rho_\parallel^2 \int d^2\boldsymbol{r}_t \, 1/r_{s,t}^2 \Psi_\alpha^2 . \end{aligned} \tag{2.21}$$

In order to evaluate the last integral the positions of t and s sites in the reference system in fig. 2.2 can be exchanged, i.e. deformation field at site $\boldsymbol{r}_s$ in the center from a dislocation placed at site $\boldsymbol{r}_t$ is studied. In polar coordinates, the integration over the polar and the angular coordinates can be separated

$$T_\alpha \approx \frac{(Gb)^2}{8\pi^2} \, n_\alpha \, \rho_\parallel^2 \int 1/r_t \, dr_t \int_0^{2\pi} \Psi_\alpha^2 \, d\vartheta_\alpha \tag{2.22}$$

The integration over the angular variable is done entirely separately. An angular factor χ_α is defined (Krivoglaz [20], Klimanek and Kužel [17])

$$\chi_\alpha = \int_0^{2\pi} \Psi_\alpha^2 \, d\vartheta_\alpha , \tag{2.23}$$

which accounts for a particular geometry of the diffraction vector and the dislocation slip system.

In order to evaluate the integral over the polar coordinate r_t it is useful to remember geometrical considerations and limits of approximations used to derive the above expression. It was required that $r_{s,t}$ as well as $\rho_\parallel$ should be smaller than a characteristic dimension L of the crystal.

$$r_{s,t} \ll L . \tag{2.24}$$

For the linear approximation (eq. 2.17) of the strain field of a dislocation, the idea depicted in fig. 2.3 resulting in eq. 2.18, it is required that

$$\rho_{\parallel}/r_{s,t} \ll 1 \ . \tag{2.25}$$

Krivoglaz [20, eq. 5.1.2] emphasizes that the effects of image forces can be neglected and the integration 2.22 can be simplified only if $\rho_{\parallel}$ is very small as compared to the crystal size L

$$\ln(\frac{L}{\rho_{\parallel}}) \gg 1 \ . \tag{2.26}$$

The last condition comes from the expansion of the cosine term in eq. 2.21. The argument has to be small

$$\frac{(Gb)}{2\pi}\rho_{\parallel}/r_{s,t} \ll 1. \tag{2.27}$$

Looking back at fig. 2.18 we can see that the length of projection of the vector $\boldsymbol{\rho}_{\parallel}$ into the xy-plane perpendicular to dislocation line plays a crucial role when evaluating differences in displacements. This is of course included in the orientation factor Ψ (eq. 2.19).[1] However, for integration over the radial coordinate r_t in eq. 2.22 it is more common [20] to accept an idea that the integral is rather a function the length $\rho_{\parallel xy}$ of the projected vector than the length $\rho_{\parallel}$ of vector itself. For similar reasons also $|\boldsymbol{Gb}|$ is used instead of (Gb) in eq. 2.27. In this way the geometrical conditions in fig. 2.18 are accounted in the integration.

Conditions 2.24 and 2.27 can be taken approximately as limits of the integration over the polar coordinate in eq. 2.22 and it is also accepted that the projection $\rho_{\parallel xy}$ is an important factor in eq. 2.27.[2] We take L as the upper integration limit and $|\boldsymbol{Gb}|/(2\pi)\rho_{\parallel xy}$ as the lower one and we obtain

$$T_{\alpha}(\rho_{\parallel}) = \frac{(Gb)^2}{8\pi^2}\chi_{\alpha}\ n_{\alpha}\ \rho_{\parallel}^2\ \ln\big(\frac{2\pi\zeta_{0,\alpha}L}{|\boldsymbol{Gb}|\rho_{\parallel xy,\alpha}}\big)\ , \tag{2.28}$$

where $\zeta_{0,\alpha}$ is a constant of order of unity $\zeta_{0,\alpha} \simeq 1$, which accounts for inaccuracies in the choice of boundary limits and particular boundary conditions. Kaganer commented [38] this as a fact that the size parameter L is in some sense ill-defined. In Krivoglaz [20, eq. 5.1.6] $\zeta_{0,\alpha} = 1/2$.

Further justification of approximations giving the logarithmic term in the above equation can be found in Kaganer's paper [38]. Kaganer justifies also neglecting of the contribution from area $r_t \leq (Gb)/(2\pi)\rho_{\parallel xy}$ as it is small in comparison with the logarithmic term if the term is much larger than unity. This is fulfilled if condition 2.26 is true. If we consider that the range of interest of $\rho_{\parallel}$ is of the order of an average distance between dislocations $r_d \sim n^{-1/2}$ and if

[1] Here in eq. 2.17 the linear expansion in $\boldsymbol{\rho}_{\parallel}$ was used. An expansion $\boldsymbol{\rho}_{\parallel xy}$ can be used as well and then there is a modification in the definition of the angular factor Ψ (eq. 2.19) and $\rho_{\parallel xy}$ appears in the theory more likely than $\rho_{\parallel}$. This is quite common e.g. in Krivoglaz [20, ch. 5.1.3] for dislocation dipoles. Similar choice was used by Kaganer and Sabelfeld [38], where they included the appropriate geometrical factor already in the definition of the reciprocal space variable $q_{\parallel}$ (see text below eq. (3) in [40]).

[2] These ideas are approximations (or rather computational *magic*) commonly used in the book of Krivoglaz [20] or e.g. in the recent (2010) paper of Kaganer [38]

we are interested in high dislocation densities $r_d \sim 20$ nm and relatively large crystals $L \sim 200$ nm the condition 2.26 should be satisfied.

Evaluating the sum of contributions (to T) from dislocations in different slip systems (eq. 2.20) it is usually assumed that the constants $\zeta_{0,\alpha}$ do not depend much on the slip system type ($\zeta_{0,\alpha} = \zeta_0$) and also that the angular factors in $|\boldsymbol{Gb}|\rho_{\parallel xy,\alpha}$ finally average themselves into $Gb\rho_\parallel$.[1] The summation is then included only in the contrast factor χ and we arrive at the famous expression (Krivoglaz [20, eq. 5.1.6], Kaganer and Sabelfeld [38, eq. 20])

$$T(\rho_\parallel) = \frac{(Gb)^2}{8\pi^2}\chi\ n\ \rho_\parallel^2\ \ln\left(\frac{2\pi\zeta_0 L}{Gb\rho_\parallel}\right)\ , \tag{2.29}$$

$$\chi = \sum_\alpha\ \frac{n_\alpha}{n}\ \chi_\alpha\ , \tag{2.30}$$

Dislocation contrast factors χ_α can be calculated from eqs. 2.19 and 2.23. It can be shown that the approximation 2.18 and the whole analysis above can also be applied to edge dislocations. Details of boundary conditions are of little importance in real cases. This is shown later in the case of correlated dislocations. Hence, expression 2.29 holds for edge dislocations too and if we want to include different types of dislocations we can account for them simply by averaging contrast factors χ_α in eq. 2.30. This has been done for dislocations in cubic and hexagonal metals e.g. in [17, 31, 42–44] or for crystals of any symmetry in [45].

T in eq. 2.29 is a growing function of $\rho_\parallel$ when condition 2.26 is satisfied. Hence, in the limit $\rho_\parallel \to \infty$ and $L \to \infty$ value of $2M$ (eq. 2.12) diverges

$$2M \equiv \mathrm{Re}\, T_\infty \to \infty\ ,$$

which confirms that randomly distributed dislocations belong to the defects of the second class.

Diffraction profile can be calculated according to eq. 2.11 by Fourier transform of $e^{-T(\rho_\parallel)}$. T in eq. 2.29 is a quadratic function of $\rho_\parallel$ modified by the logarithmic term. Therefore, it is natural to test how e^{-T} differs from the Gaussian curve. To illustrate such approximation, T and the Gaussian curve are plotted in fig. 2.4 in scaled units

$$x = \frac{Gb}{2\pi}\sqrt{\frac{\chi}{2}n}\ \rho_\parallel .$$

In this units

$$T(x) = x^2\ \ln\left(\frac{\sqrt{N_{eff}}}{|x|}\right) = \ln\sqrt{N_{eff}}\ x^2 + x^2\ln\left(1/|x|\right)\ ,$$

$$N_{eff} = \frac{\chi}{2}n\zeta_0^2 L^2 = \frac{\chi}{2}N_d\ , \tag{2.31}$$

where N_d is approximately a number of dislocation in the crystal and N_{eff} is an effective number of dislocations.

$$l_0 = \ln\sqrt{N_{eff}} \tag{2.32}$$

[1] This averaging was widely discussed for the case of the Wilkens model in the paper of Armstrong et al. [41]. It is commented more here in section 2.3.7, p. 44.

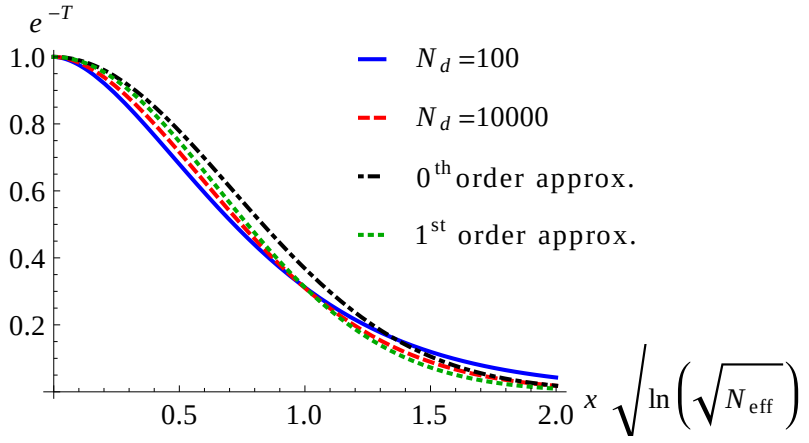

Figure 2.4: Gaussian approximation of e^{-T} (eq. 2.29) for randomly distributed dislocations. Solid blue line - e^{-T} for $N_d = 100$, dashed red - e^{-T} for $N_d = 10000$, dot-dashed black - the zero order Gaussian approximation $e^{-l_0 x^2}$, dotted green - the first order Gaussian approximation $e^{-l_1 x^2}$.

is then naturally a zero order approximation of the coefficient of the Gauss function. From fig. 2.4 it can be seen that such Gauss function roughly approximates e^{-T}.

If $|x|$ in the logarithmic term is approximated by its value in the center of the range of x plotted in fig. 2.4, $x_0 = 1/\sqrt{l_0}$, an approximation of the next order is obtained

$$l_1 = \ln\left(\sqrt{N_{eff}}\sqrt{l_0}\right) = \ln\left(\sqrt{N_{eff}}\sqrt{\ln\sqrt{N_{eff}}}\right) \tag{2.33}$$

and it is shown in fig. 2.4 that the Gaussian with l_1 coefficient approximates e^{-T} very well especially for large crystals with many dislocations N_d. For the case of the crystal with $N_d \sim 100$ discussed earlier the approximation is "satisfactory", at least for estimation of the peak width.[1][2]

Accepting the above Gaussian approximation we can write an explicit formula for the intensity distribution in the central part of the peak [20]

$$I_D(q_\parallel) = \frac{I_{Di}}{\sigma_D}\exp\left(-\pi\,\frac{q_\parallel^2}{\sigma_D^2}\right), \tag{2.34}$$

where I_{Di} is the integrated line intensity and σ_D is the integral line width, which we can approximate as[3]

$$\sigma_D^2 = 2\pi\chi n\left(\frac{Gb}{2\pi}\right)^2 l_m\ . \tag{2.35}$$

[1] In fig. 2.4 the curves are plotted for $\chi = \pi$ and $\zeta_0 = 1/2$. This explicit values can be found in the Krivoglaz book [20, eq. 5.1.7].

[2] Approximate curves of the first order for $N_d = 100$ and $N_d = 10000$ in fig. 2.4 can not be distinguished. Coefficients in the exponential differs by less than 1%. Only one curve is plotted here.

[3] There appears a contrast factor χ in our expression for $N_{eff} = \chi/2 * N_d$, which is not common [20]. However, influence of χ factor in the logarithmic term on peak width can be disregarded in this case because in all equations only $\ln(\sqrt{N_{eff}})$ appears and $\ln\sqrt{\chi/2} \ll \ln\sqrt{N_d}$ for $N_d \gg 10$.

Finally, behavior of tails of powder diffraction profiles is discussed. Krivoglaz [20, eq. 5.1.14] argues that for large $q_{\parallel}$ behavior of T for small $\rho_{\parallel}$ is important. T is given by eq. 2.29. For small $\rho_{\parallel}$ also T is small and e^{-T} can be expanded as $1-T$. Its Fourier transformation (eq. 2.11) gives [1]

$$I_D(\rho_{\parallel}) \approx \frac{1}{4\pi} I_{Di} \frac{\sigma_D^2}{|q_{\parallel}|^3} \ . \tag{2.36}$$

Tails of diffraction peaks drop with the third power of distance $q_{\parallel}$ from the peak center. This is a typical character of scattering from dislocations [20]. Scattering in this case is connected to the variation of deformation field at small distances close to dislocation cores and not influenced substantially by dislocation arrangement.[2]

In this section, the Krivoglaz [20] theory of scattering from crystals containing randomly distributed dislocations was summarized. Krivoglaz derivation of equation 2.29 for T-factor (Fourier transform) was shown. Expressions for dislocations contrast factors were given (by equations 2.19, 2.30, 2.23). It was shown that the diffraction profiles from crystals with randomly distributed dislocations are Gaussian in their central part (eq. 2.34) and drops with $1/q^3$ for large q (eq. 2.36). An approximate formula for the peak width (eq. 2.35) in the case of non-correlated dislocations was also derived.

2.3.3 Dislocations dipoles

In real materials dislocations can often be arranged in special configurations as dislocation walls, loops and dipoles etc. Such dislocation configurations are formed during deformation process or result from processes tending to minimize the deformation energy stored in the crystal.

In this section, the scattering from dislocation dipoles is described according to theory of Krivoglaz [20], Pototskaya and Ryboshapka (1968) [46]. Contrary to section 2.3.2, where derivation of basic formulas was demonstrated, here only parts of results from Krivoglaz theory [20, ch. 5.1.3] are presented. An overview of scattering from many other configurations of dislocations can be found in Krivoglaz [20] or in Czech in Kužel (1989) [31]. Here dislocation dipoles were chosen as an extremal example of correlation in dislocation distribution treated in sections 2.3.4 and 2.3.5.

Dislocation dipoles were already studied by Gilman [47], Chen [48], Kroupa [49, 50] and Forwood [51]. X-ray scattering from crystal with dislocation dipoles was theoretically described by Pototskaya and Ryboshapka [46].

Gilman [47] described formation of a dislocation dipole from jogs produced by cross-glide of a moving screw dislocation. Such a dipole, consisting from a pair of edge dislocations, is depicted in fig. 2.5. Gilman found that in elastically isotropic fcc metals edge dislocations can form two stable configurations of dislocation

[1] For large $q_{\parallel}$ only Fourier transformation of $(-T)$ is important and $\int 1/|q|^3 \exp(-iqx)dq = x^2 \ln(|x|)$ (ref: Wolfram Mathematica 8.0).

[2] Krivoglaz [20, ch. 5.2.2] proved this also in the general case using the method of smoothly varying distortions.

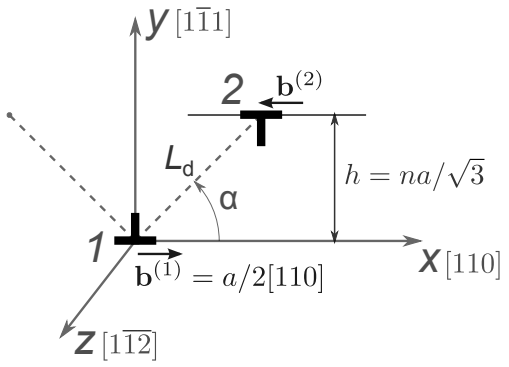

Figure 2.5: Schematic representation of a compressive dipole in fcc crystal. The dipole consists from a pair of straight edge dislocations, that are parallel to z-axis. Glide planes of dislocations are separated by distance h, which is called a dipole height. The distance of individual dislocations is L_d.
A dipole consisting of dislocations of opposite Burgers vector signs would be an extensional dipole.

dipoles with $\alpha = \pi/4$ or $3\pi/4$ (see fig. 2.5).[1] Influence of crystal anisotropy was described later by Forwood and Humble [51].

We assume here that distance L_d between dislocations in the pair is much smaller than the average distance between dislocations $r_d \sim n^{-1/2}$.[2]

$$L_d/r_d \sim \sqrt{n}L_d \ll 1$$

We can use the same notation as in the section 2.3.2 for randomly distributed dislocation and for large distances $\boldsymbol{r}_{s,t}$ from a dipole expand the scalar product $(\boldsymbol{G}\boldsymbol{u}_{s,t})$ in $r_{s,t}$ [20]

$$\boldsymbol{G}\boldsymbol{u}_{s,t} \approx (Gb)/(2\pi)\ \frac{L_d}{r_{s,t}}\ \Psi \qquad (r_{s,t} \gg L_d), \tag{2.37}$$

where Ψ is again a geometrical factor analogous to that in eqs. 2.18 and 2.19. Displacement field from the dislocation dipole decreases with the distance from the dipole and is similar to the field from the point defect in the 2D crystal. In such a case, the defect can behave both like the first and the second class defect [20]. We can substitute for $2M$ from eq. 2.37 into eq. 2.12, expand *cos* in powers and integrate in a similar way as in ch. 2.3.2. Then we obtain for the attenuation $2M$ factor of the *regular* Bragg reflection [20, eq. 5.1.32]

$$2M = \frac{(Gb)^2}{8\pi}\ \overline{\Psi^2}\ nL_d^2\ \ln\left(\frac{2\pi\zeta_d L}{GbL_d}\right), \tag{2.38}$$

where $\overline{\Psi^2}$ is the square of angular factor integrated over the directions in the plane perpendicular to the dislocation lines (it is in fact the same factor as χ for single dislocations) and $\zeta_d \sim 1$ is a constant factor. We can see that $2M$ increases with nL_d^2 and with the logarithm $\ln(L)$ of the crystal size but it is no more an increasing function of $\rho_\parallel$ and actually it is a finite constant. This would mean that the dislocation dipoles behave as the first class defects. The diffraction peak then consists of the *regular* Bragg reflection (eq. 2.14) attenuated by the e^{-2M}

[1] Kaganer [38] (ch. 2.3.6) calcualted recently also diffraction peak profiles from extensional dipoles. Unfortunately he described a different meta-stable [47] case when $\alpha = \pi/2$. Moreover in his case $L_d \geq r_d$.

[2] Essmann and Mughrabi [52] found a critical annihilation distance for dipoles in copper about 50 nm for screw dislocations and about 2 nm for edge dislocations.

factor and remaining diffuse scattering intensity in the tails (end of ch. 2.3.1). However, if $2M$ is sufficiently large the regular reflection is strongly attenuated and the diffuse scattering dominates. Mainly this case is treated here. $2M$ is large if (Gb) is large enough

$$\frac{1}{Gb} \ll \sqrt{n} L_d \sim \frac{L_d}{r_d} \ll 1. \tag{2.39}$$

This is satisfied for large densities of dipoles and high order reflections.

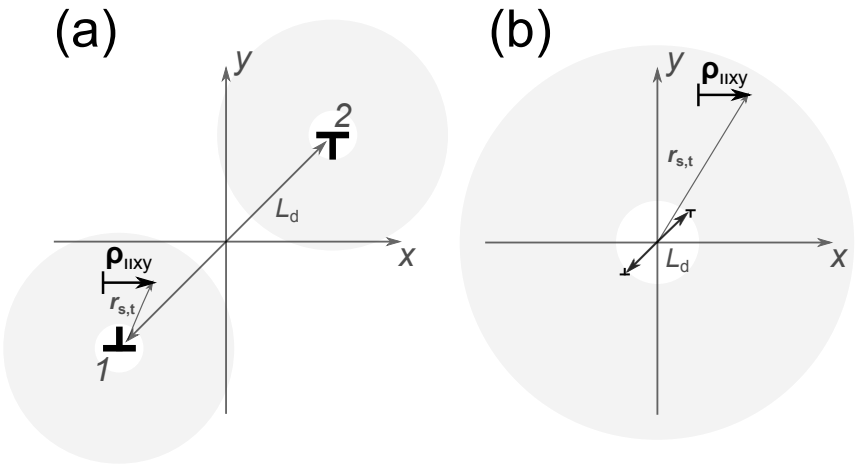

Figure 2.6: Area of the most essential contribution to T in the integration (eqs. 2.11, 2.20) over defect positions for a dislocation dipole in the case: a) $\rho_{\|xy} \ll (Gb)^{-1} L_d$ and b) $(Gb)^{-1} L_d \ll \rho_{\|xy} \ll (Gb) L_d$.

$T(\rho_\|)$ can be evaluated by integration (eqs. 2.11, 2.20) over defect positions. If $\rho_\|$ is small ($\rho_{\|xy} \ll (Gb)^{-1} L_d$), the most essential contribution to the integral comes from close vicinity of individual dislocations in the pair. This is shown in fig. 2.6 a). We can expand $(1 - e^{i\cdots})$ in the second order term for the real part of T. For the imaginary part we need the third order term [20, 38, 53] and from Krivoglaz [20, eq. 5.1.35] we have[1]

$$\begin{aligned} \mathrm{Re}\, T_\alpha &= \frac{(Gb)^2}{8\pi^2}\, \overline{\Psi_\alpha^2}\, n_\alpha\, \rho_\|^2 \ln\big(\frac{2\pi\zeta_d'(\boldsymbol{\gamma}) L_d}{Gb\rho_{\|xy,\alpha}}\big)\ , \\ \mathrm{Im}\, T_\alpha &= \frac{(Gb)^3}{16\pi^3}\, \overline{\Psi_\alpha^2 \widetilde{\Psi}_\alpha}\, n_\alpha\, \frac{\rho_\|^3}{L_d} \ln\big(\frac{2\pi\zeta_d''(\boldsymbol{\gamma}) L_d}{Gb\rho_{\|xy,\alpha}}\big)\ , \\ &\text{for } (\ \rho_{\|xy,\alpha} \ll (Gb)^{-1} L_d\ )\ , \end{aligned} \tag{2.40}$$

where $\widetilde{\Psi}_\alpha$ is a geometrical factor which reverses its sign with inversion of $\boldsymbol{G}$ or $\boldsymbol{\rho}_\|$. There can be a peak shift and asymmetry caused by a nonzero imaginary part of T but the dominating real part of T is quite similar to the case of the randomly distributed dislocations (eq. 2.29).

For longer $\rho_\|$ the interesting region of integration over defect positions is schematically depicted in fig. 2.6 b). For $\rho_\| \ll r_{s,t}$ we can expand the deformation

[1] We integrate from $(Gb)/(2\pi)\rho_{\|xy}$ to L_d.

field in a linear power of $(\rho_\parallel / r_{s,t})$ as it was done in eqs. 2.18 and 2.37[1]

$$\boldsymbol{G}(\boldsymbol{u}_{s,t} - \boldsymbol{u}_{s-\rho_\parallel,t}) \approx (Gb)/(2\pi)\ \frac{L_d \rho_\parallel}{r_{s,t}^2}\ \Psi' \ , \quad (\rho_\parallel \ll r_{s,t}) \tag{2.41}$$

where Ψ' is a geometric factor characteristic for a particular dipole type.

Now we can again substitute from eq. 2.41 into eq. 2.20 and we obtain [20, eq. 5.1.36][2]

$$\begin{aligned} \mathrm{Re}\, T_\alpha &= \frac{\pi}{8}\frac{(Gb)}{2\pi}\ \varphi'_\alpha\ n_\alpha L_d\ \rho_\parallel \ , \quad \varphi'_\alpha = \overline{|\Psi'_\alpha|} \ , \\ \mathrm{Im}\, T_\alpha &= \frac{1}{2}\frac{(Gb)}{2\pi}\ \varphi''_\alpha\ n_\alpha L_d\ \rho_\parallel \ , \\ &\text{for } (\ (Gb)^{-1} L_d \ \ll\ \rho_{\parallel xy,\alpha}\ \ll\ (Gb) L_d\ ) \ , \end{aligned} \tag{2.42}$$

where φ'_α and φ''_α are geometrical factors of order of unity. They result from integrating Ψ' over angular direction in plane perpendicular to dislocation lines. Derivation of the imaginary part of T is quite complicated [20, appendix E] and hence it is not presented here.

For even longer real space length $(\rho_{\parallel xy,\alpha} \gg (Gb)L_d)$ only deformation produced by one dislocation from the pair is essential and Krivoglaz derived for this case [20, eq. 5.1.37]

$$\begin{aligned} \mathrm{Re}\, T_\alpha &= \frac{(Gb)^2}{8\pi^2}\ \overline{\Psi_\alpha^2}\ n_\alpha L_d^2\ \ln\Big(\frac{2\pi\zeta_d(\boldsymbol{\gamma})\ \rho_{\parallel xy,\alpha}}{GbL_d}\Big) \ , \\ \mathrm{Im}\, T_\alpha &\sim \frac{1}{2}\ n_\alpha L_d^2\ \frac{L_d}{\rho_\parallel} \ln\Big(\frac{2\pi\zeta_d'''(\boldsymbol{\gamma})\rho_{\parallel xy,\alpha}}{GbL_d}\Big) \ , \\ &\text{for } (\ \rho_{\parallel xy,\alpha}\ \gg\ (Gb)L_d\ ) \ . \end{aligned} \tag{2.43}$$

Usually the case of the satisfied condition 2.39 is considered. Then T-factor is described by eq. 2.42 in the range of interest. Eq. 2.42 predicts that diffraction peaks are Lorentzian in their central part. The imaginary part of T can be included in the Fourier exponential factor $e^{iq\rho}$ and hence peaks are shifted. Krivoglaz gives for the peak width and shift [20, eq. 5.1.40]

$$\begin{aligned} I_D(q_\parallel) &= I_{Di}\frac{\sigma_D}{\pi^2(q_\parallel - q_D)^2 + \sigma_D^2} \ , \\ \sigma_D &= \frac{\pi^2}{8}\frac{(Gb)}{2\pi}\ nL_d\ \sum_\alpha \frac{n_\alpha}{n}\varphi'_\alpha \ , \\ q_D &= \frac{1}{2}\frac{(Gb)}{2\pi}\ nL_d\ \sum_\alpha \frac{n_\alpha}{n}\varphi''_\alpha(\gamma_{1,\alpha}^2 + \gamma_{2,\alpha}^2)^{1/2} \ , \end{aligned} \tag{2.44}$$

Averaged geometrical factors φ'_α and φ''_α, which determine the anisotropy of broadening and shift of peaks, were evaluated for elastically isotropic fcc crystals by Pototskaya and Ryboshapka [46].

[1] In Krivoglaz [20] Ψ' is defined from the expansion in $\boldsymbol{\rho}_{\parallel xy}$ in the case of dislocation dipoles. Here it is done in the same way as for single dislocations.

[2] Argument in eq. 2.37 decrease with $r_{s,t}^{-2}$ and hence integration can be done similarly to the case of point defects [20]. We integrate over the whole plane and we can use $\int y[1 - \cos(1/y^2)]dy = \pi/4$.

A calculation of a diffraction peak from the above formulae in a simplified case is shown for illustration at the end of this section. It must be mentioned for clarity, that not all the assumptions in this paragraph can be found in the book of Krivoglaz [20] and they are rather introduced here by the present author. So let us assume that the angular factors in $\rho_{\parallel xy,\alpha}$ can be averaged for different slip systems as in the case of non-correlated dislocations and that three expressions for T can be joined exactly at the boundaries of the approximations involved – i.e. at two points: $L_d/(Gb)$ and $L_d(Gb)$. These assumptions reduce a number of free parameters in the problem and we can write:

$$\mathrm{Re}\,T = \frac{1}{8\pi^2}\,\chi_d\,nL_d^2 \qquad \begin{cases} (Gb)^2 & x^2 & \ln\left(\frac{2\pi\zeta_d}{(Gb)|x|}\right) & |x| \le 1/(Gb) \\ (Gb) & |x| & \ln\left(2\pi\zeta_d\right) & 1/(Gb) \le |x| \le (Gb) \\ (Gb)^2 & & \ln\left(\frac{2\pi\zeta_d|x|}{(Gb)}\right) & |x| \ge (Gb) \end{cases}, \tag{2.45a}$$

$$\mathrm{Im}\,T = \frac{1}{8\pi^2}\,\chi_d''\,nL_d^2\,\frac{(Gb)}{2\pi} \begin{cases} (Gb)^2 & x^3 & \ln\left(\frac{2\pi\zeta_d''}{(Gb)|x|}\right) & |x| \le 1/(Gb) \\ & x & \ln\left(2\pi\zeta_d''\right) & 1/(Gb) \le |x| \le (Gb) \\ (Gb)^2 & \frac{1}{x} & \ln\left(\frac{2\pi\zeta_d''|x|}{(Gb)}\right) & |x| \ge (Gb) \end{cases}, \tag{2.45b}$$

where $x = \rho_\parallel/L_d$. Then T and diffraction profile $I(q_\parallel)$ can be calculated. We consider, for example, deformed fcc copper and dislocations with the Burgers vector $b \approx 2.6$ Å and reflections (331) or (420). This gives $(Gb) = 6\pi \approx 20$. To fulfill the second part of condition 2.39 let $\sqrt{n}L_d \approx L_d/r_d = 1/3$.[1] Real and imaginary Fourier coefficients e^{-T} are in that case depicted in fig. 2.7. Diffraction profile $I_D(q_\parallel)$ calculated numerically is shown in fig. 2.8. Also the Lorentzian profile 2.44 with width σ_D and shift q_D is plotted there

$$\sigma_D L_d = \frac{1}{8\pi^2}\,\chi_d\,nL_d^2\,(Gb)\,\ln\left(2\pi\zeta_d\right),$$
$$q_D L_d = \frac{1}{8\pi^2}\,\chi_d\,nL_d^2\,\frac{(Gb)}{2\pi}\,\ln\left(2\pi\zeta_d''\right).$$

It can be seen (fig. 2.7) that the exponent is identical to the real part of T for $x \le (Gb)$, which is the range of interest. For larger x the curves are different, but if we assumed two times larger G the exponential approximation would be valid for wider range of x. The difference of curves for longer x manifest itself in the dependence of diffracted intensity $I(q_\parallel)$ in the very close vicinity of the peak maximum (fig. 2.8). It can be seen from fig. 2.8 that the Lorentzian function (eq. 2.44) approximates the calculated diffraction profile very well at peak tails. It is also evident that the diffraction profile calculated from eqs. 2.45 is not shifted but it is rather asymmetric. This is not surprising because the imaginary part of T according to eqs. 2.43 and 2.45 (fig. 2.7) approaches zero when $\rho_\parallel \to \infty$.

Finally, we should comment shortly that the simplified formulas eqs. 2.45, were introduced for the first time in this work. When the original Krivoglaz approximate formulas were sticked the anisotropic geometrical (contrast) factors

[1] In addition we set $\chi_d = \chi_d'' = \pi$ and $\zeta_d = \zeta_d'' = 1/2$ as earlier (ch. 2.3.2).

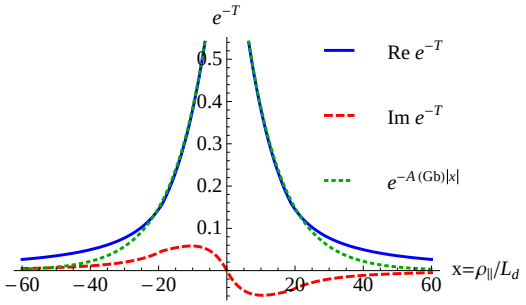

Figure 2.7: Simplified Fourier coefficients e^{-T}(eq. 2.45) for dislocation dipoles. $(Gb) = 6\pi \approx 20$, $L_d/r_d = 1/3$. Blue line - real part, dashed red - imaginary part, dotted green - exponential approximation.

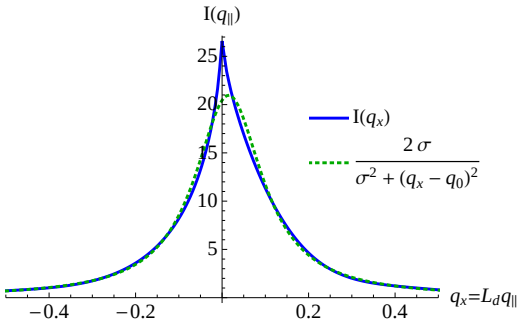

Figure 2.8: Calculated diffraction profile from a crystal containing dislocation dipoles. The same model as in fig. 2.7. Blue line - Fourier transformation of e^{-T}, dotted green - shifted Lorentzian approximation (eq. 2.44).

had to be also linked together. Hence it was assumed that

$$\begin{aligned} \overline{\Psi_\alpha^2}\ln(2\pi\zeta_d) &\leftrightarrow 1/2\ \varphi'_\alpha = 1/2\overline{|\Psi_\alpha|}\ , \quad \chi_{d,\alpha} \equiv \overline{\Psi_\alpha^2}\ , \\ \overline{\Psi_\alpha^2}\widetilde{\Psi}_\alpha\ln(2\pi\zeta''_d) &\leftrightarrow 1/2\ \varphi''_\alpha\ , \end{aligned} \tag{2.46}$$

where $\chi_{d,\alpha}$ is formally defined. It must be emphasized that it should be taken into account that this factor is probably different from the contrast factors of edge dislocations constituting the dipole because of angular dependence of the deformation field of the dipole (eqs. 2.18, p. 16, 2.41). This is considerably different from that of a single edge dislocation. The quantities χ_d and χ''_d in eqs. 2.46 for peak width and shift are not necessarily equivalent as it was assumed in the simulation in figs. 2.7 and 2.8. It was also indicated in Krivoglaz Lorentzian approximation (eq. 2.44) that calculation of these contrast factors for dipoles should be based on quantities φ'_α and φ''_α rather than on $\overline{\Psi_\alpha^2}$. Analysis of the peak broadening and shift (asymmetry) anisotropy is of interest because the dipole type could be identified in principle from the anisotropy. The values φ'_α and φ''_α were calculated by Pototskaya and Ryboshapka [46] (in Russian).[1]

Kaganer and Sabelfeld in their recent paper [38] also proposed an approximation for the imaginary part of T. Instead of eqs. 2.45 they used a peak shift and the third power expansion in $\rho_{\|}$, i.e. they used a linear combination of eqs. 2.40 and 2.42 for a whole range of $\rho_{\|}$. The (hkl) anisotropy of the peak shift and asymmetry was not discussed there. They also treated a different dipole type.

In this section, the scattering from crystal containing dislocation dipoles was theoretically studied. It was shown that dislocation dipoles can behave as both the defects of the first as well as the second class. In the former case, the diffraction peak consists of attenuated delta shaped regular maximum and diffuse scattering at peak tails. If the defect density is high enough and reflections with the

[1] Unfortunately the present author has not been able to reproduce some results from [46], which are also cited in [20], i.e. mainly the point reporting 3× stronger broadening of (hhh) reflection than of $(h00)$ in the case of the elastically isotropic fcc crystals. Moreover it must be again noted that in the case of dislocation monopoles significant influence of crystal elastic anisotropy was found [17, 42] and this effect has not been considered for the dipoles at all.

large diffraction vector G are studied, i.e. condition 2.39 is satisfied, the dipoles behave as the second class defects. Calculation of diffraction profile is complicated in the case of dipoles. Different approaches (eqs. 2.40–2.43) must be used for different parts of the profile. Krivoglaz approximated the diffraction profiles from the crystal with dipoles by a shifted Lorentzian function (eq. 2.44). It was proposed here on the basis of Krivoglaz theory that the shift is connected rather with an asymmetry of the diffraction profile (fig. 2.8). Contrast factors for the peak shift (asymmetry) and broadening in the case of dislocation dipoles were discussed and it was concluded that this problem has not been solved completely yet.

2.3.4 Correlated dislocations

Non-correlated dislocations were studied in section 2.3.2. The case of an extreme correlation of a pair of dislocations forming dislocation dipole was treated in section 2.3.3. Wilkens 1970 [18] and Krivoglaz [20] developed more general models of correlations in the dislocation arrangement. These models account for screening of deformations fields of dislocations in the crystal. This screening reduces the elastic energy accommodated in the crystal. Wilkens [19] and Krivoglaz [20] demonstrated that such screening has essential influence on the shape of diffraction profiles and developed methods of calculation of diffraction profiles from crystals with correlated dislocations. In this section, Krivoglaz approach [20, ch. 5.2.2] for the correlation of a pair of dislocations is shortly introduced. The method of Wilkens is described later in section 2.3.5.

We restrict ourselves here only to the simplest case of a correlation in positions of two defects at lattice sites $\boldsymbol{R}_t$ and $\boldsymbol{R}_{t'}$ and assume that the correlations of higher order (between more than two dislocations) can be neglected. Their influence is widely discussed by Krivoglaz [20] or e.g. by Groma [53] or Ungár [54].

We can again start from eq. 2.8 but cannot proceed to eq. 2.9 if the correlation should be accounted. Instead, the generalized cumulant expansion method [20, appendix A] is usually used. Taking into account that defect concentrations c_α are very small and by simplifying logarithmic terms (as we did to obtain eq. 2.10) we can arrive at [20, eq. A.36]

$$\begin{aligned} T(\boldsymbol{R}_s, \boldsymbol{\rho}_\parallel) &= \sum_\alpha c_\alpha \sum_t \left[1 - e^{i\boldsymbol{G}(\boldsymbol{u}_{s,t,\alpha} - \boldsymbol{u}_{s-\rho_\parallel,t,\alpha})}\right] \\ &- \sum_{\alpha\alpha'} \sum_{t<t'} \varepsilon_{\alpha\alpha'}(\boldsymbol{R}_{tt'}) \left[1 - e^{i\boldsymbol{G}(\boldsymbol{u}_{s,t,\alpha} - \boldsymbol{u}_{s-\rho_\parallel,t,\alpha})}\right] \left[1 - e^{i\boldsymbol{G}(\boldsymbol{u}_{s,t',\alpha'} - \boldsymbol{u}_{s-\rho_\parallel,t',\alpha'})}\right] \end{aligned} \tag{2.47}$$

where we introduced a (binary) *pair distribution function* describing correlation between defects of type α and α' at sites $\boldsymbol{R}_t$ and $\boldsymbol{R}_{t'}$

$$\varepsilon_{\alpha\alpha'}(\boldsymbol{R}_{tt'}) \equiv \left\langle (c_{t,\alpha} - c_\alpha)(c_{t',\alpha'} - c_{\alpha'}) \right\rangle . \tag{2.48}$$

We will discuss here the simplest case and assume only correlation between positions of parallel straight dislocations of the same type. Hence we are interested only in the pair correlation functions for which $\alpha = \alpha'$, where α marks the slip system and the edge or screw character of dislocations. However we will

be distinguishing between dislocations of opposite signs. A simple model can be accepted introduced by Krivoglaz [20, ch. 5.2.2] that the dislocations with the opposite Burgers vector sign are attracted whereas there is some repuslion between the dislocations of the same sign. We assume that the repulsive and attractive tendencies are of the same strength and can be described by the same function

$$\varepsilon_{\alpha\alpha}(r_{tt'}) \equiv \varepsilon_{\alpha\alpha}^{+-} = \varepsilon_{\alpha\alpha}^{-+} = -\varepsilon_{\alpha\alpha}^{++} = -\varepsilon_{\alpha\alpha}^{--} \ . \tag{2.49}$$

Another assumption already included in the above eq. 2.49 is uniformity of the dislocation ensemble expressed by the dependence of the pair correlation functions $\varepsilon_{\alpha\alpha}$ only on the distance $r_{tt'}$ between points where dislocations intersect the perpendicular plane. Some problems when certain conditions 2.49 are not satisfied, e.g. there is no correlation between dislocations of the opposite sign ($\varepsilon_{\alpha\alpha}^{+-} = \varepsilon_{\alpha\alpha}^{-+} = 0$), or there is a polarization ($\delta\varepsilon_{\alpha\alpha} \equiv \varepsilon_{\alpha\alpha}^{+-} - \varepsilon_{\alpha\alpha}^{-+} \neq 0$) in the dislocation distribution, are treated in detail in [20, ch. 5.2.2, appendix F] and only shortly commented here later.

In a way similar to the derivation of integral form of eq. 2.20 we can obtain integral expressions for T also for correlated dislocations [20, eqs. F.1-3]

$$T(\rho_\parallel) = \sum_\alpha T_\alpha(\rho_\parallel) \ , \quad T_\alpha = T_{0,\alpha} + T_{1,\alpha} \ , \tag{2.50}$$

$$T_{0,\alpha} = n_\alpha \int d^2\boldsymbol{r}_t \ \left(1 - \cos[\boldsymbol{G}(\boldsymbol{u}_{s,t,\alpha} - \boldsymbol{u}_{s-\rho_\parallel,t,\alpha})]\right) \ , \tag{2.51}$$

$$T_{1,\alpha} = -\frac{2}{S_0^2} \iint d^2\boldsymbol{r}_t d^2\boldsymbol{r}_{t'} \ \varepsilon_{\alpha\alpha}(r_{tt'}) \sin[\boldsymbol{G}(\boldsymbol{u}_{s,t,\alpha} - \boldsymbol{u}_{s-\rho_\parallel,t,\alpha})] \sin[\boldsymbol{G}(\boldsymbol{u}_{s,t',\alpha} - \boldsymbol{u}_{s-\rho_\parallel,t',\alpha})] \ , \tag{2.52}$$

where $\boldsymbol{u}_{s-\rho_\parallel,t,\alpha}$ is a displacement at site $\boldsymbol{R}_s$ from a dislocation of the (+) Burgers vector sign situated at site $\boldsymbol{R}_t$ in the slip system α. T_0 term is equivalent to T for uncorrelated dislocations and T_1 accounts for dislocation correlation under assumptions 2.49.

Wilkens [55],[1] Krivoglaz [20, eq. 5.2.19] and later Kaganer [38, eq. 24] introduced a *screening condition* for deformation fields of defects. T_0 is a function of the crystal size (eq. 2.29). If T should not depend on the crystal size, T_1 must cancel size dependent parts in T_0. Considering the displacements from two defects separated by $r_{tt'}$ at two points located at distance $\rho_\parallel$, (assuming that both distances $\rho_\parallel$ and $r_{tt'}$ are small in comparison to $r_t \sim r_{t'}$), we can expand the cos and sin terms in eqs. 2.51, 2.52, approximate $1/r_{t'} \approx 1/r_t$ and sum up T_0 and T_1.

[1] Theory of Wilkens is different from the approach of Krivoglaz described here, but the basic idea of *screening* of deformation fields from correlated defects is very similar.

Finally we obtain the *screening condition*[1]

$$\frac{1}{2}n_\alpha - \frac{2}{S_0^2}\int \varepsilon_{\alpha\alpha}(r_t)\ d^2\boldsymbol{r}_t = 0\ . \tag{2.53}$$

Krivoglaz evaluated T_0 term for uncorrelated dislocation at first. In [20, appendix F] he confirmed by a more accurate calculation (than it was used in ch. 2.3.2 the validity of eq. 2.28 for the case of screw dislocations.[2] Krivoglaz confirmed that there is the factor $|\boldsymbol{Gb}|\rho_{\parallel xy}$ in the denominator of the logarithm in eq. 2.28. This is important for further calculations and comparison with results of Wilkens. He also pointed out that eq. 2.28 is better valid for reflections with $(Gb)/(2\pi) \gg 1$.

Another step in the analysis of correlated dislocations is the evaluation of the T_1 term (eq. 2.52). Krivoglaz proposed a few types of analytical continuous pair distribution functions $\varepsilon_{\alpha\alpha}$ [20, eq. 5.2.23]. The Gaussian function, with only one parameter - *correlation radius* r_c, was chosen here

$$\varepsilon_{\alpha\alpha}(r_{tt'}) = \frac{1}{4\pi}n_\alpha S_0^2\ 1/r_c^2\ e^{-r_{tt'}^2/r_c^2}\ . \tag{2.54}$$

Krivoglaz calculated the T_1 term in the second order approximation in $\rho_\parallel$ under assumptions that the correlation radius r_c is not too small [20, eq. F.14]

$$T_1(\rho_\parallel) \approx -\frac{(Gb)^2}{8\pi^2}\chi_\alpha\ n_\alpha\ \rho_\parallel^2\ \ln\big(\frac{2\pi\zeta_2 L}{r_c}\big)\ ,$$

where χ_α is again the dislocation orientation factor defined by eqs. 2.19, 2.23 and for ζ_2 in the case the Gaussian correlation function (eq. 2.54) Krivoglaz [20, eq. F.15] found that

$$\ln\zeta_2 = {}^1\!/_2\ \gamma = {}^1\!/_2\ 0.577\ldots\ ,$$

where γ is the Euler-Mascheroni constant.

When we sum (eq. 2.50) T_0 (eq. 2.28) and T_1, we see that the logarithmic terms $\ln(L)$ mutually cancel each other and T is independent of the crystal size L

$$T_\alpha(\rho_\parallel) \approx \frac{(Gb)^2}{8\pi^2}\chi_\alpha\ n_\alpha\ \rho_\parallel^2\ \ln\big(\frac{2\pi\zeta_{c,\alpha}r_c}{|\boldsymbol{Gb}|\rho_{\parallel xy,\alpha}}\big)\ . \tag{2.55}$$

[1] Wilkens in his approach operates rather in terms of mean square stresses $\langle\sigma^2\rangle$ then in differences of displacements $(\boldsymbol{u}_s - \boldsymbol{u}_{s-\rho_\parallel})$, which are similar to strain ϵ when $\rho_\parallel \to 0$. If we studied an ensemble average of the variance of strain ϵ_s at the site $\boldsymbol{R}_s$ we would get

$$\big\langle(\epsilon_s - \langle\epsilon_s\rangle)^2\big\rangle \approx c\sum_t \epsilon_{s,t}^2 + \sum_{\substack{t,t'\\(t\neq t')}} \varepsilon_{t,t'}\epsilon_{s,t}\epsilon_{s,t'} = n\sum_t S_0\epsilon_{s,t}^2 - \frac{4}{S_0^2}\sum_{\substack{t,t'\\(t\neq t')}} S_0^2\varepsilon_{t,t'}\epsilon_{s,t}\epsilon_{s,t'}$$

From the above equation we can obtain the screening condition 2.53 if we require that the variance of strain from an arrangement of defects vanishes at large distances from defects.

[2] The only difference is that in [20, appendix F] $\zeta_{0,\alpha} \approx 3.05$ whereas in [20, ch. 5.1.1] $\zeta_{0,\alpha} = 1/2$. This may indicate a mistake in 2π factor or a different definition of the characteristic crystal dimension L. However, if ζ_0 had been $2\pi\times$ larger in ch. 2.3.2, then the effective number of dislocations N_{eff} would have been also larger and approximations in ch. 2.3.2 would have been more accurate. Some numerical calculation would be helpful in this point.

In the lowest approximation for small $\rho_{\parallel}$ the expression for T (eq. 2.55) has the same form as for the non-correlated dislocations (eq. 2.28), only constants $\zeta_{0,\alpha} \leftrightarrow \zeta_{c,\alpha}$, the crystal size and the correlation length $L \leftrightarrow r_c$ are replaced.

If we now recall the discussion about the line width at the end of the chapter about non-correlated dislocations (ch. 2.3.2) we can define an effective number of dislocations in the correlated area $N_{eff} \sim \pi n r_c^2$ exactly in the same way. We again only replace $\zeta_{0,\alpha} \leftrightarrow \zeta_{c,\alpha}$ and $L \leftrightarrow r_c$ in eq. 2.31.[1] It is evident that the diffraction line width is determined by the same expression (eq. 2.35) as for uncorrelated dislocations but the l_m factor (eqs. 2.32 and eqs. 2.33, $l_0 = \ln\sqrt{N_{eff}}$) is substantially smaller because we assume much lower number of dislocations in the correlated area than in the whole crystal. We assume $L \gg r_c \geq r_d$. If we now recall the fig. 2.4 showing the Gaussian approximation of the $x^2 \ln(\sqrt{N_{eff}}/|x|)$ function, we can remember that for smaller values of N_{eff} (e.g. already for $N_{eff} \sim 100$) e^{-T} significantly differs from the Gauss profile. The effect is even stronger [20, fig. 5.3] for smaller $N_{eff} \sim 2 - 10$.

In summary, the main effect of dislocation correlation on diffraction profiles is that the size of the crystal L is replaced by the correlation radius r_c. Peak broadening from dislocations does not depend on the crystal size L and does not growth with $\ln(L)$. The effective crystal size, which appears in expressions for the diffraction profile width and shape, is finite, substantially smaller than the crystal size and is of a same order as the correlation radius. It can be identified with a dimension of the area where dislocations are correlated.

In a very important case of the basic Wilkens model (ch. 2.3.5) no correlation between dislocations of the same Burgers vector sign ($\varepsilon_{\alpha\alpha}^{++} = \varepsilon_{\alpha\alpha}^{--} = 0$) is assumed . Krivoglaz [20, Appendix F, ch. 5.2.2] showed that in such a case contribution $\widetilde{T}_{1,\alpha}$ must be added to the real part of T in eq. 2.50. An explicit expression for $\widetilde{T}_{1,\alpha}$ can be found in [20, eq. F.4] and it has a similar structure as eq. 2.52 for $T_{1,\alpha}$, only the trigonometric functions are different. Krivoglaz proved [20, Appendix F] that the contribution of $\widetilde{T}_{1,\alpha}$ is comparable only with the higher order approximation of $T_{1,\alpha}$, than that used to get eq. 2.55. It is of order $\sim \rho_{\parallel}^4$ and it can be neglected for small $\rho_{\parallel}$. The absence of correlation between dislocation of the same sign influences diffraction line profiles only slightly and characteristic consequences of dislocation correlation discussed above are therefore not affected. If a polarization ($\delta\varepsilon_{\alpha\alpha} \equiv \varepsilon_{\alpha\alpha}^{+-} - \varepsilon_{\alpha\alpha}^{-+} \neq 0$) in the dislocation ensemble appears, e.g. as in the case of formation of dislocation dipoles, an additional term T_{α}'' has to be added to T in eq. 2.50. An expression for T_{α}'' has again a similar structure as $T_{1,\alpha}$ (eq. 2.52) or $\widetilde{T}_{1,\alpha}$, but T_{α}'' is purely imaginary. This imaginary term is of the order of $\sim \rho_{\parallel}^3$ [20, eq. F.18], which results in an asymmetry of diffraction profiles, as it was shown for the case of dislocation dipoles (ch. 2.3.3, figs. 2.7 and 2.8). The asymmetry of diffraction peaks is a typical attribute connected with polarization in the dislocation ensemble. It was discussed in literature, e.g. by Groma [53, 57, 58], Ungár [54] or Kaganer [38].

[1] In Krivoglaz [20, ch. 5.2.2], Klimanek and Kužel [17] and Kužel [56] $P = \sqrt{N_{eff}}$.

2.3.5 Wilkens model of dislocation correlation

After publishing Krivoglaz-Rayboshapka theory of scattering from crystals containing random dislocations Krivoglaz and Ryaboshapka [20, 59, 60] Wilkens [19, 61] showed that completely random distribution of dislocations in crystal is not realistic and developed his own approach, shortly described in this section.

Energy stored in the deformation field of dislocations in the crystal is equal to the mean square strain (stress) and through this to the the logarithm of crystal size. For the stored elastic energy density it holds [18, 30, 39, 62, 63]

$$\begin{aligned} W_d &\sim \langle \epsilon^2 \rangle \\ &= \frac{Gb^2}{4\pi\kappa} n \ln(L/4r_0) \ , \end{aligned} \tag{2.56}$$

where G is the shear modulus, r_0 the inner cut-off radius parameter ($r_0 = b$ in [64, 65]) and κ is a factor accounting for the dislocation type ($\kappa_s = 1$ for screw dislocations, $\kappa_e = (1 - \nu)$ for edge). Increasing energy density with the crystal size was found to be physically unrealistic in many cases and it was found from experimental data [63–65] that the crystal size L in eq. 2.56 should be replaced with a mean dislocation distance $r_d \sim n^{-1/2}$.[1] Wilkens thus introduced the model of a *restrictedly random distribution of dislocations* [18, 55]. Within this model Wilkens evaluated the stored energy [18, 55], the shape of diffraction profiles [19] and proposed a method of determination of dislocation density in deformed single crystals from the diffraction profiles [68]. The model has become a basis for many applications.[2]

In the model of a random dislocation distribution the dislocations intersect a whole cut of the crystal at random points. In the model of a *restrictedly random distribution of dislocations* the whole cutting area is subdivided into smaller pieces of area S_p (Wilkens used explicitly circular areas). Within each such an area S_p there should be in average $N_p = nS_p$ dislocations. Instead of placing the whole set of N_d dislocations in the crystal randomly within the whole area of the crystal cut, N_p dislocations are randomly distributed within each of the subareas S_p. Because we are distributing dislocations of two signs, we have $N_{p+} = N_{p-} = N_p/2$ dislocations of a single sign in each subarea. If dislocations were distributed completely randomly the probability P^{++} of finding two dislocation of the same (+) sign within the same area S_p would be proportional to N_{p+}^2. In the Wilkens model it is however proportional to $N_{p+}(N_{p+} - 1)$, because when we place one of N_{p+} dislocation with the subarea we have only $(N_{p+} - 1)$ dislocation available to be placed within the same subarea. Probability of finding another dislocation of the same sign at some site inside the subarea is equal to $\frac{c}{2}(1 - 1/N_{p+})$. It is reduced inside the subarea not-negligibly especially if the subarea S_p is small and there are only few ($N_p \ll N_d$) dislocations within. In the basic Wilkens model a correlation between dislocations of the opposite signs is not required.

Interpretations of the Wilkens model can be found in many papers or theses (van Berkum [70], Ribárik [75]), widely it is described in the thesis of Lynch [73].

[1] See also discussion [62, 66, 67].

[2] The Wilkens model was used e.g. in Scardi and Leoni [11], Ribárik et al. [23], Matěj [26], Kužel [31], Armstrong et al. [41], Ungár [54], Kužel [56], Wilkens [69], van Berkum [70], Kamminga and Delhez [71], Cheary et al. [72], Lynch [73], Gubicza et al. [74], Ribárik [75].

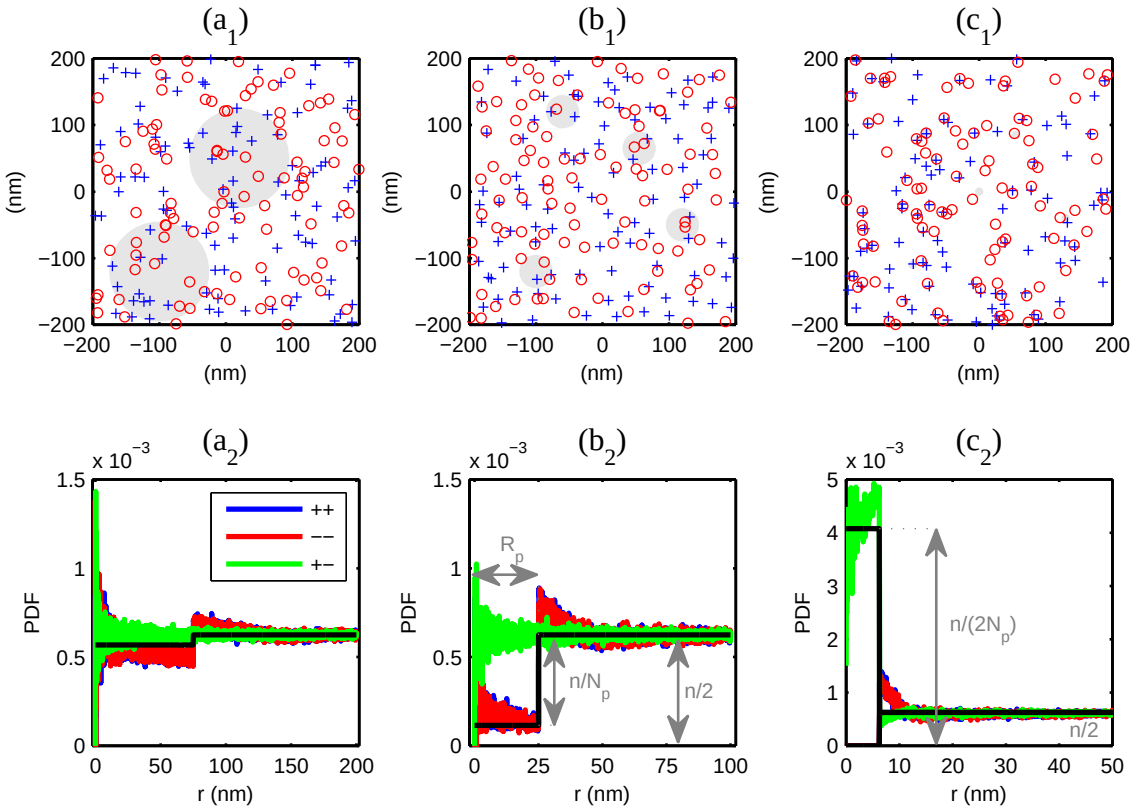

Figure 2.9: An example of the Wilkens dislocation distribution. Dislocation configurations were generated for dislocation density $n = 1.25\ 10^{-3}$ nm^{-2} and various parameters of the Wilkens model: (a) $R_p = 75$ nm ($N_p \approx 22$), (b) $R_p = 25$ nm ($N_p \approx 2.5$) and (c) $R_p = 6.25$ nm ($N_p \approx 0.15$).
The upper row of subplots shows the generated distributions. Dislocations with Burgers vector of a positive sign are depicted by blue crosses, dislocations with a negative sign by red circles. Circular areas with a radius R_p are depicted in grey to illustrate the scale. In the case (c) the grey areas are comparable with the size of red circles.
The lower row of subplots shows dislocations pair distribution functions (PDF) calculated from 5000 of such dislocation distributions as depicted above. PDF for dislocations of the same sign are plotted as blue and red lines, PDF for dislocations of the opposite sign are plotted in green.

In order to illustrate the model here some particular random defect configurations generated by a computer simulations are depicted in fig. 2.9. Usually three cases are considered.

(i) If the subareas are large enough, as compared with the mean dislocation distance ($R_p \gg r_d$), there are many dislocations inside each subarea ($N_p > 10 - 100$), correlation of dislocation positions is very weak and dislocation strain fields are only ineffectively screened as in the case of completely randomly distributed dislocations. This situation is depicted in figs. 2.9a.

(ii) If the subareas size is comparable with the mean dislocation distance $R_p \sim r_d$ there are only few dislocation inside each subarea ($N_p \sim 2 - 10$), dislocation correlation is not-negligible, dislocations of the same sign tends to distribute pseudo-regularly within the crystal cut. It can be seen in figs. 2.9b. Dislocation strain fields partially overlap and are effectively screened at long distances.

(iii) If the size of subareas is smaller than the mean dislocation distance

$R_p \ll r_d$ there is a very low probability of finding a dislocation in such an area ($N_p \approx 0-1$). If we look at the tendency of a pair distribution function depicted in figs. 2.9(a–b) we can see that the anticorrelation of dislocations of the same sign is limited. The limit is reached when less than two dislocations (one positive and one negative) have to be placed in a single subarea. However, the Wilkens model works again if correlation between dislocations of the opposite signs is allowed. This situation is shown in fig. 2.9c. In the example distribution there dislocations pairs forming small dislocations dipoles can be seen. Deformation fields in such dislocations configurations are very effectively screened.

The above consideration can be translated into the Krivoglaz notation.[1] Two cases must be distinguished. The case $N_p \geq 2$ when only anticorrelation of dislocations of the same sign is considered and the case $N_p \leq 2$ when also correlation of dislocations of the opposite signs is nonzero.

For the case $N_p \geq 2$ instead of eq. 2.49 we have

$$\begin{aligned} &\varepsilon_{\alpha\alpha}^{+-} = \varepsilon_{\alpha\alpha}^{-+} = 0 \ , \\ &\varepsilon_{\alpha\alpha}(r_{tt'}) \equiv -\frac{1}{2}\varepsilon_{\alpha\alpha}^{++} = -\frac{1}{2}\varepsilon_{\alpha\alpha}^{--} \qquad \text{(inside of } S_p) \ , \\ &\varepsilon_{\alpha\alpha}^{+-} = \varepsilon_{\alpha\alpha}^{-+} = \varepsilon_{\alpha\alpha}^{++} = \varepsilon_{\alpha\alpha}^{--} = 0 \qquad \text{(outside of } S_p) \end{aligned} \tag{2.57}$$

and instead of the *screening condition* 2.53 and the Gaussian correlation function 2.54 a step like function

$$\begin{aligned} &\varepsilon_{\alpha\alpha}(r_{tt'}) = \frac{1}{N_p}\left(\frac{nS_0}{2}\right)^2 \qquad \text{(inside of } S_p) \ , \\ &\varepsilon_{\alpha\alpha}(r_{tt'}) = 0 \qquad \text{(outside of } S_p) \ . \end{aligned} \tag{2.58}$$

For the case $N_p \leq 2$ it follows

$$\begin{aligned} &\varepsilon_{\alpha\alpha}^{++} = \varepsilon_{\alpha\alpha}^{--} = -\left(\frac{nS_0}{2}\right)^2 \qquad \text{(inside of } S_p) \ , \\ &\varepsilon_{\alpha\alpha}^{+-} = \varepsilon_{\alpha\alpha}^{-+} = (\frac{2}{N_p} - 1)\left(\frac{nS_0}{2}\right)^2 \qquad \text{(inside of } S_p) \ , \\ &\varepsilon_{\alpha\alpha}(r_{tt'}) \equiv \frac{1}{2}(\varepsilon_{\alpha\alpha}^{+-} - \varepsilon_{\alpha\alpha}^{++}) = \frac{1}{N_p}\left(\frac{nS_0}{2}\right)^2 \qquad \text{(inside of } S_p) \ . \end{aligned} \tag{2.59}$$

$\varepsilon_{\alpha\alpha}$ is the same in both cases and there is always no correlation outside S_p.

The first important result of the Wilkens model is that the effective crystal size L in the expression for the mean square stress and stored energy (eq. 2.56) is replaced by a different parameter connected with the subarea radius R_p [18, 55]

$$\ln(L/4r_0) \leftrightarrow \ln(\frac{\alpha_p R_p}{r_0}) \ , \text{where } \alpha_p \simeq 1/2 \ . \tag{2.60}$$

In a conventional theory of the line profile analysis an important quantity are cosine Fourier coefficients, which can be expanded as (see [26] or the classical

[1] Done here by the present author.

book of Klug and Alexander [5, eq. 9.57])

$$\langle\cos[\boldsymbol{G}(\boldsymbol{u}_s - \boldsymbol{u}_{s-\rho_\parallel})]\rangle = 1 - \frac{1}{2}G^2\rho_\parallel^2\langle\epsilon_{\boldsymbol{G}}(\rho_\parallel)^2\rangle + \sum_{k=2}^{\infty}\frac{(-1)^k(G\rho_\parallel)^{2k}}{(2k)!}\ \langle\epsilon_{\boldsymbol{G}}(\rho_\parallel)^{2k}\rangle\ ,$$

$$\text{where}\quad \epsilon_{\boldsymbol{G}}(\rho_\parallel) \equiv \frac{\boldsymbol{m}(\boldsymbol{u}_s - \boldsymbol{u}_{s-\rho_\parallel})}{\rho_\parallel}\ , \qquad (\boldsymbol{m}\|\boldsymbol{G}\ ,\ |\boldsymbol{m}| = 1)\ . \tag{2.61}$$

If we take only the first term in the expansion we can set

$$T = \frac{1}{2}G^2\rho_\parallel^2\langle\epsilon_{\boldsymbol{G}}(\rho_\parallel)^2\rangle\ . \tag{2.62}$$

The second success of the Wilkens model is that Wilkens was able to evaluate the mean square "smeared" strain in eq. 2.62 analytically. According to him it holds [19]

$$\langle\epsilon_{\boldsymbol{G},\alpha}(\rho_\parallel)^2\rangle = (\frac{b}{2\pi})^2\ \chi_\alpha\ n_\alpha\ f(\frac{\rho_{\parallel xy,\alpha}}{R_e})\ , \tag{2.63}$$

where $f(\dots)$ is the Wilkens function and R_e is an *outer cut-off radius*. According to Wilkens [19] it is connected with the model parameter R_p

$$R_e = e^{-1/4}\ R_p = 0.78\ R_p\ , \tag{2.64}$$

which holds for screw dislocations and approximately also for other dislocation types. For small real space length $\rho_\parallel$ Wilkens gives ([19, eq. 4.8])

$$f(\frac{\rho_{\parallel xy,\alpha}}{R_e}) = -\ln\left(\frac{\rho_{\parallel xy,\alpha}}{R_e}\right) + 2\ . \tag{2.65}$$

But Wilkens was able to evaluate f also for any $\rho_\parallel$. If we define [18, eq. A.7]

$$\eta = \frac{\rho_{\parallel xy,\alpha}}{2R_p} = \frac{1}{2}e^{-1/4}\ \frac{\rho_{\parallel xy,\alpha}}{R_e}$$

and $f = f^*(\eta)$, it follows [19, eq. A.8]

$$f^*(\eta) = \begin{cases} -\ln\eta + \left(\frac{7}{4} - \ln 2\right) + \frac{512}{90\pi}\frac{1}{\eta} + \frac{2}{\pi}\left[1 - \frac{1}{4\eta^2}\right]\ \int_0^\eta \frac{\arcsin t}{t}dt \\ \qquad -\frac{1}{\pi}\left[\frac{769}{180}\frac{1}{\eta} + \frac{41}{90}\eta + \frac{2}{90}\eta^3\right]\ \sqrt{1-\eta^2} & \text{for } \eta \le 1 \\ \qquad -\frac{1}{\pi}\left[\frac{11}{12}\frac{1}{\eta^2} + \frac{7}{2} + \frac{1}{3}\eta^2\right]\ \arcsin\eta + \frac{1}{6}\eta^2 \\ \\ \frac{512}{90\pi}\frac{1}{\eta} - \left[\frac{11}{24} + \frac{1}{4}\ln(2\eta)\right]\frac{1}{\eta^2} & \text{for } \eta \ge 1 \end{cases} \tag{2.66}$$

The Wilkens functions (eqs. 2.65 and 2.66) are plotted in fig. 2.10.[1]

[1] The expression (eq. 2.66) for $f^*(\eta)$ for $\eta \le 1$ can be substantially simplified when expanded into the powers of η. This was done by van Berkum [70] up to the third order in η. This modification of the Wilkens formula is called *van Berkum formula* and was used widely by e.g. Scardi and Leoni [11] or Matěj [26]. The van Berkum approximation introduces a small (≈ 0.001) discontinuity at $\eta = 1$, which was mentioned also by Kaganer [38]. If needed this error can be decreased below the numerical precision by the expansion of the high order.

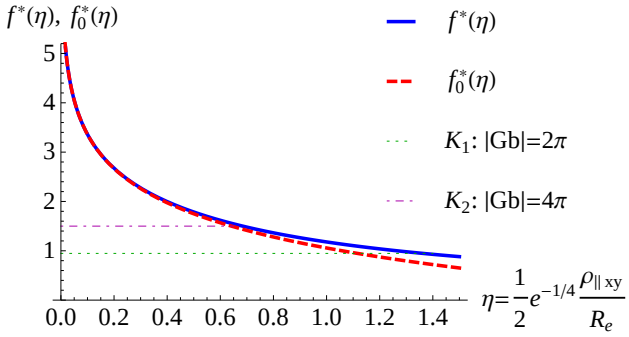

Figure 2.10: Wilkens function $f^*(\eta)$ (eq. 2.66) and its zero order approximation $f_0^*(\eta)$ (eq. 2.65). K_ν coefficients (eq. 2.67) are depicted as horizontal lines for $|\boldsymbol{Gb}| = 2\pi$ and $|\boldsymbol{Gb}| = 4\pi$.

Clear advantage of the above Wilkens formula is that $T \sim \rho_\parallel^2\, f(\eta)$ (eq. 2.62) is always positive and approaches infinity when $\rho_\parallel \to \infty$. This means that e^{-T} falls to zero and we can calculate Fourier coefficients for arbitrary parameters of the Wilkens model and real space $\rho_\parallel$. Unfortunately there is a hidden problem there. Wilkens in his paper [18] analysed also the remaining term in the expansion of cosine coefficients in eq. 2.61 and found that in the "quadratic" approximation in $\rho_\parallel$ there is a nonvanishing contribution from the infinite serie, which he evaluated for a screw dislocation as [18][1]

$$\sum_{k=2}^{\infty} \frac{(-1)^k (G\rho_\parallel)^{2k}}{(2k)!} \left\langle \epsilon_{\boldsymbol{G}}(\rho_\parallel)^{2k} \right\rangle \cong \frac{(Gb)^2}{8\pi^2}\, \chi_\alpha\, n_\alpha\, \rho_\parallel^2\, K_{\nu,\alpha}\ , \tag{2.67}$$

$$K_{\nu,\alpha} \approx \frac{7}{3} - 2\ln 2 + \ln\left(\frac{|\boldsymbol{Gb}|}{2\pi}\right)\ .$$

This contribution should be included in T. Hence Wilkens introduced T_Q joining eqs. 2.62, 2.66 and 2.67 [18, eq. 5.12b]

$$T_{Q,\alpha} = \frac{(Gb)^2}{8\pi^2}\, \chi_\alpha\, n_\alpha\, \rho_\parallel^2\, [f^*(\eta_\alpha) - K_{\nu,\alpha}]\ . \tag{2.68}$$

If we consider logarithmic terms in the eqautions for f (eq. 2.66 or 2.65) and K_ν (eq. refeq:Wilkens-Kn), which are joined together in eq. 2.68, we can see that we arrived at an expression containing $\ln(\frac{2\pi R_e}{|\boldsymbol{Gb}|\rho_\parallel})$, which is similar to the results of Krivoglaz and Ryaboshapka (eq. 2.55). This is a positive consequence of the Wilkens equation for T_Q (eq. 2.68).

K_ν are positive numbers. They are plotted for illustration in fig. 2.10. It was noted earlier that eqs. 2.62, 2.63 and 2.66 describe a well behaved Fourier coefficients. The negative implications of eq. 2.68, which contains $[f - K_\nu]$, is a fact that this is broken in T_Q (eq. 2.68) and Fourier coefficients are diverging from a critical real space length $\rho_{\parallel,c}$. This was discussed already by Wilkens in his paper [19] or widely by Lynch in his thesis [73]. Under some favourable conditions (n, R_e and G) Fourier coefficients can decrease to zero before the critical real space length $\rho_{\parallel,c}$ is reached and they can be truncated. But this is not the general case. Because we do not known $T(\rho_\parallel)$ for large $\rho_\parallel$ we have only very limited knowledge of the diffraction profiles shape $I(q_\parallel)$ in the close vicinity of the peak maximum.

[1] For $|\boldsymbol{Gb}| = 0$ Wilkens [68] set $K_0 = 0$.

Wilkens in order to ensure the convergence of Fourier coefficients for any value of $\rho_{\parallel}$ proposed the following approximation[1] [19, eq. 6.2]

$$f(\frac{\rho_{\parallel xy}}{R_e}) - K_\nu \simeq f(\frac{\rho_{\parallel xy}}{R_e}\ e^{K_\nu}) \ , \tag{2.69}$$

which can be understood as a *formal* redefinition of the outer cut-off radius R_e ([19, 73]). Including this *formal* approximation Wilkens introduced the final formula for the model of *restrictedly random dislocation distribution* [19, eq. 6.4]

$$T_{\widetilde{Q},\alpha} = \frac{(Gb)^2}{8\pi^2}\ \chi_\alpha\ n_\alpha\ \rho_\parallel^2\ f^*(\frac{1}{2}e^{-1/4}\frac{\rho_{\parallel xy,\alpha}}{R_e}\ e^{K_{\nu,\alpha}}) \ . \tag{2.70}$$

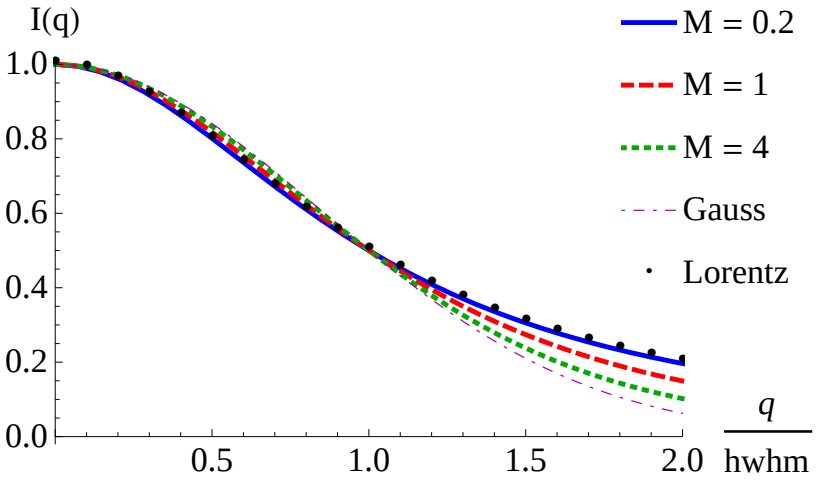

Figure 2.11: Simulated diffraction profiles shape for the Wilkens model of *restrictedly random dislocation distribution* for different values of the parameter $M = \sqrt{n}R_e$. A Gaussian and a Lorentzian function are plotted for comparison.
Profiles were simulated using eq. 2.70 for $n = 1.6\ 10^{-3}$ nm^{-2}, $\chi = \pi$, $|\boldsymbol{Gb}| = 4\pi$, (a) $M = 0.2$ ($N_p \approx 0.2$), (b) $M = 1$ ($N_p \approx 5$) and $M = 4$ ($N_p \approx 80$).

In [68] Wilkens described implications of his model on the shape of diffraction profiles. For determination of parameters of his model from diffraction data he proposed to define a dimensionless parameter M

$$M = \sqrt{n}R_e \ . \tag{2.71}$$

It can be easily realised that it has a similar meaning as the square root of the effective number of dislocations $\sqrt{N_{eff}}$ in the area of interest (crystal or correlated subarea) or a parameter P used by Krivoglaz (see the footnote at page 30; $P \approx 3M$ in [73, ch. 1.6.2]). We can expect from previous discussion that with decreasing M also the number of dislocations within the area of interest is decreasing and shape diffraction profiles becomes more distant from the Gaussian. This is depicted in fig. 2.11 were simulated diffraction profiles are plotted for

[1] Kaganer and Sabelfeld [38, Appendix A] also emphasised that inclusion of the $|\boldsymbol{Gb}|$ term is necessary to fit results the Monte-Carlo simulations described there.

different values of M (or the number of dislocations $N_p = \pi R_p^2$). For $M \gg 1$ diffraction profiles are almost Gaussian whereas for $M \ll 1$ it is difficult to distinguish them from the Lorentzian.

It is important to consider also the limits of applicability of the Wilkens model. It was described how the model of restrictedly random dislocation distribution can be interpreted for $N_p < 2$, Wilkens in [19] derived the above equations for T analytically taking into account terms of order $\rho_\parallel^2$. The theory is thus valid for small $\rho_\parallel$ where quantities of the higher order do not exceed those taken into account. It was also discussed that with introduction of K_ν there is a critical length $\rho_{\parallel,c}$ above which the expression (eq. 2.68) for T does not have physical sense. Therefore, it is important if there is a sufficiently large number of dislocations in the area of interest that the Fourier coefficients fall steeply enough to zero. On the basis of analysis of these circumstances Wilkens found that this is satisfied if $M \gtrsim 1$ ($N_p \gtrsim 5$). Using approximation 2.69 eq. 2.70 can be used for any parameters of the Wilkens model ($M > 1$), but Wilkens pointed out in [18] that for $M \ll 1$ eq. 2.70 can be applied only for a qualitative description of diffraction profile tails.

It is often useful to have an expression for diffraction line width. Wu [76, 77] adapted the theory of Krivoglaz and Wilkens for Rietveld refinement of the powder diffraction data. Wu et al. [76] used a Voigt function for simulating measured diffraction line profiles. For this purpose they introduced a simple equation for the integral breadth

$$\beta = \frac{(Gb)}{2} \sqrt{\chi/\pi} \sqrt{n} \sqrt{f_\beta(M)} , \tag{2.72}$$

where $f_\beta(M)$ is an empirical function developed in [76] by numerical fitting profiles calculated from the Wilkens theory

$$f_\beta(M) = a \ln(M+1) + b[\ln(M+1)]^2 + c[\ln(M+1)]^3 + d[\ln(M+1)]^4 , \tag{2.73}$$

where $a = -0.173$, $b = 7.797$, $c = -4.818$, $d = 0.911$ for $0.1 \leq M \leq 10$. The same formula was used also by Lynch [73] and a similar one introduced by Kužel [56, 78].

In this section, the model of *restrictedly random dislocation distribution* developed by Wilkens was specified (fig. 2.9). The model describes correlation in the dislocation distribution which results in an effective screening of strain fields from dislocations. It was shown that the stored elastic energy as well as diffraction peaks width and shape are influenced by this correlation. Shape of diffraction lines in their central part can be somewhere between the Gaussian and Lorentzian (fig. 2.11) depending on the strength of the correlation effect described by the parameter M (eq. 2.71). Analytical expressions derived by Wilkens for calculation of diffracted intensity profiles as well as an expression for the diffraction lines width (eq. 2.72) were presented (eq. 2.70).

2.3.6 Monte Carlo simulations

The approach developed by Krivoglaz, Ryaboshapka and Wilkens was based mostly on analytical formulae, complemented sometimes by numerical computations of some particular values or integrals etc. In the last decade, a completely

different approach has appeared. It is based on simulation of scattering from crystals by the Monte Carlo method.

For the Monte Carlo simulations of diffraction profiles usually eqs. 2.6 or 2.8 are used. Fourier coefficients rather than diffracted intensities are computed. In each step of a Monte Carlo simulation a set of dislocations is generated, at two points ($\boldsymbol{R}_s$ and $\boldsymbol{R}_s - \boldsymbol{\rho}_{\parallel}$) sums of displacements from all dislocations are computed and substituted into eq. 2.6. By averaging results of many such steps a volume and an ensemble average marked by $\langle \dots \rangle$ brackets are evaluated.

Kamminga and Delhez (2000) [71] simulated powder diffraction profiles from correlated dislocations in an isotropic crystal by the Monte Carlo method and compared results of their simulations with the analytical expressions derived by Wilkens, described by Wilkens in [19, 68] and here in section 2.3.5. For screw dislocations they found a good agreement between the Monte Carlo results and the Wilkens theory. The simulation results for edge dislocations in a single slip system also fitted the Wilkens theory. In this way Kamminga and Delhez [71] verified the assumption that the theory, derived originally [18] only for screw dislocations, can be used also for the edge dislocations. Kamminga and Delhez [71] simulated diffraction profiles for a single slip system (α) and sets of dislocations in multiple slip systems. For the edge dislocations in multiple slip systems they found systematic deviations between simulations and the Wilkens results and they pointed out that the analytical approach could underestimate a contribution from edge dislocations with $\boldsymbol{G} \cdot \boldsymbol{b} = 0$, which could originate from an interaction between dislocations sets in different slip systems ($\alpha \neq \alpha'$). Finally their simulations qualitatively verifies the Wilkens theory.

The Monte Carlo method was also used by Kaganer et al. [79], Kaganer and Sabelfeld [80], Holý [81] (2009) and Barchuk et al. [82] (2010) for simulations of distribution of diffracted intensity from correlated dislocations in bulk single crystals and thin epitaxial films. For polycrystalline materials the method was utilised by Holý [81] and recently mainly by Kaganer and Sabelfeld [38, 40]. It must be noted that these works of Kaganer et al. [79], Kaganer and Sabelfeld [80] are purely theoretical.

The Monte Carlo method is extremely time consuming and hence it is difficult to apply the method directly to fitting of multiple reflections in a wide range powder diffraction pattern. Kaganer and Sabelfeld [38, 40] fitted simulated data by empirical functions and parametrised their Monte Carlo simulations results. For these purpose they proposed a new simple empirical function $f^*(\eta)$ (eqs. 2.65 and 2.66) and compared their results with the results of the Wilkens model. They found a very good agreement. They also highlighted that there must be a factor Gb in the logarithmic term for T and simplified the argument in the $f^*(\eta)$ function in eq. 2.70 by extracting (Gb) out of the K_ν and including all other constants into the outer cut off radius R'_p, which is then fitted to simulated data. Hence Kaganer [38] introduced

$$\eta = \frac{(Gb)/(2\pi)\ \rho_{\parallel xy}}{2R'_p} \qquad \text{and} \tag{2.74}$$

$$f(\eta) = -\ln\left(\frac{\eta/\eta_0}{1+\eta/\eta_0}\right). \tag{2.75}$$

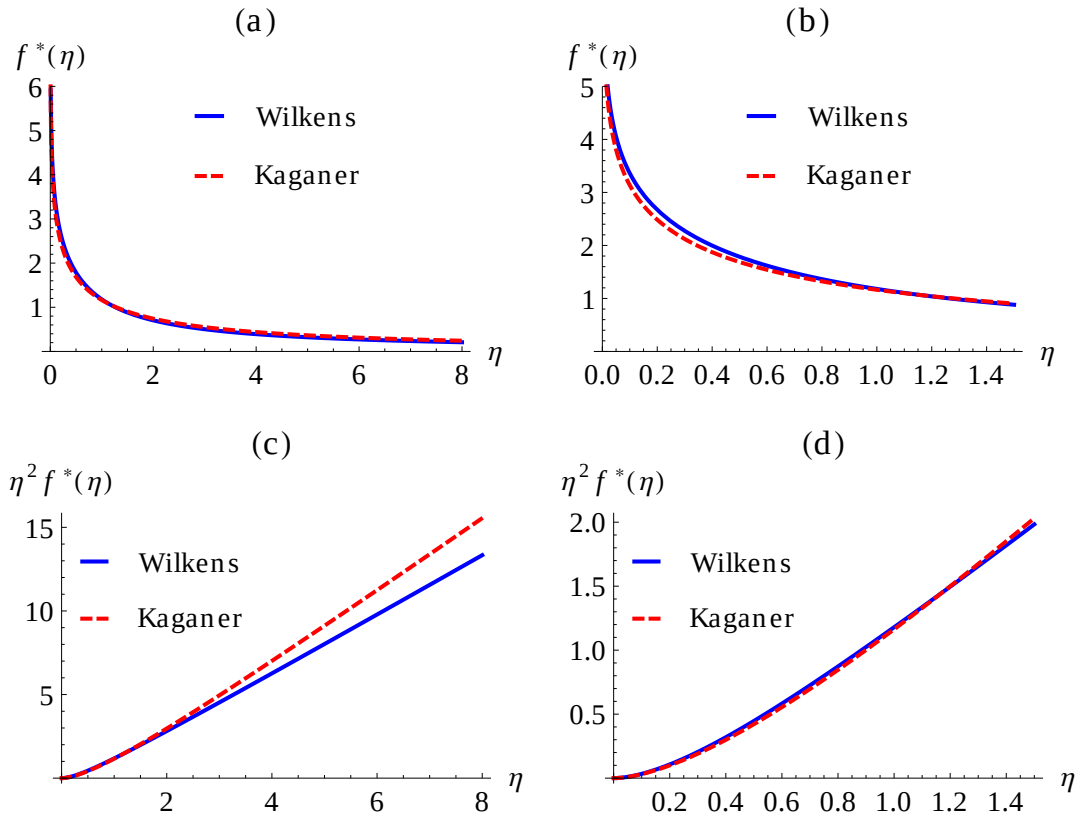

Figure 2.12: Comparison of a function $f(\eta)$ (eq. 2.66) calculated by Wilkens [19] with a more simple function (eq. 2.75) proposed by Kaganer [38], $\eta_0 = 2.2$.

Kaganer [38, Appendix A] argued that the simple function described by eq. 2.75 has the same asymptotic behavior for $\rho_\parallel$ as functions introduced by Krivoglaz or Wilkens. It behaves as $\ln(\frac{2\pi}{(Gb)\rho_\parallel})$ for $\rho_\parallel \to 0$. It is always positive and decreases to zero for $\rho_\parallel \to \infty$, hence it can be used for arbitrary $\rho_\parallel$. According to [38, Appendix A] function eq. 2.75 fits best the original Wilkens function (eq. 2.66) for $\eta_0 = 2.2$. For comparison, both functions are plotted in figs. 2.12(a-d). It can be seen that the difference is really subtle in fig. 2.12(a), which is similar to "Figure 8 (a)" in [38]. On the other hand, a difference is obvious in fig. 2.12(b), where smaller x-range is plotted. For computation, the quantity $\eta^2 f(\eta)$ is more important than the function $f(\eta)$ itself. This is plotted in figs. 2.12(c-d). It is evident that $\eta^2 f(\eta)$ for the case of the Wilkens and Kaganer functions is similar at smaller x-range but large deviations can bee seen for large $\eta = \rho_\parallel / R_e$. The influence on the shape of diffraction profiles is depicted in figs. 2.13(a-c). A figure similar to "Figure 8(d)" in [38] is plotted as fig. 2.13a. No difference can be observed in the logarithmic scale. Deviations between profiles calculated from the Wilkens and Kaganer formulae are also subtle in the linear scale in fig. 2.13b. The range of large η is important in the case when $R_e \ll r_d$. Simulated intensity profiles for such case are plotted in fig. 2.13c, where large deviations between the two profiles are visible. It should be kept in mind that both Wilkens and Kaganer pointed out that the cases when $M = R_e / r_d \ll 1$ are out of the validity limits of the theory or simulations.

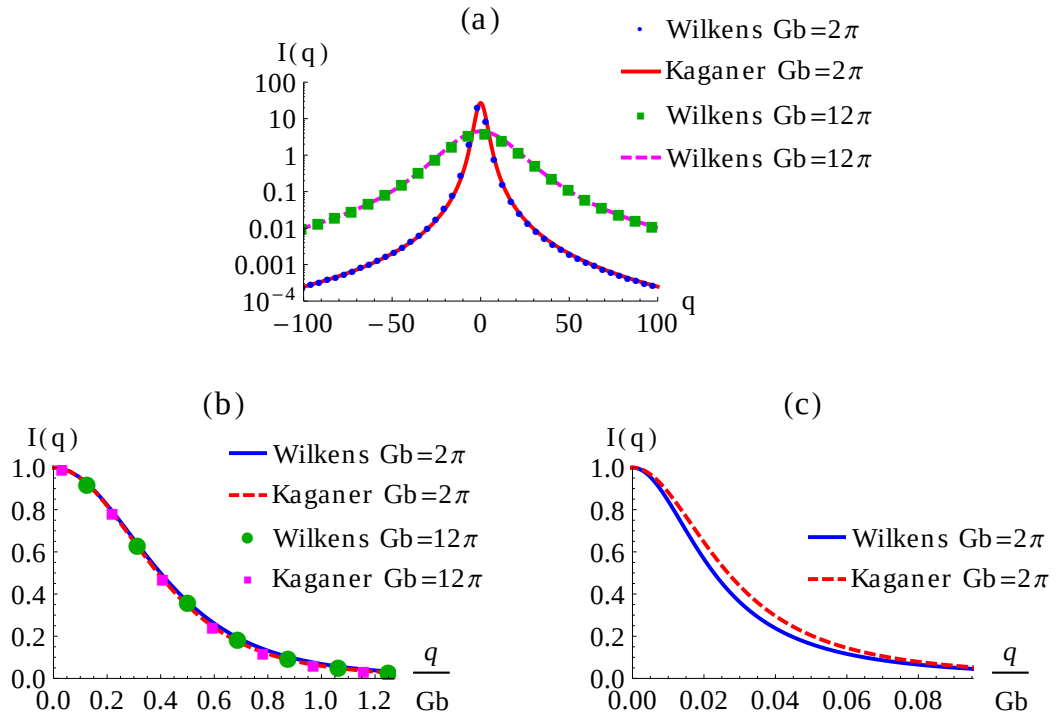

Figure 2.13: Comparison of simulated diffraction profiles when using a function $f(\eta)$ (eq. 2.66) calculated by Wilkens [19] or a function (eq. 2.75) proposed by Kaganer [38], $\eta_0 = 2.2$. Figures (a-b) were calculated for the Wilkens parameter $M = 2$. For figure (c) a small value $M = 0.1$ was set.

Profiles were simulated using eq. 2.70 for $n = 1.6\ 10^{-3}$ nm^{-2}, $\chi = \pi$, (a-b) $M = 2$ ($N_p \approx 20$), (c) $M = 0.1$ ($N_p \approx 0.05$).

Monte Carlo simulations of powder diffraction profiles done by Kamminga and Delhez [71] and Kaganer and Sabelfeld [38] in principle verifies the analytical results derived by Krivoglaz and Wilkens described in preceding sections. Kaganer [38, 40] in addition proposed a new simple function $f(\eta)$ (eq. 2.75) which can be used instead of a complicated Wilkens formula (eq. 2.66) and it gives the same results as the original one (fig. 2.13) for cases in the applicability range of the Wilkens theory, where $M \gtrsim 1$.

2.3.7 Dislocation broadening anisotropy

In this section short introduction in anisotropy - *hkl* dependence - of diffraction lines broadening from crystals containing dislocations is presented. The final T is a sum (eq. 2.20) of T_α from all types of defects. It was said that dislocations in different slip system will be considered here as such defects of different types. Hence, for the calculation of the shape of a single reflection profile *hkl* the contributions from dislocations in different slip systems α must be added. There were several α dependent terms in eq. 2.28 or eq. 2.68 for T_α for crystals containing dislocations, namely

$$n_\alpha\ ,\quad \chi_\alpha\ ,\quad \rho_{\parallel xy,\alpha}\ ,\quad e^{K_{\nu,\alpha}} \sim |\boldsymbol{Gb}|_\alpha\ .$$

The first two parameters will be discussed. The other are pure geometrical factors that appear explicitly only in the logarithmic term or in the function $f(\eta)$ and the anisotropy connected with them is often neglected. This has been mentioned earlier (ch. 2.3.2, p. 19) and it will be commented properly below.

Dislocation density n_α is usually assumed to be similar in all the symmetrically equivalent dislocation slip systems. Edge and screw dislocations are usually treated separately.. For a given dislocation type we can assume the same dislocations density in all slip systems, which is equal to an average density $n_\alpha = \bar{n}$.

The XRDline broadening anisotropy is mainly related to the *dislocation contrast factors* χ_α defined by eqs. 2.19 and 2.23. They describe the projection of a dislocation strain field onto the diffraction vector at large distances from the dislocation core. Klimanek and Kužel [17] showed that their anisotropy can be divided into two parts, a geometrical factor and a term connected directly to the crystal elastic characteristics and individual dislocation type. There were described many times in the literature, in the pioneered papers of Wilkens and Krivoglaz et al. [19, 20, 69], in works of Kužel and Klimanek [17, 31, 83, 84] and also in recent papers mainly by Ungár, Borbély and Dragomir-Cernatescu [16, 42, 43, 85, 86], Scardi, Leoni and Martinez-Garcia [44, 45, 87] or by Lynch [73]. Detailed description of their calculation for the case of cubic or hexagonal materials can be found especially in the theses of Kužel [31] or Lynch [73].

The calculation of χ_α is usually composed from few steps.

1. Define a reference dislocation slip system (Burgers vector $\boldsymbol{b}_\alpha$, line vector $\boldsymbol{l}_\alpha$).
2. Transform the crystal elastic constants C_{ij} into the reference system.
3. Find displacement field for the given dislocation type and elastic constants. In the elastically isotropic case the displacement fields from dislocation can be found in many books e.g. Valvoda et al. [30] or Hirth and Lothe [39]. If elastic anisotropy must be accounted for, it is more complicated, however the method can be found also in basic books, e.g. in Hirth and Lothe [39, ch. 13].
4. Calculate displacement field derivatives eq. 2.19 in the direction of the diffraction vector $\boldsymbol{G}$.
5. Evaluate integral eq. 2.23.

In the case of elastically isotropic crystal we have (Wilkens [19, eqs. 4.2-3])

$$\chi_{s,\alpha} = \pi \cos^2 \psi_\alpha \sin^2 \psi_\alpha \ , \quad \text{for screw dislocations,} \tag{2.76a}$$

$$\chi_{e,\alpha} = \frac{\pi}{8(1-\nu)^2}[1 - 4\nu + 8\nu^2 + 4(1-2\nu)\cos^2 \vartheta_\alpha] \sin^4 \psi_\alpha \tag{2.76b}$$

$$\text{for edge dislocations,}$$

where ν is the Poisson's ratio, ψ_α is the angle between the dislocation line $\boldsymbol{l}_\alpha$ and the the diffraction vector $\boldsymbol{G}$ and ϑ_α is the angle between the Burgers vector $\boldsymbol{b}_\alpha$ and the projection $\boldsymbol{G}_{xy,\alpha}$ of the diffraction vector into the plane perpendicular to dislocation line $\boldsymbol{l}_\alpha$.

However, real crystals are often strongly elastically anisotropic. In figs. 2.14 and 2.15 a reciprocal of Young modulus of fcc Copper is plotted for elastic constants [89, 90, table ivA]

$$C_{11} = 168.4 \text{ GPa} \ , \ C_{12} = 121.4 \text{ GPa} \ , \ C_{44} = 75.4 \text{ GPa} \ . \text{ (for fcc Cu)} \tag{2.77}$$

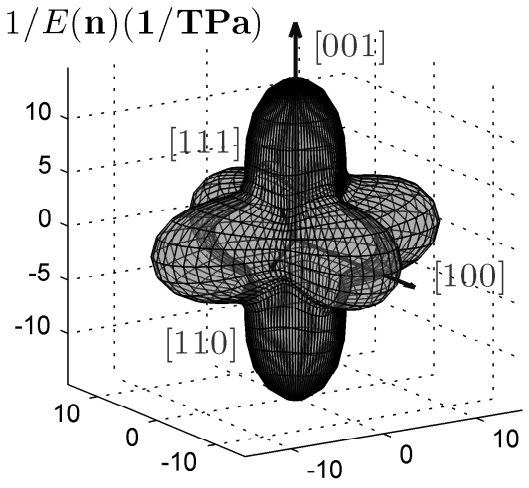

Figure 2.14: Surface representation of the Young modulus reciprocal $1/E(\boldsymbol{n})$ calculated for Copper from elastic constants eq. 2.77 similarly to [88].

Coefficient of elastic anisotropy defined for cubic crystals (e.g. in [91]) as

$$A = \frac{2C_{44}}{C_{11} - C_{12}} \doteq 3.2 \quad \text{(for Copper)} \; .$$

is for Copper essentially higher than one . Hence strong elastic anisotropy of Copper is evident and it is important to include this in the dislocation contrast factors.

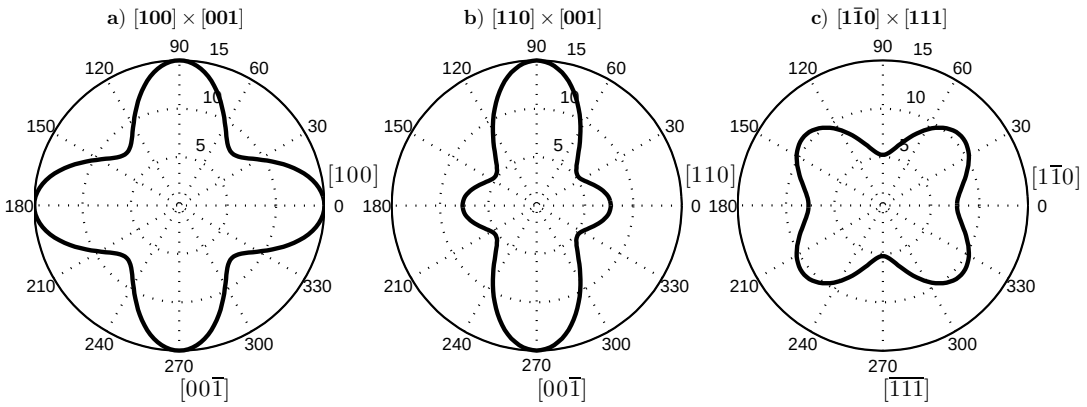

Figure 2.15: Polar projection of the Young modulus reciprocal $1/E(\boldsymbol{n})$ calculated for Copper from elastic constants eq. 2.77 similarly to [88].

The major operating slip system in fcc structures is the $\{111\}\langle 100\rangle$ [39, ch. 9.3] with the shortest possible Burgers vectors $\boldsymbol{b} = \frac{1}{2}\langle 110\rangle$ [30]. For illustration, dislocation contrast factors for a perfect edge dislocation in the fcc Copper crystal, reflection (331) and all 12 slip system $\{111\}\langle 100\rangle$ are listed in Table 2.1. The constants χ_α^{iso} in the case of elastically isotropic crystal were calculated for $\nu = 0.31$ [69]. Calculation for the case of elastically anisotropic crystal, χ_α^{ans}, were done following the recipe roughly-drawn above using elastic constants eq. 2.77 and Wolfram Mathematica computing system. More straightforward way would be to use an excellent program *ANIZC*, developed by Borbély et al. [86], which is

α					
$\boldsymbol{n}_\alpha$	$2\boldsymbol{b}_\alpha$	χ_α^{iso}/π	χ_α^{ans}/π	$\lvert\sin\psi_\alpha\rvert$	$\frac{(\boldsymbol{G}\cdot\boldsymbol{b})_\alpha}{Gb}$
$(\bar{1}11)$	$[110]$	0.494	0.403	0.982	0.973
$(\bar{1}11)$	$[0\bar{1}1]$	0.007	0.024	0.350	-0.324
$(\bar{1}11)$	$[\bar{1}0\bar{1}]$	0.100	0.074	0.662	-0.649
(111)	$[01\bar{1}]$	0.170	0.197	0.982	0.324
$(\bar{1}\bar{1}1)$	$[0\bar{1}\bar{1}]$	0.247	0.292	0.927	-0.649
$(\bar{1}\bar{1}1)$	$[\bar{1}10]$	0.027	0.009	0.662	0.000
(111)	$[1\bar{1}0]$	0.103	0.020	0.927	0.000
$(\bar{1}\bar{1}1)$	$[101]$	0.247	0.292	0.927	0.649
(111)	$[\bar{1}01]$	0.170	0.197	0.982	-0.324
$(1\bar{1}1)$	$[011]$	0.100	0.074	0.662	0.649
$(1\bar{1}1)$	$[10\bar{1}]$	0.007	0.024	0.350	0.324
$(1\bar{1}1)$	$[\bar{1}\bar{1}0]$	0.494	0.403	0.982	-0.973
$\overline{\chi}_{331,e} =$		0.181	0.167	$\cdot\pi$	

Table 2.1: Dislocation contrast factors for edge dislocations in fcc Copper, reflection 331, all 12 slip systems α, calculated for both the case of elastic isotropy χ_α^{iso} ($\nu = 0.31$), and the elastic anisotropy χ_α^{ans} (C_{ij} eq. 2.77). Also other geometrical factors $\frac{(\boldsymbol{G}\cdot\boldsymbol{b})_\alpha}{Gb}$ and $\lvert\sin\psi_\alpha\rvert$, where ψ_α is the angle between the diffraction vector and dislocation line, are listed. Slip planes are marked as $\boldsymbol{n}_\alpha$, Burgers vector directions as $\boldsymbol{b}_\alpha$.

available via its web-interface (at `http://metal.elte.hu/anizc/`). We can see from Table 2.1 that contrast factors for different slip system differs essentially in both cases, either if the isotropic or anisotropic elastic constants are used.

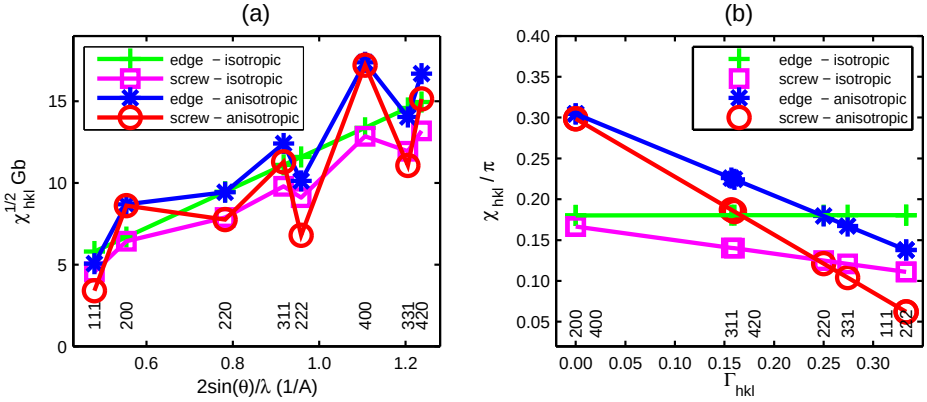

Figure 2.16: Average dislocation contrast factors $\overline{\chi}_{hkl}$ for Copper calculated for edge and screw dislocations for both the case of elastic isotropy ($\nu = 0.31$), and the elastic anisotropy (C_{ij} eq. 2.77). Figure (a) depicts a simulated Williamson-Hall plot, (b) shows the linearity of $\overline{\chi}_{hkl}$ with Γ_{hkl} (eq. ref).

Usually, when the anisotropy induced by geometrical factors in the logarithmic like term in T is neglected, all the anisotropy of the diffraction line broadening is included in the dislocation contrast factors χ_α. They appear in eqs. 2.28 or 2.68 for T_α as linear factors. Hence the summation over T_α can be reduced to averaging of dislocation contrast factors

$$\sum_\alpha T_\alpha \sim \sum_\alpha n_\alpha \chi_\alpha = n \sum_\alpha \frac{n_\alpha}{n} \chi_\alpha = n \, \frac{\sum_\alpha \chi_\alpha}{N_s} \equiv n \overline{\chi}_{hkl} \ , \tag{2.78}$$

where N_s is the number of symmetry equivalent slip systems and $\overline{\chi}_{hkl}$ is the *averaged dislocation contrast factor* for a given reflection *hkl* [16, 42, 76].

The average dislocation contrast factors $\overline{\chi}_{hkl}$ can be supplied e.g. into the equation (eq. 2.72) for the integral line breadth β_{hkl}. Line width then shows a characteristic anisotropy (hkl dependence), which is depicted in the simulated Williamson-Hall plot in fig. 2.16a. It was proved [16, 42] that for the cubic crystals (if all the symmetrically equivalent slip planes can be treated as equally populated with dislocations) $\overline{\chi}_{hkl}$ can be always described as a linear function of Γ_{hkl}

$$\overline{\chi}_{hkl} = W + V\Gamma_{hkl} \ , \quad \Gamma_{hkl} = \frac{h^2k^2 + k^2l^2 + l^2h^2}{(h^2 + k^2 + l^2)^2} \ . \tag{2.79}$$

This is depicted in fig. 2.16b, where $\overline{\chi}_{hkl}$ for all the cases can be fitted by straight lines

$$\begin{aligned}
\overline{\chi}^{iso}_{hkl,e} &= \pi(0.1803 + 0.001\ \Gamma_{hkl}) \ , \\
\overline{\chi}^{iso}_{hkl,s} &= \pi(0.167 - 0.167\ \Gamma_{hkl}) \ , \\
\overline{\chi}^{ans}_{hkl,e} &= \pi(0.305 - 0.500\ \Gamma_{hkl}) = 0.305\pi \cdot (1 - 1.64\ \Gamma_{hkl}) \ , && \text{(2.80a)} \\
\overline{\chi}^{ans}_{hkl,s} &= \pi(0.299 - 0.710\ \Gamma_{hkl}) = 0.299\pi \cdot (1 - 2.38\ \Gamma_{hkl}) \ , && \text{(2.80b)} \\
\overline{\chi}_{hkl} &= \chi_{h00} \cdot (1 + q\ \Gamma_{hkl}) \ . && \text{(2.80c)}
\end{aligned}$$

It can be seen from figs. 2.16(a-b) and from the the equations above that there is significantly more hkl-anisotropy in contrast factors if the crystal elastic anisotropy is included. The contrast factors for screw dislocations $\overline{\chi}^{ans}_{hkl,s}$ show the highest degree of anisotropy and are different from that for edge dislocations. According to linear fits (eqs. 2.80) χ_{h00} coefficients for edge and screw dislocations are quite similar and only q values are different. The q coefficient in eq. 2.80c is hence usually used to determine an edge-screw character of dislocations.

The other two geometrical factors,

$$|\boldsymbol{G} \cdot \boldsymbol{b}| \ , \quad \rho_{\parallel xy,\alpha} = \rho_{\parallel} |\sin \psi_\alpha| \ ,$$

where ψ_α is the angle between the diffraction vector $\boldsymbol{G}$ and the dislocation line $\boldsymbol{l}_\alpha$, are also listed in Table 2.1 for an edge dislocation in the fcc Copper and 331 reflection. Significant differences are visible between different slip systems. In contrast to discussion concerning line width and shape for the case of uncorrelated dislocations at 20, in the case of correlated dislocations, there are much less dislocations within the area of interest ($r_t \leq R_p$) and these geometrical factors in

$$\ln(\frac{2\pi\zeta_1\tilde{R}_p}{|\boldsymbol{Gb}||\sin\psi_\alpha|\rho_\parallel})$$

cannot be neglected. The Wilkens equation 2.70 with all these anisotropic and geometrical factors was used by Lynch [73]. Usually (e.g. by Scardi and Leoni [11], Matěj [26], Ribárik, Ungár, and Gubicza [92]) the model is significantly simplified using substitutions

$$\begin{aligned}
|\boldsymbol{G} \cdot \boldsymbol{b}| \to (Gb) \to 2\pi \ , && \text{(2.81a)} \\
\rho_\parallel |\sin \psi_\alpha| \to \rho_\parallel \ . && \text{(2.81b)}
\end{aligned}$$

Such formulation was called by Armstrong, Leoni, and Scardi [41] as the *simplified Wilkens model*, while the original model including all the factors was called

the *full Wilkens model*. They discussed in [41] deviations of Fourier coefficients resulting from the models and found that if the geometrical factors in eqs. 2.81 are "averaged" for a given *hkl* reflection they are linear with (Gb), which justifies the first substitution in eq. 2.81a. Subsequent averaging over different *hkl* reflections allows the second approximation in eq. 2.81a. Albeit it is stated by Leoni et al. [87] that using the simplified model (eqs. 2.81) introduces only a little error, significant deviations between Fourier coefficients for the *simplified* and the *full* Wilkens model are clearly visible in [41].

In this section, the dislocation broadening anisotropy has been discussed. It was shown that most of the broadening anisotropy is included in the dislocation contrast factors χ_α. In the line profile analysis usually the averaged dislocation contrast factors $\overline{\chi}_{hkl}$ (eq. 2.78) are used. For cubic materials they can be evaluated from a simple linear formula (eq. 2.80c). Necessary constants can be calculated using e.g. the program of Borbély et al. [86]. Elastic anisotropy of crystals (fig. 2.14) plays an important role (fig. 2.16). For calculation of whole diffraction profiles either the *full* or the *simplified* Wilkens model, adoppting approximations 2.81, can be used. Differences were discussed by Armstrong et al. [41].

2.3.8 Stacking faults defects in fcc structures

In addition to dislocations, the stacking faults and twin boundaries are quite common defects in many materials, namely in close packed metals. Cubic fcc metals can be considered as structures created by stacking of 111 layers in a sequence ABCABC... (fig. 2.17a). An *intrinsic stacking fault* in the fcc structure is schematically depicted in fig. 2.17b. The ideal stacking sequence is converted to AB**C**|**B**CA... by omitting one layer of type **A**. At a *twin fault* the stacking sequence ABC is reversed into CBA (fig. 2.17c). The upper part is a twin of the lower one.

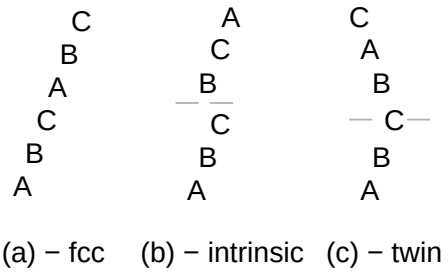

Figure 2.17: Schematic representation of stacking faults in a fcc crystal (according to Warren [6, ch. 13.5, p. 276, Fig. 13.13]). Close packed 111 layers are stacked at A, B, C positions. Figure depicts (a) a correct fcc sequnce, (b) an intrinsic stacking or deformation fault, (c) a twin or grow fault.

Stacking faults and twin boundaries are plane defects of the second type according to the Krivoglaz [20] classification. If we consider a plane fault extending over the whole crystal, diffraction from a crystal containing the planar faults can be calculated using the theory of Krivoglaz and eq. 2.7. According to Krivoglaz [20, ch. 5.1.4] stacking faults produce broadening and shift of (hkl) components of a given *hkl* reflection with

$$|L_0| = |h + k + l| \neq 3j \ , \tag{2.82}$$

where j is an integer number. The broadening is of the Lorentz form. Contrary a particular (hkl) reflection component is completely unaffected by stacking faults if $|L_0| = 3j$.

Planer faults are very common defects in the so-called layered structures and there are many methods how diffraction profiles from them are calculated. One of the most general of Treacy et al. [93] is implemented in the computer programs DIFFaX [94] and FAULTS [95]. Its applications on various materials can be found e.g. in Leoni et al. [96], Leoni [97], Martin et al. [98] etc. The DIFFaX program was used also by Balogh et al. [14] to simulate diffraction in fcc materials containing stacking faults and twin boundaries. Balogh et al. [14] fitted the patterns produced by DIFFaX by linear combinations of Lorentzians and they parametrised the results. Their model gives same results for fcc structures as the approach of Warren [6] and Velterop et al. [13], which is described below, but it can be used also for twinning on pyramidal planes in hcp crystals (Balogh et al. [99]), for which the method of Warren [6] can not adapted. Examples of the application can be found in [14, 15, 99, 100]. A completely different approach using the Debye formula was introduced by Buljan et al. [101] and applied to self-organized Ge nanocrystals in an SiO_2 matrix. Here the method, which can be found already (1969) in the book of Warren [6], is preferred. The method was improved by expansion in higher order of faulting probabilities by Velterop et al. [13] (2000) and in that form it was used by Scardi and Leoni [102], [11, 103] in their WPPM software [104].

In the Warren [6] diffraction profiles from fcc crystals containing intrinsic stacking faults and twin faults are calculated based on the assumption that the *probability* of occurrence of a *stacking fault* (α) or a *twin fault* (β) is the same in each layer independently of positions of other faults. No correlation is accounted for. It is also assumed that the probabilities of the faults are low ($\alpha, \beta \lesssim 0.1$).

The results of Warren [6], Scardi and Leoni [11], Velterop et al. [13] are in agreement with the theory of Krivoglaz [20]. For either stacking or twinning faults only the (hkl) components satisfying condition 2.82 ($|L_0| = 3j \pm 1$) are affected. The affected components can be shifted, broadened and asymmetric and the effect can be different for particular (hkl) components of the given reflection. It depends [11, 13] on the value of $|L_0|$ and $\sigma_{|L_0|}$, which is defined as [11, 13]

$$\sigma_{|L_0|} = \begin{cases} -1 & \ldots |L_0| = 3j - 1 \\ 0 & \ldots |L_0| = 3j \\ +1 & \ldots |L_0| = 3j + 1 \end{cases} .$$

If we define constants

$$\ln Z = \frac{1}{2} \ln(1 - 2\beta - 3\alpha + 3\alpha^2) ,$$
$$\beta_0 = \sqrt{3 - 6\beta - \beta^2 - 12\alpha + 12\alpha^2} ,$$
$$\gamma = \arctan \frac{\beta_0}{1 - \beta} ,$$
$$\Delta\rho = 2\pi \frac{h^2 + k^2 + l^2}{G|L_0|} ,$$

the Fourier coefficients can be written as [11, 13]

$$A_F(\rho_\parallel) = \frac{1}{m}\sum_j e^{\ln Z\cdot|\sigma_{|L_0|}|\cdot|\rho_\parallel|/\Delta\rho}\cdot\left[1 - i\sigma_{|L_0|}\frac{\beta}{\beta_0}\,\mathrm{sign}(\rho_\parallel)\right]\cdot e^{-i\Delta G_j\rho_\parallel}\ , \qquad (2.84)$$

where the summation is taken over all (hkl) components of the hkl reflection, m is its multiplicity and ΔG_j is the shift for each component [11, 13]

$$\Delta G_j = \sigma_{|L_0|}(\gamma - \frac{\pi}{3})/\Delta\rho\ .$$

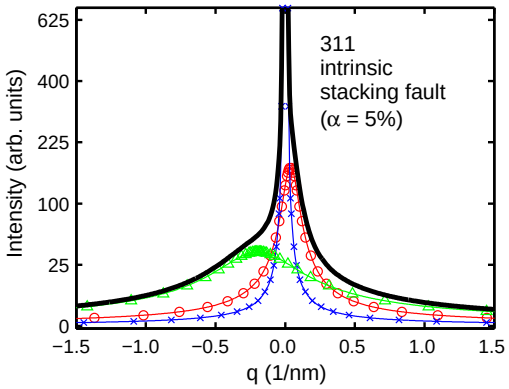

Figure 2.18: Simulated diffraction profile for a fcc copper polycrystalline specimen with intrinsic stacking faults. 311 reflection, stacking fault probability $\alpha = 0.05$. Thick black line depicts the whole diffraction profile. Colour lines show its subcomponents. The stacking fault effect was convoluted with size broadening to avoid the delta peak from unaffected components. Crystallites size was set to $D \approx 200$ nm. Similar figure can be seen in Balogh et al. [14].

The width, shape and shift of components of a given reflection vary only due to different $|L_0|$ and $\sigma_{|L_0|}$, which can take only a few possible values. Hence the (hkl) components are divided into groups with the same profile parameters [13]. This is illustrated for stacking faults at the 311 reflection in fig. 2.18. All 24 components can be divided into three groups. There are 12 components in one group. These all are unaffected because they satisfy $\sigma_{|L_0|} = 0$. Further, there are 6 components in each of remaining two groups. The components of the one group are shifted to lower diffraction angles. The components of the second one move in the opposite direction.

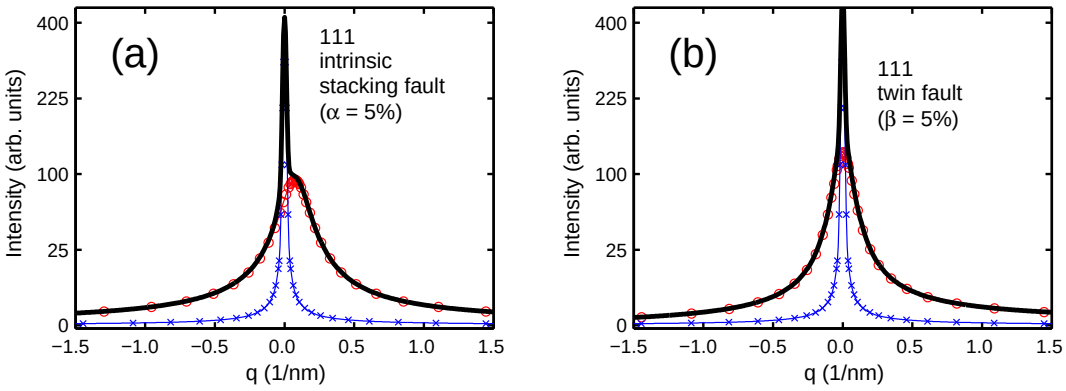

Figure 2.19: Simulated diffraction profile of the 111 reflection of a fcc copper polycrystalline specimen with (a) intrinsic stacking, (b) twin faults. The faulting probabilities are $\alpha = \beta = 0.05$. More examples can be found in Balogh et al. [14].

In fig. 2.19 another example shown by Balogh et al. [14] is depicted. Diffraction profiles of the 111 reflection for a crystal with stacking faults is shown in fig. 2.19a. Contrary the same reflection is plotted in fig. 2.19b for a crystal containing only the twin faults. We can easily see from eq. 2.84 that imaginary part of the Fourier coefficients is nonzero if twin faults are present ($\beta \neq 0$). This implies asymmetry of the diffraction profiles of affected components. On the other hand we see in fig. 2.19 only very slightly asymmetric profile in the case of twin faults, whereas the profile looks strongly asymmetric for stacking faults. The effects of asymmetry and shift are mutually combined and the results can be different from what is intuitively expected.

Furthermore, it can be realised from eq. 2.84 that the width and the absolute value of shift of components is a function of $\Delta\rho$, which does not depend on the order of the reflection. The effect of planar faults is hence anisotropic (hkl dependent) but is not proportional to G length as dislocation induced broadening. It behaves rather like size broadening.

In this section the diffraction line broadening from intrinsic stacking faults and twin boundaries in fcc crystals was theoretically treated. For these simple cases the Fourier coefficients describing the effect can be derived [11] within the model of Warren [6]. Examples, which can be found in the literature [14], show that even though the description of the effect is relatively simple (eq. 2.84) the shape of diffraction profiles is influenced in a complex way (figs. 2.18, 2.19). This is used to distinguish faulting defects from other sources of line broadening.

2.4 Whole powder pattern modelling

In the classical Rietveld programs, as in the FullProf [8, 105], GSAS [9] or MAUD [106], all microstructural effects are treated in a very general and more phenomenological way, e.g. a microstrain and crystallite size by the approach of Popa [107]. This has an advantage that the programs can be generally, systematically and often very successfully applied to materials of any symmetry. However, the model parameters don't have straightforward physical meaning, i.e it is difficult to convert for example a "phenomenological microstrain" value (ch. A.8) to the density of lattice defects or compare values for materials with different elastic properties. In material science, there is a demand of more physically relevant interpretation of results. Concerning the dislocation effects corresponding attempts can be found in 1998, where Wu et al. [76, 77] were modelling the dislocation-induced anisotropic line broadening in the Rietveld method using the Voigt function and the Krivoglaz-Wilkens model. In their analysis, the dislocation density (n), the Wilkens dislocation correlation parameter (M, eq. 2.71, p. 36) and the crystallite size were refined by the Rietveld method from the powder diffraction data [77]. At that time (1999) a simple approach (Ungár et al. [42], eq. 2.80c, p. 44) of evaluation of the average dislocation contrast factors in cubic materials has already been established and also the Fourier coefficients were used for calculation of diffraction profiles (Scardi and Leoni [102]) in the method of total pattern fitting. At the beginning, the Fourier coefficints were still combined with the analytical profile functions (Voigt, pseudo-Voigt) [102, 103, 108] and the method was called the *whole diffraction pattern fitting* (Scardi, Leoni, and Dong

[103]). Stacking faults were already included in [103], too. A similar approach with the emphasis on the analysis of dislocations was simultaneously developed by Ribárik et al. [23]. Analytical profile functions, which still imposed approximations in the modelling of diffraction profiles, were quickly excluded from the description of the physical aspects of microstructure and in 2002 the method of the *whole diffraction powder modelling* (WPPM) was developed by Scardi and Leoni [11]. The first computer programs [104] implementing the effects of dislocations and planar faults were rather slow but they have grown up in a very versatile, fast and user friendly programs as *PM2k* [24].

In summary, the WPPM method is very similar to the Rietveld approach [7]. The distinctions are the following: (i) instead of a widely general model rather a physical microstructural model designed for a particular problem in the given material is utilised. The model parameters have simple straightforward meaning, which facilitates the interpretation of the results. (ii) Instead of analytical profile functions (Gaussian, Lorentzian, Voigt) rather the Fourier coefficients or directly the intensity profiles, calculated on the basis of the microstructure models, are used. The convolutions involved are not based on an analytical formulae for profiles width and shape parameters but rather the whole profiles or Fourier coefficients are convoluted numerically in the real or reciprocal space. This drops many approximations and enables more physically correct description of complex profile shapes, e.g. from dislocations or planar defects.

Instrumental effects are usually not considered as a physically relevant part of the problem, contrary to Cheary and Coelho [109], and only elementary attention is given to them. In the PM2k [24] or the MSTRUCT (ch. A) here the instrumental broadening measured on some standard samples is usually simply parametrised and treated by analytical profile functions, which are convoluted with the microstructural effects [11]. However, some programs use different approaches, e.g. in *(eC)MWP-fit* [110] the raw measured instrumental diffraction profiles are directly convoluted with the simulated physical profiles.

2.5 Debye formula

The *Debye scattering formula* [6, 32] is commonly used for calculation of scattering by noncrystalline forms of matter for a long time. However, in the last decade it has been applied many times also to nanocrystalline materials.

Neither the translation invariance of the object nor any type of periodicity in the real space are required for derivation of the formula, but the crucial assumptions is a *random orientation* of the scattering matter. The scattering objects: molecules, atom clusters etc. must be oriented completely randomly in the sample. Then the scattered intensity can be calculated according to the *Debye formula* [6]

$$I(Q) = \sum_{m,n} f_m f_n^* \, \frac{\sin(Q r_{mn})}{Q r_{mn}} \,, \tag{2.85}$$

where r_{mn} is the distance between the m-th and n-th atom of the scattering object and $Q = 4\pi \sin(\theta)/\lambda$ is a continuous scattering length variable.

In eq. 2.85 there is a double sum over all atoms of the scattering object, which indicates highly computationally demanding problem for objects with many atoms. In 3D crystals the typical shortest distances between atoms are fractions of a nanometer and the number of atoms is increasing with the third power of the object size. Roughly guessed, the objects up to size $D \lesssim 10-15$ nm can be treated on recent personal computers. The method suitably complements the WPPM, which is still based on some classical crystallographic approximations and only with difficulties accounts for some effects in very small crystallites ($D \lesssim 5$ nm). E.g. for relaxation of surface atoms or the core shell model [111, 112].

Some fast computational approaches to the Debye equation can be found in literature (Ino and Minami [113], Cervellino et al. [21] or Derlet et al. [22]). If N is the number of atoms in the scattering system and eq. 2.85 is used directly, for each point of the diffraction pattern $\sim N^2$ operations must be done. In [22, 114] it is proposed to rather calculate the *pair distribution function* in the first step. Albeit it is still the N^2 problem, however an evaluation of the sinus function and the division is avoided. Moreover this step is done only once. In the second step the "sinc" transform of the distribution function is evaluated.

The Debye equation method has been applied very successfully to various problems concerning nanocrystalline materials by Cervellino et al. [33], [21, 115–118]. Core shell structure of nanoparticles was studied e.g. in Mullen et al. [111], Palosz et al. [112], Valeš et al. [114]. Twinning in nanocrystalline cubic materials was treated by Frøseth et al. [119] or Buljan et al. [101]. The method was applied to the system of sever crystallites by Beyerlein et al. [120] and diffraction patterns were calculated from atomistic simulations of very large systems under deformation conditions by Derlet et al. [22], Frøseth et al. [119], Brandstetter et al. [121]. A comparison of simulations done by the Debye formula and the WPPM method can be found in Beyerlein et al. [36].

Chapter 3

Study of Submicrocrystalline Metals

3.1 Introduction

In this part, the theory of diffraction line broadening (ch. 2) is used to characterise microstructure of different submicrocrystalline metals from XRD data. (i) In section 3.2 isometric gold colloidal nanoparticles prepared by a chemical route are investigated and (ii) in section 3.3 compact ultrafine-grained copper samples prepared by equal channel angular pressing (ECAP) are studied.

The main subject of this part is the analysis of XRD diffraction data by the WPPM (Whole Powder Pattern Modeling) method (ch. 2.4). The goal of the work is experimental determination of microstructural parameters — crystallite size, defects type and density etc. Correlation of these parameters with samples treatment conditions and other analytical methods then can be discussed.

3.2 Characterisation of isometric gold nanoparticles

Gold nanoparticles prepared by a by chemical reduction of $H[AuCl_4]$ water solution were studied mainly by XRD analysis. The studies were complemented by other methods like UV/vis spectroscopy and TEM. All the samples studied in this section were prepared by the group of Dr. M. Šlouf from the Institute of Macromolecular Chemistry AV ČR. He also kindly provided the UV/vis measurements and TEM images. Results were published mainly in Šlouf, Kužel, and Matěj [122].[1]

[1] List of coworkers on the work presented here: Z. Matěj (present author) and R. Kužel, Department of Condensed Matter Physics, Faculty of Mathematics and Physics, Charles University in Prague (XRD analysis); M. Šlouf, Institute of Macromolecular Chemistry, Academy of Sciences (samples preparation, UV/vis spectroscopy, TEM).

3.2.1 Motivation

Nanoparticles of metals like gold, silver, platinum or palladium have been intensively studied in last years. They found applications e.g. in catalysis, as carriers of molecules or as markers in transmission electron microscopy (TEM) [123, 124]. Metal nanoparticles can compose colloid solutions. Size of the nanoparticles can be controlled by their preparation process. The gold particles studied were synthesised to be used mainly for the biological labelling ([123, 124]). In some practical cases, quantitative results can be obtained from the XRD powder diffraction in a simpler way than by the evaluation of many TEM images. An example of present possibilities of XRD for the analysis of nanocrystalline powders can be found in next chapter 4. The initial idea of the research was to probe possibilities of XRD method in characterisation of such colloidal nanoparticles and utilisation of XRD method as an assistant tool in biological or medial diagnostics. Unfortunately, sometimes the extraction of a sufficient amount of sample for e.g. quantitative phase analysis by laboratory XRD may be too laborious and other analytical techniques e.g. energy-filtered TEM or x-rays energy-dispersive analysis) proved to be suitable in this task [125]. However, despite this failure of XRD as an auxiliary method in biological diagnostics, availability of XRD data for a series of samples with well defined particles size in the range 5–100 nm, which were in addition characterised by other methods, was a supplementary motivation of the further analysis of samples by XRD and especially by line profile analysis (LPA) and the WPPM method (ch. 2.4).

3.2.2 Sample preparation, other methods

Four colloidal solutions containing gold nanoparticles of various sizes (around 5, 10, 30 and 80 nm) were prepared. A slightly modified method [126] allowing synthesis of particles with arbitrary size was used [122]. The technique is based on several-step reduction of $H[AuCl_4]$ water solution by combination of $Na[BH_4]$ and NH_2OH solutions. Size of particles (D_{TEM}), is determined by solution concentrations, which can be precalculated for the given expected particles size (D_{theor}). It is usually found that the size of synthesised particles (D_{TEM}) is less than what was expected (D_{theor}) [122], but the discrepancy is less than 20%. The samples are labelled Au-1, ..., Au-4 and the particles sizes (D_{theor}) intended to be prepared are listed in the Table 3.1.

Transmission electron microscopy (TEM) and UV/vis optical spectroscopy were used to characterise the samples in addition to the XRD measurements. Two electron microphotographs (fig. 3.1) and final results of spectroscopic measurements (fig. 3.2) are presented here for illustration.[1]

It can be seen from the TEM images (fig. 3.1) that particles are more-or-less isometric and approximately spherical in shape. The crystal facets are observable as well, especially for larger particles (fig. 3.1b). For each sample the average *experimental* particle size (D_{TEM}), determined by image analysis of TEM

[1] See the paper by Šlouf et al. [122] for more TEM pictures, detailed description of sample preparation for TEM, instrumentation used, TEM image analyses done or UV/vis experiments.

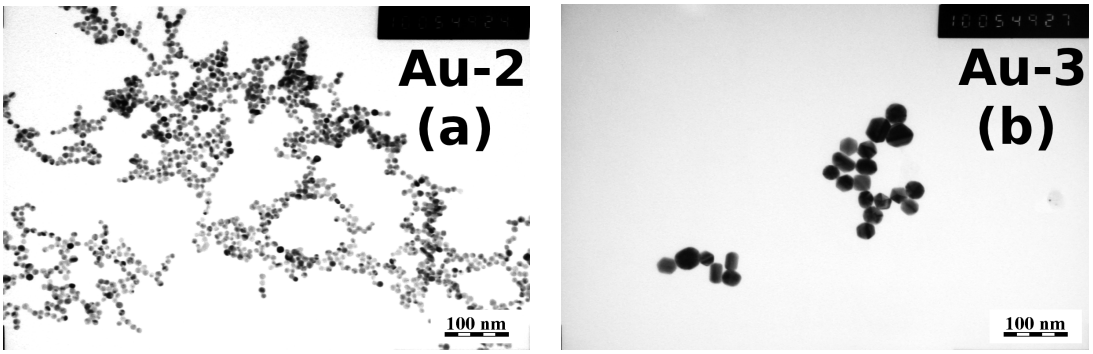

Figure 3.1: TEM microphotographs of colloid Au nanoparticles. (a) sample Au-2 ($D_{\text{theor}} = 11$ nm, (b) sample Au-3 ($D_{\text{theor}} = 33$ nm). (by M. Šlouf, IMC AV ČR)

microphotographs, is listed in the Table 3.1 and it is in quite a good agreement with the theoretical expected size (D_{theor}).

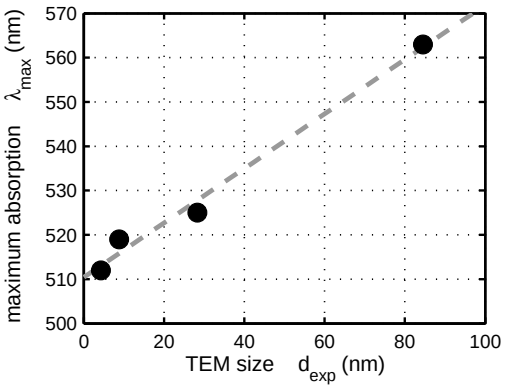

Figure 3.2: Maximum absorption ($\lambda_{\max}$) of colloidal solution of Au nanoparticles plotted against the particles size D_{TEM} determined from TEM. Data taken from Šlouf et al. [122, Table 1]

UV/vis spectra of the Au colloidal solutions exhibit, due to surface plasmon absorption, one local maximum, denoted as $\lambda_{\max}$ in fig. 3.2. The values in fig. 3.2 are taken from the Table 1 in Šlouf et al. [122]. Approximately linear dependence, as visible in fig. 3.2, was confirmed also theoretically later [3].

3.2.3 Experimental

Prepared gold nanoparticles were dispersed in colloidal solution and for the laboratory XRD experiments it had to be converted into a solid form. Hence the colloid Au particles were collected onto the surface of a microscopic glass in a form of a quite inhomogeneous thin film.

XRD signal from the Au films in the conventional Bragg-Brentano geometry was quite weak[1] hence the samples had to be measured in the parallel beam setup to enhance the intensity from the Au layer and suppress background scattering from the glass substrate.[2] This had a negative consequence in decreasing the angular resolution of the experiment. In fig. 3.3 a comparison of (i) the size broadening effect; instrumental resolution of (ii) the focusing Bragg-Brentano

[1] No suitable PSD detector was at that time available in the MFF XRD laboratory.

[2] The Bragg-Brentano and the parallel beam experimental setups used are depicted e.g. in [127], in thesis [128] or in diploma thesis [129] (in Czech).

geometry and (iii) the parallel beam geometry is schematically depicted. Modern laboratory x-ray diffractometers are usually equipped with a multilayer Göebel x-ray mirror producing parallel beam with an angular divergence $\Delta\theta \approx 0.04°$ or less. On the other side a wide diffracted beam is collected by an analysing optics. Long parallel Soller slits are usually used as analyser in the conventional powder diffraction measurement. The angular acceptance of the analyser available in the laboratory was nominally 0.27°. We can roughly guess the final resolution as a convolution of the mirror divergence and the acceptance of the analyser and it is evident that the analyser is the critical element. The instrumental resolution of the parallel beam setup used is hence approximately $2-3\times$ worse than that of the focusing Bragg-Brentano, which is limiting the range where broadening effects related to sample microstructure are stronger than the instrumental effect (fig. 3.3).

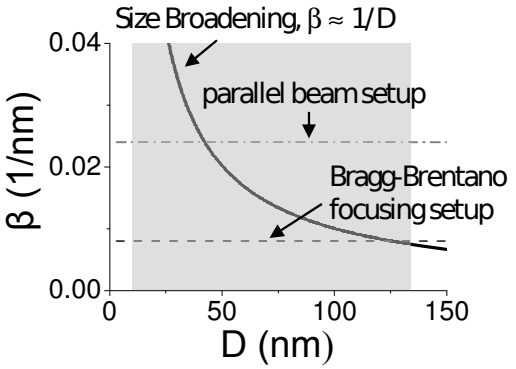

Figure 3.3: Very rough representation of an instrumental resolution of a common laboratory diffractometer in the focusing Bragg-Brentano and the parallel beam setup. Size broadening is plotted for comparison. (For the parallel beam setup an 0.3° collimator was assumed.)

Hence, measured data are finally a compromise between resolution and intensity. The samples were measured with a Philips MRD X'Pert PRO diffractometer. Laboratory X-ray Cu tube and x-ray mirror producing a parallel beam of CuK_α radiation were used. Parallel slit collimator with a flat graphite monochromator were placed in the diffracted beam. For each sample a 2θ scan was measured with an angle of incidence $\gamma = 2°$, a relatively large step $\Delta 2\theta = 0.1°$ and a counting time 30–50 s (different for various samples).

Measured diffraction pattern of the Au-1 sample is shown in fig. 3.4. Despite the low incidence angle used the background scattering from amorphous glass is visible. If the glass substrate pattern is appropriately scaled and subtracted from the pattern of the samples, the remaining background can be easier approximated by simple functions (polynomials,$1/sin(\theta)$, etc.). Hence all the measured patterns were corrected by subtracting the substrate signal and adding a constant background to not affect much the counting statistics.

In addition as a reference pattern, the NIST LaB_6 standard powder on a pure glass substrate, was measured in the same setup for correction of instrumental effects. The profiles of LaB_6 reflections were fitted by the asymmetric pseudo-Voigt function and the angular dependencies of the width and shape parameters were parametrised by appropriate polynomial functions. In this common way the instrumental function was characterised.

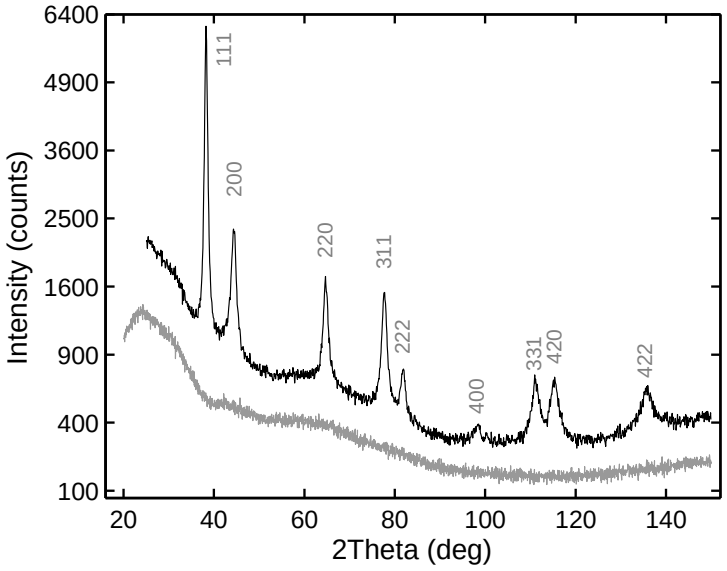

Figure 3.4: Measured diffraction pattern of the Au-1 sample (upper black line) and the pattern of a microscopic glass substrate (bottom shadow line).

3.2.4 Line width analysis

Diffraction peaks in measured Au powder patterns were fitted by the symmetric pseudo-Voigt function and integral breadths (β) of diffraction peaks were extracted (see the left column in fig. 3.5). The values plotted in the figure are already corrected for the instrumental broadening effect. Usually the method of de Keijser et al. [130] using only width and shape parameters of the profile functions is utilised, but here directly the whole analytical profile functions were deconvoluted numerically in MATLAB and the integral breadth of the physical profile was evalauted. Such numerical procedure is general and stable, because analytical functions are convoluted instead of deconvolution of raw measured profiles as described e.g. in Čerňanský [131] or [26, 132].

A huge spread of lines widths can clearly be seen in fig. 3.5. In principle, this could be a consequence of the crystallite shape anisotropy. It is easy to find two reflections in a plot for a single sample having widths more than $2-3\times$ different. However, the anisotropy would be in a strong disagreement with TEM observations. Crystal faces indicating an anisotropic shape are visible in TEM images (fig. 3.1b) but the anisotropy is not so strong and still the particles can be considered as approximately spherical. In fig. 3.5 a visible trend of increasing peak broadening with the diffraction vector length can be observed as well. This is an indication of strain. Dislocations and faulting defects can also be well known sources of the line broadening anisotropy, how it has been shown in sections 2.3.7 and 2.3.8.

From the theory (ch. 2) the Fourier coefficients are available for both types of defects and then it is quite simple to calculate the integral breadth (β) for a given model and model parameters. If the Fourier coefficients $A(\rho_{\|})$ are normalised to

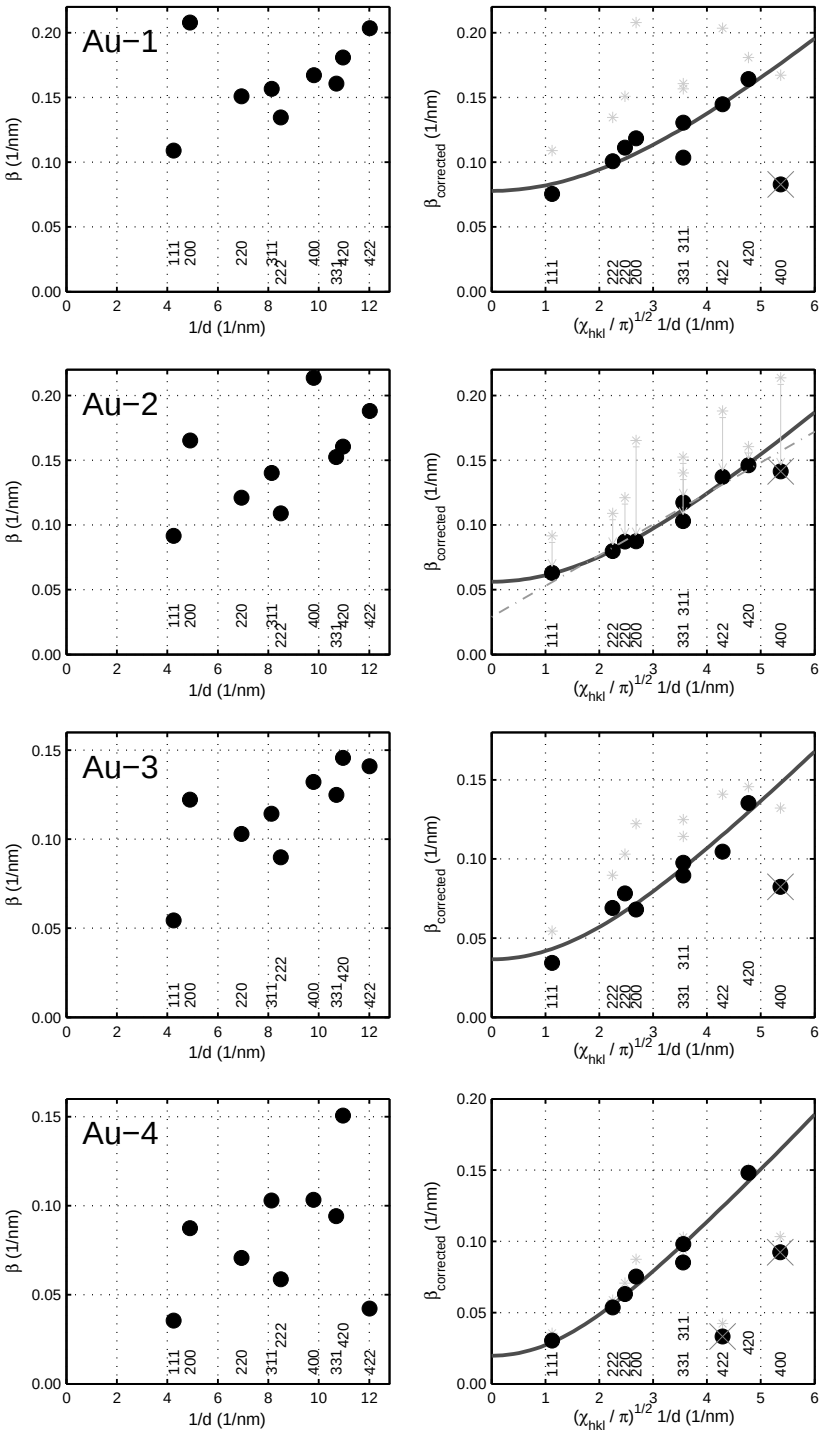

Figure 3.5: Williamson-Hall plots of Au samples (left column). The plotted integral breadth values (β) were already corrected for the instrumental broadening (see text). Modified Williamson-Hall plots [133] are depicted on the right. The integral breadths ($\beta_{\text{corrected}}$) plotted by dark bullets ($\bullet$) are the values corrected for the twin faults effect (see text). The uncorrected values are plotted by shadow stars ($*$). In the plot for the Au-2 sample in addition the corrections and a linear fit through $\beta_{\text{corrected}}$ values are depicted. (The 400 reflections of all the samples were discarded from the analysis.)

unity for $\rho_{\|} = 0$, the integral breadth β is simply the inverse of the integral

$$\beta = \left[\int_{-\infty}^{\infty} A(\rho_{\|}) \; d\rho_{\|} \right]^{-1} \; . \tag{3.1}$$

The dislocation broadening anisotropy can be described by average dislocation contrast factors ($\overline{\chi}_{hkl}$, ch. 2.3.7). The gold has the same fcc crystal structure as copper. The simples way is to use a computer program *ANIZC* by Borbély et al. [86] to calculate $\overline{\chi}_{hkl}$ also for Au. By using the elastic constants from [90, 134, table ivA]

$$C_{11} = 186 \text{ GPa} \; , \; C_{12} = 157 \text{ GPa} \; , \; C_{44} = 42 \text{ GPa} \; , \text{ (for fcc Au)}$$

the following contrast factors can be obtained by *ANIZC* for the $\{111\}\langle 100\rangle$ dislocation slip system

$$\overline{\chi}^{ans}_{hkl,e} = 0.330\pi \cdot (1 - 1.57 \; \Gamma_{hkl}) \; ,$$
$$\overline{\chi}^{ans}_{hkl,s} = 0.284\pi \cdot (1 - 2.31 \; \Gamma_{hkl}) \; .$$

The average dislocation contrast factors for Cu and Au are finally very similar.

Then the Fourier coefficients can be calculated as for the dislocation broadening effect from eqs. 2.62, 2.63 and 2.66 (or its simplified form introduced by van Berkum [70], [11]). The *simplified Wilkens model* (as denoted by Armstrong et al. [41]) and relations eq. 2.84 for the stacking faults and twin boundaries can be used. Since we study small nanoparticles the size broadening can be expected. The appropriate theory of size broadening can be found in [26] (in Czech) or in [11, 23, 135]. Alternatively, the necessary equation for spherical particles can be found here as well below, eq. 4.9 (p. 85). The Fourier coefficients can be mutually multiplied and inserted into eq. 3.1 and the integral breadth can be calculated by a numerical integration. If only the size broadening and dislocations described by the simplified Wilkens model are considered then the integral breadth is a function of $s^* = \sqrt{\overline{\chi}_{hkl}}/d_{hkl}$ and β can be plotted versus s^* and the Willimson-Hall plot should be linearised by a suitable choice of a fraction of edge and screw dislocations in the sample (e.g. [42, 78]). Such plot (β vs. s^*) is called a *modified Willimson-Hall plot* (mW-H) (e.g. [133]). If also stacking faults or twin boundaries are included the calculation can be done naturally only for distinct *hkl* reflections, but still the calculated and measured values can be directly compared and fitted by a nonlinear procedure. Such fitting was done for the samples here. Results are depicted in the right column of fig. 3.5, where the mW-H plot are shown for all the samples.

(i) It was found that that introducing a nonzero probability of twin faults (β_{twin}) improves fits substantially. Contrary, the stacking fault probability (α) could be left fixed at zero value during mW-H plots fitting. It is demonstrated later by the WPPM method that the inclusion of twinning improves also the whole patterns fits.

Integral breadth values ($\beta_{\text{corrected}}$) corrected for the twin faults broadening are shown in the mW-H plots in fig. 3.5. The correction was calculated according to the following steps: 1.) The integral breadth β_{calc} was calculated for the model parameters (from eq. 3.1); 2.) $\beta_{\text{calc}}(0)$ was calculated for the same model

parameters, but with $\beta_{\mathrm{twin}} = 0$; 3.) The correction $\delta\beta$ and the corrected integral breadth $\beta_{\mathrm{corrected}}$ were calculated as

$$\delta\beta = \beta_{\mathrm{calc}} - \beta_{\mathrm{calc}}(0) \ ,$$
$$\beta_{\mathrm{corrected}} = \beta_{\mathrm{measured}} - \delta\beta \ .$$

The measured values are depicted in the figure 3.5 as shadow stars, the corrected values are shown by black bullets. The correction is illustrated in the mW-H plot of the Au-2 sample by shadow arrows. We can see that the correction is large for the 200 reflection and small e.g. for the 420 reflection. The scale of the correction decreases with Au particles size.

Actually, the situation in the figure correspond to the β_{twin} values in the Table 3.1, which were obtained by the whole pattern modelling (WPPM) later. The results of the integral breadth analysis are less precise and the figure 3.5 depicts the final solution.

(ii) The integral breadths $\beta_{\mathrm{corrected}}$, corrected for the twinning effect, can be well fitted by the dislocation strain broadening. This is visible from fits of $\beta_{\mathrm{corrected}}$ by solid black lines in the mW-H plots in figure 3.5. There are few systematic deviations but these can be explained.

The 400 reflections does not fit model almost in any plot. However the 400 reflection is very weak (see fig. 3.4). Its profile parameters cannot be reliably determined from the measured data and the reflection had to be discarded from the analysis. There is a huge discrepancy between the model and the 422 reflection for the Au-4 sample with the largest particles ($D_{\mathrm{theor}} \approx 100$ nm). The (422) reflection of the Au-4 sample is $2\times$ stronger than expected, it is also unexpectedly narrow, it has a similar width as the 111 reflection and it is even possible to resolve well $\mathrm{K}_{\alpha 1}$ line from the $\mathrm{K}_{\alpha 2}$. This indicates that the (422) reflection can be influenced by strong scattering from a very large crystallite. Large Au particles ($D \approx 100$ nm) could somehow agglomerate when collected onto the substrate glass and subsequently recrystallise. Recrystallisation of very pure metals at room temperature is a well known phenomena, especially e.g. for Cu, which is quite similar to Au in several aspects. Hence the (422) reflection of the Au-4 sample should also be disregarded from the analysis.

The best agreement between the data and the dislocation anisotropy model is achieved for the pure screw dislocations, but it should be kept in mind that the fits are not much sensitive to that.

(iii) y-Intercept points of the solid black lines in the right column of fig. 3.5 compose a series of decreasing values, what is in an agreement with expected particles size.

It is worth mentioning another positive feature of the size-strain model used here. This is depicted in the mW-H plot of the Au-2 sample (fig. 3.5). A linear fit through the $\beta_{\mathrm{corrected}}$ is shown there by a shadow dot-dashed line. It fits the experimental points very well. Linearisation of the mW-H plot is quite common method in the literature ([42, 136, 137] etc. or later here). The figure shows that it is justified in the measured range, but it should not be extrapolated to zero reciprocal length ($s^* \sim 1/d$). The model line shows a clear hook effect below the lowest measured reflection 111. If the simple linear model had been used it

would result in an overestimated crystallite size or even an unrealistic negative y-intercept point.

(iv) From increasing slope of the solid model lines in the mW-H plots it can be expected that the dislocation density is increasing with the crystallite size.

To summarise, it follows from the integral breadth analysis, that the dislocation model with the twinning faults correction describes the experimental data very well. The crystallite size corresponds well to the particle size. The analysis gives decreasing twinning probability with the particle size. Contrary, the microstrain (dislocation density) is increasing.

3.2.5 Whole pattern analysis

Diffraction patterns were also treated by the whole powder pattern modelling method (WPPM, ch. 2.4) using the computer program PM2000 [104] [1] developed by Scardi and Leoni [11]. The same model as for the integral breadth analysis was assumed, but few points, which were omitted in the previous section, must be discussed.

The size effect model assumes spherical crystallites with the diameter distributed according to the log-normal distribution. It is properly described and widely used here later (ch. 4, p. 84), but basically the model has two parameters: the median of the crystallites size distribution and an additional parameter (σ) related to the variance of the distribution. Very good counting statistics is needed to determine a shape of the size distribution unambiguously and this is not satisfied in the case of measured data here. Information from TEM can help. It indicates that the dispersion of particles sizes is rather small. Finally for the analysis the value of σ parameter was fixed to $\sigma = \ln(1.35)$. This does not correspond to really narrow size distribution, but the size distribution with $\sigma = \ln(1.35)$ is rather often observed in the systems of nanoparticles (ch. 4). However, the exact choice of σ does not influence essentially the analysis here. An arithmetic mean crystallite size $\langle D \rangle$ is presented here as result, hence further details about the size broadening model are not important.

Slope of the mW-H plots (fig. 3.5) indicates that strains (dislocations) play an important role. It was mentioned in the theoretical chapter 2 that in many cases a possible correlation in dislocation arrangement must be considered. In Bever et al. [63], Schafler et al. [64] dislocation are not distributed completely randomly but prefer a correlated arrangement state when an average distance between dislocations is $r_d \sim n^{-1/2}$. In the Wilkens model of the *restrictedly random dislocation distribution* (ch. 2.3.5) it corresponds to the case where there are only few (N_p) dislocations in the area $S_p = \pi R_p^2$. There are many various definitions of the *outer-cut of dislocation radius* in the literature (see ch. 2.3.5 here, [11, 92] or Kaganer and Sabelfeld [38] who even pointed out that the parameter is in a physical sense rather "ill-defined"). For a reference, single definition should be choosen here. This is practically given by the choice of the program. In Scardi

[1] This is an exception in this work, because all the other WPPM analyses further were done utilising the MSTRUCT program (ch. A) of the present author. Event so, the present author is very grateful to authors of PM2000, Scardi and Leoni [104] for providing the program, which always could be used at least as a standard.

and Leoni [11] or [70] the Wilkens function (eq. 2.66) is used with a parameter R_e^*

$$R_e^* \equiv 2R_p = 2e^{1/4}R_e \ .$$

If we define the Wilkens factor M^* similarly to eq. 2.71)

$$M^* = \sqrt{n}R_e^* \ , \tag{3.3}$$

where n is the dislocation density, the nb. of dislocation in the sub-area S_p is

$$N_p \approx n \cdot \pi R_p^2 = n \cdot \frac{\pi}{4}R_e^{*2} = \frac{\pi}{4}M^{*2} \ .$$

For $M^* \doteq 1.6$ we have $N_p \approx 2$.[1] If the dislocation correlation have to be characterised, extremely high quality data, with low noise and high peak to background ratio are required. This is also shown in next section (3.3) concerning the analysis of deformed Cu samples. Here again the data quality does not allow a simultaneous determination of the parameter of dislocations correlation (M^*) and dislocation density (n). Hence the M^* was fixed on the value $M^* = 1.6$, which should represent the state described above and often found experimentally [63–65].

The above assumptions concerning σ and M^* were used in the integral breadth analysis.

The probability of intrinsic stacking (α) and twinning (β) faults can be refined with other parameters: crystallite size ($\langle D \rangle$), dislocation density (n), lattice constant (a) and zero shift ($2\theta_0$). The sample displacement correction is omitted naturally in the parallel beam geometry. The parameters of the instrumental broadening are described by polynomials functions and calibrated to the LaB6 standard sample.

In addition, a scale parameter and an isotropic temperature factor of Au atom could be refined. In the PM2000 integrated intensities of all reflections are fitted independently with o relation to crystal structure. This lets fit the peaks as well as possible and focus data optimisation to the refinement of microstructure parameters. This is equivalent to the so called *arbitrary texture* model in the MAUD [106] or *HKLIntensities* corrections in the MSTRUCT here (ch. A).[2]

Figures 3.6 and 3.7 illustrate how the quality of fits of the Au-2 sample differs when the twinning faults are included. The change is clearly visible in the difference curves of all reflections, but the effect is strongest in a region between the 111 and 200 reflections. The inclusion of the faulting effect improves the goodness of fit as $GoF(\beta_{\text{twin}} = 0) = 1.90 \rightarrow GoF(\beta_{\text{twin}} = 0.08) = 1.47$.

Whereas the fits for the first three samples give clearly nonzero values of the twinning probability (β_{twin}), the values of the stacking fault frequency (α)

[1] We have to consider such estimate of N_p with caution. For example if the *simplified model* [41] model is used the geometrical factors $|\sin\theta_\alpha|$ are averaged in some way, which itself "blurs" the physical interpretation of R_p.

[2] When the data were later refined in the MSTRUCT and reflection intensities were calculated form the crystal structure, the model including only the isotropic temperature factory of the Au atom fitted the data satisfactory but not perfectly. When the temperature factor was kept constant and the *HKLIntensities* corrections were used, the refined intensities of all the reflections were not different from the ideal calculated ones by more than 10–20% with a single exception of the 422 reflection of the Au-4 sample.

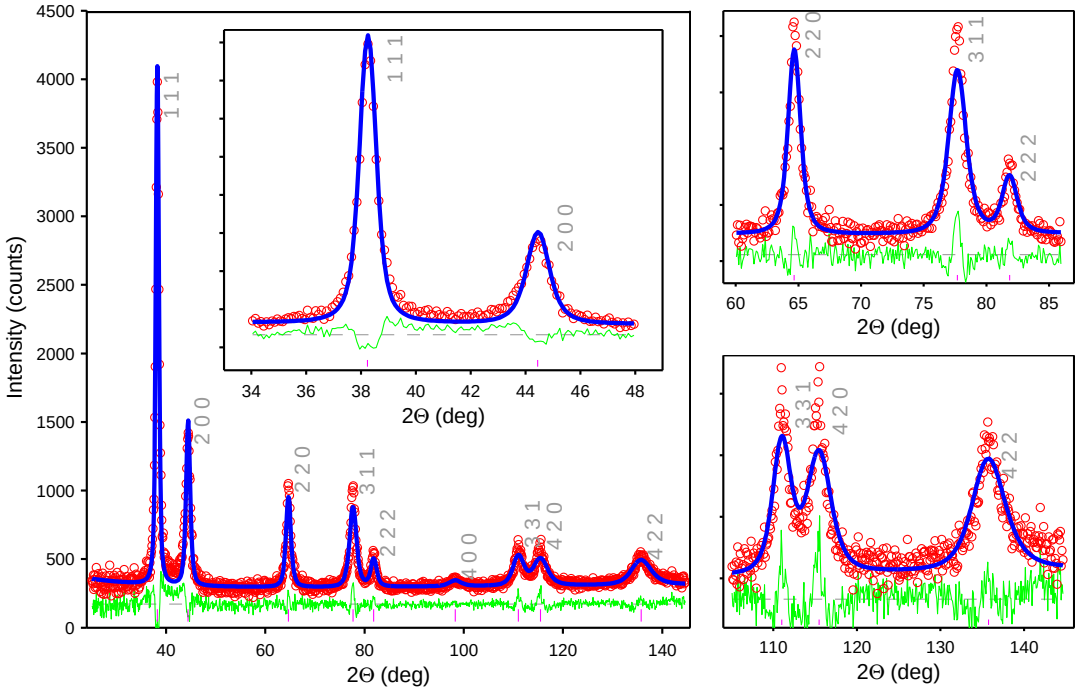

Figure 3.6: Pattern fit of the Au-2 sample using model without planar defects.
(red circles — measured points; blue line — calculated pattern; green line — difference curve)

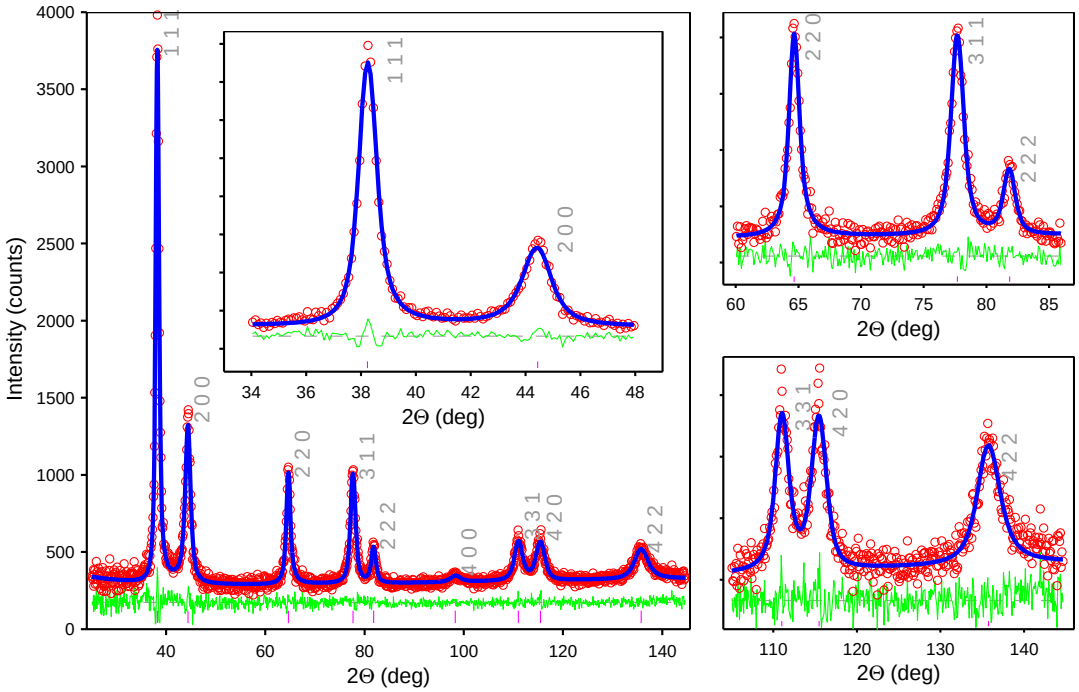

Figure 3.7: Pattern fit of the Au-2 sample using model with twin faults.

were quite low ($\alpha \lesssim 1\%$). As a nonzero stacking fault probability (α) did not improve fits significantly, it was also fixed to $\alpha = 0$ for all the samples. After this assumption the model is completely same as for the integral breadth analysis.

The values of refined microstructural parameters ($\langle D \rangle_{XRD}$, β_{twin}, n_{XRD}) and of

ID	D_{theor} (nm)	D_{TEM} (nm)	$\langle D\rangle_{\mathrm{XRD}}$ (nm)	β_{twin} (%)	n_{XRD} ($10^{15}/\mathrm{m}^2$)	a (Å)	N_{twin}
Au-1	4.5	4.3	**10**$\pm$6	**8**$\pm$2	**3.3**$\pm$1.0	4.0763(4)	3.4
Au-2	11.1	8.8	**15**$\pm$5	**7**$\pm$2	**4.3**$\pm$0.5	4.0770(6)	4.5
Au-3	33.4	28.3	**31**$\pm$5	**5**$\pm$1	**5.7**$\pm$1.0	4.0775(5)	6.6
Au-4	101.5	84.5	**92**$\pm$20	**1.2**$\pm$0.5	**8.7**$\pm$2.0	4.0787(9)	4.7

Table 3.1: Parameters of the colloid Au nanoparticles and results of the XRD analysis. D_{theor} — particles size expected from the solution concentrations; D_{TEM} — particles size from TEM; $\langle D\rangle_{\mathrm{XRD}}$ — mean crystallite size from XRD; β_{twin} — twinning probability determined from XRD; n_{XRD} — dislocation density from XRD ($M^* = 1.6$); a — Au lattice parameter; $N_{\mathrm{twin}} = \beta_{twin} \cdot \langle D\rangle_{\mathrm{XRD}}/(a/\sqrt{3})$ — rough estimate of a number of twin faults within the particle. (D_{theor} and D_{TEM} data taken from Šlouf et al. [122].)

the lattice parameter (a) are listed in the Table 3.1. The errors of the microstructural parameters are rather rough estimates of experimental uncertainties of the values in the table than the refinement errors. The data are not of the highest quality and hence they were fitted by different model configurations including also nonzero β and different σ values and the parameters uncertainties were roughly estimated.

The overall quality of the fits of the other samples was similar, but a lower ($GoF \sim 1.8 - 2.0$)) than for the Au-2 sample (fig. 3.7).

3.2.6 Summary and discussion

XRD analysis gives increasing crystallite size with the sample number (Table 3.1), but the sizes obtained from TEM and XRD are different, especially for the samples with the smallest particles (Au-1, Au-2). The sizes from TEM (D_{TEM}) are smaller, almost 2×, than values from XRD ($\langle D\rangle_{\mathrm{XRD}}$). This is rather unusual, because as we will see in the next chapters (3.3, 4), in deformed metals the crystallite domains are much smaller than grains observed by TEM (ch. 3.3, [138]) and particles of ceramics are in electron microscopy images usually larger than XRD crystallite size (ch. 4). Before explanation of this discrepancy, the data should be examined in a greater detail. The XRD sizes determined for the same sample from the integral breadth analysis and the WPPM are very similar for the samples investigated. We can clearly see in the mW-H plot of the Au-1 sample (fig. 3.5, p. 56) that the y-intercept point is lower than 0.1 nm^{-1}. This indicates crystallite size $D \gtrsim 10$ nm in agreement with the WPPM result (Table 3.1). It is clear, when corrected ($\beta_{\mathrm{corrected}}$) and uncorrected integral breadth values (β) are compared, that a huge part of diffraction broadening in these samples is related to the twinning. However, even if we look at the β values uncorrected for the twinning effect (the left side plots in fig. 3.5) we see only two reflections of width $\beta \approx 0.2$ nm^{-1}. The 422 is a high-angle reflection and few other high-angle reflections approache its width, which rather indicates strain. The 200 reflection of the Au-1 sample is the only one footprint in the data of something present of 5nm size. Hence, we have to accept either a very strong size anisotropy or the fact that the crystallites size is much larger than 5 nm also in the Au-1 sample. The

second choice fits all the XRD data presented here very well. If we exclude a systematical error in deconvolution of the instrumental broadening as well as the crystallite coherence effect of Rafaja et al. [139] requiring a strong "local" texture and accept the crystallite sizes ($\langle D\rangle_{\mathrm{XRD}}$) determined by XRD as corrected, the explanation of different TEM and XRD value must be found elsewhere. In the second part of chapter 4 it is shown that if a small number of large crystallites with very large volume are present in the sample simultaneously with a very large number of small crystallites, the total volume of which is small, though, the XRD analysis is significantly affected. It should be born in mind that the samples for TEM and XRD analyses where prepared by a slightly different ways and at least macroscopically they differ. Whereas for TEM observations the colloid particles were transferred to a carbon coated microscopic grid in quite a small amount and well separated particles were studied (figs. 3.1), for the XRD analysis a significantly larger amount of particles had to collected onto the glass in order to achieve large volume of particles to strengthen the XRD signal. It can be realistic to expect that Au nanoparticles at the glass substrate are not well mutually separated, can agglomerate and in the worst case can also grow together. An indication of partial recrystallisation was mentioned earlier in the case of the Au-4 sample. Since this reason can not be omitted, the XRD size ($\langle D\rangle_{\mathrm{XRD}}$) instead of D_{TEM} is considered in further discussion as the "true" size of crystallites studied.

The second finding concerns the twin fault probability (β_{twin}). In the Table 3.1 it is visible that β_{twin} decreases strongly with the crystallite size. However this alone still does not imply that the number of twin faults in the crystallites decreases with their size. In fcc crystalls the $\{111\}$ close packed planes are stacked in the $\langle 111\rangle$ directions with the period $a/\sqrt{3}$. If crystallite size is D, a number of twin faults in the crystal can be very roughly estimated as $N_{\mathrm{twin}} \approx \beta_{\mathrm{twin}} \cdot D/(a/\sqrt{3})$. The calculated N_{twin} values are also listed in the Table 3.1. There are about 3–7 twin faults in a single crystal and their number does not decrease with particles size. In Balogh et al. [14] they reported twinning fault probability $\beta_{\mathrm{twin}} \approx 2-7\%$ in fcc Cu prepared by inert gas condensation and hot compaction by Sanders, Weertman et al. The crystallite size in these samples was less than 30 nm. In larger Cu crystallites much smaller twin fault probability was found (see fig. 9 in [14]). In Gubicza et al. [140] the stacking fault energy $\gamma_{\mathrm{Cu}} = 78$ mJ/m^2 can be found, whereas for Au it is a lower value $\gamma_{\mathrm{Au}} = 45$ mJ/m^2. Hence an occurrence of stacking faults can be expected also in Au nanoparticles. The authors of [140] reported $\beta_{\mathrm{twin}} \doteq 0.07\%$ in a 5-passed ECAPed Cu and again a higher value $\beta_{\mathrm{twin}} \doteq 0.28\%$ in a 4-passed ECAPed Au [141]. Hence high twinning probabilities in nanocrystalline fcc metals with low stacking fault energy (γ) are quite common. If we consider a single planar fault extending thoroughout the whole crystal, its area is proportional to the crystal size squared and its boundary is related linearly to the crystal size. The energy connected with this defect is then proportional to the sum of creation energy of the defect (at surface) enclosing the planar fault and the energy of the planar fault itself $\Delta E_{\mathrm{twin}} \sim \gamma D^2$. It is then clear that it costs less energy to create such a planar fault in small nanocrystal. If the twinning probability is plotted against the crystallite size (fig. 3.8) it can be found that β_{twin} decreases exponentially with the crystallite size D rather

than with its cross section D^2. Even over a very good linearity in fig. 3.8, this results should be taken with a caution and the error bars should be considered. Nevertheless the author assumes that the Au crystal are continuously or in steps growing from the solution and new twin faults can be created on the 111 growth front. Energy necessary for the creation of a planar fault according to the discussion above is proportional to sum of contributions from the bounding defect and the fault energy itself, which is proportional to the area of the facet. The Au particles have approximately spherical shape and the fraction of {111} facets is limited. If the fraction of these facets to the total surface is decreasing with the particle size, the mechanism above would imply that the facet area will increase slower than as D^2. Unfortunately this is only one possible hypothesis and the data here are not sufficient to confirm it.

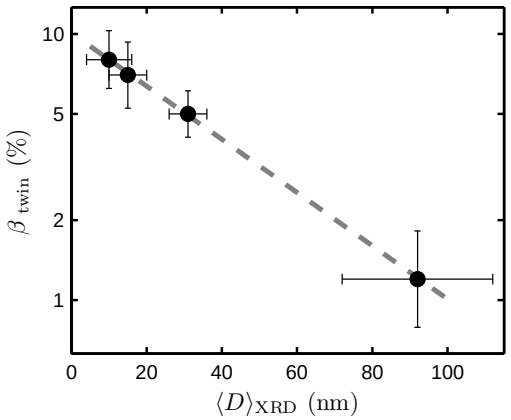

Figure 3.8: Twinning probability (β_{twin}) in colloid Au nanoparticles as a function of crystallite size $\langle D \rangle_{\mathrm{XRD}}$. (Note the logarithmic scale of the y-axis (β_{twin}). Data, determined by XRD analysis, taken from the Table 3.1.)

It should be mentioned that at the beginning it was assumed that there is also a TEM evidence of twinning in the different contrast inside a single particle in fig. 3.1b, but later a more detailed TEM investigation did not revealed the presence of twins. Cervellino, Giannini, Guagliardi, and Zanchet [115] and [33] modeled synchrotron XRD data from thiol-capped fcc Au nanoparticles by a single or multi-domain non-crystallographic nanoclusters (cuboctahedron, icosahedron, decahedron) using the Debye formula approach. Besides the quantitative analysis of the structure types and domain size distributions they also detected a strong influence of strain in nanoclusters. Their model is clearly distinct from the more classical size-strain model including dislocations and planar faults here, but they investigated Au nanoparticles in the size range 2–4 nm [115], which is different from a problem treated here.

Next findings in the Table 3.1 concerns the dislocation density (n) and lattice parameter (a). Both parameters are increasing with the crystallite size. The lattice parameter (a) approaches for the large particles a bulk value $a = 4.0786$ Å found in the crystallographic (ICDD) database, but refined dislocation densities are relatively very large. It is $n \approx 3 \cdot 10^{15}/\mathrm{m}^2$ in the Au-1 sample and even $n \approx 9 \cdot 10^{15}/\mathrm{m}^2$ in Au-4. [141], [140] reported dislocation densities in ECAPed pure Au not higher than $n \approx 2 \cdot 10^{15}/m^2$. The grain size in their deformed Au samples was $D \approx 500$ nm. A possible explanation of the unusually high dislocation densities reported here can be seen in fig. 3.9, where the dislocation density (n) is plotted versus the lattice parameter (a). Clear correlation between

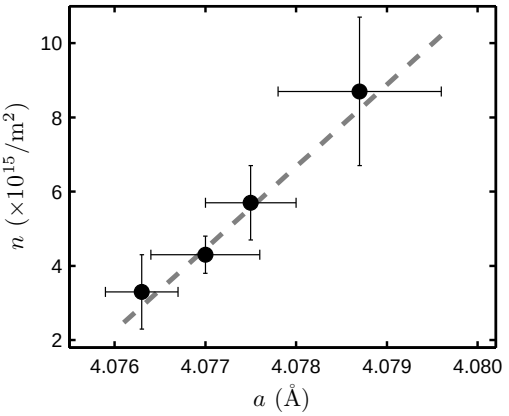

Figure 3.9: Dislocation density (n) in colloid Au nanoparticles plotted versus lattice parameter (a) of particles. (Both quantities were determined by XRD and are listed in the Table 3.1. The dislocation correlation parameter was assumed constant $M^* = 1.6$.)

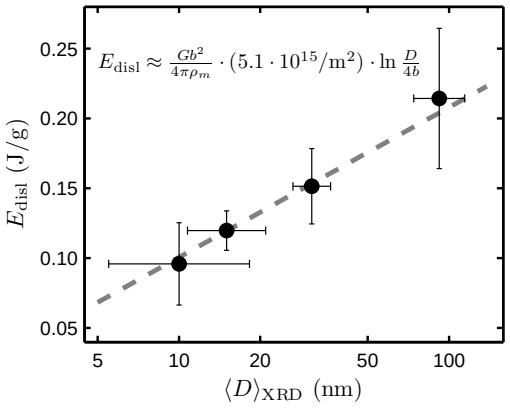

Figure 3.10: Stored energy (E_{disl}) in the dislocation strain field calculated from XRD data according to eq. 3.4. Note the logarithmic scale of the x-axis ($\langle D \rangle_{\mathrm{XRD}}$). Data, determined by XRD analysis, taken from the Table 3.1.)

these two quantities would indicate that the lattice defects (dislocations) can compensate the changes of the lattice parameters. Well-known modles called "core-shell" and "apparent lattice parameter" developed by Palosz et al. [112] are based on the idea of the crystallite core and shell with slightly different structure and lattice parameter. If we imagine new layers growing on a core of smaller particle with the lattice parameter smaller than the bulk value we can assume that defects compensating lattice parameter of the core, bulk and relaxed shell will be created. Strains in Au nanoclusters were also detected by Cervellino et al. [115], [33]. In the material research of severely deformed metals it is quite common in the last years (e.g. in [64, 65]) to convert the dislocation model parameters to an estimate of the energy stored in the dislocation deformation field (E_{disl}). Such a quantity can be compared for example with the results of calorimetry measurements. The energy considerations were actually the basis of Wilkens's model (ch. 2.3.5). A formula for the energy of E_{disl}, which does not account for the correlation is usually used [64, 65]. From the theory (ch. 2.3.5) we can derive a similar but slightly modified formula, which includes also dislocation correlation parameter M^* using eqs. 2.56 (p. 31), 2.60 and eq. 3.3 (p. 60)

$$E_{\mathrm{disl}} \approx \frac{Gb^2}{4\pi\kappa\rho_{\mathrm{m}}} \cdot n \cdot \ln \frac{M^*}{4\sqrt{n}b} \ , \tag{3.4}$$

where E_{disl} is the stored energy per unit mass, G is the shear modulus ($G =$ 26.6 GPa for Au [142]), ρ_{m} is the density ($\rho_{\mathrm{m}} = 19.30$ g/cm^3 [142]) and the other quantities were defined earlier ($\kappa = 1$ for screw dislocations, p. 31, [65]). The stored energy calculated for the values in the Table 3.1 is plotted in fig. 3.10 as a function of the logarithm of the crystallite size $\langle D \rangle_{\mathrm{XRD}}$. A linear dependence can be seen in the fig. 3.10. If the E_{disl} vs. $ln(D)$ dependence in

fig. 3.10 is fitted by eq. 2.60 it gives a constant dislocation density for all the samples, $n = 5.1 \pm 0.4\ 10^{15}/\mathrm{m}^2$. This would arise a question if the assumption $M^* = 1.6$ is satisfied. The data in Table 3.1 should be revised. If we e.g. calculate the outer-cut of dislocation parameter R_e^* for the Au-1 sample we obtain $R_e^* = M^*/\sqrt{n} \doteq 28$ nm. It follows clearly that within the Wilkens model the outer-cut of radius should be smaller than the crystal size, which is not satisfied at least for the Au-1 and Au-2 samples. In such a case the R_e^* parameter should be replaced by the crystallite size. Unfortunately in the common WPPM method, the size and dislocation broadening effects are treated separately and the computer programs are not prepared for such an option.[1] The dislocation model is usually applied to the materials with relatively large grain size and it assumed that R_e^* is much smaller than the crystallite domain size. Here, the parameter R_e^* was fixed instead of M^* at the constant value equal to the crystallite size $\langle D \rangle_{\mathrm{XRD}}$ and the dislocation density n was refined with other microstructural parameters taken from Table 3.1. The refined dislocation densities n^*_{XRD} are listed in Table 3.2. It was already mentioned from the data with such statistics it is difficult to identify dislocation correlation unambiguously. The quality of fits did not change significantly, but dislocation densities (n^*_{XRD}) changed. Now in all samples with an exception of the Au-1 sample the dislocation densities are close to $n^*_{\mathrm{XRD}} \doteq 5 \cdot 10^{15}/\mathrm{m}^2$. A higher dislocation density was estimated in the Au-1 sample. It questionable, if the method and theory used can be applied to such small crystallites. It is clear that for the crystallites of a very small size the image forces from boundary conditions at crystallite surface can play an important role and a different approach should rather be used. In summary, the assumption of constant $M^* = 1.6$ is found to be false because of it is s physically unrealistic for small particles. It was replaced by an assumption of *completely random dislocation distribution*, which implies that the outer-cut of radius R_e^* is equal to crystallites size $\langle D \rangle_{\mathrm{XRD}}$. This gives a constant dislocation density $n^*_{\mathrm{XRD}} \doteq 5 \cdot 10^{15}/\mathrm{m}^2$. The determined dislocation density is still quite high and the values should be discussed. At this point, we should remind that the assumption of uncorrelated dislocations gives the highest possible deformation energy associated with a single dislocation. Then the dislocations would have the highest "strength" and if a certain amount of deformation, revealed e.g. in the slope of the Williamson-Hall plot, must be explained, the smallest number of dislocation is necessary just in the case of random dislocation disribution. Similarly, as the y-intercept determines the smallest crystallite size, the anisotropy and the diffraction vector length dependent broadening (slope of mW-H plots) prescribes the lowest limit for dislocation density observed here. Otherwise, a different source of strain broadening must be found. In the end, it is necessary to note, that in the light of the revised model, an apparent correlation of the lattice parameter (a) and the dislocation density (n) in fig. 3.9 is a misleading effect.

A series of colloid Au nanoparticles with the size in the range 5–100 nm was characterised by XRD LPA. It was found from both the integral breadth analysis as well as from the WPPM method that the crystallite size obtained from XRD are slightly larger than the particle size determined by TEM — especially for the

[1] In the MSTRUCT this can be implemented, but it not was done at the time this work was finished.

	Au-1	Au-2	Au-3	Au-4
n^*_{XRD} ($\times 10^{15}/\mathrm{m}^2$)	**7.4**$\pm$1.1	**5.1**$\pm$0.5	**4.7**$\pm$0.3	**4.9**$\pm$0.2

Table 3.2: Dislocation densities (n^*_{XRD}) in colloid Au nanoparticles refined from XRD data if it is assumed that $R^*_e \equiv \langle D \rangle_{\mathrm{XRD}}$.

samples with the smallest particles (5–10 nm). This is difficult to explain in other way than that the samples for the TEM and XRD analyses were distinct due to different preparation procedures. For larger Au particles the sizes from both methods were similar. It was demonstrated that whereas the mW-H plots can be linearised for the measured Au reflections, an extrapolation of the linear dependence to the zero diffraction vector length is unjustified and it would result in a highly overestimated crystallite size. A proper calculation of the integral breadth based on the size-strain model has to be used. Strong anisotropy of diffraction line broadening was observed. It was explained by a combination of an anisotropic dislocation induced broadening and influence of twin faults. In the smallest particles of size 5–30 nm twinning fault probabilities of $\beta_{\mathrm{twins}} = 5 - 8\%$ were observed. The twinning probabilities were decreasing strongly with the particle size. Microstrain was detected in the particles and this was confirmed clearly by both the WPPM method and the integral breadth analysis. Under the assumption that dislocations are distributed completely randomly in the particles a lower limit of dislocation density in the particles was estimated to $n = 5.0 \pm 0.1 \cdot 10^{15}/\mathrm{m}^2$. These implies that the energy stored in the strain field of dislocations is increasing with the logarithm of particles size. Deformation energy is accommodated in large crystallites the agglomerates of which can recrystallise. The high stored energy is confirmed by the slopes of the modified Willimson-Hall plots and have to be explained by high density of dislocations or other defects. It grows linearly with the logarithm of the crystallite size. In the WPPM method usually individual effects of the size and dislocation broadening are treated independently. The problem discussed here reveals that in some cases their connection is necessary. The dislocation-induced broadening in very small crystallites ($D \lesssim 30$ nm) cannot be treated separately from the size broadening. The dislocation models used routinely for materials with crystallite domain size around 100 nm should be applied to nanomaterials only after proper consideration.

The results concerning synthesis and characterisation of nanoparticles by other techniques in the introduction together with the XRD analysis of twin probabilities were published in Šlouf, Kužel, and Matěj [122]. The above revised considerations about the dislocation correlation and density have not been published yet.

3.3 Study of ultrafine-grained Cu and Cu-Zr prepared by ECAP

This section deals with the microstructure of compact samples of ultrafine-grained (UFG) copper prepared by equal channel angular pressing (ECAP). The two series of samples, in detail described later, were prepared by doc. Miloš Janeček from

the Department of Physics of Materials and were investigated by several techniques as tensile testing, microindentation, TEM, electron backscattered diffraction (EBSD), positron annihilation spectroscopy (PAS) and by a couple of XRD techniques including Laue XRD images, texture measurements and finally the convention powder diffraction, for which analysis the WPPM method was utilised. The research is a collaboration of many coworkers,[1] the present author was responsible mainly for dislocation density determination from powder diffraction data. Results of the research were published mainly in Matěj, Kužel, Dopita, Janeček, Čížek, and Brunátová [136], Kužel et al. [137] and Dopita et al. [143]. The first article is primarily focused on the XRD analysis of dislocation densities. In the second paper XRD is utilised together with the above mentioned methods to present a more general idea of evolution of microstructure, and properties of the studied samples during the ECAP process. The last paper by Dopita et al. concerns the EBSD analysis.

3.3.1 Motivation

Equal channel angular pressing is a severe plastic deformation (SPD) technique capable of producing fully dense and bulk submicrocrystalline and nanocrystalline materials [144]. Copper represents an ideal model material to study the processes of deformation and microstructure evolution. It is low cost, has simple fcc structure and medium stacking fault energy ($\gamma = 78$ mJ/m^2, see e.g. [140] for comparison with other metals). Properties and microstructure of Cu prepared by severe plastic deformation (SPD) techniques can actually be compared with results of very wide former research of this material prepared by conventional techniques as rolling, extrusion, compression, etc. It is known (e.g.[145]) that a fine microstructure of pure Cu is unstable and recrystallisation occurs at rather low (even room) temperatures. However the structure can be stabilised by a small addition of impurities or precipitates (Kužel et al. [78], [145]). The pure Cu and Cu with an small addition of Zr samples are studied here.

Changes in dislocations networks, dislocations creation, motion, trapping, recombination and annihilation are the fundamental mechanisms of microstructure evolution influencing the grain refinement. Large fraction of deformation energy stored in the material is connected with dislocations and vacancies ([64, 140]). In the ECAPed materials so high dislocation densities ($n \sim 10^{15}$/m^2) are commonly observed ([140, 144]) that it is difficult to characterise them by direct methods as TEM or even with the aid of the positron annihilation spectroscopy [145]. XRD diffraction LPA is hence a very suitable tool which can complement the analysis especially for the higher dislocation densities ($n \gtrsim 1 \cdot 10^{15}$/m^2). Defects density and information about their character and arrangement are important factors characterising the material microstructure.

[1] List of coworkers on the work presented here: Z. Matěj (present author), T. Brunátová and R. Kužel, Department of Condensed Matter Physics (XRD analysis); M. Janeček and O. Srba, Department of Physics of Materials (sample preparation, mechanical properties, TEM); J. Čížek, Department of Low Temperature Physics, Faculty of Mathematics and Physics, Charles University in Prague (PAS analysis); M. Dopita, Institute of Materials Science, TU Bergakademie Freiberg, Germany (EBSD analysis).

Other aspects of samples microstructure (texture, recrystallisation state) can be studied by XRD as well, but here the work is concerned mainly the LPA. The aim is the determination of dislocation density and characterisation of dislocation arrangements in the sample. Temperature stability of all the properties have also been studied (as in Cherkaska [145]), but here the focus is given only to the evolution of microstructure during the ECAP process itself and its thermal stability is considered only marginally.

Cu has a similar electron configuration as Au and also the same crystal structure. Similarities in behaviour of these two metals can be expected, but the main connecting idea of sections 3.2 and 3.3 is the same microstructure model, use of the WPPM method and an attempt to characterise the dislocation state in the material.

3.3.2 Sample preparation, other methods

Technical purity (99.95%) Cu and Cu width an addition of 0.18 wt.% of Zr were deformed by ECAP to a maximum equivalent strain of 8 (this means by $N = 1$, 2, 4 and 8 passes) at room temperature following route B_c (the samples is rotated after each pass by 90° always in the same direction [146]). Prior to ECAP processing the specimens were annealed for 2 hours at 450 °C in a protective inert atmosphere. ECAP pressing was carried out using a split design die. The details of the die design as well as the ECAP pressing are given elsewhere by Janecek et al. [147].

The microstructure of the initial state of Cu is depicted in the scanning electron (SEM) micrograph in fig. 3.11. It consists of fully recrystallised grains of an average size about 30 μm. The initial state of CuZr samples is characteristic with coarse recrystallised grains with size of several hundreds of microns and numerous fine Cu_9Zr_2 precipitates (Kužel et al. [137]).

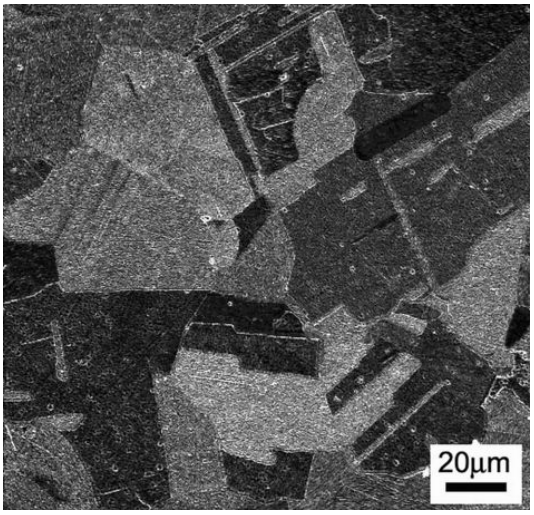

Figure 3.11: SEM microphotograph of the initial state of the pure Cu sample before ECAP. (by M. Janeček, KFM MFF UK, [137])

TEM micrographs (fig. 3.12, taken from Kužel et al. [137]) shows the evolution of the pure Cu samples during the ECAP deformation. After the first pass (fig. 3.12a) the sample microstructure consists of strongly elongated dislocation

cells and/or subgrains of average cross-sectional size of 300–400 nm. After the second pass (fig. 3.12b) the microstructure did not change significantly. Bands of elongated subgrains were found in all areas of the specimen. Most of the boundaries were still aligned along the trace of a {111} plane. After four passes (fig. 3.12c) the fraction of equiaxed subgrains increased and the larger proportion of high-angle grain boundaries was observed in the structure. The microstructure of the specimen after 8 passes (fig. 3.12d) shows an almost homogeneous microstructure with equiaxed subgrains separated mostly by the high-angle grain boundaries. The individual boundaries are straight with sharp contrast and very few dislocations in the grain interior. The average grain size achieved is between 200–300 nm.

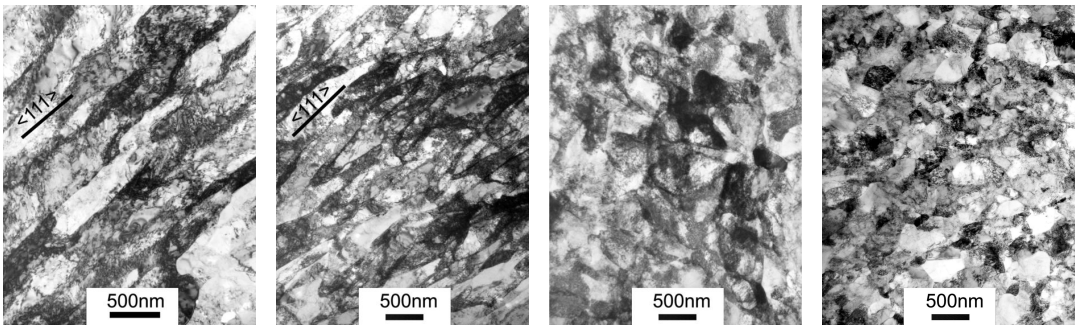

(a) $N = 1$ (b) $N = 2$ (c) $N = 4$ (d) $N = 8$

Figure 3.12: Bright-field TEM micrographs of the pure Cu samples treated by different number (N) of ECAP passes. (by M. Janeček, KFM MFF UK, [137])

In the CuZr samples details of the microstructure evolution during the ECAP processing is quite different. In the fig. 3.13 a TEM microphotograph after 8 ECAP passes is shown. The microstructure of the CuZr sample after 8 ECAP passes consists mostly of equiaxed grains with high misorientation separated by grain boundaries with typical thickness fringe contrast corresponding to equilibrium boundaries. The average size of grains was 200–300 nm. Eight passes of ECAP resulted in the strong grain refinement of a factor of 100 approximately. Much more details of TEM observations can be found in Kužel et al. [137].

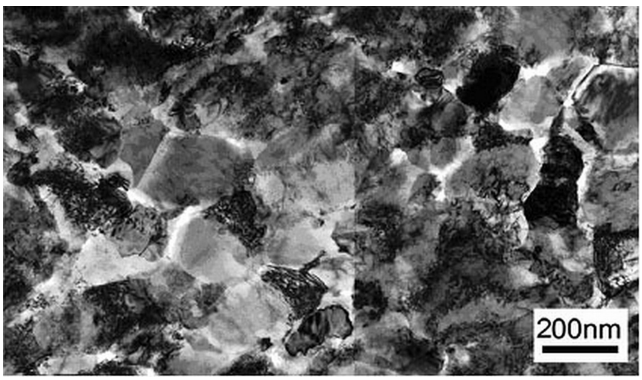

Figure 3.13: TEM microphotograph of the CuZr sample after 8 ECAP passes. (by M. Janeček, KFM MFF UK, [137])

Results of the EBSD analysis strongly confirm the above TEM observations. For illustration inverse pole figure maps of the CuZr samples after 2 and 8

ECAP passes are shown in fig. 3.14. Elongated grains still visible in the fig. 3.14a after 2 passes are finally converted to much smaller equiaxed grains (fig. 3.14b) with a high fraction of high angle grain boundaries (HAGBs). This is shown more quantitatively in fig. 3.15 where the frequency of high and low angle boundaries evaluated from EBSD is plotted as function of number of passes (N). Plot fig. 3.15a shows that in the pure Cu sample after 8 passes the most of the grain boundaries has the high angle character whereas according to fig. 3.15b in the CuZr sample even after 8 passes a nonnegligible portion of boundaries seen by EBSD has the low angle character. This was explained by the presence of Cu_9Zr_2 precipitates which may block the movement of the dislocation walls (boundaries) [137]. More details of instrumentation and analysis methods used, as well as results concerning also twin-related and other types of special grain boundaries can be found mainly in Dopita et al. [143] and Kužel et al. [137].

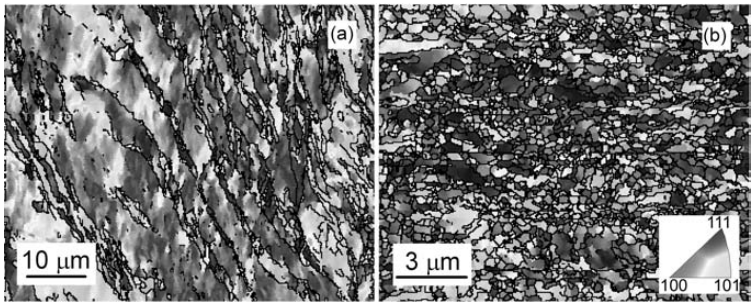

Figure 3.14: Inverse pole figure maps determined by EBSD for the CuZr samples after (a) 2 ECAP passes and (b) 8 passes. High angle boundaries (missorientation $> 15°$) are plotted as black lines. For more details see [143]. (by M. Dopita, IMS TU-Freiberg, [143])

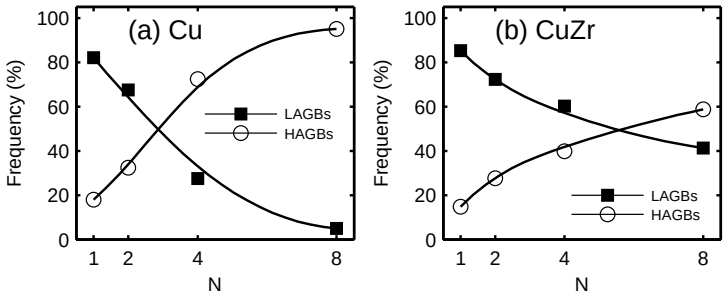

Figure 3.15: Frequency of appearance of low (L) and high (H) angle grain boundaries (AGBs) for the (a) Cu and (b) CuZr samples treated by different number (N) of ECAP passes. (■) — LAGBs, (○) — HAGBs. For more details see [143]. (by M. Dopita, IMS TU-Freiberg, [137, 143])

Positron annihilation spectroscopy (PAS) is sensitive mainly to dislocations and microvoids in the samples. It was determined by PAS that dislocation density n in the initial pure Cu sample is $n \leq 10^{12}/\mathrm{m}^2$ and in the CuZr sample $n = 8 \pm 1 \cdot 10^{12}/\mathrm{m}^2$ [137, Table IV]. The ECAP treated samples have typically a very high defect density. Practically all positrons are trapped at defects and annihilate from a localized state in some defect (so called saturated positron

trapping). It was estimated that the mean dislocation density in the samples exceeds $n \gtrsim 5 \cdot 10^{14}/\mathrm{m}^2$. X-ray powder diffraction is just sensitive to such higher dislocation densities. It is still possible to investigate by PAS a ratio of a signal contribution from positrons trapped at dislocations and microvoids. It was clearly seen in Kužel et al. [137] that the dislocation density in the specimens deformed by ECAP increases with increasing number of passes faster than the concentration of microvoids. It was also pointed out that microvoids size increases from ≈ 2 monovacancies after a single ECAP pass to ≈ 4 monovacancies after 8 passes.

More information on the microstructural studies by different methods can be found in Kužel et al. [137] and Dopita et al. [143]. However, it was illustrated that well defined UFG Cu and CuZr samples are going to be studied by XRD here.

3.3.3 Experimental

Below, the following notation is used. Pure Cu samples treated by different number (N) of ECAP passes are labelled as Cu-1, Cu-2, ..., Cu-8 and similarly the CuZr samples are labelled as CuZr-N.

The samples have a bulk form (slabs of size at least 5 mm × 5 mm × 2 mm) and contrary to the Au samples in section 3.2 can be measured by a common laboratory x-ray diffractometer in the focusing Bragg-Brentano geometry using CuK_α characteristic radiation. The experiment is sensitive to the material in a depth of few microns from the sample surface (absorption factor for density $\rho_\mathrm{m} = 8.96$ g/cm^3 [142], $\mu = 420$ 1/cm [148]) and hence the samples surface was chemically etched prior the x-ray measurement to remove the top layer, which can be affected by sample cutting, polishing etc. Because the LPA analysis and especially the WPPM method are very sensitive to samples homogeneity and good grain statistics a "powder" quality of the compact bulk polycrystalline samples was check by *Laue x-ray backscattering photos*. For experimental setup see e.g. Cherkaska [145, fig. 3.8a–b]. Especially highly pure Cu is known to recrystallise even at room temperature hence Laue backscattering photos of the ECAPed Cu samples are depicted in fig. 3.16. Unfortunately it can be clearly seen from the fig. 3.16c, where a "granular" structure of diffraction rings is visible, that the specimen of the Cu-4 sample dedicated for the XRD analysis was already recrystallised. Hence, the pure Cu sample treated by 4 ECAP passes was discarded from further XRD analysis. The laue photos (fig. 3.16) of other samples shows nice continuous diffraction rings. Intensity maxima at the rings a footprint of texture typically present in the ECAP treated samples. The Laue photos of CuZr samples are very similar and confirms good "powder" quality of all the CuZr samples.

As it has already been mentioned XRD data for LPA and WPPM were measured with the aid of Panalytical X'Pert Pro powder diffractometer in the symmetrical Bragg–Brentano geometry using filtered CuK_α-radiation and variable divergence and anti-scatter slits. A part of the measurements was performed with the PIXCel position-sensitive detector. The correction for instrumental broadening was similar as in the section 3.2.3 performed with the aid of a NIST LaB_6 standard. The utilisation of both the variable slits as well as the position sensi-

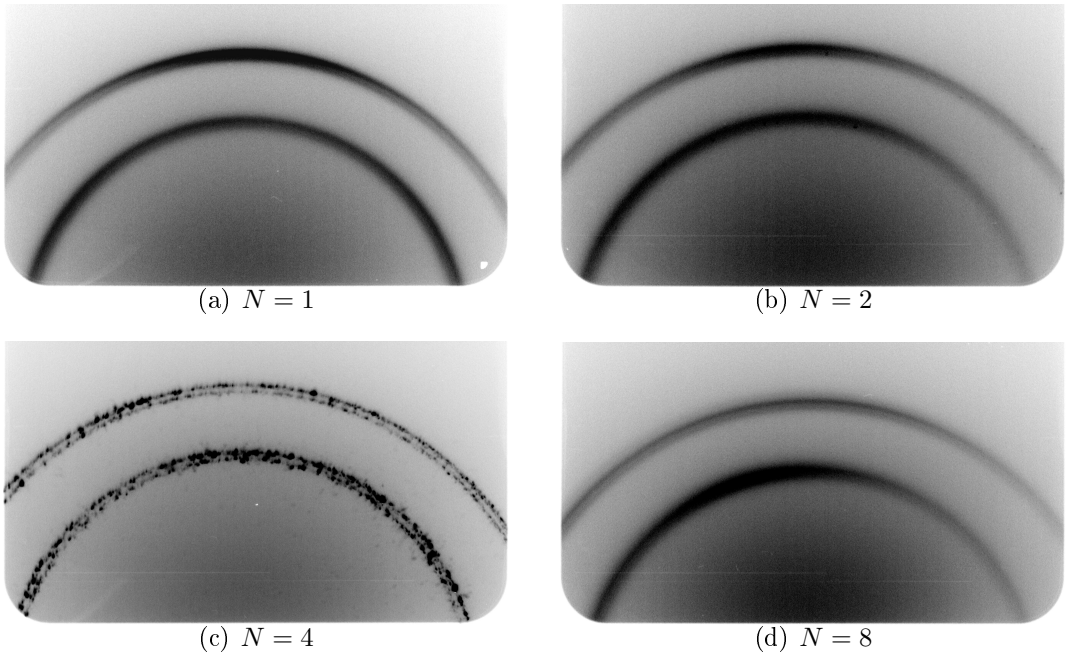

(a) $N = 1$ (b) $N = 2$

(c) $N = 4$ (d) $N = 8$

Figure 3.16: Laue x-ray backscattering photos of the pure Cu samples treated by different number (N) of ECAP passes. (by R. Kužel)

tive detector (PSD) have crucial importance, because it influences data quality substantially. PSD detector enables increasing measurement time per point by a factor of 100×. The variable slits enhances strongly the intensity and counting statistics of the high angle reflections, which play a crucial role in analysis of dislocations from diffraction data. Just remind that several approximations in the theoretical chapter 2 were rather valid only for the high angle reflections (large length of diffraction vector G). Utilisation of variable slits is not recommended, especially e.g. for temperature factors analysis, which is discussed more widely in ch. 4. But it is assumed here that the shape of diffraction profile is not affected with imperfections in variable slits operation within a narrow 2θ range of a single reflection. The intensity gain archived by them is really valuable.

3.3.4 Whole pattern analysis

The measured powder diffraction patterns were fitted using the program MSTRUCT (ch. A). Exactly the same models were used as for the colloid Au nanoparticles (ch. 3.2.5). The size effect is not the main broadening component in this case. It is comparable with the instrumental broadening but fitting the both size parameters (M_D and σ^*) gives crystallite sizes, which are difficult to compare across the samples. Hence the parameter σ^* was again set to a fixed value $\sigma^* = 1.5$ for all the samples. This had no effect on the quality of the fits. There is texture in the samples, as can be seen in the Laue images (figs. 3.16). The texture is relatively complex, hence for simplicity again the "arbitrary texture" model (ch. A.9) with peak intensities as free refinable parameters was used. In addition, peak positions were also refined independently, which is commented below (p. 75).

The most important broadening component was in this case the dislocation

effect. For illustration a fragment of the MSTRUCT parameter file is depicted.

```
// the 1st phase - Dislocation Strain broadening (Scardi & Leoni & van Berkum)
dislocSLvB+  strainProfCu   broadening component type, effect name
1       simplWilk           use MWilk instead of Re (0-No,1-Yes), formula
1.6     0.002               Mwilk, rou(1/nm^2)
0.30    -2.1    0.          Cg0, q1, q2
```

The most important word here is a name for the dislocation effect: `"dislocSLvB+"`. The second one is the codeword: `"simplWilk"` saying that the simplified Wilkens model should be used. Other parts let us choose if either M^* or R_e^* should be fitted together with the dislocation density (`"rou"` here). In the last line, the parameters of the average dislocation contrast factors are set. The first value is $C_{h00} \equiv \chi_{h00}/\pi$ and the second is q in eq. 2.80c (p. 44). Here a value $q = 2.1$, somewhere between $q_e = -1.64$ and $q_s = -2.38$ for edge and screw dislocations, is initially set. The q value can can be simply converted to e.g. the edge character (w_e) of dislocations (see below).

Planar faults are included similarly by this code:

```
// the 1st phase - Stacking Faults - Warren, Velterop (2000), Scardi, Leoni
faultsVfcc  faultsProfCu    broadening component type, effect name
0.01    0.03                alpha, beta(twins)
```

The codeword `"faultsVfcc"` specifies that the classical model of Warren [6], developed by Velterop et al. [13] and Scardi and Leoni [11], as described in the theoretical section (ch. 2.3.8), is used. The fault probabilities are set here at the last line to $\alpha = 1\%$ and $\beta_{\text{twin}} = 3\%$.

Finally, the following microstructural parameters were refined from the XRD data: median of the crystallite size distribution (M_D), fraction of edge dislocations (w_e), dislocation density (n), dislocation correlation parameter (M^*) and stacking (α) and twinning (β_{twin}) fault probabilities, respectively. The relevant determined parameters are specified in the Table 3.3.

ID	M_D (nm)	w_e	n ($\times 10^{15}$/m^2)	M^*
Cu-1	68.0(6)	0.73(3)	2.15(3)	0.48(1)
Cu-2	61.8(5)	0.57(1)	2.79(3)	0.51(1)
Cu-8	65.7(4)	0.66(1)	3.68(5)	0.39(1)
CuZr-1	57(1)	0.69(5)	1.6(1)	0.57(3)
CuZr-2	71(2)	0.61(5)	2.3(1)	0.89(6)
CuZr-4	73(2)	0.32(4)	2.3(1)	1.17(7)
CuZr-8	60(1)	0.20(4)	3.0(1)	0.82(5)

Table 3.3: Results of the WPPM analysis of XRD data of the pure Cu and CuZr samples treated by different number (N) of ECAP passes. M_D — median of the log-normal crystallite size distribution ($\sigma^* = 1.5$ assumed); w_e — fraction of edge dislocations; n — dislocation density; M^* — Wilkens dislocation correlation parameter (eq. 3.3, ch. 2.3.5).

The stacking fault probabilities (α, β_{twin}) are not listed in the table, because their refined values were $\lesssim 0.5\%$ and the effect on the shape of calculated diffraction profiles is marginal. Hence, they were set to zero. Faulting probabilities

$\approx 0.5 - 1\%$ are reported in the literature [14] for similar ECAP treated Cu samples but in our work the values were not distinct from zero within the experimental uncertainty limits.

An example of the fitted diffraction pattern is shown in figs. 3.17 and 3.18.

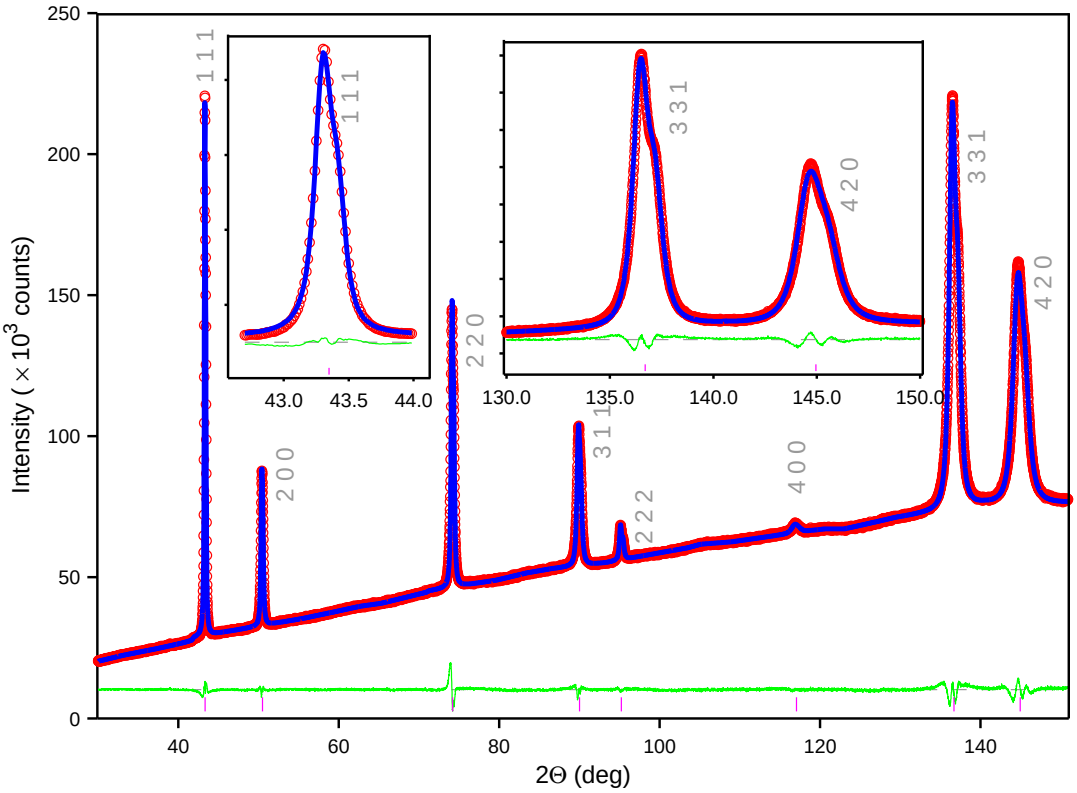

Figure 3.17: Pattern fit of the Cu-1 sample.
(red circles — measured points; blue line — calculated pattern; green line — difference curve)

3.3.5 Summary and discussion

Even though we could fit both parameters (n, M^*) of the dislocation broadening model simultaneously and they converged to reasonable values, the fits were not perfect. This can be seen mainly in the difference curve close to the 220 reflection in fig. 3.17 or in the detailed plots of the 220 and 420 reflections in fig. 3.18. Fits of the other samples are not better. This indicates that the model applied is not completely correct. The wrong fit of the central part of the 420 reflection could be attributed to the inaccuracy of the Fourier coefficients for simplified Wilkens model for the long real space lengths. However, the differences for the 220 reflection cannot be explained in this way. The model can well describe the characteristic broadening anisotropy (figs. 3.19 and 3.20), but discrepancies in the whole pattern fit remains. If the patterns were fitted by analytical profile functions and only reflections widths were extracted this problem would be ignored.

Another problem concerns the peak positions that were fitted as independent parameters rather than being treated usually as a function of the lattice

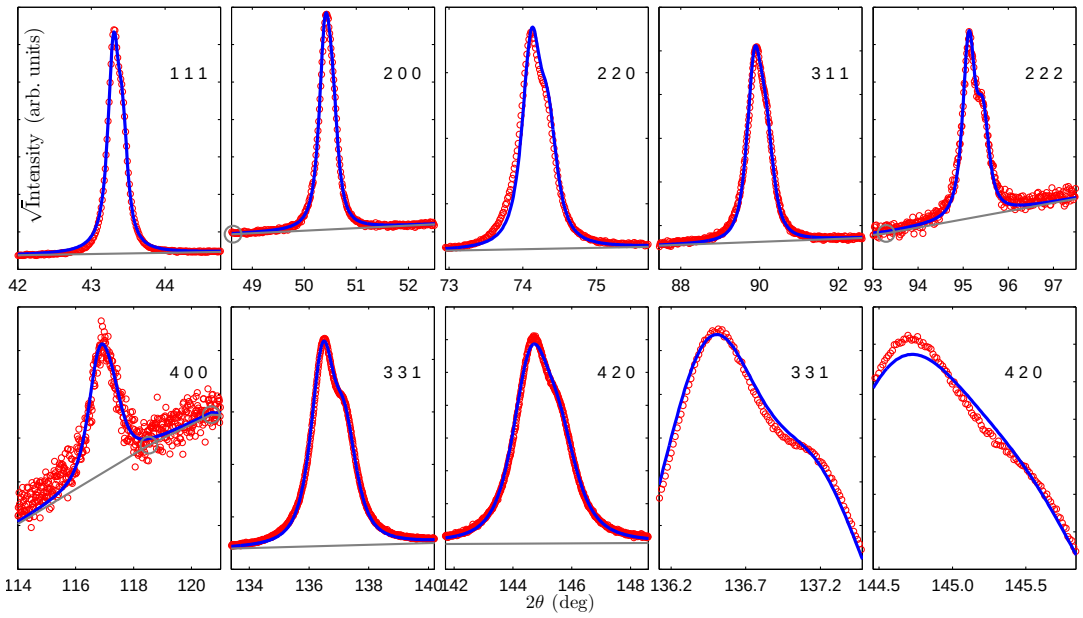

Figure 3.18: Details of the pattern fit of the Cu-1 sample. (square root scale)

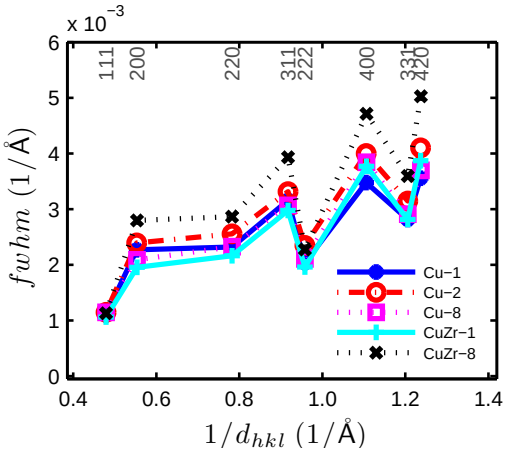

Figure 3.19: Williamson-Hall plot for selected Cu and CuZr samples treated by ECAP.

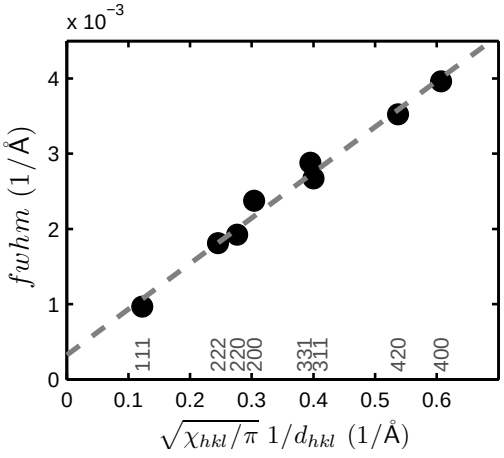

Figure 3.20: Modified Williamson-Hall plot of the Cu-1 sample.

parameter, 2θ zero error and the specimen displacement error. The refined $\Delta 2\theta$ corrections from calculated reflection positions are depicted in fig. 3.21 for the pure Cu samples. The characteristic anisotropy of the peak shifts in fig. 3.21 is the same also for the CuZr samples. Since in the focusing Bragg-Brentano geometry only the lattice planes parallel to the sample surface are measured and two instrumental aberrations mentioned above can also affect the peak positions, the data from XRD measurement in other geometries were utilised to resolve this problem. For estimation of the texture and possible residual stresses some samples were measured also on the Eulerian cradle in the parallel beam geometry

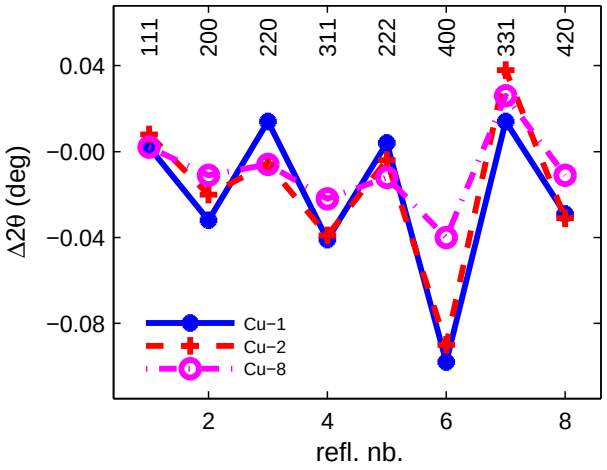

Figure 3.21: 2θ line shifts refined by WPPM from diffraction patterns of the pure Cu samples treated by ECAP. (blue stars — Cu-1; red crosses — Cu-2; empty magenta circles — Cu-8)

and by using polycapillary optics.[1] In this arrangement the above instrumental aberrations are signficicantly supressed. The peak positions were fitted and results are depicted in figs. 3.22 and 3.23. Figure 3.22 shows similar anisotropy as detected for the Cu-1 sample (fig. 3.21), but measured in the CuZr-1 sample in parallel beam geometry and peak positions are converted to the lattice parameter. The lattice parameter measured for different angles (ψ) of inclination of the diffracting lattice plane normal from the sample surface normal are plotted there. It can be seen that the anisotropy varies with this angle. In the second plot (fig. 3.23), relative strains

$$\epsilon^*_{hkl} \equiv \frac{d_{hkl}(\psi) - d_{hkl}(\psi = 0)}{d_{hkl}(\psi = 0)} \ ,$$

calculated for each measured reflection, are plotted as a function of $\sin^2\psi$. No linear dependence is clearly visible and all relative changes in the lattice spacing are $\lesssim 10^{-3}$. Only the $\langle h00\rangle$ directions show a strong dependence on the inclination angle (ψ). According to figs. 2.14 and 2.15 (p. 42) the $\langle 100\rangle$ directions are the elastically softest directions in fcc Cu.

Now three possible hypothetical explanations of the peak shifts in the patterns are specified and subsequently they are discussed on the basis of the experiments above.

(A) The shifts of diffraction lines are related to the planar defects, which were neglected. (B) The shifts are caused by the residual stresses in the samples. (C) The shifts originate from the lattice defects, but the anisotropy of the effect is beside others related to the deformation process in the samples. Samples are deformed by different number of ECAP passes. During two subsequent passes different slip systems are activated, complex microstructure of defects in the grain boundaries as well as preferred orientation of deformed grains are formed. These all result in the diffraction peak shifts, which depends on both the reflection type (hkl), as well as on the orientation of the diffracting crystallites.

[1] For details of the parallel beam setup with polycapillary optics used for texture, stress and precise lattice parameter measurements see e.g. the theses by Dopita [128] or Šimek [149] (in Czech).

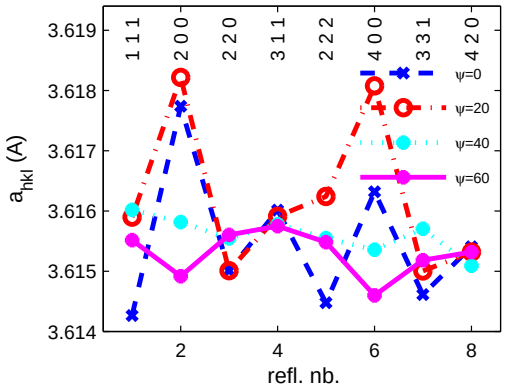

Figure 3.22: Lattice parameter a_{hkl} of the CuZr-1 sample for different inclination angles (ψ). (Data extracted from the measurements in the parallel beam geometry. Measurements for different inclination angles — 0°, 20°, 40°, 60° — marked by different symbols and colours.)

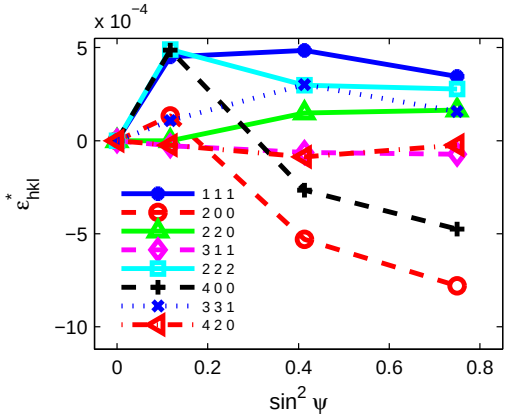

Figure 3.23: Relative strains (ϵ^*_{hkl}) from the XRD "residual stress measurements" of the CuZr-1 sample. (Values for the 200 reflection are plotted by red circles (○) and dashed line, values for the 400 reflection by black crosses (+) and black dashed line.)

The simple case (A) cannot explain the dependence on the inclination angle (ψ) clearly visible in the figure 3.22. In addition, inclusion of planar defects did not improve the WPPM fits significantly. Concerning (B). In figure 3.23, no clear linear dependence is visible, changes are rather small and hence any influence of residual stress is difficult to justify. The case (C) is the most complex one. But it follows from TEM and EBSD analyses that the grain structures of samples treated by a single ECAP pass and by 8 passes are very different. If the shifts originate from the processes and changes during the deformation, their strong dependence on the number of ECAP passes is expected. This is not observed, though. A more quantitative comparison and data from stress measurements for different samples would be suitable here, but from the basic data refined by WPPM no such tendency is visible. Hence also the hypothesis (C) can not be confirmed from the available data.

The effect of unexpected peak shifts is present in all the samples, it is observed also in more precise lattice parameter measurements in different experimental geometries and it is not related to the evaluation procedure or the computer program used. It is reported here as a systematic experimental observation which unfortunately has nto been explained yet. On the other side, the peak shifts can be corrected in the MSTRUCT and do not influence strongly the results of LPA.

Since the pattern fits cannot be improved more, the determined microstructure parameters has to be accepted as specified in the table 3.3 (p. 74).

The median of the crystallite size (M_D) is basically the same in all the samples, $M_D \approx 60 - 70$ nm. This value is much smaller than the values 200–300 nm reported from TEM and EBSD. Correlation between the size of coherently scattering crystallites and the size of subgrains or cells seen be TEM in the SPD materials is discussed in the paper by Ungár, Tichy, Gubicza, and Hellmig [138]

dedicated to the problem. The authors discuss the fact that the crystallite size reported from XRD investigations is often markedly smaller than that seen by TEM and pointed out that it cannot be explained solely by the low-angle grain boundaries, but there should exist also defect structures, e.g. "dipole" dislocations walls breaking the coherency between parts of the crystal without differences in their orientation. The crystallite size reported in SPD Cu and CuZr here is hence in very good agreement with the results reported elsewhere [150] and can be justified by the model of Ungár et al. [138].

Concerning the parameters of the dislocation model, in Table 3.3 (p. 74) a trend of changes in the dislocation character from initially higher fraction of edge dislocations to more screw dislocation character is apparent in the case of CuZr samples. TEM and/or EBSD investigations show more pronounced microstructural changes during the ECAP deformation. The evolution of other dislocation model parameters (n, M^*) determined by XRD is shown in figs. 3.24 and 3.25. The determined dislocation densities are between $1.5 - 3.7 \cdot 10^{15}$ m^{-2} and are increasing with the number of passes (N). Breuer et al. [151] reported dislocation densities up to $1.5 - 1.7 \cdot 10^{15}$ m^{-2} in plastically deformed copper. In Balogh et al. [150] they studied dislocations by XRD in pure Cu samples treated by the ECAP following route C and reported increasing dislocation density up to 4 passes and then saturated at $2.5 - 3.0 \cdot 10^{15}$ m^{-2}. Gubicza et al. [65] and [140] reported, for the B_C route pure Cu, dislocation densities of about $2 \cdot 10^{15}$ m^{-2}, which were growing up to 3 passes and then were saturated up to 10 ECAP passes. Maximum value of the dislocation density here ($3.7 \cdot 10^{15}$ m^{-2}) is slightly higher, but it is important to note, that here Cu of lower purity was studied. The dislocation correlation parameter M^* found here was in average higher for the CuZr samples than in pure Cu samples. This indicates a slightly more random dislocation arrangement in samples with an addition of Zr. In fig. 3.26 the stored energy (E_{disl}) in the dislocation strain field calculated according to eq. 3.4 (p. 65) is plotted. The stored energy is very similar for both types of samples, it increases strongly during the first two passes and saturates at $E_{\mathrm{disl}} \approx 0.23$ J/g. The increase of stored dislocation energy could be related to the formation of the non-equilibrium grain boundaries during the first few passes but this cannot be derived strictly from the present XRD data because the dislocation model used does not account well for the strain contribution coming from dislocations in the boundaries. Gubicza et al. [65] reports a slightly higher saturated values of $E_{\mathrm{disl}} \doteq 0.3$ J/g, but they do not use the same formula as eq. 3.4 here. If their formula for the stored dislocation energy was used, the energy here would also be higher ($E_{\mathrm{disl}} \approx 0.35 - 0.4$ J/g).

The dislocation model used here explains well the XRD line broadening anisotropy. Unfortunately, there are still unexplained differences between calculated and experimental XRD data of Cu samples treated by ECAP. Moreover, if the model is applied to samples showing even more Lorentzian diffraction profiles than the UFG Cu samples studied here, LPA analysis tends to prefer unreliably small values of the correlation parameter (M^*) and overestimate dislocation density (n). Asymmetry and shifts of diffraction profiles can be related to some specific dislocation structures as e.g. dipoles (ch. 2.3.3), dislocation walls or dislocations in grain boundaries. The model does not account for this and its extension would be

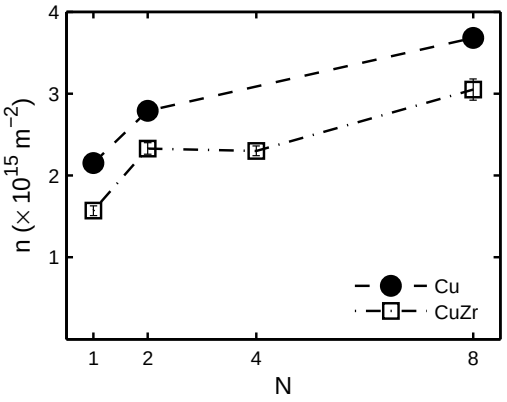

Figure 3.24: Evolution of dislocation density (n) in the pure Cu (●) and Cu with a small addition of Zr (□) samples treated by different number (N) of ECAP passes.

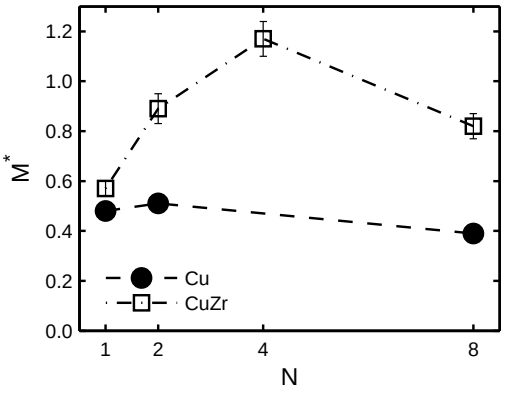

Figure 3.25: Evolution of dislocation Wilkens dislocation correlation parameter (M^*) in the pure Cu (●) and Cu with a small addition of Zr (□) samples treated by different number (N) of ECAP passes.

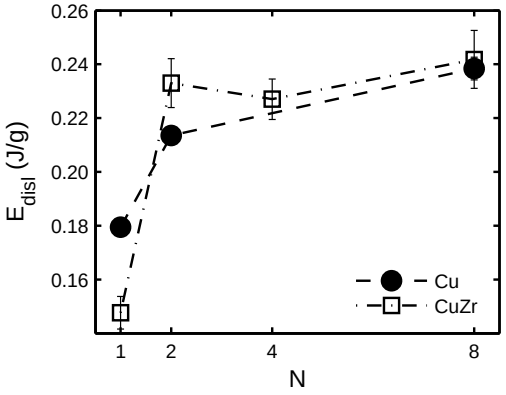

Figure 3.26: Stored energy (E_{disl}) in the dislocation strain field, calculated from XRD data according to eq. 3.4. Plotted for the pure Cu (●) and Cu with a small addition of Zr (□) samples as a function of the number (N) of ECAP passes. Data, determined by XRD analysis, taken from the Table 3.3.

grateful. It has been shown that both the geometric and elastic anisotropy appear in the problems concerning the defect-induced broadening. Hence, especially the anisotropic behaviour of such specific defects should be more investigated from a theoretical point of view and for several materials.

The XRD analysis of defects in the pure Cu and CuZr samples treated by ECAP was published mainly in Matěj et al. [136] and Kužel et al. [137].

Chapter 4

Study of Nanocrystalline TiO_2 Powders

4.1 Introduction

In contrast to chapters 2 and 3 a different type of problem is solved here. The crystallite size decreases about 10× and the defect density is much smaller than for metals studied in chapter 3. The *size broadening* becomes a dominant effect and the analysis consists mainly in the determination of crystallites size. Material selected for studies is *titanium dioxide* (TiO_2). XRD line profile analysis (LPA) and the whole powder modeling method (WPPM) [11] were used for the study of the microstructural features.

Titania (TiO_2) is a very common compound, which can be found in many products used in daily life. Low cost, non-toxicity, good chemical stability, mechanical hardness and optical transmittance with high refractive index are its traditional favourable properties. Its excellent photochemical activity and other photo-induced phenomena are subjects of research of novel applications of this apparently simple material. TiO_2 belongs to a class of porous metal oxides such as ZrO_2, SnO_2, CeO_2, Al_2O_3 etc. It is a wide band gap semiconductor (3.0–3.2 eV) [152, 153]. Nowadays, the most utilised properties of titania are - a photo-induced catalytic activity [154, 155] and super hydrophilicity [156–158] after UV light irradiation. They can found applications in various areas, e.g. in ecological disposal of environmentally unfriendly contaminants [159–163], efficient support of metal species catalysts [164, 165], as an antibacterial and selfcleaning material [166, 167], for antifogging coating [168], dye-sensitised solar cells [169, 170], in electro chromic devices [171, 172], as sensors [173] or in hydrogen production [174]. Large research effort was invested into the enhancement of the photoinduced properties by shifting the absorption edge to longer wavelengths into the visible light range [175]. Nitrogen doping [153, 176, 177] appears as one of the most promising ways. Description of the mechanism inducing the photoinduced properties of titania can be found e.g. in the thesis of Šícha [178].

Anatase, rutile and brookite are the most common crystalline phases of titania [129] (in Czech). Other crystalline phases of TiO_2 were described e.g. by Arlt et al. [179]. The application properties are often related to structure of the material (phase composition, grain size, defect density) [4, 180, 181], textural

properties (pore-size, specific surface area) or surface reconstruction etc. For example Shibata et al. [182], [183] showed that the photo-induced properties of TiO_2 can be influence also by residual stress. Generally the most important factors are phase composition and crystallite size. Both these factors are the primary subjects of diffraction analysis. It appears that nanocrystalline anatase has a superior photocatalytic activity than other forms of titania (amorphous, rutile, bulk etc.) [184]. From many works about titania at least a few devoted to its structural studies and relation between its microstructure and properties should be mentioned.

Zhang and Banfield [185, 186] found (i) that anatase is thermodynamically more stable than rutile, if crystal size $D \lesssim 14$ nm, and (ii) that for $D \lesssim 11$ nm brookite is almost as stable as anatase [185]. (iii) Nanocrystalline anatase appears often together with brookite [187] and upon heating they transform to rutile [188]. The authors of [152] studied amorphous TiO_2 and its transformation to nanocrystalline anatase by using pair-distribution function, Monte Carlo simulations and x-ray absorption spectroscopy. Residual stress in anatase was measured by Raman spectroscopy by Alhomoudi and Newaz [189]. Elastic anisotropy of anatase was studied by XRD residual stress measurements in thin films by Matěj et al. [190], Borgese et al. [191] and Bontempi et al. [192]. Size dependent elasticity in nanocrystalline titania was studied in high pressure synchrotron experiment by Chen et al. [193]. Kinetics of crystallisation of anatase nanoparticles, transformation from amorphous state to anatase nanocrystals, was studied by Zhang and Banfield [194], Li et al. [195] and Jensen et al. [196]. Dislocations in nanocrystalline anatase was characterised by the WPPM method using the same models as in chapters 2 and 3 by Spadavecchia et al. [153]. The Debye function method was used for analysis of size and shape of TiO_2 nanocrystals by Cernuto et al. [118]. Connection of anisotropic shape of anatase particles with its reactivity was discussed by Yang et al. [197]. Transmission electron microscopy (TEM), nitrogen adsorption, mercury porosimetry and XRD analysis using the Williamson-Hall (WH) plot method were applied for particle size determination by Weibel et al. [198]. Different LPA methods were compared on a set of sol-gel TiO_2 powders by Vives and Meunier [199].

4.2 Motivation

There are numerous techniques for synthesis of TiO_2 materials in form of powders or thin films. In this chapter the samples prepared by chemical methods are of main interest. Preparation of nanoparticles of a given phase composition and a given size is often one of the primary research objectives in this field. If a dependence of some material property, e.g. photocatalytic activity or contact angle characterising the material hydrophilicity [157], on crystallite size should be studied, it is desirable to have good knowledge of the crystallite size in the studied specimens. Not only the average size $\langle D \rangle$ is important, but it is useful to have at least an idea of dispersion of crystallite sizes. Other size-related phenomena can play a role as well. E.g. Yang et al. [197] has shown that because of reactivity of anatase $\{001\}$ facets is higher than reactivity of thermodynamically most stable $\{101\}$ facets, the reactivity of anatase particles can be influenced by

their anisotropic shape. In [196], [118] they observed such size anisotropy for anatase nanocrystals.

This chapter is focused on the crystallite size determination in *anatase nanopowders prepared by chemical processes* such as hydrolysis of titanium (iv) alkoxides in hydrogen peroxide solution [200], sol-gel routes [201], calcination and super/subcritical fluid extractions techniques [202]. The general objective is preparation of anatase nanoparticles with a given size and a reasonable dispersion of particles size. Hence special attention is given here to *determination of crystallite size distribution* by the x-ray LPA.

The all samples studied in this chapter were prepared by Dr. L. Matějová. Preparation conditions for a particular samples are described in the text throughout the chapter. Measurements of specific surface area (S_{BET}) and TEM or SEM (scanning electron microscopy) images presented here for illustration were done by Dr. L. Matějová, J. Franc and F. Novotný. All XRD measurements, MSTRUCT program modifications and XRD analyses presented in this chapter were performed by the present author. Results were published mainly in the following papers: (i) Matějová, Cajthaml, Matěj, Benada, Klusoň, and Šolcová [202], (ii) Matějová, Matěj, and Šolcová [200] and the most important part of the work concerning the XRD analysis in (iii) Matěj, Matějová, Novotný, Drahokoupil, and Kužel [201].[1]

4.3 Description of basic models

Theoretical chapter 2 was devoted mainly to the defect-induced diffraction line broadening. Here, the conventional theory of size-induced diffraction line broadening is shortly introduced. Next, some other aspects of microstructural models used in this chapter are very briefly commented and in section 4.4 the XRD analysis is applied to a set of nanocrystalline TiO_2 samples. Section 4.5 then describes the work concerning the histogram-like model of crystallite size distribution (CSD).

4.3.1 Size induced diffraction line broadening

Description of the *size broadening effect* is simpler than the case of the strain broadening. We can start with eq. 2.6 and supply zero displacement vectors $\boldsymbol{u}_s$ and $\boldsymbol{u}_s - \rho_\parallel$. Eq. 2.6 is then reduced to

$$I_D(q_\parallel) = \sum_{\rho_\parallel} e^{iq_\parallel \rho_\parallel} \left\langle \sum_s f_s f^*_{s-\rho_\parallel} \right\rangle . \tag{4.1}$$

[1] List of coworkers on the work presented here: Z. Matěj and R. Kužel, Department of Condensed Matter Physics, Faculty of Mathematics and Physics, Charles University in Prague (XRD analysis); L. Matějová and O. Šolcová, Department of Catalysis and Reaction Engineering, Institute of Chemical Process Fundamentals, Academy of Sciences (samples preparation, BET measurements, FE-SEM images); J. Drahokoupil, Institute of Physics, Academy of Sciences (XRD measurements with Co-radiation); J. Franc, Heyrovsky Institute of Physical Chemistry of the Academy of Sciences and F. Novotný, Department of Physical Electronics, Faculty of Nuclear Sciences and Physical Engineering, Czech Technical University (FE-SEM images).

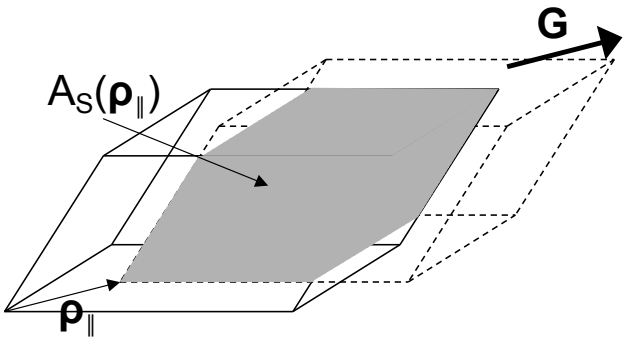

Figure 4.1: Stokes and Wilson (1942) [203] concept of a crystal and its "ghost". The "ghost" is shifted relative to the crystal by a distance $\rho_{\parallel}$ in the direction of the diffraction vector $\boldsymbol{G}$. Size Fourier coefficients $A_S(\rho_{\parallel})$ are equal to their common volume.

The first summation in eq. 4.1 is again the Fourier transform of the second part, which represents the *size Fourier coefficients* $A_S(\rho_{\parallel})$. Each term in the second summation in eq. 4.1 always gives as a contribution $|f|^2$ if both the sites $\boldsymbol{s}$ and $\boldsymbol{s} - \boldsymbol{\rho}_{\parallel}$ are inside the crystal and it is zero if one of the sites is outside the crystal. This results in the Stokes and Wilson (1942) [203] concept of a crystal and its "ghost" shifted by $\boldsymbol{\rho}_{\parallel}$ (fig. 4.1). Fourier coefficients $A_S(\rho_{\parallel})$ are simply their common volume. It is equivalent to a transformation of eq. 4.1 into an integral form

$$I_D(q_{\parallel}) = |f|^2 \int d\rho_{\parallel}\; e^{iq_{\parallel}\rho_{\parallel}} \left\langle \int d^3\boldsymbol{r_s}\; \Omega_c(\boldsymbol{r}_s)\Omega_c(\boldsymbol{r}_s - \boldsymbol{\rho}_{\parallel}) \right\rangle , \tag{4.2}$$

$$A_S(\rho_{\parallel}) = \left\langle \int d^3\boldsymbol{r_s}\; \Omega_c(\boldsymbol{r}_s)\Omega_c(\boldsymbol{r}_s - \boldsymbol{\rho}_{\parallel}) \right\rangle , \tag{4.3}$$

where $\Omega_c(\boldsymbol{r}_s)$ is a crystallite shape function, which is equal to one inside the crystallite and zero outside, and $\langle \dots \rangle$ means the average over different crystallites shapes and sizes.

Spherical crystallites with diameter D represent the most simple model. The model containing particles of the same size would result, for crystallite size $D \sim$ 5 nm and instrumental conditions commonly used, in size-oscillations at flanks of diffraction profiles. Such oscillations are usually not observed. It is assumed that smearing of these oscillations is caused by dispersion of crystallites size in the diffracting volume. Hence a crystallite size distribution (CSD) is usually adopted into the model. Moreover CSD influences strongly an overall shape of diffraction profiles (Langford et al. [204]). If small and large crystallites are present together in the sample, large crystallites forms a strong narrow maxima, whereas small crystallites contribute strongly to the profile tails [204]. E.g. in such a case it can be expected that the ratio $\varphi = FWHM/\beta$ of the full width in half of maximum (FWHM) to the integral breadth (β) is reduced.

Different analytical distributions can be assumed. Crystallite size D must be positive, hence e.g. a log-normal distribution, gamma distribution or Poisson distribution are possible choices. The log-normal distribution is the most often used in the XRD LPA. It was found to be a suitable size distribution for nanopowders of ceramic particles in [12, 198, 199, 204]. For the log-normal distribution the probability of finding a crystallite with diameter D is [205]

$$p(D) = \frac{1}{D \cdot \sigma\sqrt{2\pi}} \exp\left\{ -\frac{1}{2\sigma^2}[\ln(D/M)]^2 \right\} , \tag{4.4}$$

where M is the median of the distribution and σ is an additional shape parameter. The arithmetic mean crystallite diameter $\langle D\rangle$, the variance var^2 of the crystallite size distribution and the area weighted crystallite diameter $\langle D\rangle_A$ can be calculated from these parameters according to simple formulas

$$\langle D\rangle = M \cdot e^{1/2\sigma^2} \ , \tag{4.5}$$

$$var^2 = \langle D\rangle^2 \cdot (e^{\sigma^2} - 1) \ , \tag{4.6}$$

$$\langle D\rangle_A = \langle D\rangle \cdot e^{2\sigma^2} \ . \tag{4.7}$$

Whereas the median M of the crystallite diameter, which is equal also to the geometric mean value, has a simple physical interpretation, the parameter σ has no direct meaning. In an overview article, Limpert et al. [205] pointed out that the log-normal distribution is used across the sciences and emphasised its multiplicative character as compared with an additive character of the well known normal distribution. If a dimensionless *multiplicative standard deviation* σ^* is defined by a back transformation of σ according to [205]

$$\sigma^* = \exp(\sigma) \ , \tag{4.8}$$

then size distribution can be interpreted [205] correspondingly with the normal distribution as that 68.3% of crystallites have a diameter within the interval $[M/\sigma^*,\ M\cdot\sigma^*]$, 95.5% in the interval $[M/\sigma^{*2},\ M\cdot\sigma^{*2}]$ etc. For the log-normal distribution Limpert et al. proposed to use instead of a classical notation $(\bar{x}\pm c)$ a notation $(M\ ^{\times}\!/\ \sigma^*)$ [205].

For spherical crystallites and the log-normal distribution of their diameters a bulky but analytical formula can be derived for the size Fourier coefficients (Ribárik et al. [23],[75], Scardi and Leoni [11], Vives and Meunier [199])[1]

$$\begin{aligned} A_S(\rho_\parallel) = \ & \left\{ \frac{M^3 \exp\left[\frac{9}{4}(\sqrt{2}\sigma)^2\right]}{3} \ \operatorname{erfc}\left[\frac{\ln(\frac{|\rho_\parallel|}{M})}{\sqrt{2}\sigma} - \frac{3}{2}\sqrt{2}\sigma\right] \right. \\ & - \frac{M^2 \exp\left[(\sqrt{2}\sigma)^2\right]}{2}|\rho_\parallel| \ \operatorname{erfc}\left[\frac{\ln(\frac{|\rho_\parallel|}{M})}{\sqrt{2}\sigma} - \sqrt{2}\sigma\right] \\ & \left. + \frac{|\rho_\parallel|^3}{6} \ \operatorname{erfc}\left[\frac{\ln(\frac{|\rho_\parallel|}{M})}{\sqrt{2}\sigma}\right] \right\} \left\{ \frac{2M^3 \exp[\frac{9}{4}(\sqrt{2}\sigma)^2]}{3} \right\}^{-1} . \end{aligned} \tag{4.9}$$

Ribárik [75] generalised this formula also for an anisotropic case of crystals of a shape of rotational ellipsoid. A very general approach including different CSD functions and various polyhedral shapes of crystals was developed by Scardi and Leoni [11, 135].

The size broadening effect is described in the MSTRUCT program by the following lines in the input file.

```
// the 1st phase - Size broadening - log-normal size distribution
SizeLn  sizeProfAnatase     broadening component type, effect name
5.0     0.3                 M(nm), sigma
```

The codeword `"SizeLn"` sets here the model of spherical crystallites with diameter distributed according to the log-normal distribution. Median of the distribution is set to $M = 5$ nm and the multiplicative deviation is $\sigma^* = \exp(0.3)$.

[1] $\operatorname{erfc}(x) = \frac{2}{\sqrt{\pi}} \int_x^\infty e^{-t^2} dt$ is a complementary error function.

4.3.2 Other broadening effects

XRD measurements of all samples presented in this chapter were done using PANalytical-MPD diffractometer in the conventional focusing Bragg-Brentano geometry with variable slits. Ni-filtered characteristic CuK_α radiation produced by a laboratory x-ray tube was used and diffracted intensity was registered by PIXcel PSD detector. The patterns were acquired in the diffraction angle range $2\theta = 8^\circ - 140^\circ$, with $\Delta 2\theta \approx 0.013^\circ - 0.1^\circ$ step and measurement time $6 - 20 \times$ 300 s per step. Standard powder samples holders with a circular cavity were used. The irradiated sample area was kept constant at 5 mm $\times$ 10 mm for the first set of samples studied in section 4.4. In that case 0.04 rad Soller slits were inserted into the incident and diffracted beam to control the axial divergence. For samples analysed in section 4.5 a slightly different configuration - with 0.02 rad Soller slits in the incident beam and irradiated area 10 mm $\times$ 5 mm - was used.

Instrumental broadening effects were described by fitting the pseudo-Voigt function to the NIST LaB_6 standard sample measured in the same instrumental configurations as the studied samples. A detailed description of the effect treatment in the MSTRUCT program can be found in section A.7.

Micro-Strain effects were accounted phenomenologically using the pseudo-Voigt function. Model is described in section A.8, it has two parameters: (i) a parameter (η) characterising Gauss-Lorentz character of the shape of strain-induced component of diffraction line broadening and (ii) the phenomenological microstrain $e(\%)$, characterising the defects effect strength. There are more physically relevant models for micro-structural defects, especially that used by Scardi & Leoni in [153] for description of dislocation induced broadening in nanocrystalline anatase. For simplicity only the phenomenological model was used here, because the microstrain in the studied samples was quite weak and the phenomenological approach was found to be satisfactory. To illustrate the strength of the micro-strain effect as compared to the size effect Willamson-Hall plots for two samples are depicted in fig. 4.2.

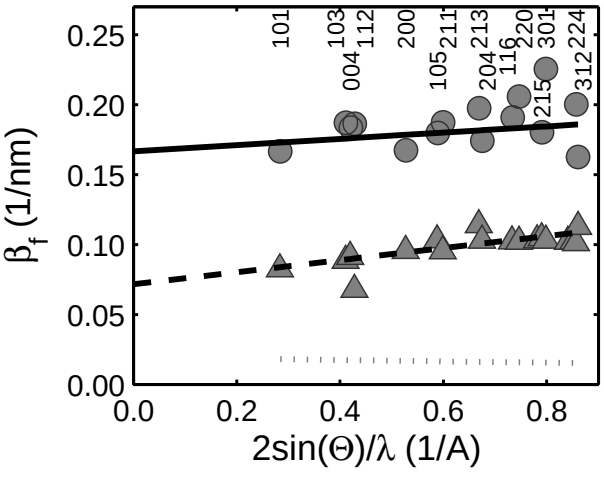

Figure 4.2: Williamson-Hall plot for nBUT-300 (circles) and nBUT-450 (triangles). Integral breadths β_f are plotted for different reflections with instrumental broadening already deconvoluted. The breadth of instrumental broadening is depicted by a dotted line just for comparison. It has to be also considered that there is a very strong peak overlap - especially for the nBUT-300 sample.

4.3.3 Intensities - crystal structure

For the XRD analysis of all samples in this chapter the MSTRUCT program was used. Samples are nanocrystalline and there is a huge peak overlap. The diffraction line positions and intensities for all crystalline phases were calculated from known structural models. The MSTRUCT is derived from FOX, which is not basically a Rietveld program and anisotropic thermal factors are implemented there only partially, hence the choice was restricted to the isotropic case. The major crystalline phase in the samples - anatase - is the main subject of interest here. As a reference model for anatase a structure similar to ICSD#154603 [206] data was taken. Details can be found in the Table 4.1. Crystal structure data for other phases - rutile and brookite - can be found e.g. in [129] (in Czech).

ICSD#154603, ref.: [206]

TiO_2 – anatase (nanocrystalline), I $4_1/a\ m\ d$ (141)
a = 3.785 Å , c = 9.482 Å , $\rho_{\mathrm{calc}} = 3.91$ g/cm^3 ,

Atom	site	x	y	z	occp	B_{iso}
Ti4+	4b	0	1/4	3/8	1.	1.3
O2-	8e	0	1/4	0.166	1.	1.1

Table 4.1: Crystal structure parameters of anatase.

During a typical data fitting procedure the lattice parameters of anatase, z-position of the oxygen atom, isotropic temperature factors B_{iso} of both scattering atoms and the occupancy of the titanium position were refined. At the beginning it was supposed that the oxygen position could not be fully occupied due to presence of oxygen vacancies. However, the refinement of the oxygen occupancy did not improved the data agreement and it slightly destabilised the whole procedure. Hence the oxygen occupancy was set to be equal one.

It was possible to fit all the samples quite well with the above simple model but still same deviations between measured and calculated data are visible. LPA (4.5) was the main aim in this work. In order to fit the diffraction patterns as well as possible the intensities of a few anatase reflections were refined independently of the crystal structure. In the MAUD program by Lutterotti [106], [25] this method is called *"arbitrary texture model"*. In the MSTRUCT it is implemented as well and it is called "HKLIntensities" correction (ch. A.9).

The "arbitrary texture model" gives the refinement procedure more freedom and let it focus on fitting of diffraction line profiles. Refined integrated intensities of 004, 215, 316, 411, 404 and 415 reflections finally differ from those derived from the crystal structure by $5 - 10\%$ in maximum with an exception of 404 reflection and the case of the reference sample REF-400, where the difference was about 30%. These small deviations (of about all the 40 anatase lines) are considered here as a marginal effect which does not affect the results achieved. Data agreement factors (GoFs, Table 4.3) changed when the "HKLIntensities" correction was included only marginally as $GoF = 1.53 \rightarrow 1.43$ for the REF-400 and $1.45 \rightarrow 1.41$ for the REF-450 sample.

4.4 XRD study of TiO_2 nanopowders prepared by different methods

4.4.1 Samples preparation

In this section a series of samples prepared by different chemical routes are studied by XRD. List of samples is presented in the Table 4.2. The samples can be divided according to the method of their preparation into three groups.

(i) A set of nBUT and ISOP-400 samples prepared by *low-temperature hydrolysis* of different titanium (iv) alkoxides in hydrogen peroxide solution *followed by calcination* at temperature 300°C and higher.

(ii) Two samples REF-400 and REF-550 prepared by *calcination of rigid titania organogels* synthesised by a sol-gel process. These samples are used as reference samples in section 4.5.

(iii) A single selected sample ISOP-SubWE/PFE prepared by *super/subcritical fluid extractions*.

ID	alkoxide	method	Temp./Time	ref.
nBUT-300	n-butox.	hydrolysis/ calcination	300°C/4h	[200]
nBUT-330			330°C/4h	
nBUT-380			380°C/4h	
nBUT-450			450°C/4h	
ISOP-400	isopropox.		400°C/4h	
ISOP-400/10			400°C/10h	
REF-400		sol/calcination	400°C/4h	[201]
REF-550			550°C/12h	
ISOP-SubWE/PFE		sol/extraction	200°C/10MPa	[202]

Table 4.2: List of studied TiO_2 nanocrystalline powder samples.

Samples nBUT(300–450), ISOP400 and ISOP400/10 were prepared by low-temperature hydrolysis of titanium (iv) alkoxides in hydrogen peroxide solution followed by calcination of the amorphous titania peroxo-product in a furnace at temperature 300°C and higher. The advantage of this method is avoidance of using any surfactant and consequently a much higher synthesis yield.

Samples labelled as nBUT were prepared from *n*-butoxide. Samples named as ISOP were prepared from titanium (iv) isopropoxide. All samples were calcined for 4 hours with an exception of the sample ISOP-400/10, which was calcined for 10 hours. The synthesis was done at the Department of Catalysis and Reaction Engineering, Institute of Chemical Process Fundamentals, Academy of Sciences (UCHP AV) by Dr. L. Matějová and Dr. O. Šolcová. Details of the preparation procedure can be found in the thesis of Matějová [207] (in Czech) or in a forthcoming publication of Matějová et al. [200].

Samples REF-400 and REF-550 were prepared by calcination of rigid titania organogels synthesised by a sol-gel process.

Titanium (iv) isopropoxide was added drop by drop into the formed reverse micellar environment of cyclohexane, nonionic surfactant Triton X-100 and water. After 24 hours ageing on the air the prepared sol converted into the rigid organogel. Organogel was calcined in a muffle furnace at (i) 400°C (4 hours, 1°C/min) and (ii) 550°C (12 hours, 2°C/min). The synthesis was done by Dr. L. Matějová at UCHP AV. More details are described in [201].

Sample ISOP-SubWE/PFE was prepared from a surfactant-mediated titania organogel by a combination of subcritical water extraction and pressurised solvent extraction.

Titanium (iv) isopropoxide was added drop by drop into the formed reverse micellar environment of cyclohexane, nonionic surfactant Triton X-114 and water. The sol was left in an open bowl for 24 hours. The obtained rigid gel was extracted at temperature 200°C and pressure 10 MPa by subcritical water extraction (SubWE) followed by pressurised solvent extraction (PFE) using subcritical CH_3OH. The synthesis was done again by Dr. L. Matějová at UCHP AV. More details are described in [202].

4.4.2 XRD analysis

All the samples (Table 4.2) were fitted by using the above described models by the MSTRUCT program. Results of the refinement of their structural and microstructural parameters are summarised in Table 4.3. Samples are sorted in the table by their crystallite size. Meaning of parameters is specified in the table caption. Final agreement of the measured and calculated data is illustrated in addition by few figures of fitted patterns (figs. 4.3–4.9). The results are discussed here and compared with similar experiments in literature.

Discussion starts here from the end of the Table 4.3. The last column shows values of the *goodness of fit factor* (*GoF*), which should indicate the fit quality. If it is close to unity then the model describes data very well. If it is below one it means the model contains too many parameters for data of such quality and the fit is unexpectedly "too much good". If it is higher than unity it indicates that better model parameters or different model should be found to describe data correctly.

The values of *GoF* differs substantively across the samples. All samples have a quite good statistics thanks to a linear detector used for data collection. For example there are more than 25 kcps at the 101 reflection of the nBUT-300 and nBUT-330 samples even though they were measured only for 1 hour. Both these samples have $GoF \approx 2$. Samples nBUT-380 and nBUT-450 were measured during a night for approx. 12 hours and there are over 200 kcps at the 101 reflection. They have $GoF \approx 5$. This indicates that *GoF* factors are somehow related to the measurements statistics. The samples were measured as multiple repeated scans. If a majority of scans in the samples with a better statistics is removed and data are fitted with the same model the *GoF* goes down to values typical for data with lower statistics. This means that differences in *GoF*s in the Table 4.3 do

sample ID	M **(nm)**	σ^*	a (Å)	c (Å)	B(Ti) (Å²)	B(O) (Å²)	z(O)	Occ(Ti)	e **(%)**	η	**minor phase**	x_{anatase} **(wt.%)**	M_{m} (nm)	GoF
ISOP-SubWE/PFE	**3.2**(3)	**1.49**(4)	3.789(1)	9.465(4)	2.8(1)	9.7(3)	0.170(1)	0.72(2)	**0.8**(1)	0.0(1)	**B**	**77**(1)	3.7(2)	2.56
nBUT-300	**4.5**(2)	**1.46**(1)	3.7881(4)	9.483(1)	0.43(4)	2.5(1)	0.1651(3)	0.87(1)	**0.2**(2)	0.7(8)	**B**	**93.2**(4)	5*	2.05
REF-400	**6.2**(1)	**1.473**(6)	3.7868(1)	9.5033(3)	0.55(1)	1.94(3)	0.1664(1)	0.95(1)	**0.19**(8)	0.9(5)	**R**	**99.58**(3)	32*	1.53
nBUT-330	**6.4**(3)	**1.45**(2)	3.7872(3)	9.482(1)	0.33(3)	2.6(1)	0.1671(3)	0.90(1)	**0.3**(2)	1.0(7)	**B**	**93.1**(5)	5*	2.30
nBUT-380	**8.6**(2)	**1.39**(1)	3.7873(2)	9.4931(5)	0.01(2)	1.10(6)	0.1665(2)	0.95(1)	**0.33**(4)	0.9(1)	**B**	**95.4**(3)	5*	5.29
nBUT-450	**10.3**(4)	**1.51**(2)	3.7872(1)	9.5060(3)	0.00(2)	0.35(3)	0.1658(1)	1.00(1)	**0.23**(3)	0.7(1)	**B**	**98.1**(4)	5*	5.06
ISOP-400/10	**13**(1)	**1.79**(5)	3.78691(5)	9.5070(4)	0.14(1)	0.50(2)	0.1666(1)	1.00(1)	**0.345**(4)	0.59(2)	**R**	**98.7**(5)	8*	2.97
ISOP-400	**13**(2)	**1.80**(5)	3.78647(5)	9.5078(2)	0.00(1)	0.36(2)	0.1668(1)	1.00(1)	**0.350**(5)	0.54(2)	**none**	–	–	1.71
REF-550	**20.9**(3)	**1.481**(7)	3.7850(1)	9.5179(2)	0.02(1)	0.41(2)	0.1666(1)	1.00(1)	**0.067**(6)	1.0(1)	**R**	**93.24**(5)	32.3(5)	1.45

Table 4.3: Refined structural and microstructural parameters of the studied TiO_2 nanocrystalline powder samples. Values marked by a star superscript (*) were not refined but set to a fixed value.

M ... median of anatase CSD,
σ ... multiplicative standard deviation of anatase CSD,
a, c ... anatase lattice parameters,
B(Ti), B(O) ... isotropic temperature factors of Ti and O,
z(O) ... fractional z-coordinate of the Ti-atom,
Occ(Ti) ... occupancy of the Ti-position in anatase cell,
e ... microstrain in anatase crystallites,
η ... shape parameter of the microstrain effect in anatase (0 ... Gaussian, 1 ... Lorentzian),
mirror phase ... identified in the pattern (B ... brookite, R ... rutile),
x_{anatase} ... weight fraction of anatase,
M_{m} ... median of minor phase CSD (assumed the log-normal distrib. with $\sigma^*_{\text{m}} = 1.35$),
GoF ... Goodness of fit

$\left(GoF = \frac{R_w}{R_{ex}}\ ,\ \text{where } R_w = \sqrt{\frac{\sum_{i=1}^{N} w_i (y_i^c(\boldsymbol{a}) - y_i)^2}{\sum_{i=1}^{N} w_i y_i^2}} \text{ and } R_{ex} = \sqrt{\frac{N-n}{\sum_{i=1}^{N} w_i y_i^2}}\ ,\ n \ldots \text{nb. of ref. params.}\right)$
$\left(\text{wt. } x_j = \frac{S_j m_{\text{cell},j} V_{\text{cell},j}}{\sum_i S_i m_{\text{cell},i} V_{\text{cell},i}}\ ,\ S_j \ldots \text{scale factor}\right)$

not indicate that the model describes microstructure of a particular sample very well and microstructure of a different sample very poorly, but shows that with better statistics finer details in data are unhidden, which can not be described within the model used. This details are visible in figures of samples measured with better statistics (figs. 4.5, 4.6). The *GoF* values listed in the Table 4.3 are hence useful when different models are compared for the same sample and the same data.

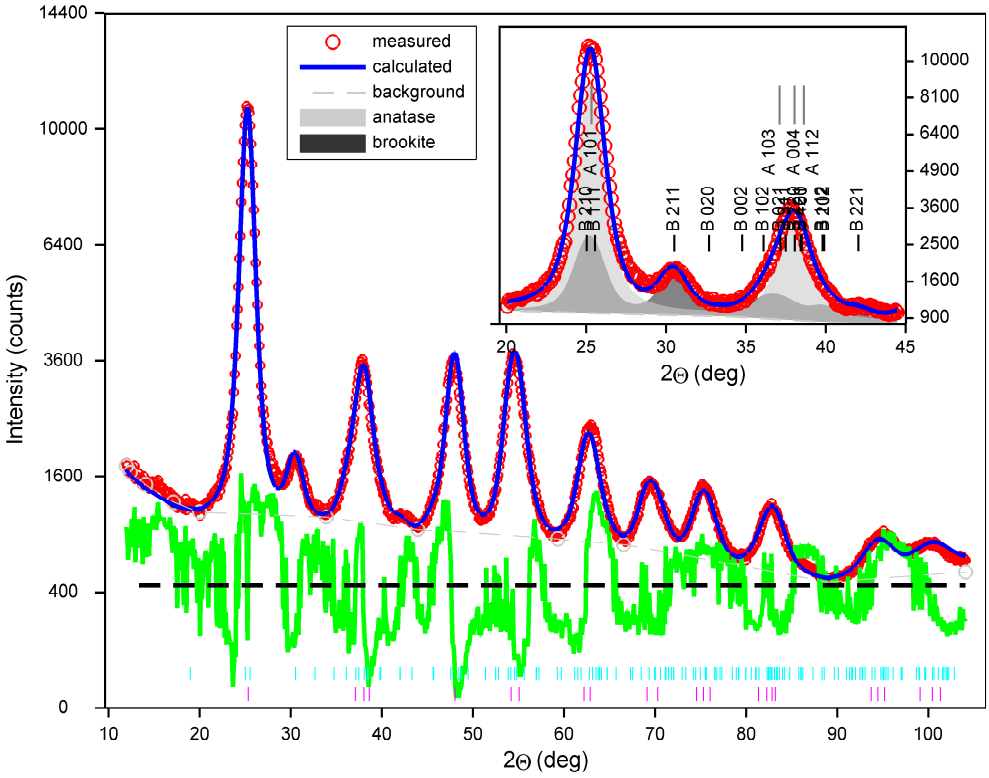

Figure 4.3: Pattern fit of the ISOP-SubWE/PFE sample. Brookite peaks are clearly visible in the whole pattern plot as well as in the inset. Small magenta ticks at the bottom mark the anatase reflections, whereas the cyan ticks above indicate reflections from the minor phase (here brookite).

The next three columns from the end of the table describe a *minor crystalline phase* detected in the samples. Anatase is always the major crystalline phase. In the ISOP-SubWE/PFE sample, which was prepared from the sol by extraction (without calcination), fingerprints of brookite are clearly visible (see fig. 4.3). Unfortunately only a single intense brookite peak is not overlapped with reflections of anatase. This complicates refinement of a crystallite size M_{m} and a global temperature factor of brookite, which both can affect its scale factor and hence also a value of brookite fraction in the sample. The determined value of a weight fraction of brookite 23 ± 1 wt.% and especially its experimental uncertainty have to be taken into consideration with caution. All uncertainties in Table 4.3 are refinement errors, which do not account for other sources of errors and can often strongly underestimate the real uncertainty of experimental deter-

mination of a particular parameter. When the brookite weight fraction in the ISOP-SubWE/PFE sample is compared to anatase weight fractions (x_{anatase}) in other samples it can be pointed out, that in the ISOP-SubWE/PFE sample an essential amount of nanocrystalline brookite was detected. Brookite crystallites size was roughly estimated to $M_{\mathrm{m}} \approx 4$ nm. The size of anatase crystallites is in this case $M \approx 3$ nm (Table 4.4), hence presence of brookite together with anatase is not surprising as it was already predicted and observed by Zhang and Banfield [185], [187]. Small brookite peaks close to $2\theta \approx 30°$ are also visible in patterns of the nBUT samples (figs. 4.4, 4.5). According to Table 4.3 the weight fraction of brookite in the nBUT samples is decreasing with calcination temperature from $x \approx 7$ wt.% in nBUT300 to $x \approx 2$ wt.% in nBUT450. The values again should be considered only as very rough estimates. It was even not possible to refine the brookite crystallites size and it had to be set to a fixed value $M_{\mathrm{m}} = 5$ nm. In the samples REF-400, ISOP-400, ISOP-400/10 none or only a very small amount of any minor phase was detected. In contrast to the nBUT samples the minor phase in the most of ISOP samples was assigned as rutile. Rutile crystallites size could not be refined and it was set to a fixed value. The refined fraction of rutile was roughly estimated to a marginally small value $x \approx 2$ wt.%. Whereas in these samples rutile contribution to diffracted intensity is negligibly small (see figs. 4.7, 4.8), rutile can be clearly identified in the REF-550 sample (see fig. 4.9), which was calcined at the highest temperature (550°C). The median of the crystallite size of rutile particles in the REF-550 sample was estimated to $M_{\mathrm{m}} \approx 32$ nm. Quantitative phase analysis of an anatase and rutile mixture is a classical problem, and even though the crystallites size of both phases is small and there is a strong overlap of many peaks, it was possible to determine the weight fraction of rutile in the REF-550 sample with a good accuracy to $x \approx 7$ wt.%. Increasing fraction of rutile with higher calcination temperature is again in agreement with observations of Zhang and Banfield [188].

The next two columns in the Table 4.3 concern *microstrain model* parameters, the microstrain $e(\%)$ and the shape character of the microstrain broadening component η. The shape parameters η takes a random value across the samples. The microstrain effect (e.g. fig. 4.2) is weak compared to the size one in most of the samples hence fitting is poorly sensitive to exact value of η. Microstrain in the most of samples takes the value $e \approx 0.2\% - 0.3\%$, with exceptions of the the ISOP-SubWE/PFE and REF-550 samples. The ISOP-SubWE/PFE sample exhibits the largest microstrain $e \approx 0.8\%$. It must be mentioned that in this case microstrain parameter e correlates with temperature factors and the quantities are difficult to evaluate unambiguously. The problem can be related to the fact that this sample was not measured for higher diffraction angles $2\theta \gtrsim 100°$ (see fig. 4.3). The lowest microstrain value $e \approx 0.07\%$ was found in the REF-550 sample, which was calcined at the highest temperature. It can be explained by a generally accepted presupposition that at higher temperatures crystal defects can be removed more effectively. Nonzero microstrain and dislocation densities were found also by Vives and Meunier [199], Weibel et al. [198] or in [153] and presence of lattice defects in TiO_2 nanocrystallites prepared from sol was emphasised by them. Fig. 4.10 depicts a Williamson-Hall plot for anatase in the ISOP-400 sample. It is obvious that if the microstrain effect, slope of the linear

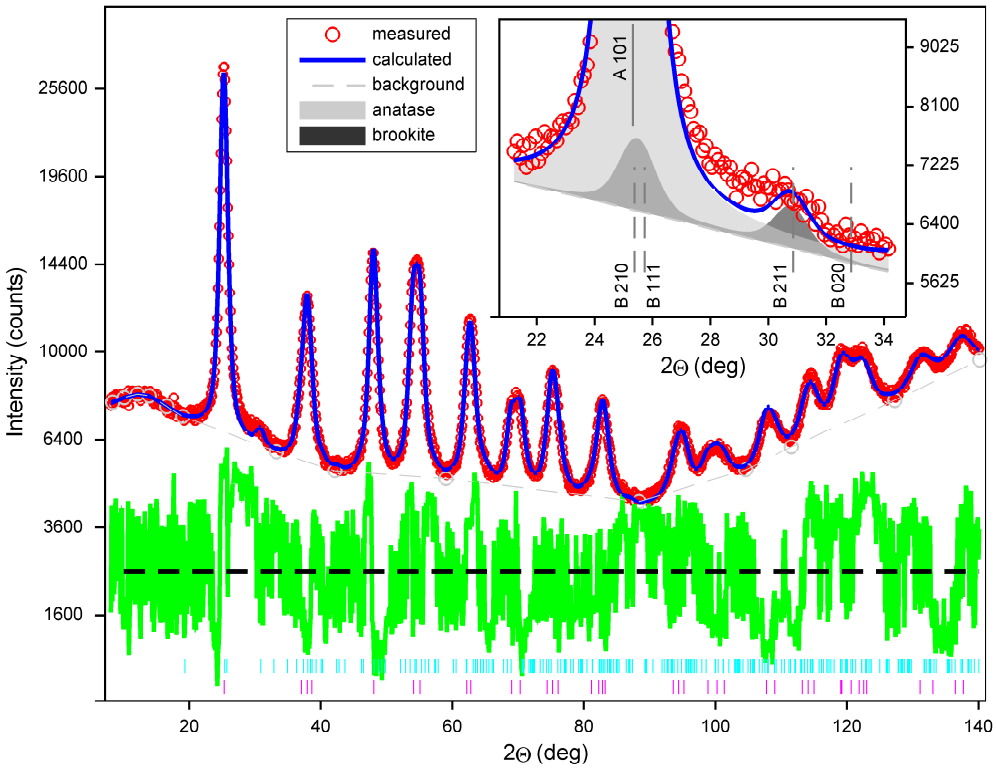

Figure 4.4: Pattern fit of the nBUT-300 sample. Brookite 211 reflection is only slightly visible in the inset plot.

fit, is ignored the crystallites size is strongly underestimated. Event so the Scherrer formula [28, 208] is still widely used to determine the crystallites size from a single reflection.

The next two columns in the Table 4.3 concern parameters of *anatase atomic crystal structure*, the fractional z-coordinate of the oxygen atom $z(\mathrm{O})$ and the occupancy of the titanium position $Occ(\mathrm{Ti})$. The oxygen z-coordinate $z(\mathrm{O})$ takes the value $z(\mathrm{O}) \approx 0.166$ close to value found in literature [206] and structural databases. The ISOP-SubWE/PFE sample exhibits again the most distinct value $z(\mathrm{O}) \approx 0.170$ from all the samples. It was already mentioned that the refinement required the oxygen occupancy $Occ(\mathrm{O}) = 1$ and only the titanium occupancy $Occ(\mathrm{Ti})$ could be refined. For samples with larger grain size $Occ(\mathrm{Ti}) = 1$ and $Occ(\mathrm{Ti})$ was lower than one for small crystalline samples, especially for the ISOP-SubWE/PFE sample, for which $Occ(\mathrm{Ti}) \approx 0.7$. If we disregard the REF-400 sample in the $Occ(\mathrm{Ti})$ column of the Table 4.3 and follow the values for the nBUT series, a trend of increasing occupancy can be observed. Occupancy for the first nBUT-300 sample is $Occ(\mathrm{Ti}) \approx 0.9$ and increases monotonously to one for the last nBUT-450 sample. See fig. 4.11. This work is specialised in the LPA and the present author does not presume to discuss this point fully rigorously. The problem deals with very small crystallites ($D \lesssim 10$ nm) and assumptions of the classical diffraction theory may not fulfilled for such small crystals and rather the Debye-formula method (ch. 2.5, [32]) should be used to simulate diffraction data

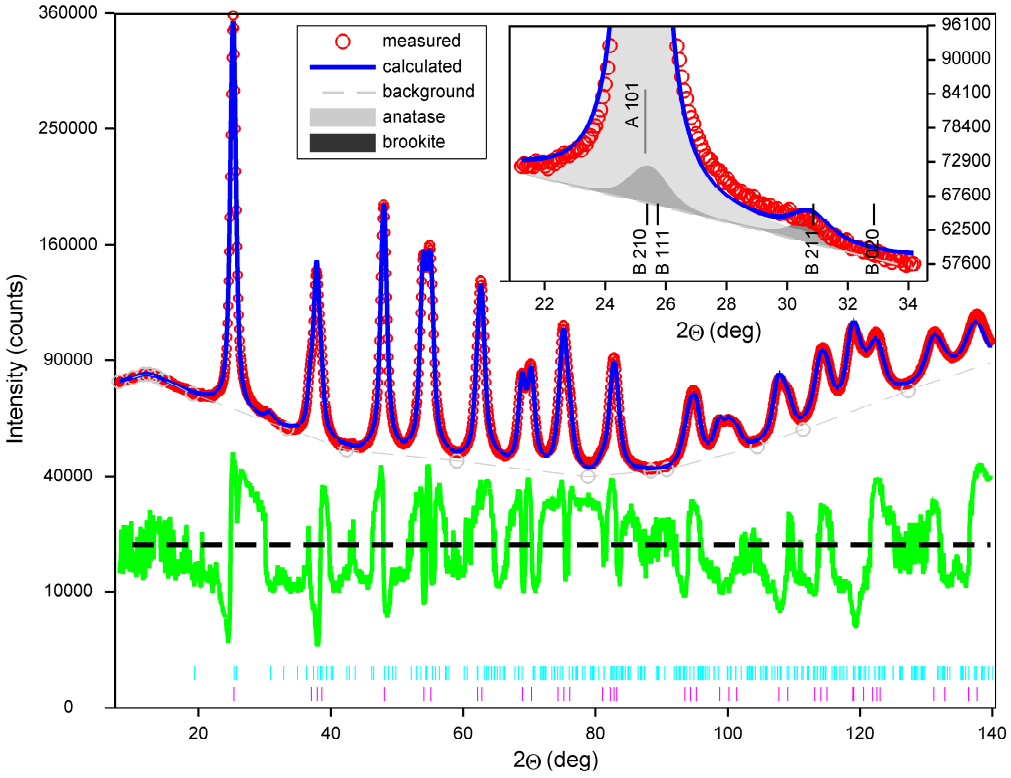

Figure 4.5: Pattern fit of the nBUT-380 sample. The measured pattern of this sample has a better statistics than e.g. the pattern of nBUT300 (fig. 4.4). Diffraction patterns and difference curves are here usually plotted in the square-root scale. For comparison the pattern of this sample is plotted in the linear scale in fig. 4.6.

correctly. In this point the present author only addresses the works of Cervellino et al. [33], [21, 36, 116, 117].

The next two columns in the Table 4.3 concern *isotropic temperature factors*, $B(\mathrm{Ti})$ and $B(\mathrm{O})$. At first it should be reminded that variable divergence slits were used in all the measurements to enhance scattered intensity at high diffraction angles. Inaccurate operation of slits, misalignment in slits configuration, using PSD, etc. can introduce essential systematical aberrations in the registered intensity when such setup is used and variable slits configuration is often not recommended if temperature factors should be studied. Hence again the obtained values should be considered with caution. On the other hand all the measurements were done using the same diffractometer and very similar setup. The values of isotropic temperature factors are unusually high, especially the values for oxygen $B(\mathrm{O})$ in the case of samples with very small crystallites ($D \lesssim 10$ nm). The ISOP-SubWE/PFE sample shows exerted values $B(\mathrm{Ti}) \approx 2.8$ Å^2 and $B(\mathrm{O}) \approx 9.7$ Å^2. Values of $B(\mathrm{O})$ are decreasing with growing crystallites dimension for the set of nBUT samples. From the point of view of diffraction theory described in chapter 2, the $2M$ factor in eq. 2.14 plays a similar role as the temperature factors. It describes attenuation of intensity of regular reflections of an infinite crystal due to crystal structure defects. The concept can not be directly used for nanocrys-

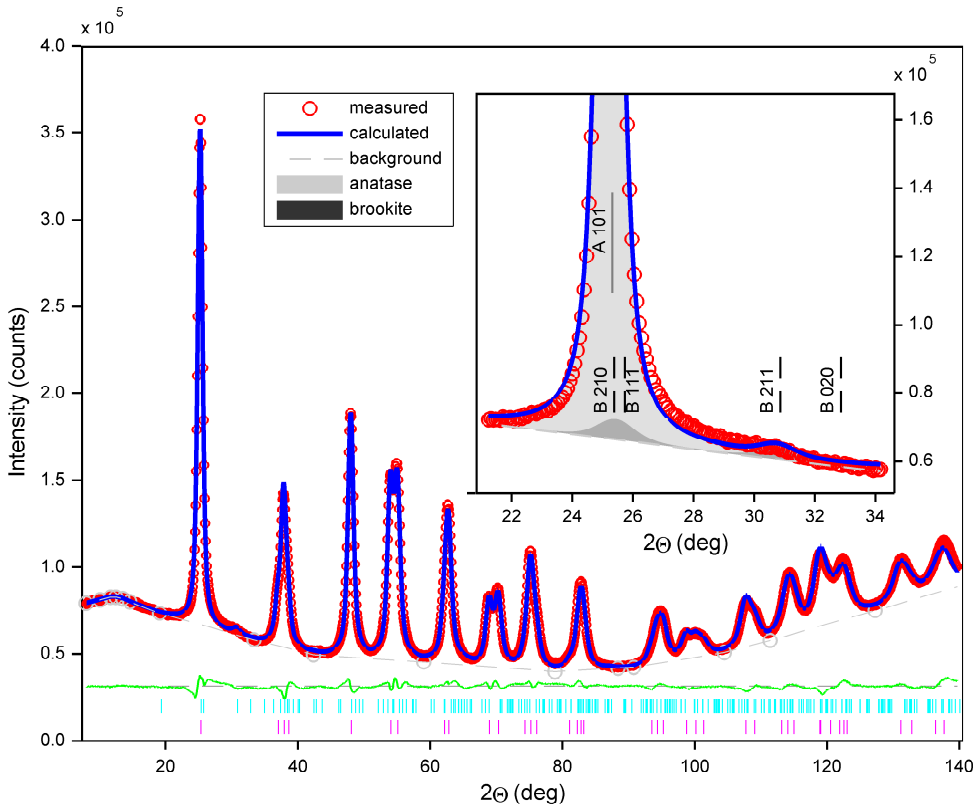

Figure 4.6: Pattern fit of the nBUT-380 sample. Diffraction patterns are here usually plotted in the square-root scale. For comparison the pattern of this sample is plotted in the linear scale here and in the square-root scale in fig. 4.5.

tals, but it can be expected that the temperature factors here include also a contribution from static disorder and defects in nanocrystallites. High values of temperature factors indicate high level of "disorder" in the atomic structure, freedom of surface atoms and possibly imitate some effects at the particles surface. Again the Debye-formula method (ch. 2.5) should be more suitable for study of this effect. Another trend visible is that temperature factors for titanium $B(\mathrm{Ti})$ are systematically lower than $B(\mathrm{O})$ for oxygen. For the samples with the largest crystallites even $B(\mathrm{Ti}) \approx 0$ Å^2 within the refinement error. Zero temperature factors have no physical meaning and it may be connected with the instrumental aberrations introduced by variable slits. The values of isotropic temperature factors $B(\mathrm{Ti})$, $B(\mathrm{O})$ are different for the ISOP-400 and ISOP400/10 samples. These two samples differ in calcination time, and this difference in temperature factors is the only distinction between the samples observed by XRD (Table 4.3). The temperature factors for the ISOP400/10 sample, which was calcined for the longer time, are slightly higher than values for the ISOP-400 sample.

The next two columns in the Table 4.3 concern refined *lattice parameters* of anatase. The ISOP-SubWE/PFE sample shows again extremal values. The basal lattice parameter a for the samples calcined at higher temperatures, with larger crystallites size ($D \gtrsim 10$ nm), takes the value $a \doteq 3.787$ Å, which is very close to values reported by Vives and Meunier [199], refined by the present author and

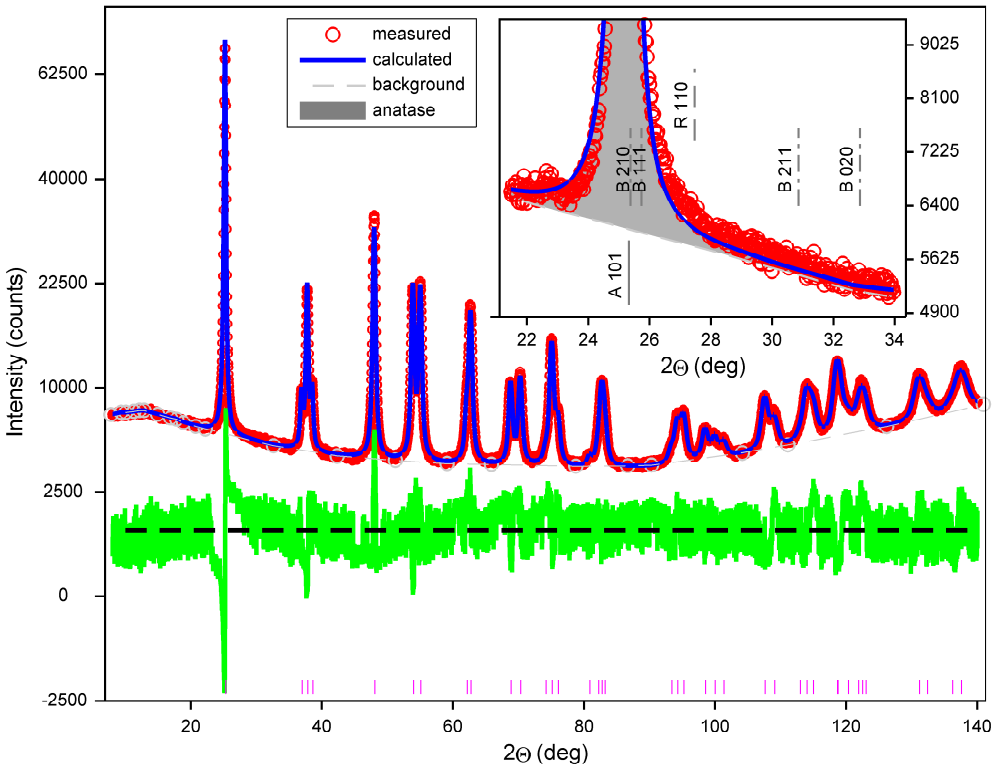

Figure 4.7: Pattern fit of the ISOP-400 sample. No peaks of brookite neither rutile are visible.

its coworkers on a different set of samples (Matěj, Kužel, and Nichtová [190]) or bulk values [129]. The c parameter of anatase is systematically increasing with the position in the Table 4.3 with an exception of the REF-400 sample. This exception indicates that it depends rather on the calcination temperature than on the crystallite size (fig. 4.12). The values $c \doteq 9.503$ Å at 400°C and $c \doteq 9.518$ Å at 550°C corresponds again with Matěj et al. [190], Vives and Meunier [199] or Nichtová [129].

Finally the first two columns in the Table 4.3 show the *crystallite size distribution* (CSD) parameters, M and σ^*, which are the most important values here from a technological point of view. We can see that samples with different crystallites sizes (3–20 nm) were synthesised. The order of samples in the Table 4.3, constituted according to the median of the log-normal distribution M, is not changed if M and σ^* values are converted to the arithmetic mean crystallite size $\langle D \rangle$ or the area weighted crystallites diameter $\langle D \rangle_A$ using eqs. 4.5 (see Table 4.4, p. 103). CSDs for all the samples are depicted in fig. 4.13. It can be seen that (i) the ISOP-SubWE/PFE sample with the smallest crystallites has a bell shaped CSD. (ii) The same is true for all the nBUT samples, which form a nice series of samples of different crystallite sizes. (iii) Also the ISOP samples REF-400 and REF-550 calcined from sol at different temperatures have clearly different sizes. The REF-400 sample has crystallites with the median $M \approx 6$ nm, whereas the REF-550 sample has larger crystallites with $M \approx 21$ nm. CSD of REF-400 can

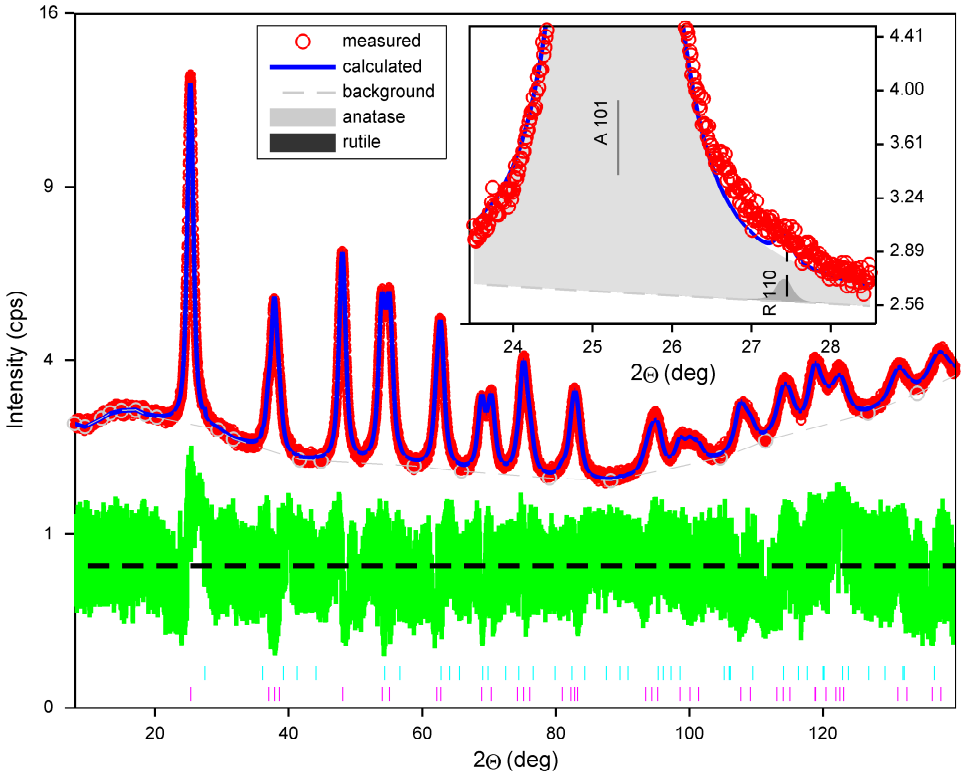

Figure 4.8: Pattern fit of the REF-400 sample. Rutile contribution is clearly negligible. This sample together with REF-550 (fig 4.9) is later used as a reference sample in section 4.5.

only hardly be distinguished from CSD of nBUT-330 (see fig 4.13). (iv) CSDs of the ISOP samples ISOP-400 and ISOP-400/10 prepared by low-temperature hydrolysis and calcined for different time are indistinguishable as it can be seen from fig. 4.13 or values in the Table 4.3, which are equal within the experimental error. (v) In addition it can be seen that CSDs of the ISOP-400 and ISOP-400/10 samples exhibit larger relative dispersion of crystallite sizes. Their multiplicative standard deviation σ^*, which determines the variance relative to crystallites size M, takes the value $\sigma^* \doteq 1.8$ and it is less, $\sigma^* \approx 1.4 - 1.5$, for all other samples.

In Li et al. [195], Vives and Meunier [199] or Audebrand et al. [209] a method of determination of activation energy E_a of grain grow from grain size dependence on time and temperature was described. Unfortunately the activation energy appears to be slightly different for samples prepared by different methods [199, 209] and hence here it can be evaluated only for the series of the nBUT samples, for which XRD measurement for different calcination temperatures are available. According to [195, 199, 209] if $\ln(D^n)$, where n is a kinetic particle grow exponent, is plotted against $1/T$ the slope is equal to negative of E_a/R, where R is the universal gas constant $R = 8.31$ Jmol^{-1}K^{-1}. The kinetic grow exponent can be determined from the dependence of the grain size on the calcination time [209]. Li et al. [195] found a value for nanocrystalline anatase $n = 2$. This was later used for TiO_2 also by Vives and Meunier [199]. In fig. 4.14 $\ln(\langle D\rangle_V^2)$, where $\langle D\rangle_V$ is a

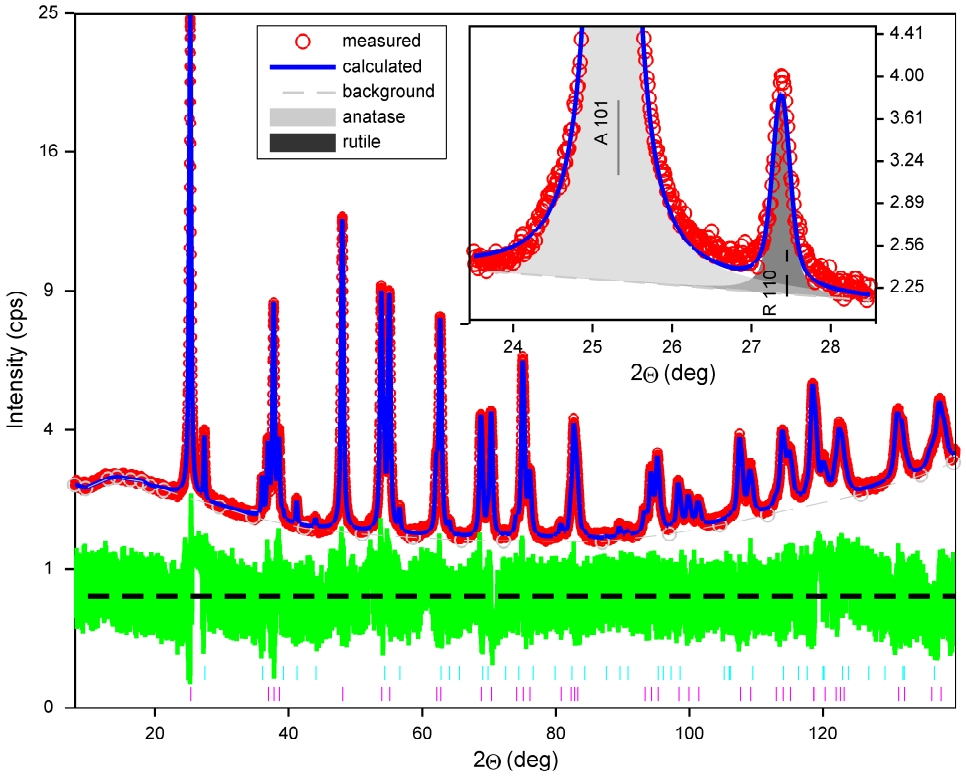

Figure 4.9: Pattern fit of the REF-550 sample. Rutile is evident in the pattern. In comparison with REF-400 (fig 4.8) anatase peaks are clearly narrower.

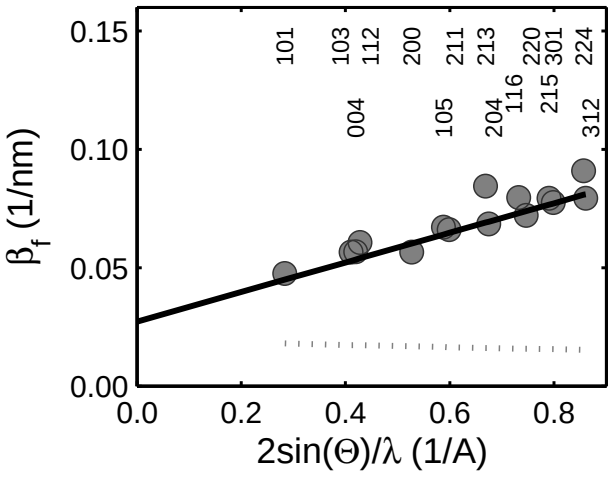

Figure 4.10: Williamson-Hall plot for of anatase reflections and the ISOP-400 sample. Integral breadths β_f are plotted for different reflections with instrumental broadening already deconvoluted. The breadth of instrumental broadening is depicted by a dotted line just for comparison.

volume weighted size, is plotted against $1/T(\mathrm{K})$ for the nBUT samples and from the slope a value of activation energy $E_a = 40 \pm 3$ kJ/mol was determined. Li et al. [195] reported $E_a = 30$ kJ/mol and Vives and Meunier [199] a range of values $E_a \approx 20 - 60$ kJ/mol in dependence of synthesis conditions and methods of XRD LPA used. The value determined here approximately agrees with these results [195, 199].

In this section crystallites size and other parameters were determined from the XRD data. Crystallite size depends on the synthesis method and tempera-

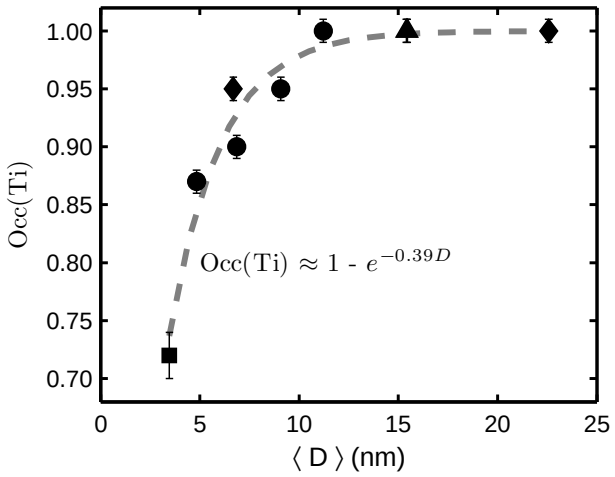

Figure 4.11: Refined occupancy Occ(Ti) of the titanium position in the anatase cell of the studied TiO_2 nanocrystalline powder samples as a function of the arithmetic mean crystallite size $\langle D \rangle$. The dependence was interpolated by an analytical function $Occ(\mathrm{Ti}) = 1 - \exp(-0.39\ \langle D \rangle)$. [ISOP-SubWe/PFE (square), nBUTs (circles), REFs (diamonds), ISOPs-400 (triangles)]

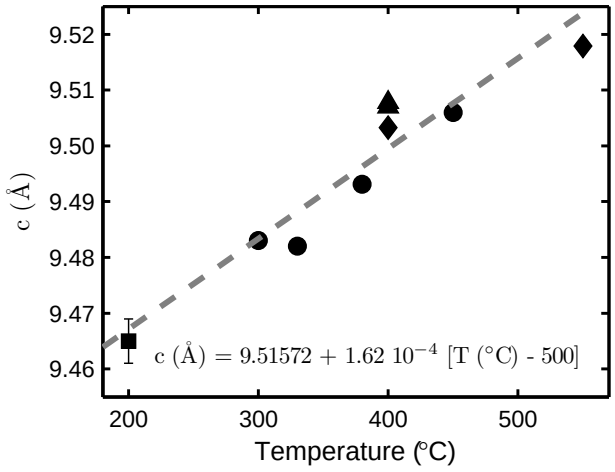

Figure 4.12: Refined lattice parameter c of the studied TiO_2 nanocrystalline powder samples as a function of the temperature T of sample treatment. The dependence was approximated by a straight line $c(\text{Å}) = 9.51572 + 1.62\ 10^{-4}[T(°\mathrm{C}) - 500]$. [ISOP-SubWe/PFE (square), nBUTs (circles), REFs (diamonds), ISOPs-400 (triangles)]

ture of thermal treatment (fig. 4.13). At higher calcination temperatures anatase crystallites are larger and tends to transform to rutile. In samples with very small crystallites non-negligible fraction of brookite was found (fig. 4.3). Some structural parameters, lattice parameters (c, fig. 4.12), temperature factors B, occupation Occ(Ti) (fig. 4.11), systematically vary with grain size and temperature. Increasing calcination time to 10 hours for the ISOP samples prepared by low-temperature hydrolysis has no effect on samples microstructure from XRD point of view.

4.4.3 SEM images

XRD diffraction is an indirect technique for analysis of material microstructure. Scanning electron microscopy (SEM) images of some of the studied samples are presented in this section for comparison with XRD results.

The SEM microphotographs were not taken by the present author. The original authors, who kindly provided them, are listed in figure captions. Their full affiliations were specified earlier (see footnote at page 83). All the images were taken using field emission scanning electron microscopes (FE-SEM). Details can be found in [200, 201].

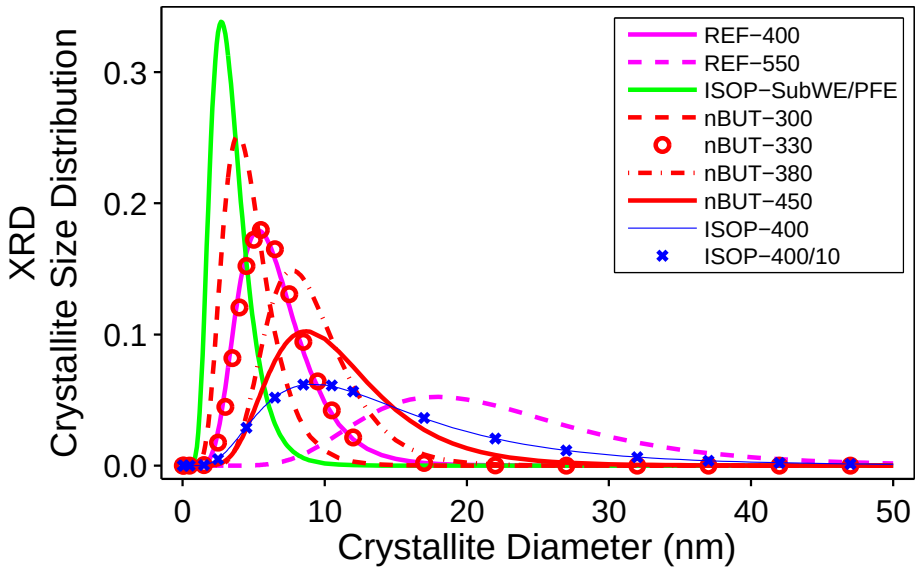

Figure 4.13: Refined crystallite size distributions (CSDs) of the studied TiO_2 nanocrystalline powder samples. Values of the log-normal distribution parameters, M and σ^*, can be found in the Table 4.3.

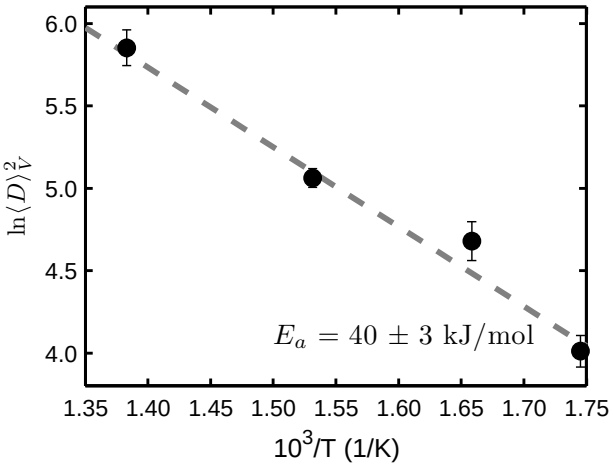

Figure 4.14: Determination of a grow activation energy E_a according to [195, 199]. $\langle D\rangle_V$ is the volume weighted crystallites size calculated from the refined values in the Table 4.3. T(K) is the temperature (in Kelvins) at which samples were calcined.

Figure 4.15 shows two FE-SEM microphotographs of the nBUT-450 sample. According to the Table 4.4 the arithmetic mean crystallite size from XRD analysis is $\langle D\rangle \approx 11$ nm and this is in qualitative good agreement with particles visible in the images. The particles do not look as ideal spheres, they are rather confined by blurred facets, but their shape is not clearly anisotropic and the spherical crystallites model used for XRD analysis is quite satisfied.

Figure 4.16 shows FE-SEM images of the ISOP-400/10 sample. The left side images can be directly compared as they have the same magnification. According to the Table 4.4 crystallite size of the ISOP-400/10 sample should be $\langle D\rangle \approx$ 15 nm, which is about 1.5× larger than nBUT-450. On the other hand from fig. 4.13 of CSDs it appears that most of the crystallites have approximately the same size ($D \approx 15$ nm), but there are larger ($D \gtrsim 15$ nm) crystallites in the ISOP-400 samples. This is difficult to realise from the SEM images.

From SEM microphotographs one can get an idea of particles morphology.

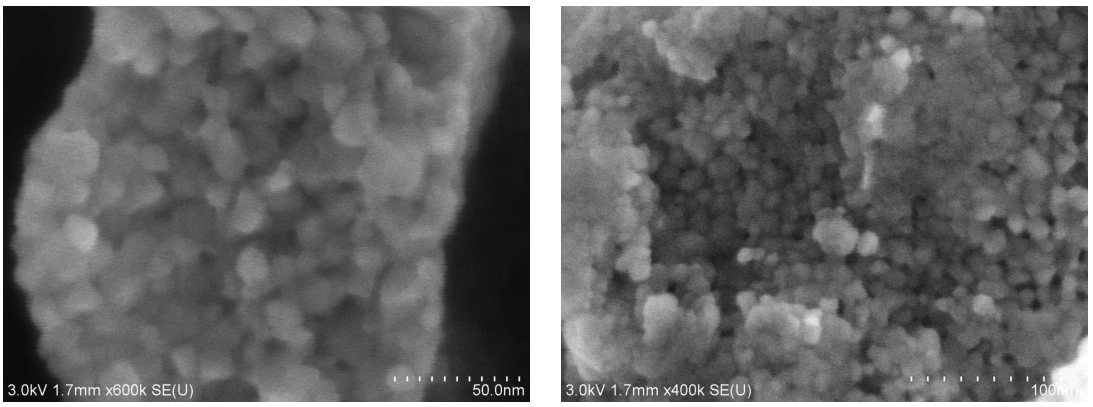

Figure 4.15: FE-SEM images of the nBUT-450 sample [200] (by J. Franc, Heyrovsky Inst. Phys. Chem., AVČR). XRD crystallite size $\langle D \rangle \approx 11$ nm (Table. 4.4).

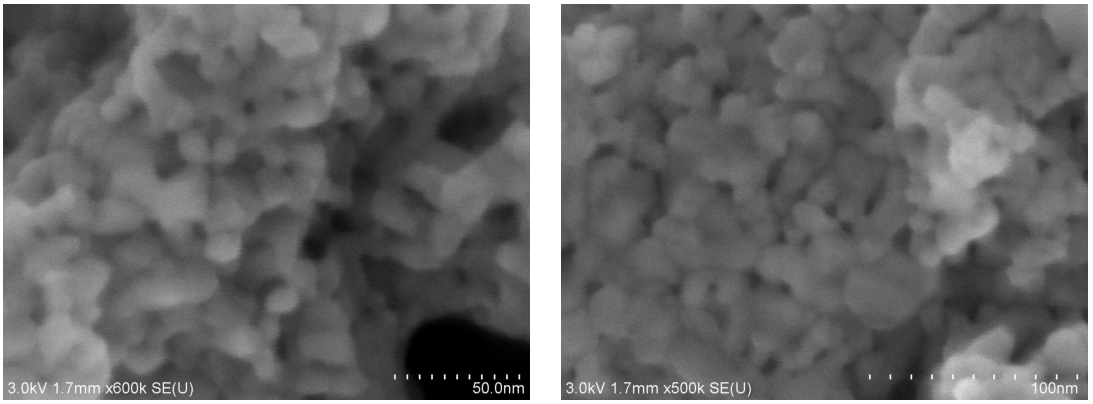

Figure 4.16: FE-SEM images of the ISOP-400/10 sample [200] (by J. Franc). XRD crystallite size $\langle D \rangle \approx 15$ nm (Table. 4.4).

The particles in figs. 4.16 are blurred but it still can be seen that they are not ideally spherical and rather form ovals or short oval rods. The effect is quite weak and it was ignored in the XRD analysis, because (i.) XRD patterns fits are good when using the simple model of spherical crystallites, (ii.) it is systematic to use the same model for XRD analysis of all the samples and (iii) the model of anisotropic crystallite shape was not developed enough in the MSTRUCT at the time the analysis was done. This problem is discussed more also later in section 4.4.6.

Next few figures 4.17–4.19 show FE-SEM microphotographs of the samples REF-400 and REF-550, which are used as reference samples in section 4.5. According to the Table 4.4 and fig. 4.13 the crystallite size of the samples differ significantly. The mean crystallite size is $\langle D \rangle \approx 7$ nm for REF-400 and $\langle D \rangle \approx 23$ nm for REF-550. XRD size is in quite good qualitative agreement with the SEM images (figs. 4.17, 4.18).

From all the images it can be seen that TiO_2 particles likely form agglomerates. Hence the REF-550 powder was dispersed in ethanol solution by sonication (by F. Novotný, FJFI, ČVUT) and fixed by dropcasting onto a carbon coated TEM grid. The FE-SEM images of the dispersed REF-550 powder are shown as fig 4.19. Both larger and smaller crystallites are visible, which justifies the inclusion of CSD

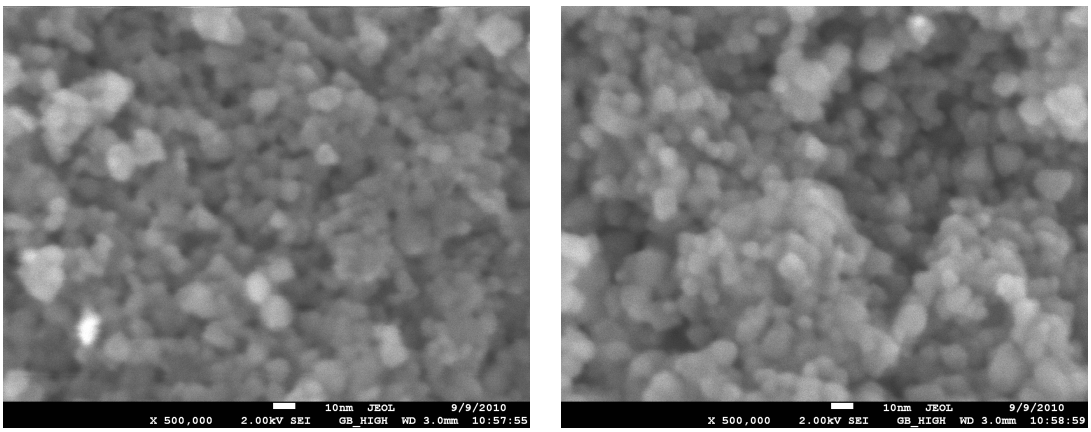

Figure 4.17: FE-SEM images of the REF-400 sample (by F. Novotný, Dep. Phys. Elec., FJFI, ČVUT and L. Matějová, Inst. Chem. Proc. Fund., AVČR). XRD crystallite size $\langle D \rangle \approx 7$ nm (Table. 4.4).

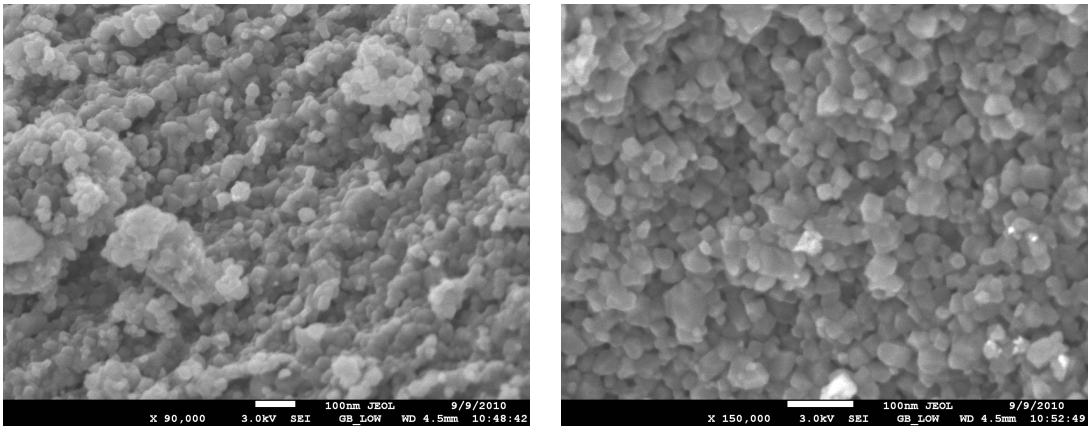

Figure 4.18: FE-SEM images of the REF-550 sample (by F. Novotný and L. Matějová). XRD crystallite size $\langle D \rangle \approx 23$ nm (Table. 4.4).

in the model. Unfortunately the photos of particles are not very sharp.

4.4.4 Comparison of XRD results with specific surface measurements

The powder samples studied were originally prepared for applications in catalysis and hence their *specific surface area* is a technologically important parameter. The specific surface area of the powder or porous solid sample in contact with a gas phase per unit mass of the sample can be characterised by a quantity called S_{BET} (m^2/g) (BET - Brunauer, Emmett, and Teller [210]). It is usually measured [198, 209] by nitrogen physisorption and S_{BET} values are available (Table 4.4) for all the samples studied here. They were measured by Dr. L. Matějová. Details can be found in Matějová et al. [200, 202]. From XRD crystallite size a theoretical total surface area S_{XRD} of crystallites per unit mass of the sample can be calculated. It measures crystallites surface from the "inner" side, whereas S_{BET} is proportional to the surface accessible for a gas from the "outer" side of particles. It is quite

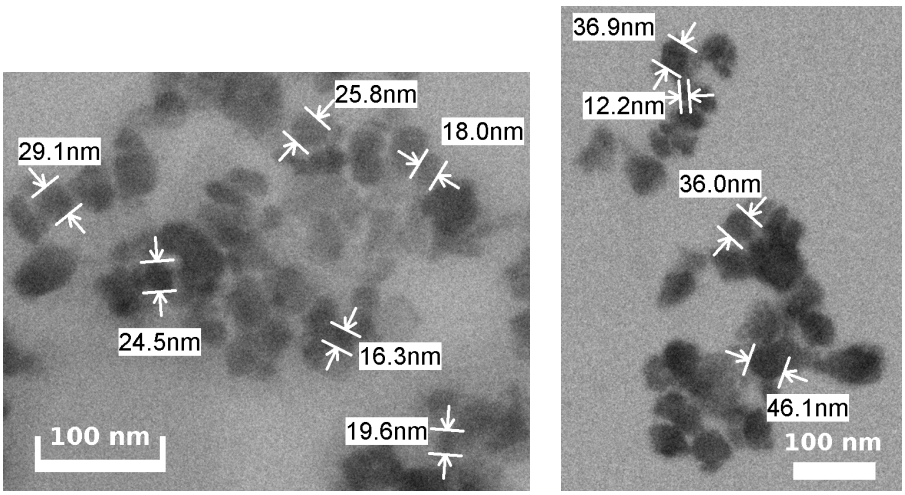

Figure 4.19: FE-SEM images of the REF-550 sample after dispersing the powder in ethanol solution by sonication [201] (by F. Novotný). XRD crystallite size $\langle D \rangle \approx 23$ nm (Table. 4.4).

common to find in literature comparison of these two values (e.g. for CeO_2 in Audebrand, Auffrédic, and Louër [209] or for TiO_2 in Weibel et al. [198]).

ID	$\mathbf{FWHM_f^{101}}$ **(deg)**	$\langle D \rangle$ (nm)	$\boldsymbol{\langle D \rangle_A}$ **(nm)**	S_{XRD} (m^2/g)	$\boldsymbol{S_{\mathrm{BET}}}$ **(m^2/g)**	D_{BET} (nm)
ISOP-SubWE/PFE	**1.76**	3.5	**4.8**(5)	323	**283**	5.4
nBUT-300	**1.24**	4.8	**6.4**(3)	239	**170**	9
REF-400	**0.92**	6.7	**9.0**(2)	171	**72**	21
nBUT-330	**0.96**	6.9	**9.0**(5)	170	**135**	11
nBUT-380	**0.82**	9.1	**11.3**(3)	136	**96**	16
nBUT-450	**0.54**	11.2	**15.7**(7)	98	**12.3**	125
ISOP-400/10	**0.28**	15.4	**30**(5)	51	**57**	27
ISOP-400	**0.30**	15.5	**31**(5)	50	**72**	21
REF-550	**0.29**	22.6	**30.7**(5)	50	**11.7**	132

Table 4.4: Arithmetic mean crystallite size $\langle D \rangle$ and area weighted crystallite size $\langle D \rangle_A$ calculated from CSD parameters from the Table 4.3. Crystallites surface S_{XRD} per unit mass calculated according to eq. 4.10 with $\rho_{\mathrm{anatase}} = 3.89$ g/cm^3. Measured value of specific surface area S_{BET} [200, 202] (by L. Matějová, ÚCHP AVČR) and BET particles size D_{BET} according to eq. 4.11. $FWHM$ values of anatase 101 reflection with deconvoluted instrumental broadening are also listed.

Surface per unit mass of the sample with structural density ρ and with spherical crystallites with size distributed according to CSD $p(D)$ is

$$S_{\mathrm{XRD}} = \frac{\int \pi D^2 \; p(D) dD}{\int \rho \frac{1}{6} \pi D^3 \; p(D) dD} = K \frac{\langle D^2 \rangle}{\rho \langle D^3 \rangle} = \frac{K}{\rho \langle D \rangle_A} \; , \tag{4.10}$$

where $K = 6$ for spheres and it is a constant $K \geq 6$ for other shapes of crystallites, which have a higher surface to volume ratio. Equation 4.10 shows that surface

area of crystallites per unit volume S_{XRD} is inversely proportional to the area weighted crystallites size $\langle D\rangle_A$. In literature [198, 209] the expression 4.10 is rather used in an opposite way to estimate the particles size D_{BET} from the measured S_{BET} [209]

$$D_{\mathrm{BET}}[\mathrm{nm}] = \frac{K\ 10^3}{\rho[\mathrm{g/cm^3}] S_{\mathrm{BET}}[\mathrm{m^2/g}]}\ , \quad K = 6\ . \tag{4.11}$$

Here the present author would like add a very simple extension of the expression 4.10 for S_{XRD}. As we can see there are possibly multiple crystalline phases in the samples. A large fraction ($x \approx 23\ wt.\%$, Table 4.3) of a minor brookite phase was detected in the ISOP-SubWE/PFE sample. If surface of all crystalline fraction should be included in S_{XRD} we have to consider that in the sample of weight M there are

$$N_i = \frac{x_i M}{\int \rho_i \frac{1}{6}\pi D^3\ p_i(D) dD}$$

spherical crystallites of a phase labelled i, which weight fraction in the sample is x_i. If we include all crystalline phases than we have for S_{XRD}

$$S_{\mathrm{XRD}} = \sum_i \frac{x_i K_i}{\rho_i \langle D\rangle_{i,A}}\ , \quad (\sum_i x_i = 1)\ . \tag{4.12}$$

Values of S_{XRD} and D_{BET} calculated according to eqs. 4.10 and 4.11 are listed in Table 4.4. The structural density of anatase calculated by MSTRUCT was used $\rho_{\mathrm{anatase}} = 3.89\ \mathrm{g/cm^3}$. For the ISOP-SubWE/PFE sample the eq. 4.12 and $\rho_{\mathrm{brookite}} = 4.13\ \mathrm{g/cm^3}$ were used, but because the crystallite sizes of anatase and brookite are very similar the correction resulted in only a small change $S_{\mathrm{XRD}} \doteq 323 \rightarrow 321\ \mathrm{m^2/g}$. The values S_{BET} vs. S_{XRD} are plotted also in fig. 4.20.

In fig. 4.20 and Table 4.4 we can see that the total surface of crystallites per unit mass S_{XRD} and the specific surface area S_{BET} are comparable very well at least in the order of magnitude for most of the samples with exceptions of the nBUT-450 and REF-550 samples, which were calcined at the highest temperatures. They have $S_{\mathrm{BET}} \approx 10\ \mathrm{m^2/g}$, what is by an order of size less than $S_{\mathrm{XRD}} \approx 50 - 100\ \mathrm{m^2/g}$ as expected from their XRD size. Also their D_{BET} size is much larger than XRD $\langle D\rangle$ (Table 4.4). This indicates [209] a high level of agglomeration of crystallites into larger particles, which reduces their effective specific surface. In fig. 4.20 we can see that S_{BET} values of the other samples from the nBUT series are nicely proportional to $1/\langle D\rangle_A$. In addition, the slope of the linear dependence is very close to the ideal value depicted by a dotted line, which indicates that not much surface is missing. The ISOP-SubWE/PFE sample with the smallest crystallites shows even better agreement between XRD and specific surface. Lookin at all the samples calcined at 400°C we can see in fig. 4.20 that their S_{BET} values are very close, whereas their crystallite sizes differ. It is emphasised by a horizontal dotted line in fig. 4.20. It may indicate that S_{BET} is strongly influenced by temperature of sample treatment rather than only by crystallite size. It is also clearly apparent that much better ratio of S_{BET} to S_{XRD} was achieved for the ISOP-400 samples prepared by low-temperature hydrolysis than those from the sol (REF-400). This can be explained by to ways. (i.) The

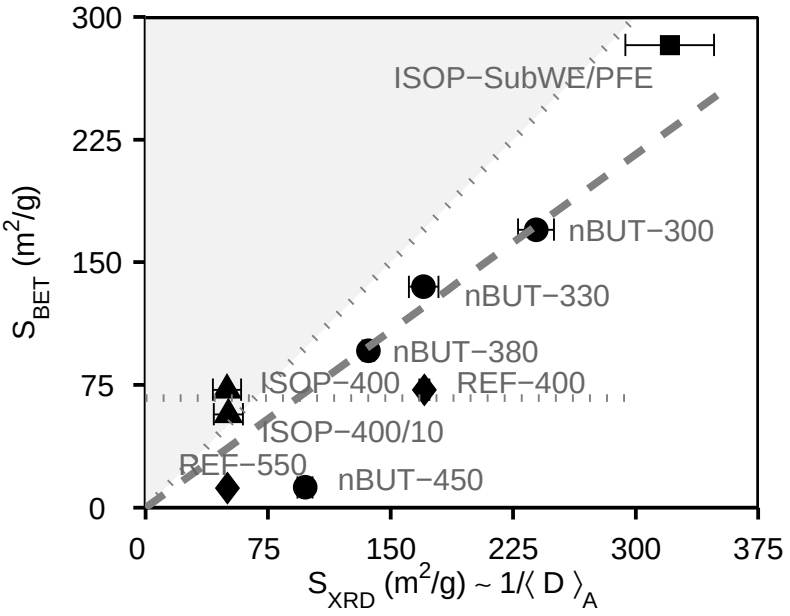

Figure 4.20: Comparison of measured surface area S_{BET} and theoretical surface area S_{XRD} calculated from XRD CSD parameters from Table 4.3. Values are taken from Table 4.4, S_{BET} value for ISOP-SubWE/PFE corrected according to eq. 4.12.

crystallites of ISOP-400 samples are larger ($> 2\times$) than crystallites of REF-400, hence smaller surface area to volume ratio is expected. (ii.) In the REF-400 samples probably nonideally fine network of pores is formed. Compare SEM images figs. 4.16 and 4.17 (p. 101–102). We can also see that S_{BET} to S_{XRD} ratios are unexpectedly high for the ISOP-400 samples and the value for ISOP-400 is even higher than one. This can have various reasons. (i.) There is some surface accessible for gas in S_{BET}, which is not accounted in S_{XRD}. This can be e.g. surface of an amorphous fraction in the sample. (ii.) There is better surface/volume ratio for the particles, which is possible e.g. for crystallites of nonspherical shape, what again corresponds with the morphology of particles in SEM images (fig. 4.16) of the ISOP-400/10 sample.

The last comment concerns comparison of the effective particles size D_{BET} from the specific surface measurements with the SEM images. Especially for the case of the nBUT-450 and REF-550 samples, for which $D_{\mathrm{BET}} \gtrsim 130$ nm and XRD $\langle D \rangle \approx 11 - 23$ nm, the XRD size clearly better corresponds with dimensions of particles in the SEM images (figs. 4.15 and 4.17).

4.4.5 Summary

In this section, TiO_2 nanocrystalline powder samples were studied by XRD line profile analysis utilising the whole powder pattern modelling method. The XRD results were compared with SEM microphotographs of studied samples and specific surface measurements.

From the analysis correlation between crystallite size, samples preparation conditions, calcination temperature, phase composition and other structural parameters (lattice parameter c, occupancy Occ(Ti) and isotropic temperature fac-

tors B) were studied.

The main distinction of the WPPM method from a classical Rietveld refinement is an adoption of the model of spherical crystallites distributed according the log-normal distribution. Parameters of crystallite size distribution (CSD), M, σ^*, are refined from XRD data (Table 4.3) and the whole distribution is determined (fig. 4.13). Dispersion of crystallite sizes can be simply described and analysed. From the CSD parameters other quantities such as area weighted crystallite size etc. can be simply evaluated and compared with other methods as SEM or specific surface area (fig. 4.20). The spherical crystallites model with the log-normal CSD has been included in common crystallographic software (e.g. MAUD) and also in some commercial programs, in last years. The method has two restrictions. Both can be bypassed Leoni and Scardi [12], Scardi and Leoni [135]. One is shortly discussed in the next paragraph and the second is solved in section 4.5.

The work concerning XRD analysis of the TiO_2 nanocrystalline powders in the section 4.4 was partially published together with samples synthesis conditions and results found by other methods in Matějová et al. [200, 202].

4.4.6 Further outlook

Real crystals often have highly anisotropic shape that can be related to anisotropy of their surface energy density. It takes extremal values at specific directions and this results in creation of crystal facets. The phenomenon is described by the well known Wulff construction. Ceria (CeO_2), a material similar to TiO_2, is often studied in many diffraction papers [12, 211] as a model material because it is cubic and tends to form simple spherical crystallites. Titania is more complicated. Anatase is tetragonal and it is believed that its crystals typically have shape of bipyramids formed by {101} facets. Barnard and Zapol [212] theoretically studied phase stability and morphology of titania nano-particles and they found that anatase crystallites prefer shape of a truncated bipyramid (fig. 4.21), which proportions can be influenced by e.g. surface hydrogenation. Anatase crystals of a shape of truncated bipyramids were synthesised by Yang et al. [197]. The crystallites were strongly shortened in the c-direction having large fraction of {001} facets but they were about few microns large. In recent papers of Cernuto et al. [118], Jensen et al. [196] anatase nanocrystals of anisotropic shape were reported. In [118, 196] nanocrystallites were on the contrary elongated along the c-direction.

In this point we can refresh discussion concerning particles of oval rods shape in the SEM images (fig. 4.16, p. 101) of the ISOP-400/10 sample. At first let us assume that the elongated direction of crystals is independent of orientation of their crystal lattice. If the spherical crystallites model is used, this results in apparent broadening of the refined CSD. This effect can partially explain the higher crystallite size dispersion evaluated in the ISOP-400 samples. The CSDs of the both ISOP-400 samples are quite wide (fig. 4.13 as compared with other samples and it was already mentioned that the multiplicative standard deviation is also higher $\sigma^* = 1.8$. In the second case when the elongated particle direction is connected to the crystal lattice orientation, an anisotropic (hkl dependent)

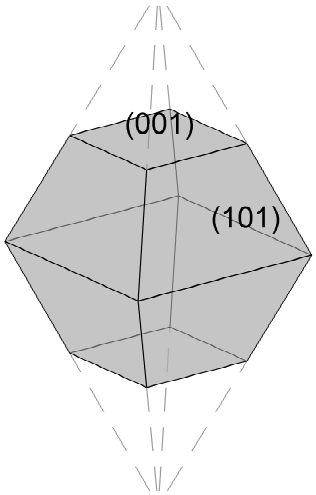

Figure 4.21: Crystal with a shape of a truncated bipyramid [197, 212].

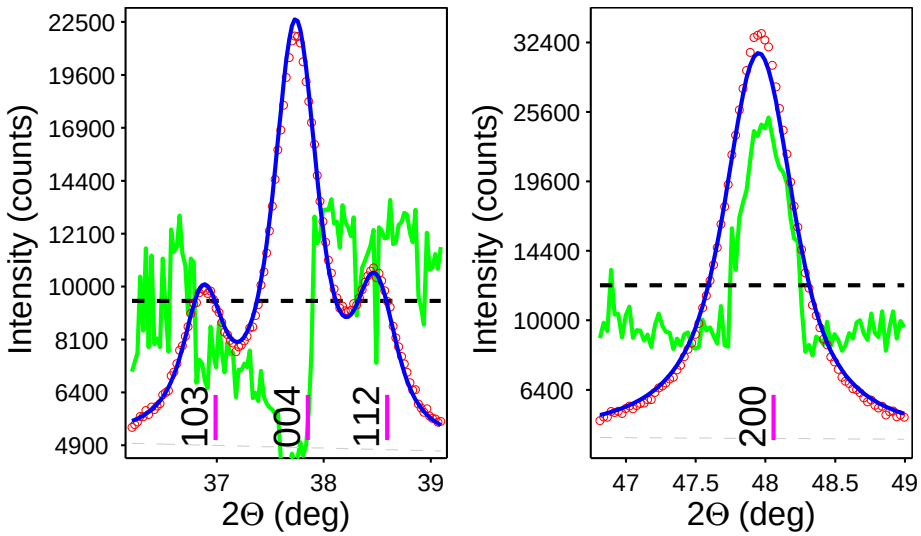

Figure 4.22: Detail of the pattern fit of the ISOP-400 sample (fig. 4.7). Deviations between the measured and calculated patterns close to the anatase 004 and 200 reflections are depicted.

diffraction line broadening is expected. In the pattern fit of the ISOP-400 sample (fig. 4.7, p. 96) besides the strongest feature in the differences curve at $2\theta \approx 25.3°$ (the 101 reflection) a less pronounced mutually opposite effects are visible at $2\theta \approx 37.9°$ and $2\theta \approx 48°$. The problem is better visible in the detail in fig. 4.22, where anatase 004 and 200 reflections of the ISOP-400 sample are depicted. In fig. 4.22 it is clearly visible that deviations between the measured and the calculated curves are of opposite sign at anatase reflections 004 and 200. If crystallites shortened along the c-direction relative to the basal a-direction were assumed, the 004 peak would be wider and lower in absolute intensity, whereas the 200 peak would be narrower and higher in absolute intensity and the overall fit may be better. Described effects are very weak and were not treated in this work,

but the anisotropic crystallite size model assuming e.g. the anatase crystallites of the bipyramidal shape (fig. 4.21) propose a simple physically relevant model. Theory including such simple polyhedral shapes in the WPPM, that replaces the basic equation 4.9 for the size Fourier coefficients $A_S(\rho_{\|})$, was already developed by Scardi and Leoni [135] or Komrska [213], [214, 215].

4.5 Histogram like Crystallite Size Distribution

4.5.1 Introduction

In the previous section 4.4 a standard WPPM method was applied to a series of TiO_2 nanocrystalline powder samples. Size broadening was the most essential effect determining width and shape of diffraction lines. The effect was described by the model ([11, 23, 204]) of spherical crystallites with crystallite diameter distributed according to the log-normal distribution (eq. 4.4). Different analytical function can also be utilised as a model of CSD [135], but the choice of a particular function for CSD is always an presumption of the model. However Leoni and Scardi [12] introduced a generalised approach. Electron microscopy (EM) histogram like representation of the CSD was assumed and the histogram frequencies were refined from the XRD data. The method was applied to metal oxide (CeO_2,Cu_2O) nanocrystalline powders in [10, 12, 36, 216–218]. It was implemented in PM2k software by Leoni et al. [24] and in TOPAS by David et al. [218].

In this section, the WPPM method with the size distribution histogram model [12] is tested for analysis of nanocrystalline TiO_2 samples. The slightly modified model used in the MSTRUCT is described in the next paragraph (4.5.2). It is applied to the REF-400 and REF-550 samples and their mixtures (section 4.5.4). Pros and cons of the method are discussed.

4.5.2 Histogram model - Fourier coefficients

The spherical crystallites are assumed again. The quality of all experimental patterns treated in this section is practically the same as these of the reference samples REF-400 and REF-550 (figs. 4.8 and 4.9, p. 97–98). In difference curves in these figures the same features can be observed, which were discussed in section 4.4.6 (fig. 4.22). This could be a fingerprint of anisotropic crystallites shape. But the differences are even less pronounced than for the ISOP-400 sample (fig. 4.7) and the $GoF \sim 1.5$ factors (Table 4.3) are good. Hence for simplicity the spherical crystallites model was chosen.

An implementation of the model here differs a little from the original one of the Leoni and Scardi [12]. It was considered that the peak width ($FWHM$) is inversely proportional to the crystallite size (D) and if the peak width can be determined with a fixed experimental uncertainty ($\Delta FWHM$) the error of determination of the crystallite size decreases with the size $\Delta D \approx D^2 \cdot \Delta FWHM$. Distinguishing between a 5nm and a 10nm crystal is easier than between a 80nm and a 85nm one. The aim of the work was also testing, how small and large crystallites of the same phase can be distinguished in their mixture. For this

reason a wide range of crystallite sizes in the histogram was required. The implementation in the MSTRUCT allowed that the bins in the histogram did not have equal widths and were logarithmically spaced in the range $(D \dots D_{min} - D_{max})$ 1–100 nm (see e.g. fig. 4.23). This is more similar to what has been used by David et al. [218] than originally in [12].

Each bin is described by the lower $D_{1(i)}$ and the upper limit $D_{2(i)}$ of the crystallite sizes. The crystallite size D within the bin has an equal *probability density* $P_{(i)}$ (fig. 4.23). Since the crystallites contribute to the integrated intensity proportionally to their volume [11, 12] it is useful to introduce in addition an *auxiliary volume weighted distribution*

$$P^w_{(i)} \equiv P_{(i)} \cdot D^3_{(i)} \ , \quad \text{where} \quad D_{(i)} \equiv (D_{1(i)} + D_{2(i)})/2 \tag{4.13}$$

is an *arithmetic mean crystallite size* in the i-th bin. Histogram-like CSD is depicted in fig. 4.23. It should be mentioned that $P^w_{(i)}$ defined by eq. 4.13 and depicted in the right part of fig. 4.23 is not a "true" volume weighted distribution, but rather only its approximation.[1]

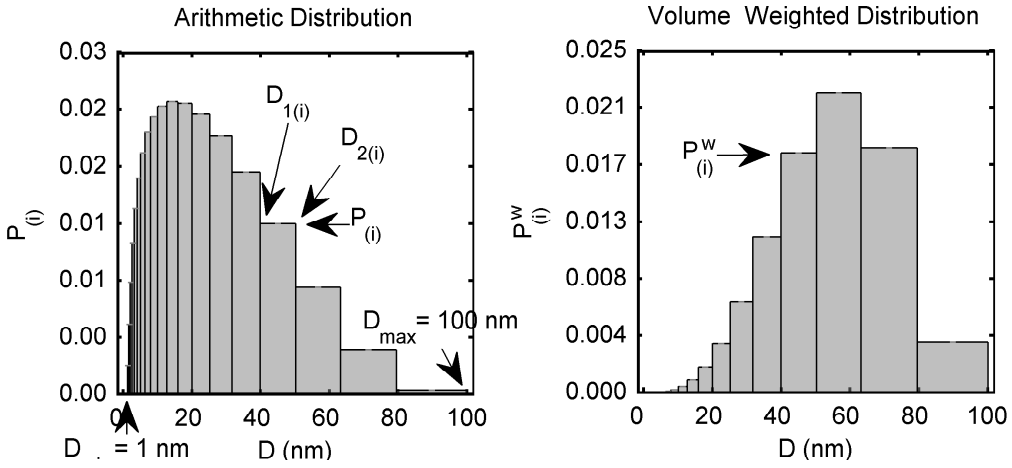

Figure 4.23: Histogram representation of CSD. The left plot represents the arithmetic CSD $P_{(i)}$, the right plot the auxiliary volume weighted distribution defined by eq. 4.13. The figure shows the starting histogram configuration.

Size Fourier coefficients are needed now. We can use a general formalism derived by Scardi and Leoni [135] or equivalently evaluate eq. 4.3. In the first step $A_S(\rho_\parallel)$ can be calculated for a sphere of diameter D [11, 26, 135]

$$\begin{aligned} A^{sph}_S(\rho_\parallel, D) &= \int d^3\boldsymbol{r_s}\ \Omega_{sph}(\boldsymbol{r}_s)\Omega_{sph}(\boldsymbol{r}_s - \boldsymbol{\rho}_\parallel) \\ &= \frac{\pi}{6}D^3\left(1 - \frac{3}{2}\frac{\rho_\parallel}{D} + \frac{1}{2}\frac{\rho^3_\parallel}{D^3}\right) \ , \quad 0 \le \rho_\parallel \le D \\ &= \frac{\pi}{6}D^3\left(1 - \frac{3}{2}\frac{\rho_\parallel}{D} + \frac{1}{2}\frac{\rho^3_\parallel}{D^3}\right)\mathrm{H}(D - \rho_\parallel) \ , \end{aligned}$$

[1] If CSD is defined by a histogram-like arithmetic distribution $P_{(i)}$ then shape of each histogram bar representing the "true" volume weighted distribution is modified by D^3 function.

where H(x) is the Heaviside step function. In the next step the sample averaging $\langle \dots \rangle$ in eq. 4.3 must be evaluated, which means in this case the integration over CSD

$$A_{(i)}(\rho_\parallel) = \int_{D_{1(i)}}^{D_{2(i)}} A_S^{sph}(\rho_\parallel, D)\ dD$$

$$= \frac{\pi}{24} \begin{cases} D_{2(i)}^4 - D_{1(i)}^4 - 2\rho_\parallel (D_{2(i)} - D_{1(i)}) \cdot \\ \qquad (D_{1(i)}^2 + D_{1(i)} D_{2(i)} + D_{2(i)}^2 - \rho_\parallel^2) & \dots 0 \le \rho_\parallel \le D_{1(i)} \\ (D_{2(i)} - \rho_\parallel)^3 (D_{2(i)} + \rho_\parallel) & \dots D_{1(i)} \le \rho_\parallel \le D_{2(i)} \\ 0 & \dots D_{2(i)} \le \rho_\parallel \ , \end{cases}$$

$$A_S(\rho_\parallel) = \sum_i A_{(i)}(\rho_\parallel) P_{(i)} \ / \ \sum_i A_{(i)}(0) P_{(i)} \ . \tag{4.14}$$

Fourier coefficients (eq. 4.14) are normalised to $A_S(\rho_\parallel = 0) = 1$, which means that they do not include a total volume of crystallites. The volume is accounted in the MSTRUCT elsewhere, in the *Scale* factors.

Few constraints were imposed on the histogram CSD. It is assumed that there are no crystallites smaller than D_{min} and larger than D_{max}

$$P_{(i)}(D_{min}) = P_{(i)}^w(D_{min}) = 0 \ , \tag{4.15a}$$

$$P_{(i)}(D_{max}) = P_{(i)}^w(D_{max}) = 0 \ . \tag{4.15b}$$

It is clear from the expression 4.14 for $A_S(\rho_\parallel)$ that diffraction image does not depend on a normalisation factor of the histogram frequencies and if we require an unique solution, the distribution should be normalised. For the reasons clarified later the area below the auxiliary volume weighted distribution is kept constant during refinement

$$\sum_{i=1}^{N} P_{(i)}^w (D_{2(i)} - D_{1(i)}) = const \ . \tag{4.16}$$

Starting distribution, a wide bell shaped peak settled in the middle of the $P_{(i)}^w$ histogram is depicted in fig. 4.23. At the beginning of the MSTRUCT run it is loaded from a file, where histogram bins, starting histogram frequencies and frequencies refinement flags (fixed/refined status) are defined. The number of bins was always $N = 20$.

```
# example: wD_AnataseITF.dat - input file for a histogram CSD model
#     D1(nm)    D2(nm)     distrib   fixed (0-No/1-Yes)
        1.00      1.26       0.000       0
        1.26      1.58       0.003       0
        1.58      2.00       0.019       0
         ...
       63.10     79.43   29200.549       0
       79.43    100.00    7607.890       0
```

It must be also noted that the refined parameters in the MSTRUCT are directly *distrib* values in the above example file. They are equal to area of each bin in the volume weighted distribution

$$\begin{aligned} N_{(i)} &= P^{w}_{(i)}(D_{2(i)} - D_{1(i)}) \\ &= P_{(i)} \left(\frac{D_{1(i)} + D_{2(i)}}{2} \right)^3 (D_{2(i)} - D_{1(i)}) \\ &\equiv distrib \ . \end{aligned} \tag{4.17}$$

It is now clear that normalisation condition 4.16 reduces to $\sum_i N_{(i)} = const.$

To ensure validity of the distribution normalisation constraint 4.16 the LSQ-algorithm in the ObjCryst had to be slightly modified. In a standard nonlinear LSQ-fitting method a vector of corrections $\delta \boldsymbol{a}$ of the current model parameters $\boldsymbol{a}$ is searched by solving a set of linear equations [219, ch. 15]

$$\sum_l \alpha_{kl} \delta a_l = \beta_k \ ,$$

where α_{kl} is the curvature matrix (an approximation of a half of Hessian). The condition 4.16 can be transformed to a simple linear constraint

$$\sum_l C_{kl} \delta a_l = 0 \ ,$$

where C_{kl} is generally a matrix of constraints. Couple of methods are available [220, ch. 12], [221, 222] for including a linear constraints into the LSQ-algorithm. In the MSTRUCT the one using the generalised singular value decomposition [222, 223] was utilised.[1]

The basic histogram-like CSD model was established in this section. Histogram frequencies can now be refined in the MSTRUCT as any other ordinary parameters.

4.5.3 Reference samples - refinement algorithm

The ISOP samples REF-400 and REF-550 prepared from sol were chosen for testing the histogram CSD model. As it can be seen from fig. 4.13 (p. 100) the samples form a couple with essentially different crystallite size. The maxima of their arithmetic distributions are clearly separated. The mean crystallite size is $\langle D \rangle \doteq 6.7$ nm in the REF-400 sample and $\langle D \rangle \doteq 22.6$ nm in the REF-550 sample. The quality of fits of the REF-400 and REF-550 patterns (figs. 4.8 and 4.9, p. 97–98) with the log-normal CSD model is very good, hence the model can be used here as a reference. The histogram CSD model is used only for the major anatase phase, whereas the basic log-normal model is kept for the minor rutile fraction in the REF-550 sample.

[1] Unfortunately because for simplicity Lapack GSVD routines [224] are utilised, which complicates implementation of the CSD histogram model in Windows, the MSTRUCT does not implement the model on Windows correctly on the date this work was finished. The model is available only in the Linux version [225].

The histogram frequencies were refined from the REF-400 and REF-550 diffraction patterns. The quality of the fit was practically the same as for the log-normal distribution model and also the *GoF* factors were very similar. Refined distributions are depicted in fig. 4.24 for the REF-400 sample and in fig. 4.25 for REF-550. Whereas the refined histogram CSD for the REF-400 sample looks reasonably and fits the reference log-normal CSD very well, the results are not so good for the REF-550 sample. The refined volume weighted CSD ($P^w_{(i)}$ (the right-side subplot in fig 4.25) corresponds to the reference CSD, but the arithmetic CSD (the left-side subplot) has no physical validity. This is clearly connected with small crystallites (low D) noisy bins in the volume weighted CSD. When the refined values $N_{(i)}$ (eq. 4.17) are transformed to $P_{(i)}$, they are dived by very small numbers for the case of small crystallites and errors are enhanced. The noise in the low bins of $P^w_{(i)}$ originates from difficulties in separation of diffraction signal from the background. Very small crystallites contribute to diffracted intensity with their volume very weakly as compared to large crystallites. Intensity diffracted by them is also spread in tails of the peaks and possibly hidden by peak overlap, difficult to be separated correctly from background.

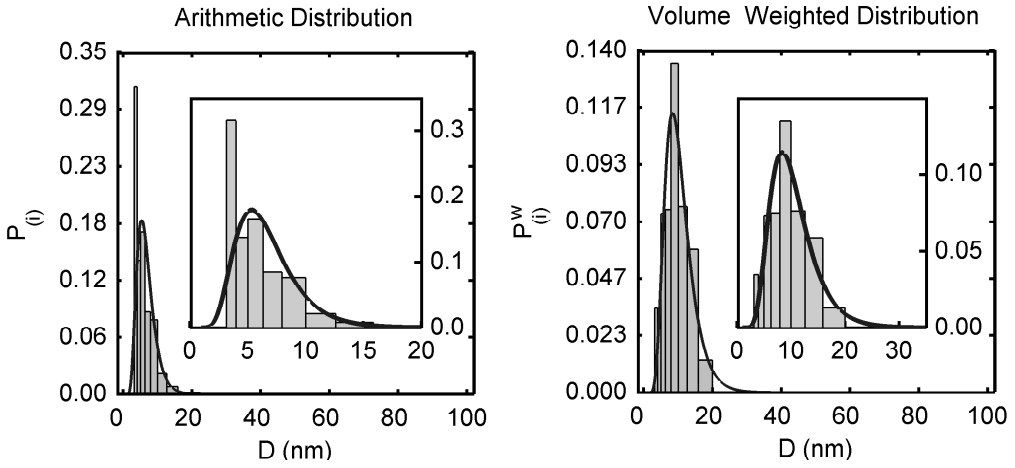

Figure 4.24: Refined histogram CSD of the REF-400 sample. No regularisation was used. ($GoF = 1.43$, $\chi^2_{deriv} = 2 \cdot 10^5$, $\chi^2_{w-deriv} = 0.7 \cdot 10^4$)
Solid line - the reference log-normal distribution (Table 4.3).

The background was modeled by two components for the studied samples. The first component was an interpolated background with manually defined points. This is visible as a shadow dashed line and shadow points in the patterns fits (fig. 4.37). The second component was a Chebyshev polynomial in $\sin\theta$ of a quite low order, usually of the first or the second order, which was superimposed to the interpolated background. The coefficients of the polynomial were refined. Hence, the fitting algorithm in the MSTRUCT has a possibility to slightly transpose the intensity between the background and peaks tails. But this is actually not wrong.

The problem is rather related to the choice of the log-spacing for the CSD histogram. The refinement would be more stable if the low ($D_{(i)}$) bins were wider and less numerous. But it would result in poorer resolution on the other side. Such problem is usually solved in physics by a simple algorithm. Histogram refinement is started with a very roughly spaced grid and the histogram spacing

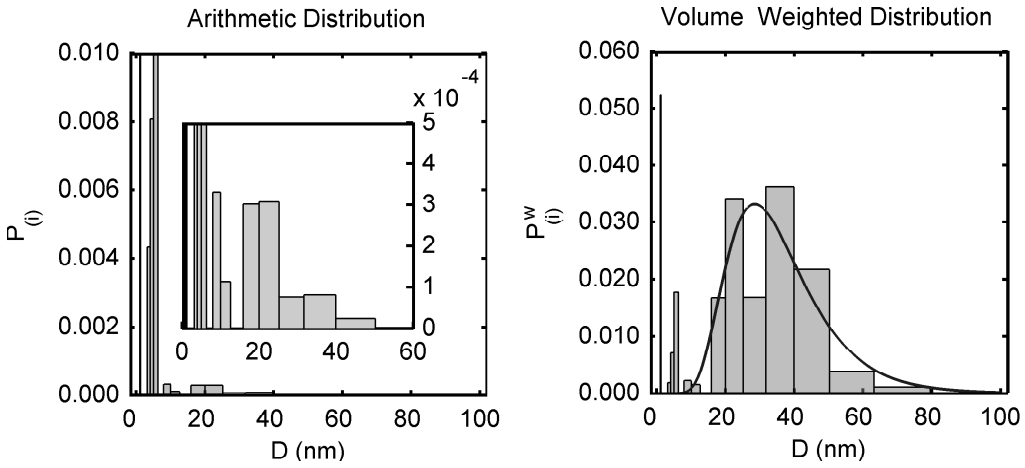

Figure 4.25: Refined histogram CSD of the REF-550 sample. No regularisation was used. ($GoF = 1.42$, $\chi^2_{deriv} = 6 \cdot 10^7$, $\chi^2_{w-deriv} = 1.3 \cdot 10^4$)
Solid line - the reference log-normal distribution.

is gradually decreased by dividing each bin in iterative steps. This was used by [12]. In this work a different strategy was utilised. An assumption of a smooth CSD was declared in the method explicitly by applying regularisation conditions to the searched CSD. An advantage of this approach is that the refined object, CSD histogram here, is not changed during the refinement, the number of bins is not multiplied, only an additional optimisation function has to be added to the pattern chi-square ($\chi^2_{pattern}$). This is easier to implement in the MSTRUCT and also more general than the single-purpose method.

The regularisation methods are widely used in crystallography to reach smoothness of solution, e.g. in the problem of deconvolution [26, 131, 132, 226]. A measure of smoothness is taken as an integral of the square of the derivative

$$\chi^2_{reg} = \int \left[\frac{dP(D)}{dD}\right]^2 dD \qquad (4.18)$$
$$\approx \frac{P^2_{(1)}}{D_{(1)}} + \sum_{i=2}^{N} \frac{(P_{(i)} - P_{(i-1)})^2}{D_{(i)} - D_{(i-1)}} + \frac{P^2_{(N)}}{D_{max} - D_{(1)}} \equiv \boldsymbol{P} \cdot \hat{\boldsymbol{H}} \cdot \boldsymbol{P} \ ,$$

where conditions 4.15a were used. The sum can be formally casted into the matrix formalism, by defining a regularisation matrix $\hat{\boldsymbol{H}}$ and a CSD vector $\boldsymbol{P}$. The regularisation operator χ^2_{reg} (eq. 4.18) multiplied by a weighting factor λ can be added to $\chi^2_{pattern}$ and form the chi-problem

$$\chi^2_{problem} = \chi^2_{pattern} + \lambda \cdot \chi^2_{reg} \ ,$$

which is minimised. In the same way the arithmetic CSD is regularised, the volume weighted distribution $P^w_{(i)}$ can be treated. The regularisation weighting factor λ has to be somehow set. This is described later, but it is important to note here that for all the results presented the total value of the regularisation factor ($\lambda \cdot \chi^2_{reg}$) was kept on a very small fraction of $\chi^2_{pattern}$.

The method was applied to the REF-550 sample. In the first case the arithmetic CSD was regularised and in the second the regularisation was imposed

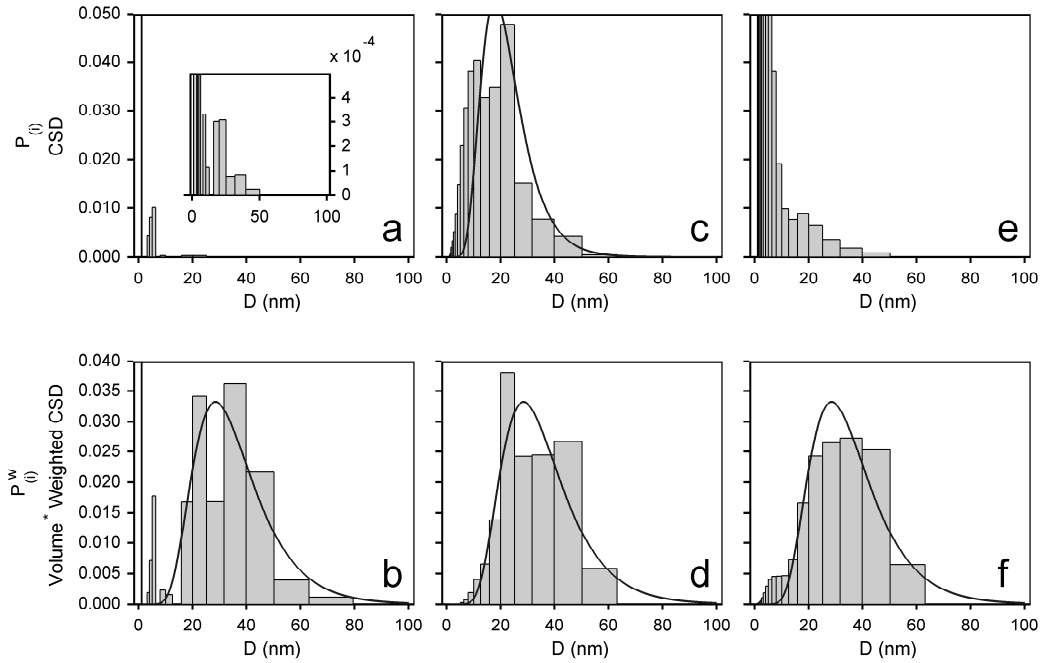

Figure 4.26: Refined histogram CSDs of the REF-550 sample. Different types of regularisation were used. Subplots (a–b) depict the case no regularisation was used, in (c–d) the arithmetic CSD ($P_{(i)}$) was regularised and in (e–f) the volume weighted CSD ($P^w_{(i)}$) was regularised.
(a-b) $GoF = 1.42$, $\chi^2_{deriv} = 6 \cdot 10^7$, $\chi^2_{w-deriv} = 1.3 \cdot 10^4$,
(c-d) $GoF = 1.45$, $\chi^2_{deriv} = 4.5 \cdot 10^2$, $\chi^2_{w-deriv} = 2.2 \cdot 10^2$,
(e-f) $GoF = 1.44$, $\chi^2_{deriv} = 2.5 \cdot 10^5$, $\chi^2_{w-deriv} = 0.8 \cdot 10^2$.
Solid line shows the reference log-normal distribution.

to the volume weighted distribution $P^w_{(i)}$. Refined distributions are depicted in fig. 4.26. The volume weighted CSDs (b, d, f) mutually differ only in details of their shape. Their centers are located at the same positions and their variances are similar. If any type of regularisation is employed all the distributions are smoother. Unfortunately the arithmetic CSDs strongly depend on the type of regularisation. If the volume weighted size distribution $P^w_{(i)}$ is regularised, it results in an extremely asymmetric exponential-like arithmetic size distribution $P_{(i)}$ (fig. 4.26e). There is a huge number of the smallest crystallites, which arise from the requirement of the smoothness of $P^w_{(i)}$. If regularisation is applied to the arithmetic CSD the best result is achieved (see fig. 4.26 c–d). An erroneous and noisy arithmetic distribution obtained without regularisation is converted to a smoother peak-like distribution. Unfortunately, the refined CSD differs from the expected log-normal (fig. 4.26c). The histogram distribution reveals larger fraction of small crystallites ($D \lesssim 10$ nm). The worst message comes from the fact that, whereas the arithmetic CSDs depend strongly on the regularisation type, the difference in measured and calculated XRD data is the same independent of the regularisation, as can be seen from GoF values listed in the caption of the figure 4.26. This clearly indicates that from the measured REF-550 XRD pattern, with its statistical quality, it is not possible to determine the arithmetic CSD unambiguously. On the other hand the similarity of volume weighted CSDs

shows that the method can determine reasonably at least the volume weighted CSD and the problem is in converting it to the arithmetic CSD if both small and large crystallites can be present in the sample. Remember that for small crystallites (REF-400) the method was working fine even without regularisation (fig. 4.24) and it would behave well for the large crystallites if the bin width and the minimum crystallite size (D_{min}) were larger.

It can be concluded that any type of regularisation to not affect essentially the resulting volume weighted CSD but influences strongly the arithmetic CSD. The best results were finally archived when both type of regularisation were used. An algorithm, described below, was adopted and tuned on reference samples and applied in further analysis.

In the MSTRUCT the CSD histogram refinement was described with the following input. The first lines implies only a modification in the refinement for the histogram CSD model. The central part describes the histogram CSD model for the anatase phase. Control parameters of the refinement procedure are specified at the last line.

```
// Job type
3                    job type (0-data refinement,...,3-histogram ref.)
 ...
 ...
// the 1st phase - Size broadening - refinable Size Distribution model
SizeDistrib sProfA   broadening component type, effect name
file                 distribution type (file/create)
wD_AnataseITF.dat    name of file with prescribed weighted distribution
2                    number of LSQ regularization methods used
deriv     1.e-1      LSQ regularization method type, LSQ weight factor
vol-deriv 1.e+1      LSQ regularization method type, LSQ weight factor

//create             distribution type/source (file/create)
//log 1.0 100. 20    type(linear/log/sqrt),Dmin(nm),Dmax(nm),nb. bins
 ...
 ...
// number of refinement interactions
-5  20  5  0.02      nb reduced, nb full iter., nb cycles, tuning coef.
 ...
```

Some special words are highlighted in the code. `"SizeDistrib"` is the name for the histogram CSD effect. `"deriv"` and `"vol-deriv"` are labels for the regularisation type. Numbers beside them are related to λ weighting factors. The first number at the last line specifies the number of refinement iterations with the reduced set of model parameters. It is negative, which means that exactly the number of iterations are done independently the optimisation converged or not during them. The second value specifies the number of iterations with full parameters set. For some parameters, e.g. scale factors or histogram frequencies, the calculation of derivatives needed for the Levenberg–Marquardt algorithm, can be highly optimised, these parameters form the reduced parameters set. Contrary for some parameters as e.g. microdeformation (e), or crystal structure data the MSTRUCT is not optimised and they are not included in the reduced parameters set. In summary, during the first stage with the fixed number of iterations only the scale factors and histogram parameters are refined, whereas during the second stage with more maximum iterations (but the converge can be achieved more

quickly), all parameters are refined. This is not essential part of the algorithm. It only can save some computation time. The third value is the number of repeating cycles. The reduced and full refinement procedures are repeated subsequently. Hence the maximum possible number of iterations is the sum of absolute values of the first two parameters multiplied by the third one. The reason of repeating the refinement procedure is related to the last parameter, which is a small floating point value specifying the starting fraction the regularisation operators contribute to the total minimised chi-square. This value is set small (e.g. `"0.02"`), which means that the regularisation part of the problem chi-square should be only 2% of the pattern chi-square. Namely in this case it holds

$$\chi^2_{problem} = \lambda^*_1 \cdot \chi^2_{deriv} + \lambda^*_2 \cdot \chi^2_{w-deriv} \ ,$$

where χ^2_{deriv} is the chi-square of the regularisation operator of the arithmetic CSD and $\chi^2_{w-deriv}$ is the same quantity for the volume weighted CSD. At the start of the whole refinement and generally at the beginning of each repeating cycle the λ^*_i factors are scaled to fulfil

$$0.02 \cdot \chi^2_{problem} = \lambda^*_1 \cdot \chi^2_{deriv} + \lambda^*_2 \cdot \chi^2_{w-deriv} \ .$$

From the user specified λ_i the relative values of λ^*_i are set at the same time

$$\lambda^*_i = \lambda_i \cdot \chi^2_{reg-i} \ ,$$

which implies that in the next top cycle the weight of the regularisation operator is proportional to its current value. If the given operator is small, the distribution is smooth, its weight in the next turn will be small, whereas if the operator is still high, strong force will be applied in next iterations to minimise it.

In figure captions (figs. 4.24 or 4.26) χ^2_{deriv} and $\chi^2_{w-deriv}$ values are specified for different CSDs. The values can be very different for e.g. narrow distributions of small crystallites or for large crystallites with a high size dispersion. It is difficult to pre-estimate them and hence they are treated by the algorithm described above. Manually only the λ_i factors can be set. They were tuned on the data of the reference samples (REF-400 and REF-550) and the same settings was used for all other.

The final histogram CSDs for the REF samples when both the regularisation methods were applied are shown in fig. 4.27. The histogram CSDs and the reference log-normal distributions fit very well. In the case of REF-400 sample both the arithmetic and the volume distribution were practically only slightly smoothed, whereas the shape of the arithmetic CSD of the REF-550 sample changed substantially due to regularisation.

4.5.4 Mixed samples

A set of mixtures of the reference samples (REF-400 and REF-550) was prepared to test the method. Measured XRD patterns of these mixed samples were fitted by the WPPM method using the histogram model and the described algorithm. The anatase crystallites originating from both the reference samples were considered as a single phase and the histogram CSD was determined for each sample. The

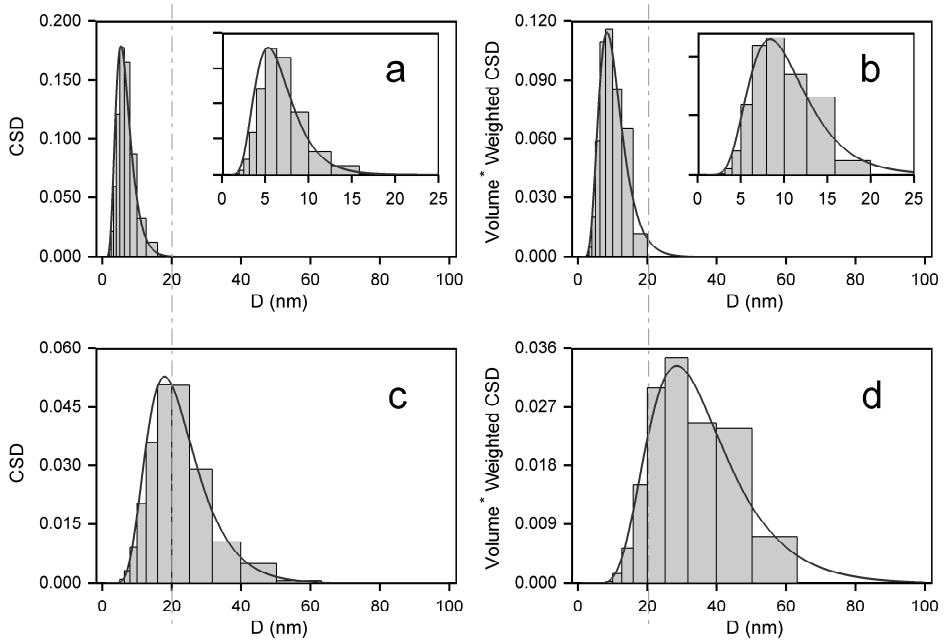

Figure 4.27: Refined histogram CSDs of the REF-400 and REF-550 samples. These solutions were obtained from the noisy distributions by including both type of regularisation ($\lambda_{deriv} = 0.1$, $\lambda_{w-deriv} = 1.0$). Subplots (a–b) show CSDs of the REF-400 sample, (c–d) results for the REF-550 sample.
`(REF-400 a,b)` $GoF = 1.50$, $\chi^2_{deriv} = 1.4 \cdot 10^4$, $\chi^2_{w-deriv} = 4.7 \cdot 10^3$,
`(REF-550 c,d)` $GoF = 1.47$, $\chi^2_{deriv} = 3.5 \cdot 10^2$, $\chi^2_{w-deriv} = 1.2 \cdot 10^2$.
Solid lines depict the reference log-normal CSDs.

refined histogram CSDs in the mixed samples then can be compared with the CSDs calculated from the known fractions of reference samples.

It was shown in section 4.4, that some structural parameters, e.g lattice parameters (fig. 4.12, p. 99), depend on the crystallite size and also the values for the REF-400 and REF-550 samples are different (see Table 4.2, p. 4.2). Hence the model assumption, that the crystallites originating from the couple of the reference samples can be considered as the same crystalline phase, is clearly not valid. Because the variability of structure parameters with crystallite size is a general problem, the mistake introduced here by adopting the assumption mirrors the systematic error possibly always present in such a XRD analysis. In order to avoid the approximation a more sophisticated model based on some empirical data or on ab-initio simulations should be introduced. This is well above the scope of this work and hence the above assumption is included and the results and the quality of fits can be slightly affected.

Six mixtures were prepared. The weights of components in the mixtures are listed in the Table 4.5. We focus the attention to the analysis of anatase, however small fraction of rutile was present in the REF-550 sample. For further analysis it is suitable to know how big fraction (x) of anatase in the given mixed sample comes from one of the reference samples, e.g. from the REF-400. This can be calculated from weight values (m_{400}, m_{550}) (Table 4.5) and the minor phase fractions in the REF samples determined by XRD (Table 4.2, p. 88). It

must be emphasised here, that no knowledge about rutile is used in refinement of anatase CSDs and anatase and rutile scale factors in mixtures constitute a data set, which can be used for an independent quantitative phase analysis (QPA). The rutile weight fractions (x_{R-XRD}) can be evaluated from the XRD data using equation in Table 4.2. On the other hand, if we assume a rutile weight fraction r_{400} in the REF-400 sample and r_{550} in REF-550, the rutile fraction in each sample can be easily calculated as

$$x_{R-W} = \frac{r_{400} \cdot m_{400} + r_{550} \cdot m_{550}}{m_{400} + m_{550}} \ .$$

The values obtained from both methods can be compared and rutile weight fractions in the reference samples can be optimised to fit the whole data set (six mixtures, two reference samples). The fit depicted in fig. 4.28 gives

$$r_{400} = 0.25 \pm 0.15 \text{ wt.\%} \ , \quad r_{550} = 6.2 \pm 0.1 \text{ wt.\%} \ . \tag{4.19}$$

The obtained values are in good agreement with results obtained earlier for the pure reference samples (p. 88, Table 4.2: $r_{400} \doteq 0.4$ wt.%, $r_{550} \doteq 6.8$ wt.%).[1] Good linearity and no large discrepancies in fig 4.28 between the rutile fractions evaluated from the sample weights (x_{R-W}) and the values from QPA (x_{R-QPA}) confirm also consistency of the samples set.[2]

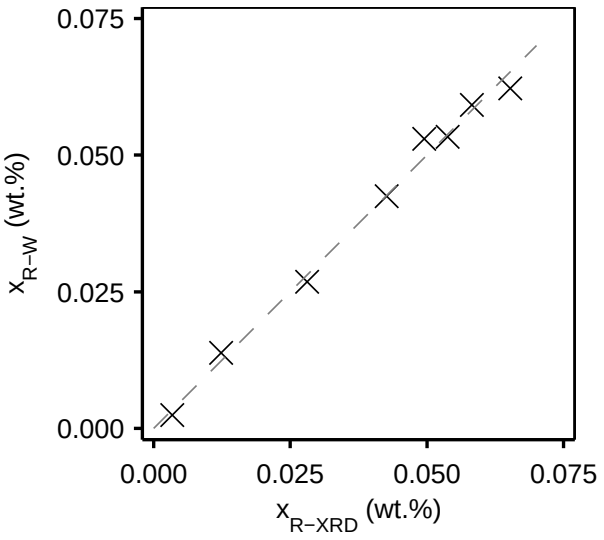

Figure 4.28: Correlation between rutile fraction (x_{R-XRD}) in the samples determined by the conventional QPA of the XRD data and the fraction (x_W) evaluated from sample weights (Table 4.5) and weight fractions (eq. 4.19) of rutile in the reference samples. Dashed line is a diagonal guide for the eye.

From values in eq. 4.19 the weight fraction of anatase crystallites originating from the REF-400 sample can be simply evaluated

$$x_{W-QPA} = \frac{m_{400} \cdot (1 - r_{400})}{m_{400} \cdot (1 - r_{400}) + m_{550} \cdot (1 - r_{550})} \ . \tag{4.20}$$

The values are listed in the Table 4.5 for comparison with values determined by a different method later. They are close to nominal values f_0, which are listed also there.

[1] The value for REF-400 (r_{400}) is nonzero only formally. It is clear that there is most likely no rutile in REF-400 (see fig. 4.8, p. 97).

[2] A significant random error can be introduced e.g. during preparation of mixtures of reference samples as easily some part of the powder can be lost or the sample in the diffraction holder does not represent an ideal mixture of weighted reference samples.

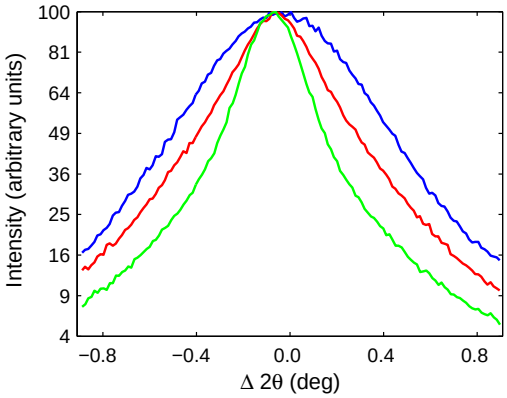

Figure 4.29: Central part of the anatase 101 reflection. The reference sample REF-400 (blue line), the mixed sample no. 8 with $f_0 = 0.8$ (red line) and the sample no. 4 with $f_0 = 0.6$ (green line).

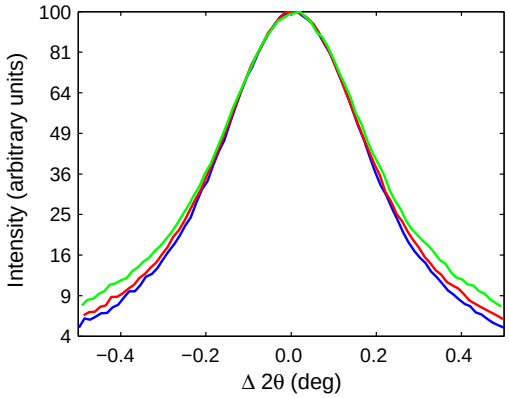

Figure 4.30: Central part of the anatase 101 reflection. The reference sample REF-550 (blue line), the mixed sample no. 6 with $f_0 = 0.05$ (red line) and the sample no. 5 with $f_0 = 0.15$ (green line).

Six mixtures had approximately the following nominal fractions: $f_0 = 0.05$, 0.30, 0.60, 0.80 and two samples have $f_0 = 0.15$.. A detail of the anatase 101 reflection for the samples is depicted in figs. 4.29–4.30. Fig. 4.29 depicts the small crystallites reference sample REF-400 and two mixed samples. Huge changes in peak width and shape with increasing fraction of large crystallites are apparent. Fig. 4.30 depicts the large crystallites reference sample REF-550 and two mixed samples with small (0.05 and 0.15) nominal fractions of anatase from REF-400. The differences are visible in the tails of the peaks only because the small crystallites scatter mainly there.

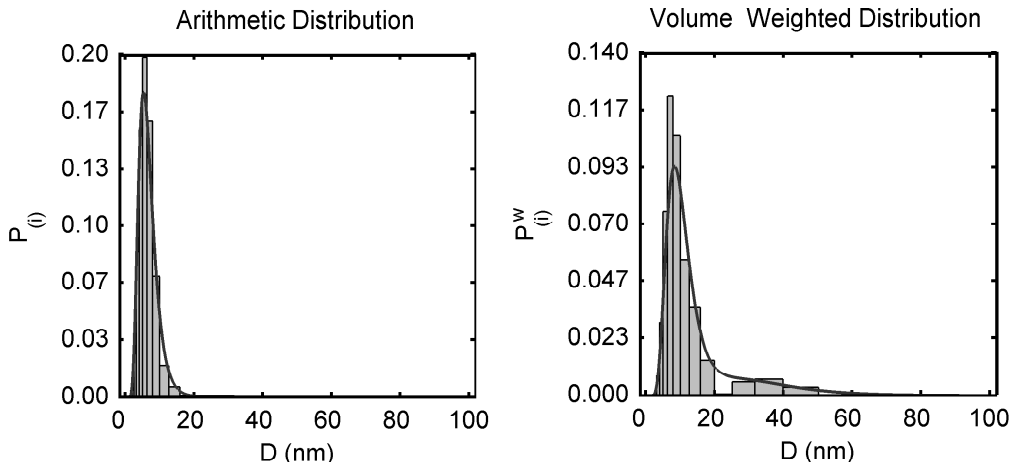

Figure 4.31: Refined histogram CSD of the mixed sample no. 8 with $f_0 = 0.8$. Solid line depicts CSD expected from the parameters of the log-normal distribution of the reference samples and their weights in the sample.

The CSD histograms of all the mixed samples were refined by the WPPM. Some of the histograms look very reasonable. Mainly these containing large fractions of the REF-400 sample. See figs. 4.31 and 4.32, where small volume

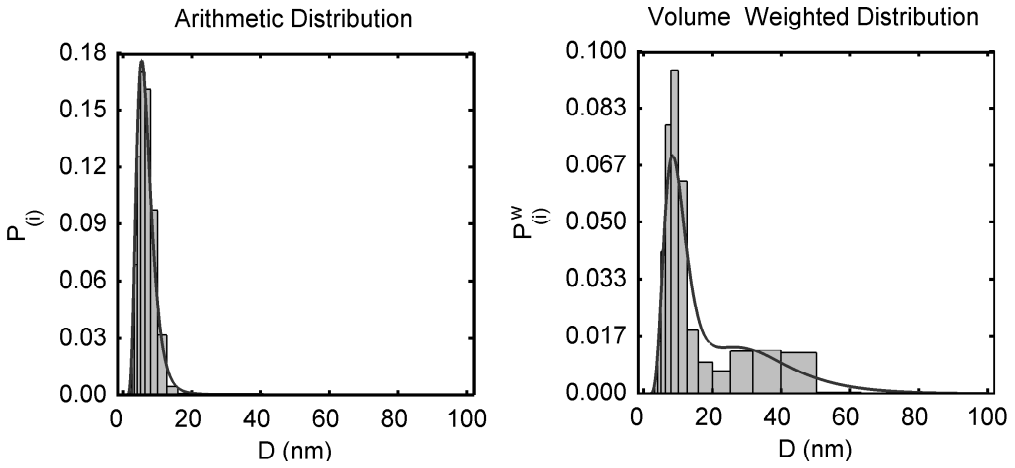

Figure 4.32: Refined histogram CSD of the mixed sample no. 4 with $f_0 = 0.6$.

fractions of large crystallites originating from the REF-550 sample are clearly distinguishable from the small peaks (at large $D \gtrsim 20$ nm) in the volume weighted CSDs. Contrary, the results for samples with small f_0 are not so good. In fig. 4.33 of sample no. 5 with $f_0 = 0.15$ the reference log-normal distribution does not fit well the refined histogram CSD. However, in this case it is still possible to reveal bimodal crystallite size distribution from the two peaks in the volume-weighted CSD. Unfortunately, this is difficult to see in the refined CSD of the no. 6 sample (fig. 4.34) with the lowest fraction of REF-400 ($f_0 = 0.05$). A broad volume weighted CSD is visible in fig. 4.34 and the arithmetic CSD does not correspond to the reference one. There is significantly a lower number of small crystallites than expected. The problem is similar to the CSD determination in the REF-550 sample. See fig. 4.30, where only small differences in peak tails are visible between samples. It indicates that the task of CSD determination in the case of large crystallites has not been solved completely. It is still difficult to separate intensity contribution of small crystallites from the background intensity if also strong signal from large crystallites is present. It can be concluded that the sensitivity of the CSD determination from XRD data was overestimated at the beginning and in such case the histogram bins for small crystallites should be made wider and reduced in number. On the other side it was shown that the method can detect a small volume fraction ($\sim$ 20 vol.%) of large crystallites contaminating a fine noncrystalline powder (fig. 4.31). This could be essential information e.g. for optimising the technology to produce nanopowders with well defined crystallites size.

More precise quantitative refinement of histograms was performed in order to make conclusions discussed above. The fits can be compared not only with the reference log-normal distributions, as it is depicted in figs. 4.31–4.34, but also with the histogram CSDs of the reference samples, which were determined in the previous section (fig. 4.27). The histogram of reference samples can be linearly combined and fitted to the histogram distributions of the mixed samples. This was done for all the mixed samples. Such a fit of the sample no. 3 ($f_0 = 0.3$) is depicted in fig. 4.35. The scale factor and the volume ratio of anatase originating from the REF-400 or the REF-550 sample were the only two fitted parameters.

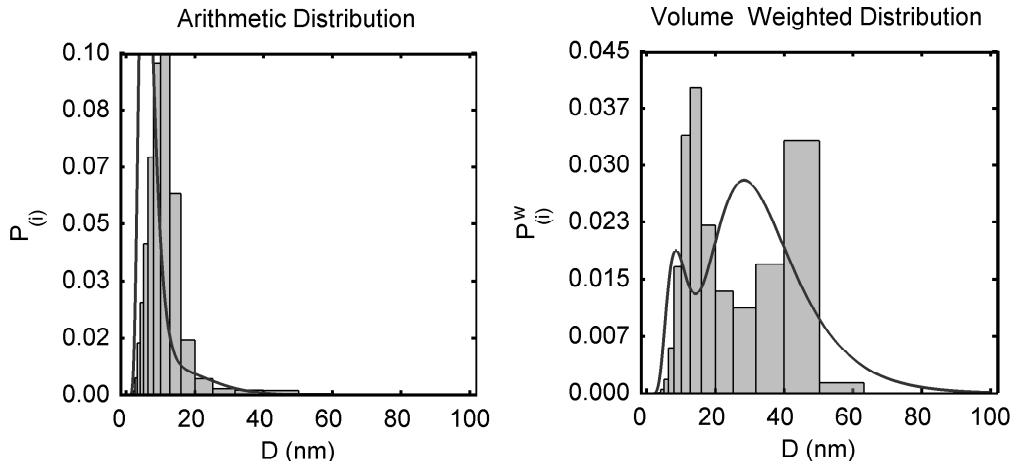

Figure 4.33: Refined histogram CSD of the mixed sample no. 5 with $f_0 = 0.15$. Solid depicts CSD expected from the parameters of the log-normal distribution of the reference samples and their weights in the sample.

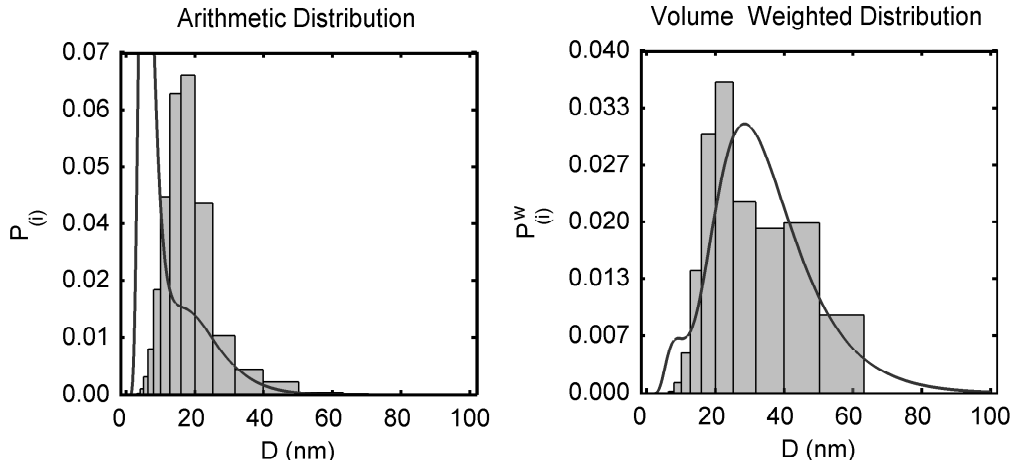

Figure 4.34: Refined histogram CSD of the mixed sample no. 6 with $f_0 = 0.05$.

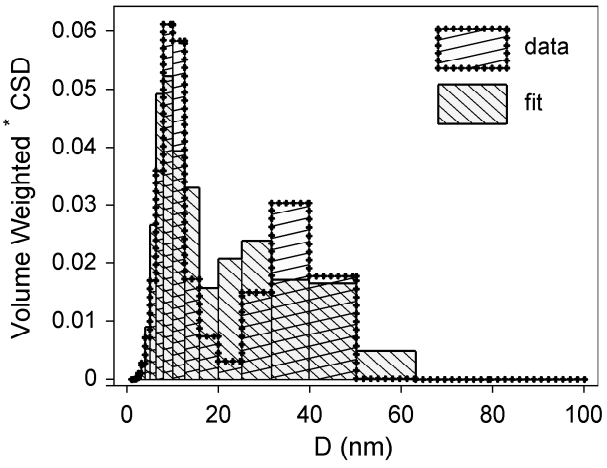

Figure 4.35: Volume weighted CSD of the mixed sample no. 3 ($f_0 = 0.3$) refined by WPPM (marked as "data"). The data are fitted by a linear sum of the reference samples histogram CSDs (marked as "fit"). ($Scale = 1.43 \pm 0.12$, $x_{\mathrm{LPA}} = 0.39 \pm 0.05$ vol.%)

no.	f_0	m_{400} (g)	m_{550} (g)	$x_{\text{W-QPA}}$	x_{LPA}
1	1.00	–	–	–	–
2	0.00	–	–	–	–
3	0.30	0.193	0.392	0.344	0.39(5)
4	0.60	0.305	0.210	0.607	0.62(3)
5	0.15	0.093	0.513	0.162	0.17(5)
6	0.05	0.030	0.565	0.053	0.03(2)
7	0.15	0.080	0.459	0.156	0.18(4)
8	0.80	0.463	0.109	0.819	0.85(2)

Table 4.5: List of mixed samples. The nominal weight fractions of the anatase REF-400 crystallites in the samples are denoted as f_0. True measured weights of the reference samples (REF-400 and REF-550) are denoted as m_{400} and m_{550}. $x_{\text{W-QPA}}$ are the weight fractions of the anatase crystallites originating from the REF-400 sample as determined from weights and QPA according to eq. 4.20. Contrary the volume fractions x_{LPA} were evaluated from histograms determined by LPA (WPPM).

The scale factors appeared to be close to unity. The volume fractions are listed in the Table 4.5. They are called x_{LPA} because they are understood as volume fractions of anatase from different reference samples determined by WPPM.

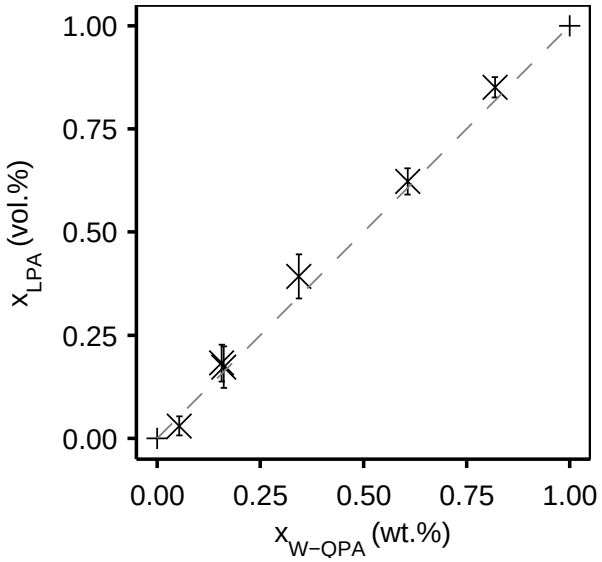

Figure 4.36: Final regression of the weight fractions ($x_{\text{W-QPA}}$), determined from the sample weights and QPA, and the anatase volume fractions (x_{LPA}) determined from fitting the histogram CSDs determined by LPA from XRD data. Two reference samples (+), six mixed samples (×). Dashed line is a diagonal guide for the eye.

Anatase fractions evaluated from the sample weights and QPA ($x_{\text{W-QPA}}$) can be compared with the fractions determined from the histogram fitting (x_{LPA}). It can be seen from the Table 4.5 or fig. 4.36 that they are equal within the error limits. The uncertainties of x_{LPA} values are quite high, up to $\Delta x_{\text{LPA}} \approx 5$ vol.%, which is related to the qualitative agreement of the expected and refined CSDs. The value of Δx_{LPA} could be considered according to the present author as the precision limit of the LPA method for determination of anatase fractions in the mixtures. Problems which appeared for samples with $f_0 \lesssim 15\%$ were discussed already in the previous paragraph.

Finally, a powder pattern fit of the sample no. 3 ($f_0 = 0.3$) is shown in fig. 4.37. The very good quality of the fit is typical for all the samples studied in this chapter.

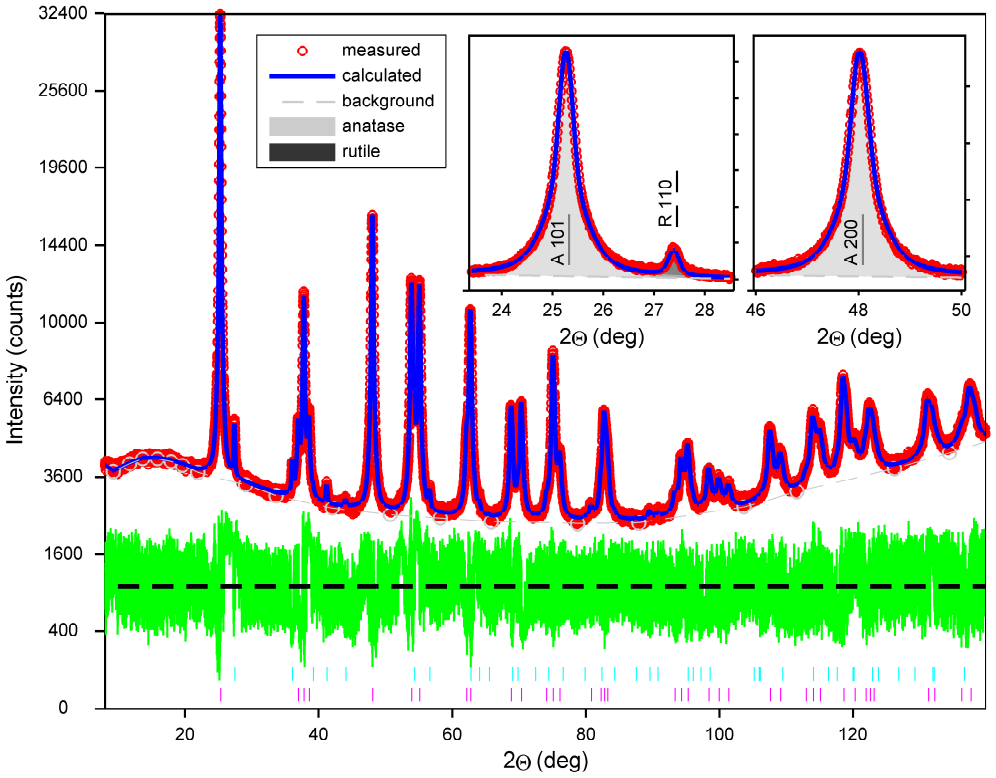

Figure 4.37: Pattern fit of the the mixed sample no. 3 ($f_0 = 0.3$). ($GoF \approx 1.43$; 10^4 points in the pattern, 1.5 10^3 sec per point)

4.5.5 Summary and discussion

The WPPM method [11] for the determination of histogram like CSD from XRD data was applied to TiO_2 nanocrystalline powders here. The original model [12] of histogram like representation of CSD was slightly modified — mainly by introducing logarithmic sampling of the CSD histogram and regularisation conditions for the distribution. The method appears to be able to distinguish qualitatively: (i) small and (ii) large crystallites present simultaneously in a mixture of samples with different mean crystallite sizes in the range 4–30 nm (figs. 4.31–4.33). The problem was encountered when small volume fractions of small crystallites ($D \lesssim 10$ nm) had to be characterised quantitatively in a presence of majority of large crystallites ($D \gtrsim 20$ nm) (figs. 4.25, 4.33–4.34). For such case the method shows an uncertainty in the distribution shape (fig. 4.26, p. 114). Problem concerns the arithmetic CSD. The volume weighted distribution can be determined quite unambiguously.

Two TiO_2 powder samples calcined at different temperatures and their mixtures were analysed. The size of crystallites of the sample calcined at 400°C was

$\langle D \rangle \approx 6.7$ nm. For the sample calcined at 550°C it was $\langle D \rangle \approx 22.6$ nm. CSDs in all samples were refined from XRD data. The histogram CSDs refined for both reference not-mixed samples were in a very good agreement with the log-normal distribution determined earlier in section 4.4. From crystallite sizes histograms it was possible to evaluate volume ratios of the original reference samples in the mixtures. A very good correlation with expected values was found (fig. 4.36). The volume fractions determined by LPA were different from the values expected from QPA by $\Delta \approx 5$ vol.%. This value can be considered as the precision limit of the CSD analysis done here.

Analysis of small crystallites at the presence of large ones is affected by difficulties in an unambiguous separation of a background signal from the intensity scattered by small crystallites in peak tails. This problem appears if a major intensity contribution comes from a volume of the large crystallites. This was also mentioned in Beyerlein et al. [36] and David et al. [218]. Here it was more highlighted in the extremely noise bins when the log-spaced histogram was used (fig. 4.25). The choice of logarithmic sampling of CSD makes it possible to treat small and large crystallites simultaneously. Unfortunately it magnifies the problem and shows that the determination of arithmetic CSD from XRD data presented here is partially an ill-posed problem. Applications of regularisation was helpful in this case. A different, more physically reliable solution would be reducing the number of bins and coarsening the histogram sampling.

If the results achieved in section 4.4 should be revised in the light of experiences with the refinement of the histogram CSDs, it can be concluded that (i) the use of the log-normal distribution is quite justified. The histogram CSD of the REF-400 sample fits well the reference log-normal distribution (fig. 4.27a). Problems with the analysis of large-crystallite sample REF-550 and mixed samples showing wide CSDs (figs. 4.33 or 4.34) indicate that (ii) the wide log-normal distribution of the ISOP-400 samples (fig. 4.13, p. 100) should be taken with caution, though. It was shown here that the volume weighted CSD is the relevant quantity measured in diffraction experiment. Arithmetic CSDs with high variance show a high volume fraction of large crystallites. In that case it is difficult to characterise small ones.

From the volume weighted CSDs refined from the XRD data it was possible to determine the volume fractions of small and large crystallites of the same crystalline phase (anatase) in one sample. This is certainly a big challenge for any analytical method.

Determination of histogram like CSDs in TiO_2 nanopowders from XRD data was accepted for publication in Matěj et al. [201].

Chapter 5

Conclusions

The main focus of the work was given to the problem of application of X-ray powder diffraction profile analysis for microstructural characterisation of nanocrystalline and submicrocrystalline materials. Primarily, the method of the whole powder pattern modelling (WPPM) or fitting was discussed and tested. Since no computer program including all necessary features for characterisation of nanomaterials in a wide scale (powders, bulk materials, thin films) has been available a new program system called MSTRUCT has been developed. It has been constructed by using the objects in C++ in such a way that further extension is relatively simple. In general, it includes many aspects required for the mentioned characterisation of materials, i.e. corresponding instrumental corrections, possibility of texture correction and determination of residual stresses. However, main attention was given to the line profile analysis and appropriate physically realistic models. This means correct description of the crystallite size broadening by means of their distributions including general histogram-like one and dislocation models including correlated dislocation arrangements.

The methods enabled also to reveal some unexpected aspects of microsutures of the samples investigated. In order to verify and test the method several classes of samples with different weights of the above effects were selected. It should be mentioned that all these materials are of high technological interest and were studied in the framework of different projects.

Studied Au colloid nanoparticles selected originally more for study of crystallite size broadening were surprisingly found to be also a suitable model material for studying lattice defects. One unexpected feature was the strong anisotropy (hkl dependence) of diffraction line broadening that could not be explained by the anisotropic shape of crystallites (not observed by TEM either) but it was well interpreted by a combination of the effect of twin faults and the anisotropic dislocation-induced broadening. Twinning fault probabilities were high ($\sim 8\%$) in small particles (size 5–30 nm) and were decreasing strongly with the crystallite size. The anisotropy of diffraction broadening from the present microstrain can be well described by dislocation contrast factors but the dislocations densities have to be rather high to explain such an effect. Anyway, despite the low statistical quality of diffraction data it was possible to estimate the limits of dislocation density in this case.

In the studied ECAP deformed samples (Cu, Cu with small addition of Zr) the microstructure was much more complex compared to the colloid Au nanoparticles. Dislocation structures in grain boundaries play a crucial role in the deformed materials. It was apparent from TEM and EBSD that dislocation boundaries were evolving from non-equilibrium low angle grain boundaries formed after 1–2 ECAP passes to high angle grain boundaries after 4–8 passes. XRD line broadening was again very well described by dislocation contrast factors and reasonable values of dislocation densities were evaluated. The values are slightly higher than those reported in the literature and were increasing with the number of passes. Some deviations from the literature data could be explained by different purity of samples which is quite important parameter. It was possible to estimate the Wilkens dislocation correlation parameter indicating a slightly more random dislocation arrangement in the CuZr samples. The fits of the diffraction patterns were not optimal, slight systematic deviations in line shape and positions could be observed. This indicates that the currently used dislocation models with not too strong correlation in their arrangements are not completely sufficient for the description of the microstructure of these metals after severe plastic deformation. The microstructure model should account also for diffraction broadening from dislocations within the grain boundaries and/or dislocation dipoles rather than only for dislocation correlation within the classical Krivoglaz-Wilkens models. This is a challenging problem for future work.

Analysis of TiO_2 nanopowders was much more straighforward compared to the investigation of the metal samples. This is related not only to good reciprocal space resolution and good statistical quality of diffraction data, but mainly to the relative simplicity of the size-broadening model as compared to models of dislocation arrangement. The WPPM procedure was fully utilised, because in this case: (i) the peak overlap is so huge, that only two diffraction lines can be independently analysed and even then their separation from the background scattering is a difficult problem; (ii) the intensities of diffraction lines were calculated completely from the structural model in this case. Simplified microstrain model was applied since this was a minor effect and the attention was given more to the crystallite size, namely, the crystallite size distribution and anisotropic crystallite shape, because this is related to the properties of the studied material and it is a problem interesting in general. In the studied TiO_2 nanopowders prepared by different chemical routes crystallite size distribution could be determined. The surface area calculated from the XRD data could be compared with specific surface measurements. It was found that for the prepared samples the data were in a very good agreement up to approximately the calcination temperature 400°C. Then the fine porous structure in the material degraded whereas the crystallite size did not show any abrupt changes. This indicates that a disintegration of the porous structure is not connected with some type of fast TiO_2 recrystallisation at the critical temperature.

In addition to the above analysis, histogram-like crystallite size distribution model was tested and it was found that the crystallite size distribution can be determined from the diffraction data also without assumptions on analytical type of distribution. However, it should be taken into account that diffraction is sensi-

tive mainly to the volume weighted distribution. In particular, this is important in the case of a high number of very small crystallites whose total volume can still be small compared to the volume of a few large crystallites. In this work, the problem was related also to an unfavourable choice of the histogram sampling, but the general problem is in a correct separation of the diffracted and background scattering signal. If the background cannot be suppressed in the experiment, only a physically correct treatment, such as e.g. simulation of the scattering from amorphous fraction by the Debye formula, could help to partially avoid this problem.

The computer program MSTRUCT developed for the XRD analyses done here was successfully applied not only to the samples described in this work, but was used extensively in the analysis of thin film samples in [127, 227–238]. where also the residual stress and/or texture played and important role. However, this is out of the scope of this thesis.

Appendix A

MStruct program

A.1 Introduction

For the most of diffraction analyses done in this work a computer program MSTRUCT ([225], `http://xray.cz/mstruct/`), developed by the present author, was used. Some details concerning the program were already specified at various places in the work in order to illustrate how the physical models are implemented in the software and which particular parameters are involved.

- The **dislocation model** was described in section 3.3 (p. 74),
- the **planar faults** in fcc crystals were described at the same place (p. 74),
- the **size brodendnig model** of spherical crystallites with size distributed according to the log-normal distribution was specified in section 4.3.1 (p. 85),
- its extension using **histogram-like distribution** was described in section 4.5.2 (p. 115).

In this part other features of the program, which were used, but were not of physical importance to be included in the main text, are described. A brief general introduction to the program is also given. In addition, because also an adaptation of the methods for thin film analysis was one of the initial aims, the related microstructural effects are presented here briefly. Some examples are shown and relevant references are given. This part is not a manual to the program, but should rather present a brief overview of what is possible in the program and for what applications it is designed.

A.2 Computer program, basic description and design

The MSTRUCT is a computer program/library for **M**icro**Struct**ure analysis from powder (x-ray) diffraction data:

- It is basically a typical Rietveld [7] program like many others famous programs: *FullProf* (Rodriguez-Carvajal, [105]); *GSAS* (Larson & Von Dreele & Toby, [239]); *TOPAS* (Kern, [240]), *MAUD* (Lutterotti, [106]); *BRASS* (Birkenstock et al., [241]); *Jana* (Petríček et al., [242]); etc.
- It includes physically relevant models for peak broadening and shifts like *PM2k* (Leoni & Scardi, [24]) and *CMWP-fit* (Ribárik & Ungár, [110]).
- It accounts for simple residual stress models, thin film absorption correction, reffraction correction and asymmetrical diffraction geometries like *MAUD* (Lutterotti, [106]).

The program was not build from a "zero point". Nowadays, several crystallographic programs are freely available (*FullProf, FOX, Maud*), together with their source codes and suggestions to extend the programs for particular purposes. One of the most known — *FullProf* [105] offers its Fortran Modules Library *CrysFML*. The same is true also for the FOX [243] developed by Favre-Nicolin & Černý [244–246]. FOX is a free, open-source program for the ab initio structure determination from powder diffraction. This is a relatively distant issue from LPA. However, in principle the FOX program calculates the powder pattern from the structural data, which is the basic requirement also here. Fot the use of the program for the LPA, the only necessary steps are (i) extending the routines for profile calculation and (ii) switching-on the standard least-square optimisation algorithm. The author was the first who made such modifications of the existing program FOX. FOX [243] is distributed under the GPL license [247] and hence it allows such modification but requires reciprocally that the derived work has to be distributed under the same conditions. The MSTRUCT binary as well as its source code can be found at `http://xray.cz/mstruct/`. A side effect related to the utilisation of an existing projects is that partially also the "design patterns" and the structure of the original project are mirrored in the new project. This can be either an advantage, if both the projects mutually fits well and even cooperate, or contrary a disadvantage, if the incorporation of the projects is rather laborious.

The design of the FOX program is depicted in fig. A.1. The FOX is based on its own library of routines for diffraction data simulations and optimisation. The library is called OBJCRYST. The FOX and the OBJCRYST also utilise another crystallographic library: the Computational Crystallography Toolbox (CCTBX) [248, 249] developed by Grosse-Kunstleve. The design of the MSTRUCT program is schematically shown in fig. A.2. The FOX program itself is not utilised, the program is based on OBJCRYST and CCTBX. Routines for LPA, WPPM and thin films correction are encapsulated in the MSTRUCT library and a small program utilising them is the MSTRUCT binary itself. The MSTRUCT program is very simple but do not have any graphical user interface

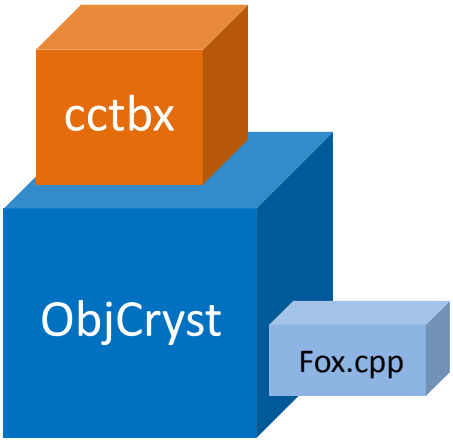

Figure A.1: Sketch of the FOX [243] design. The FOX program is build on the original OBJCRYST library, which utilises the free Computational Crystallography Toolbox (CCTBX) [248].

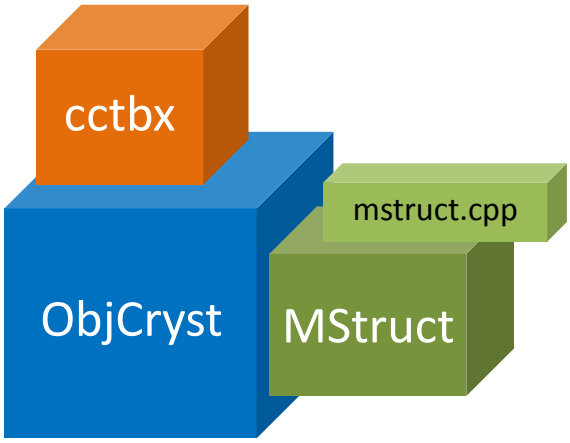

Figure A.2: Sketch of the MSTRUCT [225] design. The MSTRUCT heavily utilises the OBJCRYST, on which it is basically build, but also calls the CCTBX, which is a part of the FOX project.

yet. When it is started, it asks the user by simple questions and this drives its execution. Since the number of questions can be quite high, the answers, including comments, can be stored in an input parameters file. A part of the parameter file is shown here

```
// Job type
0                       job type (0-data refinement, 1-grid refinement)

// Input Data Files and Formats
tio2-400.xys    1       data filename , data format type (0-xy,1-xysigma)
0.609                   maximum sin(theta)/lambda

// Background
general         2       background, number of background components
interpolated            background component type (chebyshev,invX,...)
...
```

The program waits here for a `"job type"`, the answer is `"0"`, which means normal data refinement, other parameters are the name of the data file with measured data and its format, ..., background etc.

In the following code, the program requires a name ("diffDataAnatase" is the answer) of new crystalline phase in the pattern. The phase can be later identified by this name in the program. Then the program needs a name of the file with the structural data (structural database) and at the same line a name of the crystal ("AnataseITF"), which should be loaded from the database.

```
// the 1st phase
diffDataAnatase                 phase name (diffDataCrystal)

// the 1st phase - crystal data
structures.xml  AnataseITF      xml-filename, crystal-name
```

Crystal structures are saved in a separated XML file ("structures.xml"), which contains a database of crystal structures (lattice parameters, atom positions etc.). A new structure can be created/added very simply e.g. using the original FOX.

The program has no own interface to show the fitted data. Instead a few scripts for MATLAB and GNUPLOT are included in the distribution. Hence the data can be visualised very simply e.g. in these environments. More details, a guide how to setup the program and run the data refinement can be found on the MSTRUCT web page [225].

A.3 List of effects

A list of effects implemented in the MSTRUCT by the present author is specified here. Some of the features were already specified in the work, a few of them have not been finished yet completely. The list includes a short description of the effects and an informative list of features present implemented in other programs (PM2k, CMWP-fit, MAUD).

1. **Convolutional kernel** is a general procedure, which convolutes various broadening effects described by Fourier coefficients in real space or by intensity profiles in reciprocal space. The **instrumental function** is by defaul treated by this kernel. More detailed description of the instrumental broadening can be found in section A.7.
   Some type of a convolutional procedure is implemented in all three programs: PM2k, CMWP-fit, MAUD; the effect is of an auxiliary type.

2. **Arbitrary texture** model as known from MAUD is better described in section A.9. It enables arbitrary corrections of reflection intensities calculated from the crystal structure.
   The effect can be found in all three programs: PM2k, CMWP-fit, MAUD; and as the effect is "unphysical" it must be considered as an auxiliary feature.

3. **Texture calculator & simple texture models** enables intensity corrections using measured or model crystallites orientation distribution function, or some other type of simpler texture correction suitable also for thin films and possible to apply in asymmetrical diffraction geometries.
   This can be found basically only in MAUD, which is a very useful tool in this field; the effect is "physical", it is rather still under *development*, but results presented at Size-Strain V (2007) and also in [231].

4. **Pseudo-Voigt function**, which width and shape dependence on the diffraction angle (2θ) is described by some polynomials, can be in addition convoluted with the instrumental function and with other effects. In section A.8 this is for example used to include a phenomenological microstrain effect.
   Something very similar is possible also in PM2k or MAUD; the effect is rather auxiliary.

5. **Spherical crystallites model with log-normal size distribution** was described widely in section 4.3.1 (p.85). PM2k, CMWP-fit, MAUD; physical effect.

6. **Histogram size distribution** model was used in section 4.5.2 (p. 115). Only in PM2k; physical effect.

7. **Dislocation broadening** was described in section 3.3 (p. 74). PM2k, CMWP-fit; physical effect.

8. **Planar faults in fcc crystals** were described also in section 3.3 (p. 74). PM2k, CMWP-fit; physical effect; in MSTRUCT both the approaches in [11, 13] and [99] are available.

9. **Additional (*hkl*) peak dependent broadening** enables to convolute an additional pseudo-Voigt function to any peak. The width, shape and position parameter of the function can be specific for a particular reflection. In section 3.3 this effect was used to introduce additional shifts, without peak broadening, of individual reflections.
   Can be done also in PM2k; auxiliary effect.

10. **Interface to sum different broadening effects** make it possible to e.g. combine two log-normal size distribution effects with crystallites of different sizes to model a bimodal size distribution. The fraction of large and small crystallites is then refined.
    Possible also in PM2k; auxiliary effect.

11. **Thin film absorption correction** accounts correctly for absorption in the coplanar grazing incidence geometry suitable for thin film analysis (see ch. A.6).
    Available in MAUD; physical effect.

12. **Residual stress correction** accounts for reflections shifts due to a simple residual stress state in the films (ch. A.5).
    More models can be found in the MAUD; physical effect.

13. **Refraction correction** accounts for reflections shift due to an x-ray refraction effect at the film interface (ch. A.5).
    Available probably only in the MSTRUCT; physical effect.

It must be noted that the list concerns only effects, which are implemented in the MSTRUCT. The PM2k [24] is a very flexible program as it is partially almost a programming environment to model various phenomena in powder diffraction patterns. In the CMWP-fit [110] many microstructural effects concerning mainly some defects very common in metals are implemented, which cannot be found elsewhere and in the MAUD many unique features concerning mainly texture and stress are implemented.

In the following sections, a few features from the list above will be described in greater detail. In particular, those for thin films analysis and those explicitly mentioned in the main text.

A.4 Refraction correction

In addition to bulk nanocrystalline TiO_2 nanopowders also titania films were investigated by XRD.[1] During testing the possibilities of the coplanar grazing exit (GE) geometry (Matěj et al. [235]) in principle the same as the grazing incidence (GI) case — for an investigation of such thin film samples it was found that diffraction lines are systematically shifted from their regular positions. See fig. A.3, where for higher angles ω, which correspond to lower exit angles $\alpha = 2\theta - \omega$, diffracted intensity is clearly shifted to higher diffraction angles (2θ). The shift is clearly visible especially close to the critical angle (α_c) of the total external reflection at the film and it depends on the exit/incidence angle (α) — in the GI geometry $\alpha = \omega$ in fig. 2.1 (p. 10) or fig. A.4 here. The effect is related to the refraction of x-rays at the interface between the air (vacuum) and the film. It was studied beside others by Lim et al. [250], Hart et al. [251], Toney and Brennan [252], Noma et al. [253] or later by Colombi et al. [254, 255].[2] It can be easily accounted for by using the Snell's law at the interface [252–254]

$$\Delta 2\theta = \alpha - \frac{1}{\sqrt{2}}\sqrt{(\alpha^2 - 2\delta) + \sqrt{(\alpha^2 - 2\delta)^2 + 4\beta^2}}\,, \tag{A.1}$$

where δ and β are the real and the imaginary parts of the refractive index of the film ($n = 1 - \delta - i\beta$). It is assumed here that the second angle (exit or incidence) is high. Then the correction is not a function of the diffraction angle (2θ). It depends only on the material of the film and the angle α. For a typical anatase film ($\chi_0 = -2.30 \cdot 10^{-5} - i\,1.16 \cdot 10^{-6}$, $n \approx 1 + \chi_0/2$) the critical angle is $\alpha_c \approx \sqrt{2\delta} \doteq 0.27°$ and the 2θ shifts are

$$\begin{aligned}
\Delta 2\theta &\doteq 0.25°\,, \quad \text{for} \quad \alpha = 0.27°\,,\\
\Delta 2\theta &\doteq 0.09°\,, \quad \text{for} \quad \alpha = 0.5°\,,\\
\Delta 2\theta &\doteq 0.04°\,, \quad \text{for} \quad \alpha = 1.°\,.
\end{aligned}$$

Modern laboratory x-ray diffractometers dedicated for thin films analysis are usually equipped with x-rays mirrors producing quite parallel x-ray beam with relatively small divergence. Hence the use of such low incidence angles (α) as above is quite common. In the MFF laboratory the standard characterisation of e.g. TiO_2 films is done with the incidence angle $\alpha = 0.5°$. This gives the shift almost $\Delta 2\theta \approx 0.1°$ only due to refraction. It is usually less, because the film is less dense, but even then this is a significant effect. Usually a 2θ scan with a constant incidence angle ($\omega = \alpha$) is measured and hence principally the shift due to refraction is constant in such an experiment, it can be corrected in any Rietveld program by a "zero shift error". However, this is at least unpleasant from two reasons: (i.) the "zero error" value will be unrealistically high and (ii.) it

[1]The present author would like kindly acknowledge here prof. J. Musil, Dr. J. Šícha and D. Heřman from the Faculty of Applied Sciences at the University of West Bohemia and M. Morozová and S. Krejčíková from the group of Dr. O. Šolcová from the Institute of Chemical Process Fundamentals, AS ČR for providing the thin films samples.

[2]The present author would like to express his thanks to J. Drahokoupil from the Institute of Physics, AS ČR, for supplying many useful references here.

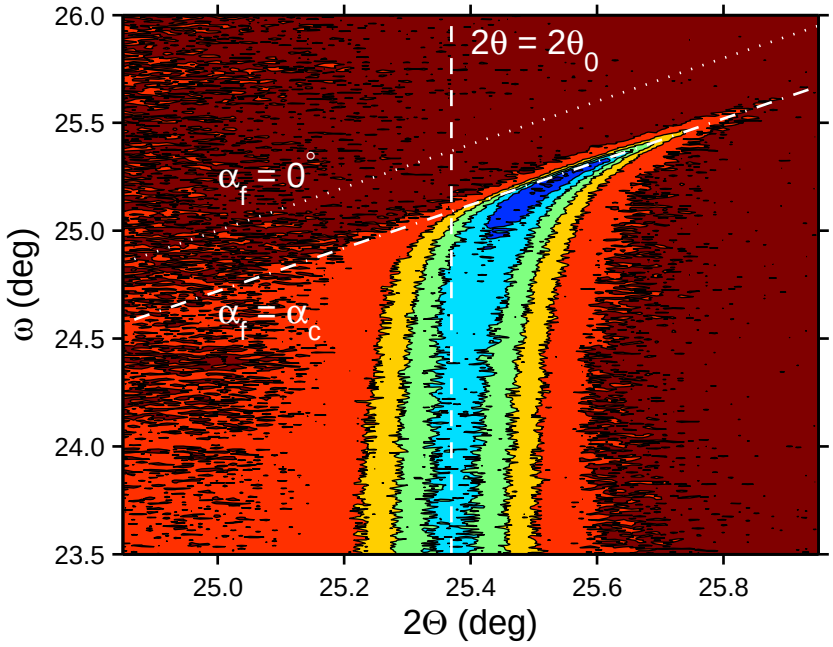

Figure A.3: Part of the measured intensity distribution map around the anatase 101 reflection of a magnetron sputtered TiO_2 thin film, approximately 50 nm thick. The map was measured in the grazing exit geometry [235]. Some lines of constant exit angle ($\alpha = 2\theta - \omega$) are plotted for orientation. $2\theta_0$ denotes the regular reflection position, α_c is the critical angle of total external reflection.

will change strongly when a different incidence angle is used or a material with different refraction index (n) is studied. In Matěj [256] there is an example of the diffraction pattern of TiO_2/ITO electrode (ITO . . . tin doped indium oxide). ITO has relatively high electron density — critical angle $\alpha_c \approx 0.35°$. This means that at $\alpha = 0.5°$ even higher 2θ correction is required for ITO reflections. Moreover the corrections for anatase (TiO_2) and ITO peaks are different. Such case is difficult to treat in an ordinary Rietveld software, because the "zero error" is considered as an instrumental effect similar for all the crystalline phases in the diffraction pattern.

The effect can be accounted for by using e.g. eq. A.1 and this is included in the MSTRUCT. The necessary information is the refraction index (n) or the electric susceptibility (χ_0). It can be calculated for a given radiation and material from its chemical composition and its density using e.g. web application of Stepanov [148] or it can be estimated directly in the MSTRUCT from the crystal structure. The effect is not included by default, but need to be activated for each crystalline phase individually by the following code

```
// the 1st phase - Refraction reflection position correction
RefractionCorr  refractionCorrAnatase   effect type, effect name
crystal                                 chi0 calculated from - crystal
1.                                      relative density
```

The codeword `"RefractionCorr"` specifies the effect. The codeword `"crystal"` tells that the susceptibility (χ_0) should be calculated from the crystal structure. A single parameter of the model is "relative density" (n_r) of the material, which

is set at the last line.

The relative density (n_r) can be refined from x-ray data, but it is not recommended if only a single scan is available. The parameter correlates absolutely with the 2θ "zero error". Instead a simple recipe can be advised. During the specimen alignment in the parallel beam geometry often the x-ray reflectivity from the sample can be measured. Such an experiment is usually not too time demanding and at least the critical angle of the film (α_c^{exp}) can be roughly determined from the reflectivity curve. The MSTRUCT gives in its output an information about the critical angle ($\alpha_c^{\mathrm{theor}}$) calculated for a film with the full density ($n_r = 1$).

```
MStruct::RefractionPositionCorr::GetChi0(...): ...
           ...   Chi0 and absolute density computed for Crystal: AnataseITF
chi0: (-2.3988e-05,-1.2128e-06) (n=1-delata-ii*beta~=1+chi0/2)
critical angle: 0.28(deg)
density:  3.892 (g/cm3)
```

It can be shown that the correct relative density should then be set to

$$n_r \approx \left(\frac{\alpha_c^{\mathrm{exp}}}{\alpha_c^{\mathrm{theor}}} \right)^2 .$$

Despite its relative simplicity the refraction correction is not commonly included in the software for powder diffraction analysis. However the correction has proved itself to be useful for particular samples as well in connection with the residual stress effect, which is described in the section A.5.

A.5 Residual stress correction

Residual stresses can be found in both bulk materials as well as thin films. They were found also in a particular series of TiO_2 thin film samples studied in the department (Nichtová [129], Kužel et al. [257, fig. 6]). Moreover diffraction line shift due to these stresses showed a very strong anisotropy (hkl dependence). The films were amorphous, as deposited by magnetron sputtering, and after annealing at $\approx 250°C$ (Nichtová [129]) they crystallised into the anatase form. Single crystal elastic constants of anatase were not known at that time (2005)[1] and hence it was difficult to treat the anisotropy. However, after some time, at least calculated values from ab initio simulation were reported [258–261], which could explain the anisotropy of XRD data very well (Matěj et al. [190]) on the basis of a classical Reuss-Voigt stress model (e.g. [262] and references therein). In Nichtová [129] and Matěj et al. [190] dedicated XRD stress measurements using an Eulerian cradle and parallel beam polycapillary optics were done, but the effect is principally present also in basic 2θ-scans with the constant small incidence angle ($\alpha = \omega$).

As it can be seen in a schematic figure A.4 in such an experiment the lattice planes diffracting at the angle $2\theta_{hkl}$ are inclined from the sample surface by an angle $\psi_{hkl} = \theta_{hkl} - \omega$. Reflections in the pattern carry information about lattice spacing (d_{hkl}), from the crystallites differently oriented with respect to the sample. This is a basis of the residual stress diffraction measurements.

[1] The theoretical work of Sato et al. [258] (2003) was missed.

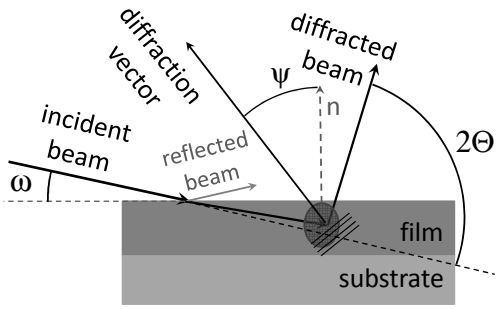

Figure A.4: Scheme of a parallel beam geometry experiment. X-rays come from the left side and impinge the sample surface at the incidence angle ω. Intensity is measured at the diffraction angle 2θ from a direction of the incident x-ray beam. Normals of diffracting lattice planes take an angle $\psi = \theta - \omega$ from the sample surface normal. In the figure also the refraction of the incident beam is indicated. Lengths of vectors have not correct scale, see fig. 2.1 for the right reciprocal space construction.

It was found [190] that it is sufficient to consider a very simple homogeneous bi-axial stress state in the samples. Only components of the stress tensor in the plane parallel to surface are assumed to be nonzero and the problem is in addition rotationally symmetric. If the z-axis is parallel to the sample surface normal the stress tensor has a form

$$\boldsymbol{\sigma} = \begin{pmatrix} \sigma & & \\ & \sigma & \\ & & 0 \end{pmatrix} , \tag{A.2}$$

where all nondiagonal components are zero. Then, under a hypothesis of Voigt or Reuss [262, 263] about the grain interaction in the sample, the relative change of lattice spacing measured by diffraction due to the stress can be written as [262]

$$\begin{aligned} \varepsilon_{hkl,\psi} &= \frac{d_{hkl}(\psi) - d_{hkl}^{\sigma-\mathrm{free}}}{d_{hkl}^{\sigma-\mathrm{free}}} \\ &= \frac{1}{2} S_2(hkl)\, \sigma \sin^2 \psi + 2 S_1(hkl)\, \sigma \ , \end{aligned} \tag{A.3}$$

where $S_1(hkl)$ and $S_2(hkl)$ are the so called x-ray elastic constants (XECs) and $d_{hkl}^{\sigma-\mathrm{free}}$ is the "stress-free" lattice spacing, which can be calculated from the "stress-free" lattice constants. The XECs are generally hkl dependent. Using eq. A.2 and the Bragg equation

$$1/d_{hkl} = 2 \sin \theta_{hkl} / \lambda \ ,$$

the residual stress (σ) can be determined from diffraction data if the XECs (S_1, S_2) are known. The peak shifts in the "2θ-scan" diffraction pattern can accounted as well. This is done in the MSTRUCT by the `"StressSimple"` correction. This correction requires a XECs calculator. Two models are available: (i) a `"isotropic"`, which calculates XECs from the Yong's modulus and the Poisson ratio, but it is not able to account for elastic anisotropy, and (ii) a `"Reuss-Voigt"` XECs calculator using single crystal elastic constants.

Expressions for any crystal symmetry can be found in Behnken and Hauk [264], but in the MSTRUCT rather a general formalism of Popa [263] is used in the `"Reuss-Voigt"` XECs calculator.

To calculate XECs (S_1^{V} and S_2^{V}) in the Voigt model we can use directly [263,

eqs. 12a-b] and calculate the isotropic Voigt stiffness constants

$$C_{11}^{\mathrm{V}} = (C_{11} + C_{22} + C_{33})/5 + 2(C_{12} + C_{13} + C_{23} + 2C_{44} + 2C_{55} + 2C_{66})/15 \ ,$$
$$C_{12}^{\mathrm{V}} = (C_{11} + C_{22} + C_{33} - 2C_{44} - 2C_{55} - 2C_{66})/15 + 4(C_{12} + C_{13} + C_{23})/15 \ ,$$

which can be converted using [263, eqs. 30a-b] to the compliance constants

$$S_{11}^{\mathrm{V}} = \frac{C_{11}^{\mathrm{V}} + C_{12}^{\mathrm{V}}}{C_{11}^{\mathrm{V}}(C_{11}^{\mathrm{V}} + C_{12}^{\mathrm{V}}) - 2(C_{12}^{\mathrm{V}})^2} \ ,$$
$$S_{12}^{\mathrm{V}} = \frac{-C_{12}^{\mathrm{V}}}{C_{11}^{\mathrm{V}}(C_{11}^{\mathrm{V}} + C_{12}^{\mathrm{V}}) - 2(C_{12}^{\mathrm{V}})^2}$$

and finally assuming the simple stress state in eq. A.2, $\boldsymbol{B} = (\sin\psi, 0, \cos\psi)$ in [263] and by simplifying [263, eqs. 29] we finally get XECs for the Voigt model

$$2S_1^{\mathrm{V}} = 2S_{12}^{\mathrm{V}} \ ,$$
$$1/2 \ S_2^{\mathrm{V}} = (S_{11}^{\mathrm{V}} - S_{12}^{\mathrm{V}}) \ .$$

For the calculation of XECs within the Reuss model it is suitable to specify more in detail, how the stiffness (C_{ij}) and compliance tensors (S_{ij}) are defined in the reduced notation ($\varepsilon_{11} \leftrightarrow \epsilon_1$, $\varepsilon_{12} \leftrightarrow \epsilon_6$, $\sigma_{12} \leftrightarrow \sigma_6$) in Popa [263]. In [263] it holds

$$\epsilon_i = \sum_{j=1}^{6} S_{ij}\rho_j\sigma_j \ , \quad \sigma_i = \sum_{j=1}^{6} C_{ij}\rho_j\epsilon_j \ ,$$
$$\text{where} \quad \boldsymbol{\rho} = (1,1,1,2,2,2) \ .$$

The last equation for C_{ij} is the conventional Hook's law used e.g. in Nye [265] and the equation above implies that in this notation (Popa [263]) the compliance values S_{ij} can be obtained from an inversion of the symmetric "block" C_{ij} matrix

$$S_{ij} = (\rho_i \, C_{ij} \, \rho_j)^{-1} = \begin{pmatrix} C_{11} & \cdots & C_{13} & 2\cdot C_{14} & \cdots & 2\cdot C_{16} \\ & \ddots & \vdots & \vdots & \ddots & \vdots \\ & & C_{33} & 2\cdot C_{34} & \cdots & 2\cdot C_{36} \\ & & & 4\cdot C_{44} & \cdots & 4\cdot C_{46} \\ & & & & \ddots & \vdots \\ & & & & & 4\cdot C_{66} \end{pmatrix}^{-1} \ .$$

In [263] few other auxiliary vectors are defined

$$\boldsymbol{\delta} = (1,1,1,0,0,0) \ ,$$
$$\boldsymbol{E}(hkl) = (q_1^2, q_2^2, q_3^2, q_2q_3, q_3q_1, q_1q_2) \ ,$$

where q_i are directional cosines of the $\{hkl\}$ diffracting lattice plane normals in the coordinate system of the crystal. With all the above definitions, in the simplified case here, using Popa [263, eqs. 8, 13, 2a, 3a, 7] we can write for XECs

$(S_1^{\mathrm{R}},\, S_2^{\mathrm{R}})$ within the Reuss model

$$2S_1^{\mathrm{R}}(hkl) = \sum_{i,j=1}^{6} E_i\rho_i\; S_{ij}\; \rho_j(\delta_j - E_j)\ ,$$
$$1/2\; S_2^{\mathrm{R}}(hkl) = \frac{1}{2}\sum_{i,j=1}^{6} E_i\rho_i\; S_{ij}\; \rho_j(3E_j - \delta_j)\ .$$

The theoretical paper of Popa [263] describes much more general case, but here the simplification is sufficient.

The Reuss and Voigt grain interaction models are limiting cases and the real case is often somewhere between. Hence it is quite common to take the XECs constants as an average of the Voigt and Reuss values

$$S_1(hkl) = w_\sigma \cdot S_1^{\mathrm{v}} + (1 - w_\sigma) \cdot S_1^{\mathrm{R}}(hkl)\ ,$$
$$S_2(hkl) = w_\sigma \cdot S_2^{\mathrm{v}} + (1 - w_\sigma) \cdot S_2^{\mathrm{R}}(hkl)\ .$$

The model has two parameters: the stress (σ) and the Voigt model weight (w_σ).

Using the above recipe the residual stress peak position correction is accounted for in the MSTRUCT for crystal phases of any symmetry. The effect is activated with the following code.

```
// the 1st phase - Residual stress correction - simple stress model
StressSimple  stressCorrAnatase     effect type,effect name
Reuss-Voigt   0.                    XECs model, stress (GPa)
// material C11 C12 C13 C33 C44 C66 constants (in GPa) ...
//                  ... - in the format: C11 "value" C12 "value" etc.
C11 320  C12 151  C13 143           // anatase Cij (GPa)
C33 190  C44  54  C66  60           // ref:M.Iuga,Eur.Phys.J.B(2007)58,127-33
0.0                                 model weight (0..Reuss, 1..Voigt)
```

At first the effect is activated by a codeword `"StressSimple"` and a name for the effect in the running instance is given. At the second line it is specified that the `"Reuss-Voigt"` model for XECs is used and the stress (σ) is set initially set to zero. Due to the choice of the anisotropic model single crystal elastic constants are required. Program generates a list of required stiffness constants (C_{ij}) considering the crystal symmetry. The values from the literature (Iuga et al. [259]) are set. At the last line, the Voigt model weight (w_σ) is specified.

The described model was successfully applied to the analysis of the already mentioned particular series of TiO_2 thin films in Matěj, Kužel, and Nichtová [190]. The XECs were calculated using the above schema for a particular case of tetragonal symmetry of anatase (Laue group $4/mmm$). The whole powder pattern fitting/modelling including the residual stress correction was also applied to the same series of samples (in Matěj et al. [236]). It was difficult to determine both model parameters unambiguously solely from a single 2θ scans, measured in the range $2\theta = 15° - 145°$, which implies the range of $\psi \approx 10° - 70°$. Since it was clear that rather the Reuss model is appropriate to fit the data, the Voigt model weight was fixed at a constant value $\sigma = 0.3$. Then it was quite straightforward to refine the stress value (σ) for each sample. The inclusion of the stress correction improved fits significantly. The stresses in the films were between 200–800 MPa.

The values refined from the 2θ-scans showed relatively large uncertainties, but were not distinct from the results of the dedicated stress measurements [190] by more than 50–100 MPa. It must be emphasised that the refraction correction (ch. A.4) played a crucial role in the analysis. It was because in the case of the residual stress determination from such single 2θ scans, an uncertainty in the "zero error" implies a large error in the analysis. The correction for refraction reduced the "zero error" by an order of its size below $\pm 0.01°$. More detils can be found in [236].

A.6 Absorption correction

Absorption correction for a simple 2θ-scan in a parallel beam geometry with constant incident angle (fig. A.4) is not directly available in many Rietveld programs despite the fact that its basic variant is very simple.

In the conventional theory of powder diffraction it is assumed that x-rays are absorbed at their path through the sample (fig. A.4). The linear absorption coefficient (μ) is a measure of this effect. It is related to the imaginary part of the electric susceptibility as

$$\mu = \frac{2\pi}{\lambda} |\chi_{0,im}|$$

and for the given material it can be calculated using the web application of Stepanov [148] or from the χ_0 value calculated by the MSTRUCT using the refraction correction calculator (ch. A.4).

If the absorption at the path of both the incident as well as the diffracted beam in the sample is considered, the intensity contribution from a film of the thickness T with the absorption coefficient μ is given by (e.g. Šimek et al. [266])

$$I = \frac{T_p}{\sin(\omega)} \left[1 - \exp(-T/T_p)\right] \ , \tag{A.4}$$

where ω is the incidence angle and T_p is the *penetration depth*, for which it holds

$$\frac{1}{T_p} = \mu \left[\frac{1}{\sin(\omega)} + \frac{1}{\sin(2\theta - \omega)} \right] \ .$$

In the parallel beam geometry with a constant incidence angle (ω) the penetration depth (T_p) is almost constant with the diffraction angle (2θ) (see e.g. Dopita [128] or [127, fig. 4] for the TiO_2 case) and decreases with ω. In the symmetrical Bragg-Brentano geometry ($\omega = \theta$) the penetration depth increases with $\sin(\theta)$, whereas the first factor in eq. A.4, which accounts for an irradiated sample length, decreases. This gives for an infinitely thick sample in the Bragg-Brentano geometry a constant absorption correction

$$I_{\infty,\mathrm{BB}} = \frac{1}{2\mu} \ . \tag{A.5}$$

The absorption effect in the MSTRUCT is a part of standard description of each effect and it is set using the following line of code. Scattering geometry is specified elsewhere, in the instrumental part (ch. A.7).

```
// the 1st phase - thin film absorption correction (TiO2, density=3.75g/cm3)
-1.e4   0.  470.    absorp corr: thickness(nm), depth(nm), abs.factor(1/cm)
```

Here the first and third parameter are important. The third parameter is the absorption coefficient (μ) in the (1/cm) units and the first parameter is the film thickness (T) in nanometres. It is surprisingly a negative value here, which denotes that the film/substrate of the given material is infinitely thick. This is important to specify for bulk samples and especially for the Bragg-Brentano geometry. The correction A.4 is used also in this geometry and if only some very large but a finite value of the sample thickness is set, the value can either be too small, which strongly affects e.g. refinement of temperature factors, or it can unnecessarily introduce a numerical instability.

In the above way the absorption correction is implemented in the MSTRUCT. Unfortunately, there are another problems of physical basis. The correction A.4 is valid only for incidence angles $\omega \gg \alpha_c$. This is indicated in a detail of the fig. A.4. Again the refraction of x-rays (ch. A.4) must be included for incidence/exit angles (α) close to the critical angle (α_c). This can be done by an appropriate modification of the expression for the penetration depth (T_p) [235, 255]. The second problem concerns a detail in the map in fig. A.3. There can be seen an intensity maximum close to the critical exit angle (line $\alpha = \alpha_c$). It was shown in literature [267, 268] and later by Colombi et al. [255] that this effect comes from the maximum in the Fresnel coefficients of the interface. Hence its origin is similar to the well known "Yoneda wings" in the nonspecular x-ray reflectivity. The effect is well known in the theory of scattering from the epitaxial thin films and layers (Holý et al. [34]). The appropriate correction can be found also in the paper of the present author [235], where the theory was applied to a series of TiO_2 thin films and the films thicknesses were determined from XRD data as in fig. A.3.

A.7 Instrumental broadening

The instrumental function is described by an analytical function in the reciprocal space rather than in the angular one. This should be similar rather to the original PM2000 [104], description in the original article by Scardi and Leoni [102] or the author's diploma thesis [26, ch. 2.5], than to conventional Rietveld programs. But the real distinction is very small. In this convention the profile is described by the pseudo-Voigt function defined as

$$I(s) = (1-\eta) \cdot \exp\left(-\ln 2\,\frac{s^2}{\sigma^2}\right) + \eta \cdot \left(1 + \frac{s^2}{\sigma^2}\right)^{-1}, \qquad \text{(A.6)}$$

where $s = q/2\pi \approx \Delta 2\theta(\mathrm{rad}) \cdot \cos(\theta)/\lambda$ is the reciprocal space variable in $1/d$ units, η is a shape parameter and σ is a half-width parameter.

It is mentioned in the main text that the profile functions (as e.g. A.6) are usually fitted to reflections of a measured profile standard and the angular dependence of width and shape parameters is described by suitable polynomials. In

the MSTRUCT parameters of A.6 are described as

$$\sigma = \frac{FWHM_{2\theta}(deg)}{2} \cdot \frac{\pi}{180} \cdot \frac{\cos(\theta)}{\lambda} \ , \tag{A.7a}$$

$$FWHM^2_{2\theta}(deg) = W + U \cdot \tan^2(\theta) + V \cdot \tan(\theta) \ , \tag{A.7b}$$

$$\eta = \eta_0 + \eta_1 \cdot 2\theta(rad) \ , \tag{A.7c}$$

$$A = \begin{cases} A_0 + A_1/\sin(2\theta) + A_2/\sin^2(2\theta) & \text{when} \quad 2\theta \leq 2\theta_{\text{AsymMax}} \ , \\ 1 & \text{when} \quad 2\theta > 2\theta_{\text{AsymMax}} \ , \end{cases} \tag{A.7d}$$

where eq. A.7d introduces another parameter describing an asymmetry of diffraction profiles for diffraction angles (2θ) lower than a fixed angle $2\theta_{\text{AsymMax}}$.

When disregarding a few negligible differences, the instrumental profile description is the same in the MSTRUCT as in the most of Rietveld programs. But the typical feature of the WPPM programs is a "true" convolution of all the effects.

The effect is included in the MSTRUCT by default and it is described by the following code.

```
// Instrumental Parameters
// ... -1.0: 2Theta/Theta scan, -2.0: 2Theta/Theta scan with variable slits
-2.0                            incidence angle (deg) - 2Theta scan
// Instrumental Parameters (MPD-pixcel: inc-0.02rad, det-0.04rad, 5mm x 5mm)
2.463e-3  2.654e-3  -1.201e-3   instrumental profile params (W,U,V)
0.47  0.18                      instrumental profile params (Eta0,Eta1)
0.86  0.22  0.  60.             instrumental profile params (Asym0,Asym1, ...
//                                      ... Asym2,Asym2ThetaMax(deg))
Cu      0.0                     wavelength type (Cu,CuA1), ...
// ... linear polarization rate (A=0.8,f=(1-A)/(1+A)=0.36 graphite mon., ...
//                                  ... f=0. unmonochromatized)
```

At first line the incidence angle (ω) is specified. It is a fixed positive number for a 2θ-scan. If it is a negative number, it is an indication of asymmetric scan in the Bragg-Brentano geometry. If it is equal or less than -2, it is in addition assumed that variable slits are used. The coefficients of polynomials A.7b–A.7d are set at next few lines. The last line contains a mark (`"Cu"`) saying that CuK_α doublet radiation is used. It is also specified at the same line that radiation is unpolarised $f = 0$. If a graphite monochromator for the Cu-radiation were used, the rate would be $f = 0.36$.

A.8 Phenomenological strain broadening

A *phenomenological strain broadening* is actually not a feature of the MSTRUCT. However, it can be simulated in the MSTRUCT using a possibility to convolute various types of effects. We can take the same pseudo-Voigt as for the instrumental function in section A.7. We let all the polynomial coefficients with exception of U and η_0 to be zero. In addition $A_0 = 1$, because we require a symmetrical profile. Such an effect can be loaded as any other effect. The codeword for the pseudo-Voigt function, which we want to add, is `"pVoigtA"`.

```
// the 1st phase - Strain broadening - modeled by pseudoVoigt function
// - only U-Cagliotu param. (W=V=0.) and shape Eta0 (Eta1=0.) params. refined
pVoigtA  strainProfAnatase  broadening component type, effect name
0.  0.  0.                  profile params (W,U,V)
0.  0.                      profile params (Eta0,Eta1)
1.  0.   0.   60.           profile params (Asym0,Asym1,Asym2,Asym2ThetaMax)
```

The U and η_0 parameters are zero here. They are set later in the program input (See [225] for more details).

Parameter η_0 drives the profile shape. It is Gaussian for $\eta_0 = 0$ and pure Lorentzian for $\eta_0 = 1$. The parameter U is related to the profile width (eq. A.7b)

$$FWHM_{2\theta}(deg) = \sqrt{U} \cdot \tan(\theta) \ .$$

For the integral breadth (β) of the profile A.6 we can write

$$\beta = \frac{\int I(s)ds}{I(0)} = 2\sigma \left[\frac{1-\eta}{\varphi_G} + \frac{\eta}{\varphi_C} \right] \ ,$$

where $\varphi_G = 2\sqrt{\ln(2)/\pi}$ and $\varphi_C = 2/\pi$ are the Gaussian and Lorentzian shape parameters. If we substitute from eq. A.7a and compare the result with the expression for the integral breadth from Wilson [269, p. 5] or Klug and Alexander [5, eq. 9-80]

$$\beta_{2\theta}(rad) = 4e \cdot \tan(\theta) \ ,$$

where e is the microstrain parameter, we obtain an equivalence

$$4e = \left[\frac{1-\eta}{\varphi_G} + \frac{\eta}{\varphi_C} \right] \cdot \sqrt{U} \cdot \frac{\pi}{180} \ . \tag{A.8}$$

The model [229, 236] now has two parameters: (i) the shape parameter of the strain distribution (η_0) and (ii) the microstrain (e) related to the Caglioti coefficient (U) and the shape parameter (η_0) by eq. A.8.

A.9 HKL Intensities corrections

When intensities of diffraction lines are not of a primary interest or in cases of complicated texture in the sample, it is suitable to have an option to break the relation between intensities and crystal structure. In the MAUD [106] it is possible in the so called *arbitrary texture model*. In the MSTRUCT it can be realised using *HKL Intensities corrections*. This effect is rather auxiliary and unphysical. Intensities of reflections in the diffraction pattern are still calculated from the crystal structure and corrected for other effects, but with this correction intensity of an arbitrary *hkl* reflections can be multiplied by a factor, which can be even fitted.

The effect is described in the input file by a single line, where two switches can be found. The second one only controls if the corrections should be also printed at the end of the refinement. This can be useful for later storage of results. The first switch drives the effect.

```
// HKLIntensities corr. - Arbitrary texture model
3   0              hkl file(0-not use,1-generate,2-free all,3-read), ...
//                                  ... print HKLIntensities(0-no,1-yes)
```

If it is set to "zero", nothing is done and no intensities are affected. If it is set to "one" a file with name `"Ihkl_DiffDataName.dat"` is generated, where `"DiffDataName"` is the name in the program assigned to the given crystalline phase (e.g. `"diffData_Anatase"`). The generated file contains a list of peaks.

```
#    h   k   l   2Theta(deg)    |Fhkl|^2        Icor   fixed
     1   0   1         25.316    2.62e+04        1.00       1
     1   0   3         36.996    3.39e+03        1.00       1
     0   0   4         37.868    1.33e+04        0.92       0
     1   1   2         38.592    3.93e+03        1.00       1
     2   0   0         48.049    3.04e+04        1.00       1
```

Informations about reflections indexes and 2θ positions are included, but the last two columns are the most important. The second column from the end (`"Icorr"`) contains the intensity correction factor each *hkl* reflection. By this factor its regular intensity is multiplied. The last column is a refinement flag for the factor. If it is unfixed (`"fixed=0"`) it is refined by the program.

The file itself has no real effect on the results if the option in the input parameter file above is not set to a higher value than "one". If it is set to "three", the information in the file is loaded by the program and the corrections are used/refined. If it is set to "two", the file is generated similarly as in the case "one", but intensities correction are unfixed by default for all reflections. In such case it is highly recommended to fix all the other parameters affecting diffraction line intensities, including crystal structure parameters and scale factors.

Bibliography

[1] R. Z. Valiev, R. K. Islamgaliev, and I. V. Alexandrov. Bulk nanostructured materials from severe plastic deformation. *Progress in Materials Science*, 45(2):103 – 189, 2000. ISSN 0079-6425. doi: DOI:10.1016/S0079-6425(99)00007-9, ►.

[2] Prashant K. Jain, Kyeong Seok Lee, Ivan H. El-Sayed, and Mostafa A. El-Sayed. Calculated absorption and scattering properties of gold nanoparticles of different size, shape, and composition: applications in biological imaging and biomedicine. *The Journal of Physical Chemistry B*, 110(14): 7238–7248, 2006. doi: 10.1021/jp057170o, ►. PMID: 16599493.

[3] Nikolai G. Khlebtsov. Determination of size and concentration of gold nanoparticles from extinction spectra. *Analytical Chemistry*, 80(17):6620–6625, 2008. doi: 10.1021/ac800834n, ►.

[4] Andrew Mills and Stephen Le Hunte. An overview of semiconductor photocatalysis. *Journal of Photochemistry and Photobiology A: Chemistry*, 108(1):1 – 35, 1997. ISSN 1010-6030. doi: DOI:10.1016/S1010-6030(97)00118-4, ►.

[5] Harold Philip Klug and Leroy E. Alexander. *X-Ray Diffraction Procedures: For Polycrystalline and Amorphous Materials*. John Wiley & Sons, Inc., 2nd edition, 1974.

[6] Bertram Eugene Warren. *X-ray diffraction*. Metallurgy and Materials. Addison-Wesley, 1969.

[7] H. M. Rietveld. A profile refinement method for nuclear and magnetic structures. *Journal of Applied Crystallography*, 2(2):65–71, Jun 1969. doi: 10.1107/S0021889869006558, ►.

[8] Juan Rodríguez-Carvajal. Recent advances in magnetic structure determination by neutron powder diffraction. *Physica B: Condensed Matter*, 192(1-2):55 – 69, 1993. ISSN 0921-4526. doi: DOI:10.1016/0921-4526(93)90108-I, ►.

[9] Allen C. Larson and Robert B. Von Dreele. General structure analysis system (gsas). Technical Report LAUR 86-748, Los Alamos National Laboratory, 1994.

[10] Paolo Scardi and Matteo Leoni. Line profile analysis: pattern modelling *versus* profile fitting. *Journal of Applied Crystallography*, 39(1):24–31, Feb 2006. doi: 10.1107/S0021889805032978, ►.

[11] P. Scardi and M. Leoni. Whole powder pattern modelling. *Acta Crystallographica Section A*, 58(2):190–200, Mar 2002. doi: 10.1107/S0108767301021298, ►.

[12] Matteo Leoni and Paolo Scardi. Nanocrystalline domain size distributions from powder diffraction data. *Journal of Applied Crystallography*, 37(4): 629–634, Aug 2004. doi: 10.1107/S0021889804013366, ►.

[13] L. Velterop, R. Delhez, Th. H. de Keijser, E. J. Mittemeijer, and D. Reefman. X-ray diffraction analysis of stacking and twin faults in f.c.c. metals: a revision and allowance for texture and non-uniform fault probabilities. *Journal of Applied Crystallography*, 33(2):296–306, Apr 2000. doi: 10.1107/S0021889800000133, ►.

[14] Levente Balogh, Gábor Ribárik, and Tamás Ungár. Stacking faults and twin boundaries in fcc crystals determined by x-ray diffraction profile analysis. *Journal of Applied Physics*, 100(2):023512, 2006. doi: 10.1063/1.2216195, ►.

[15] Tamás Ungár, Levente Balogh, and Gábor Ribárik. Defect-related physical-profile-based x-ray and neutron line profile analysis. *Metallurgical and Materials Transactions A*, 41:1202–1209, 2010. ISSN 1073-5623, ►. 10.1007/s11661-009-9961-7.

[16] T. Ungár and A. Borbély. The effect of dislocation contrast on x-ray line broadening: A new approach to line profile analysis. *Applied Physics Letters*, 69(21):3173–3175, 1996. doi: 10.1063/1.117951, ►.

[17] P. Klimanek and R. Kužel. X-ray diffraction line broadening due to dislocations in non-cubic materials. I. General considerations and the case of elastic isotropy applied to hexagonal crystals. *Journal of Applied Crystallography*, 21(1):59–66, Feb 1988. doi: 10.1107/S0021889887009580, ►.

[18] M. Wilkens. The mean square stresses $\langle\sigma^2\rangle$ for a completely random and a restrictedly random distribution of dislocations in a cylindrical body. In John A. Simmons, R. de Wit, and R. Bullough, editors, *Fundamental aspects of dislocation theory*, volume 317, II, pages 1191–1193. U.S. National Bureau of Standards, 1970.

[19] M. Wilkens. Theoretical aspects of kinematical x-ray diffraction profiles from crystals containing dislocation distributions. In John A. Simmons, R. de Wit, and R. Bullough, editors, *Fundamental aspects of dislocation theory*, volume 317, pages 1195–1221. U.S. National Bureau of Standards, 1970.

[20] Mikhail A. Krivoglaz. *X-Ray and Neutron Diffraction in Nonideal Crystals*. Springer, 1996. (original: Difraktsiia rentgenovskikh luchei i neitronov v neidealnykh kristallakh, Naukova Dumka, Kiev, 1983).

[21] A. Cervellino, C. Giannini, and A. Guagliardi. On the efficient evaluation of fourier patterns for nanoparticles and clusters. *Journal of Computational Chemistry*, 27(9):995–1008, JUL 15 2006. ISSN 0192-8651. doi: {10.1002/jcc.20407}.

[22] P. M. Derlet, S. Van Petegem, and H. Van Swygenhoven. Calculation of x-ray spectra for nanocrystalline materials. *Phys. Rev. B*, 71(2):024114, Jan 2005. doi: 10.1103/PhysRevB.71.024114.

[23] G. Ribárik, T. Ungár, and J. Gubicza. *MWP-fit*: a program for multiple whole-profile fitting of diffraction peak profiles by *ab initio* theoretical functions. *Journal of Applied Crystallography*, 34(5):669–676, Oct 2001. doi: 10.1107/S0021889801011451, ►.

[24] M. Leoni, T. Confente, and P. Scardi. PM2K: a flexible program implementing Whole Powder Pattern Modelling. *Zeitschrift für Kristallographie Supplements*, 23:249–254, 2006. doi: 10.1524/zksu.2006.suppl_23.249, ►.

[25] Luca Lutterotti and Mauro Bortolotti. Object oriented programming and fast computation techniques in maud, a program for powder diffraction analysis written in java. *IUCr: Computing Commission Newsletter*, (1): 43–50, jan 2003, ►.

[26] Zdeněk Matěj. Analysis of real structure of nanocrystalline materials by x-ray diffraction. Diploma thesis, Charles University in Prague, Faculty of Mathematics and Physics, May 2003. (in Czech, Rentgenografické difrakční studium reálné struktury nanokrystalických materiálů).

[27] B. E. Warren and B. L. Averbach. The effect of cold-work distortion on x-ray patterns. *Journal of Applied Physics*, 21(6):595–599, 1950. doi: 10.1063/1.1699713, ►.

[28] P. Scherrer. Bestimmung der größe und der inneren struktur von kolloidteilchen mittels röntgenstrahlen. *Nachrichten von der Gesellschaft der Wissenschaften zu Göttingen, Mathematisch-Physikalische Klasse*, pages 98–100, 1918, ►.

[29] G. K. Williamson and W. H. Hall. X-ray line broadening from filed aluminium and wolfram. *Acta Metallurgica*, 1(1):22 – 31, 1953. ISSN 0001-6160. doi: 10.1016/0001-6160(53)90006-6, ►.

[30] Václav Valvoda, Milena Polcarová, and Pavel Lukáč. *Základy Strukturní Analýzy*. Karolinum, Charles University in Prague, 1st edition, 1992. (in Czech).

[31] Radomír Kužel. *X-ray diffraction line profile analysis and study of dislocations in hexagonal metals*. PhD thesis, Charles University in Prague,

Faculty of Mathematics and Physics, 1989. (in Czech, Analýza profilů rentgenových difrakčních linií a studium dislokací v hexagonálních látkách).

[32] P. Debye. Zerstreuung von röntgenstrahlen. *Annalen der Physik*, 351(6): 809–823, 1915. ISSN 1521-3889. doi: 10.1002/andp.19153510606, ►.

[33] Antonio Cervellino, Cinzia Giannini, and Antonietta Guagliardi. Determination of nanoparticle structure type, size and strain distribution from X-ray data for monatomic f.c.c.-derived non-crystallographic nanoclusters. *Journal of Applied Crystallography*, 36(5):1148–1158, Oct 2003. doi: 10.1107/S0021889803013542, ►.

[34] Václav Holý, Ullrich Pietsch, and Tilo Baumbach. *High-resolution X-ray scattering from thin films and multilayers*. Springer, 1999. ISBN 978-3540620297.

[35] F. de Bergevin. *X-ray and Neutron Reflectivity Principles and Applications*, volume 770 of *Lecture Notes in Physics*, chapter 1, The Interaction of X-Rays (and Neutrons) with Matter. Springer, 2009. doi: 10.1007/978-3-540-88588-7.

[36] K. Beyerlein, A. Cervellino, M. Leoni, R. L. Snyder, and P. Scardi. Debye equation versus Whole Powder Pattern Modelling: Real versus reciprocal space modelling of nanomaterials. *Zeitschrift für Kristallographie Supplements*, 30:85–90, 2009. doi: 10.1524/zksu.2009.0012, ►.

[37] Stanislav Daniš and Václav Holý. Diffuse X-ray scattering from GaN/SiC (0001) thin films. *Z. Kristallogr. Suppl.*, 23:141–146, 2006. doi: 10.1524/zksu.2006.suppl_23.141, ►.

[38] Vladimir M. Kaganer and Karl K. Sabelfeld. X-ray diffraction peaks from correlated dislocations: Monte Carlo study of dislocation screening. *Acta Crystallographica Section A*, 66(6):703–716, Nov 2010. doi: 10.1107/S0108767310033544, ►.

[39] John Price Hirth and Jens Lothe. *Theory of Dislocations*. Krieger Publishing Company, Malabar, Florida, 1992.

[40] Vladimir M. Kaganer and Karl K. Sabelfeld. Diffraction peaks from correlated dislocations. *Zeitschrift für Kristallographie*, 225:581–587, 2010. doi: 10.1524/zkri.2010.1346, ►.

[41] N. Armstrong, M. Leoni, and P. Scardi. Considerations concerning Wilkens' theory of dislocation line-broadening. *Zeitschrift für Kristallographie Supplements*, 23:81–86, 2006. doi: 10.1524/zksu.2006.suppl_23.81, ►.

[42] T. Ungár, I. Dragomir, Á. Révész, and A. Borbély. The contrast factors of dislocations in cubic crystals: the dislocation model of strain anisotropy in practice. *Journal of Applied Crystallography*, 32(5):992–1002, Oct 1999. doi: 10.1107/S0021889899009334, ►.

[43] I. C. Dragomir and T. Ungár. Contrast factors of dislocations in the hexagonal crystal system. *Journal of Applied Crystallography*, 35(5):556–564, Oct 2002. doi: 10.1107/S0021889802009536, ►.

[44] Jorge Martinez-Garcia, Matteo Leoni, and Paolo Scardi. Analytical expression for the dislocation contrast factor of the ?001?100 cubic slip-system: Application to cu_2o. *Phys. Rev. B*, 76(17):174117, Nov 2007. doi: 10.1103/PhysRevB.76.174117.

[45] Jorge Martinez-Garcia, Matteo Leoni, and Paolo Scardi. A general approach for determining the diffraction contrast factor of straight-line dislocations. *Acta Crystallographica Section A*, 65(2):109–119, Mar 2009. doi: 10.1107/S010876730804186X, ►.

[46] V. V. Pototskaya and K. P. Ryboshapka. Theory of Scattering of X-rays by Crystals Containing Dislocation Dipoles. In V. N. Svechnikov, editor, *Defects and Properties of Crystal Structures of Metals and Alloys*, volume 24, pages 97–109. Naukova Dumka, Kiev, 1968. in Russian.

[47] J. J. Gilman. Influence of dislocation dipoles on physical properties. *Discussions of the Faraday Society*, 38:123–137, 1964. doi: 10.1039/DF9643800123, ►.

[48] H. S. Chen, J. J. Gilman, and A. K. Head. Equilibrium of extended dislocations within edge dislocation dipoles. *Philosophical Magazine*, 10(103): 35–42, 1964. doi: 10.1080/14786436408224205, ►.

[49] F. Kroupa. Long-range elastic field of semi-infinite dislocation dipole and of dislocation jog. *physica status solidi (b)*, 9(1):27–32, 1965. ISSN 1521-3951. doi: 10.1002/pssb.19650090103, ►.

[50] F. Kroupa. Annihilation of a dislocation dipole. *Czechoslovak Journal of Physics*, 17:220–226, 1967. ISSN 0011-4626. doi: 10.1007/BF01724335, ►.

[51] C. T. Forwood and P. Humble. Dislocation dipoles in elastically anisotropic crystals. *Australian Journal of Physics*, 23:697–718, 1970, ►.

[52] U. Essmann and H. Mughrabi. Annihilation of dislocations during tensile and cyclic deformation and limits of dislocation densities. *Philosophical Magazine A*, 40:731–756, 1979. ISSN 0141-8610. doi: 10.1080/01418617908234871, ►.

[53] I. Groma, T. Ungár, and M. Wilkens. Asymmetric X-ray line broadening of plastically deformed crystals. I. Theory. *Journal of Applied Crystallography*, 21(1):47–54, Feb 1988. doi: 10.1107/S0021889887009178, ►.

[54] T. Ungár. The dislocation-based model of strain broadening in X-ray line profile analysis. In Robert. L. Snyder, J. Fiala, and Hans J. Bunge, editors, *Defect and Microstructure Analysis by Diffraction*, IUCR monographs on Crystallography, chapter 10, pages 165–199. Oxford University Press, 1999.

[55] M. Wilkens. Das mittlere spannungsquadrat $\langle\sigma^2\rangle$ begrenzt regellos verteilter versetzungen in einem zylinderförmigen körper. *Acta Metallurgica*, 17 (9):1155 – 1159, 1969. ISSN 0001-6160. doi: DOI:10.1016/0001-6160(69) 90092-3, ►.

[56] R. Kužel. Dislocation line broadening. *Zeitschrift für Kristallographie Supplements*, 23:75–80, 2006. doi: 10.1524/zksu.2006.suppl_23.75, ►.

[57] I. Groma. X-ray line broadening due to an inhomogeneous dislocation distribution. *Phys. Rev. B*, 57(13):7535–7542, Apr 1998. doi: 10.1103/PhysRevB. 57.7535.

[58] I. Groma and F. Székely. Analysis of the asymptotic properties of X-ray line broadening caused by dislocations. *Journal of Applied Crystallography*, 33(6):1329–1334, Dec 2000. doi: 10.1107/S002188980001058X, ►.

[59] M. A. Krivoglaz and K. P. Ryaboshapka. Theory of scattering of X-rays and thermal neutrons by real crystals. *Fizika Metallov I Metallovedenie*, 15:18–25, 1963.

[60] Mikhail A. Krivoglaz. *Theory of Scattering of X-rays and Thermal Neutrons by Real Crystals*. Nauka, Moskva, 1967. (in Russian).

[61] M. Wilkens. Zur Röntgenstreuung an Kristallen mit Versetzungen I. Zylinderförmiger Kristall axialer Schraubenversetzung. *physica status solidi (b)*, 2(6):692–712, 1962. ISSN 1521-3951. doi: 10.1002/pssb.19620020607, ►.

[62] M. Wilkens. Das spannungsfeld einer anordnung von regellos verteilten versetzungen. *Acta Metallurgica*, 15(8):1412 – 1415, 1967. ISSN 0001-6160. doi: DOI:10.1016/0001-6160(67)90020-X, ►.

[63] M. B. Bever, D. L. Holt, and A. L. Titchener. The stored energy of cold work. *Progress in Materials Science*, 17:5 – 177, 1973. ISSN 0079-6425. doi: DOI:10.1016/0079-6425(73)90001-7, ►.

[64] E. Schafler, G. Steiner, E. Korznikova, M. Kerber, and M.J. Zehetbauer. Lattice defect investigation of ecap-cu by means of x-ray line profile analysis, calorimetry and electrical resistometry. *Materials Science and Engineering: A*, 410-411:169 – 173, 2005. ISSN 0921-5093. doi: DOI:10.1016/j.msea. 2005.08.070, ►. The Langdon Symposium: Flow and forming of Crystalline Materials.

[65] J. Gubicza, S.V. Dobatkin, and E. Khosravi. Reduction of vacancy concentration during storage of severely deformed cu. *Materials Science and Engineering: A*, 527(21-22):6102 – 6104, 2010. ISSN 0921-5093. doi: DOI:10.1016/j.msea.2010.05.088, ►.

[66] U.F Kocks. On internal stresses due to a quasiuniform distribution of dislocations. *Acta Metallurgica*, 15(8):1415 – 1417, 1967. ISSN 0001-6160. doi: DOI:10.1016/0001-6160(67)90021-1, ►.

[67] M. Wllkens. Reply to the note "On internal stresses due to a quasi-uniform distribution of dislocation". *Acta Metallurgica*, 15(8):1417 – 1417, 1967. ISSN 0001-6160. doi: DOI:10.1016/0001-6160(67)90022-3, ►.

[68] M. Wilkens. The determination of density and distribution of dislocations in deformed single crystals from broadened x-ray diffraction profiles. *physica status solidi (a)*, 2(2):359–370, 1970. ISSN 1521-396X. doi: 10.1002/pssa.19700020224, ►.

[69] M. Wilkens. X-ray Line Broadening and Mean Square Strains of Straight Dislocations in Elastically Anisotropic Crystals of Cubic Symmetry. *physica status solidi (a)*, 104(1):K1–K6, 1987. ISSN 1521-396X. doi: 10.1002/pssa.2211040137, ►.

[70] Johannes Gerardus Maria van Berkum. *Strain Fields in Crystalline Materials, Methods of Analysis Based on X-Ray Diffraction-Line Broadening*. PhD thesis, Delft University of Technology, 1994.

[71] J.-D. Kamminga and R. Delhez. Calculation of diffraction line profiles from specimens with dislocations. A comparison of analytical models with computer simulations. *Journal of Applied Crystallography*, 33(4):1122–1127, Aug 2000. doi: 10.1107/S0021889800006750, ►.

[72] R. W. Cheary, E. Dooryhee, P. Lynch, N. Armstrong, and S. Dligatch. X-ray diffraction line broadening from thermally deposited gold films. *Journal of Applied Crystallography*, 33(5):1271–1283, Oct 2000. doi: 10.1107/S0021889800009936, ►.

[73] Peter Lynch. *X-ray Diffraction Line Broadening From Gold Thin Films*. PhD thesis, University of Technology, Sydney, 2003.

[74] J. Gubicza, N. H. Nam, K. Máthis, and V. V. Stolyarov. Microstructure of severely deformed metals from x-ray line profile analysis. *Zeitschrift für Kristallographie Supplements*, 23:93–98, 2006. doi: 10.1524/zksu.2006.suppl_23.93, ►.

[75] Gábor Ribárik. *Modeling of diffraction patterns based on microstructural properties*. PhD thesis, Eötvös Loránd University, 2008, ►.

[76] E. Wu, E. Mac A. Gray, and E. H. Kisi. Modelling Dislocation-Induced Anisotropic Line Broadening in Rietveld Refinements Using a Voigt Function. I. General Principles. *Journal of Applied Crystallography*, 31(3):356–362, Jun 1998. doi: 10.1107/S002188989701217X, ►.

[77] E. Wu, E. H. Kisi, and E. Mac A. Gray. Modelling Dislocation-Induced Anisotropic Line Broadening in Rietveld Refinements Using a Voigt Function. II. Application to Neutron Powder Diffraction Data. *Journal of Applied Crystallography*, 31(3):363–368, Jun 1998. doi: 10.1107/S0021889897012181, ►.

[78] R. Kužel, J. Čížek, I. Procházka, F. Chmelík, R. K. Islamgaliev, and N. M. Amirkhanov. Structural Studies of Ultrafine Grained Copper Obtained by Severe Plastic Deformation. *Materials Science Forum*, 378–381:463–468, 2001. doi: 10.4028/www.scientific.net/MSF.378-381.463, ►.

[79] Vladimir M. Kaganer, Oliver Brandt, Henning Riechert, and Karl K. Sabelfeld. X-ray diffraction of epitaxial films with arbitrarily correlated dislocations: Monte carlo calculation and experiment. *Phys. Rev. B*, 80(3): 033306, Jul 2009. doi: 10.1103/PhysRevB.80.033306.

[80] Vladimir M. Kaganer and Karl K. Sabelfeld. X-ray diffraction peaks from partially ordered misfit dislocations. *Phys. Rev. B*, 80(18):184105, Nov 2009. doi: 10.1103/PhysRevB.80.184105.

[81] Václav Holý. Diffuse x-ray scattering from correlated dislocations in epitaxial layers. In *Acta Crystallographica Section A*, volume 66, page s213, 2010. (26th European Crystallography Meeting, ECM26 Darmstadt, poster).

[82] M. Barchuk, V. Holý, B. Miljević, B. Krause, T. Baumbach, J. Hertkorn, and F. Scholz. X-ray diffuse scattering from threading dislocations in epitaxial gan layers. *Journal of Applied Physics*, 108(4):043521, 2010. doi: 10.1063/1.3460803, ►.

[83] R. Kužel and P. Klimanek. X-ray diffraction line broadening due to dislocations in non-cubic materials. II. The case of elastic anisotropy applied to hexagonal crystals. *Journal of Applied Crystallography*, 21(4):363–368, Aug 1988. doi: 10.1107/S002188988800336X, ►.

[84] R. Kužel and P. Klimanek. X-ray diffraction line broadening due to dislocations in non-cubic crystalline materials. III. Experimental results for plastically deformed zirconium. *Journal of Applied Crystallography*, 22(4): 299–307, Aug 1989. doi: 10.1107/S0021889889001585, ►.

[85] E. Schafler, M. Zehetbauer, and T. Ungár. Measurement of screw and edge dislocation density by means of x-ray bragg profile analysis. *Materials Science and Engineering A*, 319-321:220 – 223, 2001. ISSN 0921-5093. doi: DOI:10.1016/S0921-5093(01)00979-0, ►.

[86] András Borbély, Juliana Dragomir-Cernatescu, Gábor Ribárik, and Tamás Ungár. Computer program *ANIZC* for the calculation of diffraction contrast factors of dislocations in elastically anisotropic cubic, hexagonal and trigonal crystals. *Journal of Applied Crystallography*, 36(1):160–162, Feb 2003. doi: 10.1107/S0021889802021581, ►.

[87] Matteo Leoni, Jorge Martinez-Garcia, and Paolo Scardi. Dislocation effects in powder diffraction. *Journal of Applied Crystallography*, 40(4):719–724, Aug 2007. doi: 10.1107/S002188980702078X, ►.

[88] J. J. Wortman and R. A. Evans. Young's Modulus, Shear Modulus, and Poisson's Ratio in Silicon and Germanium. *Journal of Applied Physics*, 36 (1):153–156, 1965. doi: 10.1063/1.1713863, ►.

[89] W. C. Overton and John Gaffney. Temperature Variation of the Elastic Constants of Cubic Elements. I. Copper. *Phys. Rev.*, 98(4):969–977, May 1955. doi: 10.1103/PhysRev.98.969.

[90] H.B. Huntington. The Elastic Constants of Crystals. volume 7 of *Solid State Physics*, pages 213 – 351. Academic Press, 1958. doi: 10.1016/S0081-1947(08)60553-6, ►.

[91] David Rafaja, Christina Wüstefeld, Jürgen Kutzner, Arutiun P. Ehiasarian, Michal Šíma, Volker Klemm, Dietrich Heger, and Jens Kortus. Magnetic response of (Cr,Al,Si)N nanocrystallites on the microstructure of Cr—Al—Si—N nanocomposites. *Zeitschrift für Kristallographie*, 225:599–609, 2010. doi: 10.1524/zkri.2010.1347, ►.

[92] G. Ribárik, T. Ungár, and J. Gubicza. *MWP-fit*: a program for multiple whole-profile fitting of diffraction peak profiles by *ab initio* theoretical functions. *Journal of Applied Crystallography*, 34(5):669–676, Oct 2001. doi: 10.1107/S0021889801011451, ►.

[93] M. M. J. Treacy, J. M. Newsam, and M. W. Deem. A General Recursion Method for Calculating Diffracted Intensities from Crystals Containing Planar Faults. *Proceedings of the Royal Society of London. Series A: Mathematical and Physical Sciences*, 433(1889):499–520, 1991. doi: 10.1098/rspa.1991.0062, ►.

[94] Michael M. J. Treacy. DIFFaX manual. `http://www.public.asu.edu/~mtreacy/DIFFaX.html`, May 2009, ►.

[95] M. Casas-Cabanas, J. Rodriguez-Carvajal, and M. R. Palacin. FAULTS, a new program for refinement of powder diffraction patterns from layered structures. *Zeitschrift für Kristallographie Supplements*, 23:243–248, 2006. doi: 10.1524/zksu.2006.suppl_23.243, ►.

[96] Matteo Leoni, Alessandro F. Gualtieri, and Norberto Roveri. Simultaneous refinement of structure and microstructure of layered materials. *Journal of Applied Crystallography*, 37(1):166–173, Feb 2004. doi: 10.1107/S0021889803022787, ►.

[97] Matteo Leoni. Diffraction analysis of layer disorder. *Zeitschrift für Kristallographie*, pages 561–568, 2008. doi: 10.1524/zkri.2008.1214, ►.

[98] Stefan Martin, Christiane Ullrich, Daniel Šimek, Ulrich Martin, and David Rafaja. Stacking fault model of ε-martensite and its *DIFFaX* implementation. *Journal of Applied Crystallography*, 44(4), Aug 2011. doi: 10.1107/S0021889811019558, ►.

[99] Levente Balogh, Géza Tichy, and Tamás Ungár. Twinning on pyramidal planes in hexagonal close packed crystals determined along with other defects by X-ray line profile analysis. *Journal of Applied Crystallography*, 42 (4):580–591, Aug 2009. doi: 10.1107/S0021889809022936, ►.

[100] Gábor Ribárik and Tamás Ungár. Characterization of the microstructure in random and textured polycrystals and single crystals by diffraction line profile analysis. *Materials Science and Engineering: A*, 528(1):112 – 121, 2010. ISSN 0921-5093. doi: DOI:10.1016/j.msea.2010.08.059, ►. Special Topic Section: Local and Near Surface Structure from Diffraction.

[101] Maja Buljan, Uroš V. Desnica, Nikola Radić, Goran Dražić, Zdeněk Matěj, Václav Valeš, and Václav Holý. Crystal structure of defect-containing semiconductor nanocrystals – an X-ray diffraction study. *Journal of Applied Crystallography*, 42(4):660–672, Aug 2009. doi: 10.1107/S0021889809017476, ►.

[102] Paolo Scardi and Matteo Leoni. Fourier modelling of the anisotropic line broadening of X-ray diffraction profiles due to line and plane lattice defects. *Journal of Applied Crystallography*, 32(4):671–682, Aug 1999. doi: 10.1107/S002188989900374X, ►.

[103] P. Scardi, M. Leoni, and Y.H. Dong. Whole diffraction pattern-fitting of polycrystalline fcc materials based on microstructure. *The European Physical Journal B - Condensed Matter and Complex Systems*, 18:23–30, 2000. ISSN 1434-6028, ►. 10.1007/s100510070073.

[104] Scardi Scardi and Matteo Leoni. PM2000 VER. 1.59K (Guide), February 2002.

[105] Juan Rodriguez-Carvajal and Thierry Roisnel. FullProf Suite. `http://www.ill.eu/sites/fullprof/`, jul 2011, ►.

[106] Luca Lutterotti. Maud - Materials Analysis Using Diffraction. `http://www.ing.unitn.it/~maud/`, may 2011, ►.

[107] N. C. Popa. The (hkl) Dependence of Diffraction-Line Broadening Caused by Strain and Size for all Laue Groups in Rietveld Refinement. *Journal of Applied Crystallography*, 31(2):176–180, 1998. ISSN 1600-5767. doi: 10.1107/S0021889897009795, ►.

[108] Y. H. Dong and P. Scardi. *MarqX*: a new program for whole-powder-pattern fitting. *Journal of Applied Crystallography*, 33(1):184–189, Feb 2000. doi: 10.1107/S002188989901434X, ►.

[109] R. W. Cheary and A. Coelho. A fundamental parameters approach to X-ray line-profile fitting. *Journal of Applied Crystallography*, 25(2):109–121, Apr 1992. doi: 10.1107/S0021889891010804, ►.

[110] G. Ribárik, T. Ungár, and J. Gubicza. Convolutional Multiple Whole Profile fitting Main Page. `http://www.renyi.hu/cmwp/`, jul 2011, ►.

[111] Katharine Mullen, Victor Krayzman, and Igor Levin. Atomic structure analysis at the nanoscale using the pair distribution function: simulation studies of simple elemental nanoparticles. *Journal of Applied Crystallography*, 43(3):483–490, Jun 2010. doi: 10.1107/S0021889810008460, ►.

[112] Bogdan Palosz, Svetlana Stelmakh, Ewa Grzanka, Stanislaw Gierlotka, and Witold Palosz. Application of the apparent lattice parameter to determination of the core-shell structure of nanocrystals. *Zeitschrift für Kristallographie*, 222(11):580–594, 2007. doi: 10.1524/zkri.2007.222.11.580, ►.

[113] T. Ino and N. Minami. X-ray diffraction by small crystals. *Acta Crystallographica Section A*, 35(1):163–170, 1979. ISSN 1600-5724. doi: 10.1107/S0567739479000280, ►.

[114] Václav Valeš, Jana Poltierová-Vejpravová, Václav Holý, Václav Tyrpekl, Petr Brázda, and Stephen Doyle. Study of the phase composition of Fe2O3 and Fe2O3/TiO2 nanoparticles using X-ray diffraction and Debye formula. *physica status solidi (c)*, 7(5):1399–1404, 2010. ISSN 1610-1642. doi: 10.1002/pssc.200983385, ►.

[115] A. Cervellino, C. Giannini, A. Guagliardi, and D. Zanchet. Quantitative analysis of gold nanoparticles from synchrotron data by means of least-squares techniques. *The European Physical Journal B - Condensed Matter and Complex Systems*, 41:485–493, 2004. ISSN 1434-6028, ►. 10.1140/epjb/e2004-00342-3.

[116] A. Cervellino, C. Giannini, A. Guagliardi, and M. Ladisa. Nanoparticle size distribution estimation by a full-pattern powder diffraction analysis. *Physical Review B*, 72(3), JUL 2005. ISSN 1098-0121. doi: {10.1103/PhysRevB.72.035412}.

[117] C. Giannini, A. Cervellino, A. Guagliardi, F. Gozzo, D. Zanchet, T. Rocha, and M. Ladisa. A Debye function based powder diffraction data analysis method. *Zeitschrift für Kristallographie Supplements*, 26:105–110, 2007. ISSN 0044-2968. doi: 10.1524/zksu.2007.2007.suppl_26.105, ►.

[118] Giuseppe Cernuto, Norberto Masciocchi, Antonio Cervellino, Gian Maria Colonna, and Antonietta Guagliardi. Size and Shape Dependence of the Photocatalytic Activity of TiO2 Nanocrystals: A Total Scattering Debye Function Study. *Journal of the American Chemical Society*, 133(9):3114–3119, 2011. doi: 10.1021/ja110225n, ►.

[119] A. G. Frøseth, P. M. Derlet, and H. Van Swygenhoven. Twinning in nanocrystalline fcc metals. *Advanced Engineering Materials*, 7(1-2):16–20, 2005. ISSN 1527-2648. doi: 10.1002/adem.200400163, ►.

[120] Kenneth R. Beyerlein, Robert L. Snyder, Mo Li, and Paolo Scardi. Application of the debye function to systems of crystallites. *Philosophical Magazine*, 90(29):3891–3905, 2010. doi: 10.1080/14786435.2010.501769, ►.

[121] S. Brandstetter, P.M. Derlet, S. Van Petegem, and H. Van Swygenhoven. Williamson-hall anisotropy in nanocrystalline metals: X-ray diffraction experiments and atomistic simulations. *Acta Materialia*, 56(2):165 – 176, 2008. ISSN 1359-6454. doi: DOI:10.1016/j.actamat.2007.09.007, ►.

[122] M. Šlouf, R. Kužel, and Z. Matěj. Preparation and characterization of isometric gold nanoparticles with pre-calculated size. *Zeitschrift für Kristallographie Supplements*, 23:319–324, 2006. doi: 10.1524/zksu.2006.suppl_23.319, ►.

[123] Jürgen Roth. The silver anniversary of gold: 25 years of the colloidal gold marker system for immunocytochemistry and histochemistry. *Histochemistry and Cell Biology*, 106:1–8, 1996. ISSN 0948-6143. doi: 10.1007/BF02473197, ►.

[124] F. D'Amico and E. Skarmoutsou. Quantifying immunogold labelling in transmission electron microscopy. *Journal of Microscopy*, 230(1):9–15, 2008. ISSN 1365-2818. doi: 10.1111/j.1365-2818.2008.01949.x, ►.

[125] Miroslav Slouf, Ewa Pavlova, Monika Bhardwaj, Josef Plestil, Heidemarie Onderková, Anatoly A. Philimonenko, and Pavel Hozák. Preparation of stable Pd nanoparticles with tunable size for multiple immunolabeling in biomedicine. *Materials Letters*, 65(8):1197 – 1200, 2011. ISSN 0167-577X. doi: 10.1016/j.matlet.2011.01.046, ►.

[126] John Turkevich, Peter Cooper Stevenson, and James Hillier. A study of the nucleation and growth processes in the synthesis of colloidal gold. *Discuss. Faraday Soc.*, 11:55–75, 1951. doi: 10.1039/DF9511100055, ►.

[127] Zdeněk Matěj, Lea Nichtová, and Radomír Kužel. Microstructural characterisation of nanocrystalline powders and thin films by x-ray powder diffraction. In *Nanocon 2009*, pages 53–60. Tanger, Ltd, 2009. ISBN 978-80-87294-13-0, ►.

[128] Milan Dopita. *Microstructure and properties of nanocrystalline hard coatings and thin film nanocomposites*. PhD thesis, Charles University in Prague, Faculty of Mathematics and Physics, July 2009.

[129] Lea Nichtová. X-ray study of thin nanocrystalline films. Diploma thesis, Charles University in Prague, Faculty of Mathematics and Physics, Septemeber 2005. (in Czech, Rtg strukturní studium nanokrystalických tenkých vrstev).

[130] Th. H. de Keijser, J. I. Langford, E. J. Mittemeijer, and A. B. P. Vogels. Use of the Voigt function in a single-line method for the analysis of X-ray diffraction line broadening. *Journal of Applied Crystallography*, 15(3):308–314, Jun 1982. doi: 10.1107/S0021889882012035, ►.

[131] Marian Čerňanský. Restoration and processing of physical profiles from measured data. In Robert. L. Snyder, J. Fiala, and Hans J. Bunge, editors, *Defect and Microstructure Analysis by Diffraction*, IUCR monographs on Crystallography, chapter 26, pages 613–651. Oxford University Press, 1999. ISBN 0-19-850189-7.

[132] Derk Reefman. Towards higher resolution: a mathematical approach. In Robert. L. Snyder, J. Fiala, and Hans J. Bunge, editors, *Defect and Microstructure Analysis by Diffraction*, IUCR monographs on Crystallography, chapter 27, pages 652–670. Oxford University Press, 1999. ISBN 0-19-850189-7.

[133] P. Scardi, M. Leoni, and R. Delhez. Line broadening analysis using integral breadth methods: a critical review. *Journal of Applied Crystallography*, 37 (3):381–390, Jun 2004. doi: 10.1107/S0021889804004583, ►.

[134] J. R. Neighbours and G. A. Alers. Elastic constants of silver and gold. *Phys. Rev.*, 111(3):707–712, Aug 1958. doi: 10.1103/PhysRev.111.707.

[135] Paolo Scardi and Matteo Leoni. Diffraction line profiles from polydisperse crystalline systems. *Acta Crystallographica Section A*, 57(5):604–613, Sep 2001. doi: 10.1107/S0108767301008881, ►.

[136] Zdeněk Matěj, Radomír Kužel, Milan Dopita, Miloš Janeček, Jakub Čížek, and Tereza Brunátová. XRD profile analysis of ECAP Cu and Cu + Zr samples. *International Journal of Materials Research (formerly Z. Metallkd.)*, 100(6):880–883, 2009. ISSN 1862-5282. doi: 10.3139/146.110112, ►.

[137] R. Kužel, M. Janeček, Z. Matěj, J. Čížek, M. Dopita, and O. Srba. Microstructure of Equal-Channel Angular Pressed Cu and Cu-Zr Samples Studied by Different Methods. *Metallurgical and Materials Transactions A*, 41:1174–1190, 2010. ISSN 1073-5623. doi: 10.1007/s11661-009-9895-0, ►.

[138] T. Ungár, G. Tichy, J. Gubicza, and R. J. Hellmig. Correlation between subgrains and coherently scattering domains. *Powder Diffraction*, 20(4): 366–375, 2005. doi: 10.1154/1.2135313, ►.

[139] David Rafaja, Volker Klemm, Gerhard Schreiber, Michael Knapp, and Radomír Kužel. Interference phenomena observed by X-ray diffraction in nanocrystalline thin films. *Journal of Applied Crystallography*, 37(4):613–620, Aug 2004. doi: 10.1107/S0021889804012701, ►.

[140] J. Gubicza, N.Q. Chinh, J.L. Lábár, S. Dobatkin, Z. Hegedus, and T.G. Langdon. Correlation between microstructure and mechanical properties of severely deformed metals. *Journal of Alloys and Compounds*, 483(1-2):271 – 274, 2009. ISSN 0925-8388. doi: DOI:10.1016/j.jallcom.2008.07.200, ►. 14th International Symposium on Metastable and Nano-Materials (ISMANAM-2007).

[141] J. Gubicza, N.Q. Chinh, P. Szommer, A. Vinogradov, and T.G. Langdon. Microstructural characteristics of pure gold processed by equal-channel angular pressing. *Scripta Materialia*, 56(11):947 – 950, 2007. ISSN 1359-6462. doi: DOI:10.1016/j.scriptamat.2007.02.018, ►.

[142] Werner Martienssen and Hans Warlimont. *Springer Handbook of Condensed Matter and Materials Data*. Springer, 2005. ISBN 3-540-44376-2.

[143] Milan Dopita, Miloš Janeček, David Rafaja, Jaromír Uhlíř, Zdeněk Matěj, and Radomír Kužel. EBSD investigation of the grain boundary distributions in ultrafine-grained Cu and Cu–Zr polycrystals prepared by equal-channel angular pressing. *International Journal of Materials Research (formerly Z. Metallkd.)*, 100(6):785–789, 2009. ISSN 1862-5282. doi: 10.3139/146.110111, ►.

[144] N. Chinh, J. Gubicza, and T. Langdon. Characteristics of face-centered cubic metals processed by equal-channel angular pressing. *Journal of Materials Science*, 42:1594–1605, 2007. ISSN 0022-2461. doi: 10.1007/s10853-006-0900-3, ►.

[145] Viktoriya Cherkaska. *Microstructure of Submicrocrystalline Metals after Severe Plastic Deformation and Its Thermal Stability*. PhD thesis, Charles University in Prague, Faculty of Mathematics and Physics, September 2008.

[146] Jens Christofer Werenskiold. *Equal Channel Angular Pressing (ECAP) of AA6082: Mechanical Properties, Texture and Microstructural Development*. PhD thesis, The Norwegian University of Science and Technology, Faculty of Natural Science and Technology, October 2004.

[147] M. Janecek, B. Hadzima, R. J. Hellmig, and Y. Estrin. The influence of microstructure on the corrosion properties Cu polycrystals prepared by ECAP. *Metallic Materials*, 43(4):258–271, 2005. ISSN 1338-4252, ►.

[148] Sergey Stepanov. χ_{0h} on the Web. `http://sergey.gmca.aps.anl.gov/x0h.html`, jul 2011, ►.

[149] Daniel Šimek. *Complex diffraction study of thin polycrystalline films*. PhD thesis, Charles University in Prague, Faculty of Mathematics and Physics, September 2008. (Komplexní difrakční studium tenkých polykrystalických vrstev, in Czech).

[150] L. Balogh, J. Gubicza, R. J. Hellmig, Y. Estrin, and T. Ungár. Thermal stability of the microstructure of severely deformed copper. *Zeitschrift für Kristallographie Supplements*, 23:381–386, 2006. doi: 10.1524/zksu.2006.suppl_23.381, ►.

[151] D. Breuer, P. Klimanek, and W. Pantleon. X-ray determination of dislocation density and arrangement in plastically deformed copper. *Journal of Applied Crystallography*, 33(5):1284–1294, Oct 2000. doi: 10.1107/S0021889800008256, ►.

[152] Hengzhong Zhang, Bin Chen, Jillian F. Banfield, and Glenn A. Waychunas. Atomic structure of nanometer-sized amorphous *tio*2. *Phys. Rev. B*, 78(21):214106, Dec 2008. doi: 10.1103/PhysRevB.78.214106.

[153] Francesca Spadavecchia, Giuseppe Cappelletti, Silvia Ardizzone, Claudia L. Bianchi, Serena Cappelli, Cesare Oliva, Paolo Scardi, Matteo Leoni, and Paola Fermo. Solar photoactivity of nano-n-tio2 from tertiary amine: role of defects and paramagnetic species. *Applied Catalysis B: Environmental*, 96(3-4):314 – 322, 2010. ISSN 0926-3373. doi: DOI:10.1016/j.apcatb.2010.02.027, ►.

[154] Akira Fujishima and Xintong Zhang. Titanium dioxide photocatalysis: present situation and future approaches. *Comptes Rendus Chimie*, 9(5-6):750 – 760, 2006. ISSN 1631-0748. doi: DOI:10.1016/j.crci.2005.02.055, ►. Conversion photochimique et stockage de l'énergie solaire - 2e partie.

[155] Kazuhito Hashimoto, Hiroshi Irie, and Akira Fujishima. Tio_2 photocatalysis: A historical overview and future prospects. *Japanese Journal of Applied Physics*, 44(12):8269–8285, 2005. doi: 10.1143/JJAP.44.8269, ►.

[156] Rong Wang, Kazuhito Hashimoto, Akira Fujishima, Makota Chikuni, Eiichi Kojima, Atsushi Kitamura, Mitsuhide Shimohigoshi, and Toshiya Watanabe. Light-induced amphiphilic surfaces. *Nature*, 388(6641):431–432, 1997. ISSN 0028-0836. doi: 10.1038/41233, ►.

[157] Nobuyuki Sakai, Akira Fujishima, Toshiya Watanabe, and Kazuhito Hashimoto. Quantitative evaluation of the photoinduced hydrophilic conversion properties of tio2 thin film surfaces by the reciprocal of contact angle. *The Journal of Physical Chemistry B*, 107(4):1028–1035, 2003. doi: 10.1021/jp022105p, ►.

[158] Andrew Mills, George Hill, Sharan Bhopal, Ivan P. Parkin, and Shane A. O'Neill. Thick titanium dioxide films for semiconductor photocatalysis. *Journal of Photochemistry and Photobiology A: Chemistry*, 160(3):185 – 194, 2003. ISSN 1010-6030. doi: DOI:10.1016/S1010-6030(03)00206-5, ►.

[159] Iis Sopyan, Mitsuru Watanabe, Sadao Murasawa, Kazuhito Hashimoto, and Akira Fujishima. An efficient TiO2 thin-film photocatalyst: photocatalytic properties in gas-phase acetaldehyde degradation. *Journal of Photochemistry and Photobiology A: Chemistry*, 98(1-2):79 – 86, 1996. ISSN 1010-6030. doi: DOI:10.1016/1010-6030(96)04328-6, ►.

[160] Dianbo Dong, Peijun Li, Xiaojun Li, Qing Zhao, Yinqiu Zhang, Chunyun Jia, and Peng Li. Investigation on the photocatalytic degradation of pyrene on soil surfaces using nanometer anatase tio2 under uv irradiation. *Journal of Hazardous Materials*, 174(1-3):859 – 863, 2010. ISSN 0304-3894. doi: DOI:10.1016/j.jhazmat.2009.09.132, ►.

[161] Emad S. Elmolla and Malay Chaudhuri. Photocatalytic degradation of amoxicillin, ampicillin and cloxacillin antibiotics in aqueous solution using uv/tio2 and uv/h2o2/tio2 photocatalysis. *Desalination*, 252(1-3):46 – 52, 2010. ISSN 0011-9164. doi: DOI:10.1016/j.desal.2009.11.003, ►.

[162] Tianyou Peng, De Zhao, Ke Dai, Wei Shi, and Kazuyuki Hirao. Synthesis of titanium dioxide nanoparticles with mesoporous anatase wall and high photocatalytic activity. *The Journal of Physical Chemistry B*, 109(11): 4947–4952, 2005. doi: 10.1021/jp044771r, ►.

[163] G. Waldner, M. Pourmodjib, R. Bauer, and M. Neumann-Spallart. Photoelectrocatalytic degradation of 4-chlorophenol and oxalic acid on titanium dioxide electrodes. *Chemosphere*, 50(8):989 – 998, 2003. ISSN 0045-6535. doi: DOI:10.1016/S0045-6535(02)00612-4, ►.

[164] H.L. Tidahy, S. Siffert, J.-F. Lamonier, E.A. Zhilinskaya, A. Aboukaïs, Z.-Y. Yuan, A. Vantomme, B.-L. Su, X. Canet, G. De Weireld, M. Frère, T.B. N'Guyen, J.-M. Giraudon, and G. Leclercq. New Pd/hierarchical macro-mesoporous ZrO2, TiO2 and ZrO2-TiO2 catalysts for VOCs total oxidation. *Applied Catalysis A: General*, 310:61 – 69, 2006. ISSN 0926-860X. doi: DOI:10.1016/j.apcata.2006.05.020, ►.

[165] J.-M. Giraudon, T.B. Nguyen, G. Leclercq, S. Siffert, J.-F. Lamonier, A. Aboukaïs, A. Vantomme, and B.-L. Su. Chlorobenzene total oxidation over palladium supported on zro2, tio2 nanostructured supports. *Catalysis Today*, 137(2-4):379 – 384, 2008. ISSN 0920-5861. doi: DOI: 10.1016/j.cattod.2008.02.019, ►. AWPA Symposium 2007.

[166] Tadashi Matsunaga, Ryozo Tomoda, Toshiaki Nakajima, and Hitoshi Wake. Photoelectrochemical sterilization of microbial cells by semiconductor powders. *FEMS Microbiology Letters*, 29(1-2):211–214, 1985. ISSN 1574-6968. doi: 10.1111/j.1574-6968.1985.tb00864.x, ►.

[167] P. Evans and D.W. Sheel. Photoactive and antibacterial tio2 thin films on stainless steel. *Surface and Coatings Technology*, 201(22-23):9319 – 9324, 2007. ISSN 0257-8972. doi: DOI:10.1016/j.surfcoat.2007.04.013, ►. Euro CVD 16, 16th European Conference on Chemical Vapor Deposition.

[168] P. Zeman and S. Takabayashi. Self-cleaning and antifogging effects of tio[sub 2] films prepared by radio frequency magnetron sputtering. *Journal of Vacuum Science & Technology A: Vacuum, Surfaces, and Films*, 20(2): 388–393, 2002. doi: 10.1116/1.1446445, ►.

[169] J. N. Hart, R. Cervini, Y. B. Cheng, G. P. Simon, and L. Spiccia. Formation of anatase tio2 by microwave processing. *Solar Energy Materials and Solar Cells*, 84(1-4):135 – 143, 2004. ISSN 0927-0248. doi: DOI:10.1016/j.solmat.2004.02.041, ►. International Solar Energy Society World Congress 2003.

[170] Yang-Qin Wang, Si-Guang Chen, Xiang-Hai Tang, Oleg Palchik, Arie Zaban, Yuri Koltypin, and Aharon Gedanken. Mesoporous titanium dioxide: sonochemical synthesis and application in dye-sensitized solar cells. *J. Mater. Chem.*, 11:521–526, 2001. doi: 10.1039/B006070O, ►.

[171] T. Ivanova, A. Harizanova, T. Koutzarova, N. Krins, and B. Vertruyen. Electrochromic TiO2, ZrO2 and TiO2-ZrO2 thin films by dip-coating

method. *Materials Science and Engineering: B*, 165(3):212 – 216, 2009. ISSN 0921-5107. doi: DOI:10.1016/j.mseb.2009.07.013, ►. 5th International Workshop on Nanosciences and Nanotechnologies.

[172] César O. Avellaneda, Luis O. S. Bulh oes, and Agnieszka Pawlicka. The CeO2-TiO2-ZrO2 sol-gel film: a counter-electrode for electrochromic devices. *Thin Solid Films*, 471(1-2):100 – 104, 2005. ISSN 0040-6090. doi: DOI:10.1016/j.tsf.2004.04.039, ►.

[173] Georg Waldner, Roberto Gómez, and Michael Neumann-Spallart. Using photoelectrochemical measurements for distinguishing between direct and indirect hole transfer processes on anatase: Case of oxalic acid. *Electrochimica Acta*, 52(7):2634 – 2639, 2007. ISSN 0013-4686. doi: DOI: 10.1016/j.electacta.2006.09.019, ►.

[174] Meng Ni, Michael K.H. Leung, Dennis Y.C. Leung, and K. Sumathy. A review and recent developments in photocatalytic water-splitting using tio2 for hydrogen production. *Renewable and Sustainable Energy Reviews*, 11 (3):401 – 425, 2007. ISSN 1364-0321. doi: DOI:10.1016/j.rser.2005.01.009, ►.

[175] Dambar B. Hamal and Kenneth J. Klabunde. Synthesis, characterization, and visible light activity of new nanoparticle photocatalysts based on silver, carbon, and sulfur-doped tio2. *Journal of Colloid and Interface Science*, 311 (2):514 – 522, 2007. ISSN 0021-9797. doi: DOI:10.1016/j.jcis.2007.03.001, ►.

[176] Danzhen Li, Hanjie Huang, Xu Chen, Zhixin Chen, Wenjuan Li, Dong Ye, and Xianzhi Fu. New synthesis of excellent visible-light tio2-xnx photocatalyst using a very simple method. *Journal of Solid State Chemistry*, 180(9): 2630 – 2634, 2007. ISSN 0022-4596. doi: DOI:10.1016/j.jssc.2007.07.009, ►.

[177] Enrique Camps, L. Escobar-Alarcón, Marco Antonio Camacho-López, and Dora A. Solis Casados. Visible-light photocatalytic activity of nitrided tio2 thin films. *Materials Science and Engineering: B*, 174(1-3):80 – 83, 2010. ISSN 0921-5107. doi: DOI:10.1016/j.mseb.2010.03.020, ►. Advances in Semiconducting Materials.

[178] Jan Šícha. *Pulsed reactive deposition of photoactive oxide films*. PhD thesis, Faculty of Applied Sciences, University of West Bohemia, Plzeň, 2008.

[179] T. Arlt, M. Bermejo, M. A. Blanco, L. Gerward, J. Z. Jiang, J. Staun Olsen, and J. M. Recio. High-pressure polymorphs of anatase *tio*2. *Phys. Rev. B*, 61(21):14414–14419, Jun 2000. doi: 10.1103/PhysRevB.61.14414.

[180] Masakazu. Anpo, Takahito. Shima, Sukeya. Kodama, and Yutaka. Kubokawa. Photocatalytic hydrogenation of propyne with water on small-particle titania: size quantization effects and reaction intermediates. *The Journal of Physical Chemistry*, 91(16):4305–4310, 1987. doi: 10.1021/ j100300a021, ►.

[181] Satoshi Takeda, Susumu Suzuki, Hidefumi Odaka, and Hideo Hosono. Photocatalytic TiO2 thin film deposited onto glass by DC magnetron sputtering. *Thin Solid Films*, 392(2):338 – 344, 2001. ISSN 0040-6090. doi: DOI:10.1016/S0040-6090(01)01054-9, ►.

[182] Tatsuo Shibata, Hiroshi Irie, and Kazuhito Hashimoto. Enhancement of photoinduced highly hydrophilic conversion on tio2 thin films by introducing tensile stress. *The Journal of Physical Chemistry B*, 107(39):10696–10698, 2003. doi: 10.1021/jp0357830, ►.

[183] Tatsuo Shibata, Hiroshi Irie, Donald A. Tryk, and Kazuhito Hashimoto. Effect of residual stress on the photochemical properties of tio2 thin films. *The Journal of Physical Chemistry C*, 113(29):12811–12817, 2009. doi: 10.1021/jp904037t, ►.

[184] Lian Gao and Qinghong Zhang. Effects of amorphous contents and particle size on the photocatalytic properties of tio2 nanoparticles. *Scripta Materialia*, 44(8-9):1195 – 1198, 2001. ISSN 1359-6462. doi: DOI: 10.1016/S1359-6462(01)00681-9, ►.

[185] Hengzhong Zhang and Jillian F. Banfield. Understanding polymorphic phase transformation behavior during growth of nanocrystalline aggregates: insights from tio2. *The Journal of Physical Chemistry B*, 104(15):3481–3487, 2000. doi: 10.1021/jp000499j, ►.

[186] Hengzhong Zhang and Jillian F. Banfield. Thermodynamic analysis of phase stability of nanocrystalline titania. *J. Mater. Chem.*, 8:2073–2076, 1998. doi: 10.1039/A802619J, ►.

[187] Hengzhong Zhang, Michael Finnegan, and Jillian F. Banfield. Preparing single-phase nanocrystalline anatase from amorphous titania with particle sizes tailored by temperature. *Nano Letters*, 1(2):81–85, 2001. doi: 10.1021/nl0055198, ►.

[188] Hengzhong Zhang and Jillian F. Banfield. Polymorphic transformations and particle coarsening in nanocrystalline titania ceramic powders and membranes. *The Journal of Physical Chemistry C*, 111(18):6621–6629, 2007. doi: 10.1021/jp067665t, ►.

[189] Ibrahim A. Alhomoudi and G. Newaz. Residual stresses and Raman shift relation in anatase TiO_2 thin film. *Thin Solid Films*, 517(15):4372 – 4378, 2009. ISSN 0040-6090. doi: DOI:10.1016/j.tsf.2009.02.141, ►.

[190] Z. Matěj, R. Kužel, and L. Nichtová. X-ray diffraction analysis of residual stress in thin polycrystalline anatase films and elastic anisotropy of anatase. *Metallurgical and Materials Transactions A*, pages 1–10, 2010. ISSN 1073-5623, ►. 10.1007/s11661-010-0468-z.

[191] L. Borgese, E. Bontempi, M. Gelfi, L.E. Depero, P. Goudeau, G. Geandier, and D. Thiaudière. Microstructure and elastic properties of atomic layer

deposited tio2 anatase thin films. *Acta Materialia*, 59(7):2891 – 2900, 2011. ISSN 1359-6454. doi: DOI:10.1016/j.actamat.2011.01.032, ►.

[192] Elza Bontempi, Paolo Zanola, Marcello Gelfi, Marcello Zucca, Laura E. Depero, Baptiste Girault, Philippe Goudeau, Guillaume Geandier, Eric Le Bourhis, and Pierre-Olivier Renault. Elastic behaviour of titanium dioxide films on polyimide substrates studied by in situ tensile testing in a x-ray diffractometer. *Nuclear Instruments and Methods in Physics Research Section B: Beam Interactions with Materials and Atoms*, 268(3-4):365 – 369, 2010. ISSN 0168-583X. doi: DOI:10.1016/j.nimb.2009.09.034, ►. X-ray Techniques for Advanced Materials, Nanostructures and Thin Films: from Laboratory Sources to Synchrotron Radiation - Proceedings of the EMRS 2009 Spring Meeting - Symposium R.

[193] Bin Chen, Hengzhong Zhang, K. A. Dunphy-Guzman, D. Spagnoli, M. B. Kruger, D. V. S. Muthu, M. Kunz, Sirine Fakra, J. Z. Hu, Q. Z. Guo, and Jillian F. Banfield. Size-dependent elasticity of nanocrystalline titania. *Phys. Rev. B*, 79(12):125406, Mar 2009. doi: 10.1103/PhysRevB.79.125406.

[194] Hengzhong Zhang and Jillian F. Banfield. Kinetics of crystallization and crystal growth of nanocrystalline anatase in nanometer-sized amorphous titania. *Chemistry of Materials*, 14(10):4145–4154, 2002. doi: 10.1021/cm020072k, ►.

[195] Guangshe Li, Liping Li, Juliana Boerio-Goates, and Brian F. Woodfield. High purity anatase tio2 nanocrystals: near room-temperature synthesis, grain growth kinetics, and surface hydration chemistry. *Journal of the American Chemical Society*, 127(24):8659–8666, 2005. doi: 10.1021/ja050517g, ►. PMID: 15954771.

[196] Grethe Vestergaard Jensen, Martin Bremholm, Nina Lock, G. Roshan Deen, Torben R. Jensen, Bo B. Iversen, Markus Niederberger, Jan Skov Pedersen, and Henrik Birkedal. Anisotropic Crystal Growth Kinetics of Anatase TiO2 Nanoparticles Synthesized in a Nonaqueous Medium. *Chemistry of Materials*, 22(22):6044–6055, 2010. doi: 10.1021/cm100469y, ►.

[197] Hua Gui Yang, Cheng Hua Sun, Shi Zhang Qiao, Jin Zou, Gang Liu, Sean Campbell Smith, Hui Ming Cheng, and Gao Qing Lu. Anatase tio2 single crystals with a large percentage of reactive facets. *Nature*, 453(7195):638–641, 2008. ISSN 0028-0836. doi: 10.1038/nature06964, ►.

[198] A. Weibel, R. Bouchet, F. Boulc', and P. Knauth. The big problem of small particles: a comparison of methods for determination of particle size in nanocrystalline anatase powders. *Chemistry of Materials*, 17(9):2378–2385, 2005. doi: 10.1021/cm0403762, ►.

[199] Serge Vives and Cathy Meunier. Influence of the x-ray diffraction line profile analysis method on the structural and microstructural parameters determination of sol-gel tio_2 powders. *Powder Diffraction*, 24(3):205–220, 2009. doi: 10.1154/1.3187212, ►.

[200] Lenka Matějová, Zdeněk Matěj, and Olga Šolcová. A new facile synthesis of well-defined titania nanocrystallites; study on their growth, morphology and surface properties. *Microporous and Mesoporous Materials*, 2011. (submitted Jul 16th, 2011).

[201] Z. Matěj, L. Matějová, F. Novotný, J. Drahokoupil, and R. Kužel. Determination of Crystallites Size Distribution Histogram in Nanocrystalline Anatase Powders by XRD. *Zeitschrift für Kristallographie Supplements*, pages 1–6, 2011. accepted for publication.

[202] L. Matějová, T. Cajthaml, Z. Matěj, O. Benada, P. Klusoň, and O. Šolcová. Super/subcritical fluid extractions for preparation of the crystalline titania. *The Journal of Supercritical Fluids*, 52(2):215 – 221, 2010. ISSN 0896-8446. doi: DOI:10.1016/j.supflu.2009.12.008, ►.

[203] A. R. Stokes and A. J. C. Wilson. A method of calculating the integral breadths of debye-scherrer lines. *Mathematical Proceedings of the Cambridge Philosophical Society*, 38(03):313–322, 1942. doi: 10.1017/S0305004100021988, ►.

[204] J. I. Langford, D. Louër, and P. Scardi. Effect of a crystallite size distribution on X-ray diffraction line profiles and whole-powder-pattern fitting. *Journal of Applied Crystallography*, 33(3 Part 2):964–974, Jun 2000. doi: 10.1107/S002188980000460X, ►.

[205] Eckhard Limpert, Werner A. Stahel, and Markus Abbt. Log-normal distributions across the sciences: Keys and clues. *BioScience*, 51(5):pp. 341–352, 2001. ISSN 00063568, ►.

[206] I. Djerdj and A.M. Tonejc. Structural investigations of nanocrystalline TiO2 samples. *Journal of Alloys and Compounds*, 413(1-2):159 – 174, 2006. ISSN 0925-8388. doi: DOI:10.1016/j.jallcom.2005.02.105, ►.

[207] Lenka Matějová. *Nanostructural Materials - texture from physical adsorption*. PhD thesis, Faculty of Chemical Technology, Institute of Chemical Technology, Prague, 2008. (in Czech).

[208] J. I. Langford and A. J. C. Wilson. Scherrer after sixty years: A survey and some new results in the determination of crystallite size. *Journal of Applied Crystallography*, 11(2):102–113, Apr 1978. doi: 10.1107/S0021889878012844, ►.

[209] Nathalie Audebrand, Jean-Paul Auffrédic, and Daniel Louër. An x-ray powder diffraction study of the microstructure and growth kinetics of nanoscale crystallites obtained from hydrated cerium oxides. *Chemistry of Materials*, 12(6):1791–1799, 2000. doi: 10.1021/cm001013e, ►.

[210] Stephen Brunauer, P. H. Emmett, and Edward Teller. Adsorption of gases in multimolecular layers. *Journal of the American Chemical Society*, 60: 309–319, 1938.

[211] D. Balzar, N. Audebrand, M. R. Daymond, A. Fitch, A. Hewat, J. I. Langford, A. Le Bail, D. Louër, O. Masson, C. N. McCowan, N. C. Popa, P. W. Stephens, and B. H. Toby. Size–strain line-broadening analysis of the ceria round-robin sample. *Journal of Applied Crystallography*, 37(6):911–924, Dec 2004. doi: 10.1107/S0021889804022551, ►.

[212] A. S. Barnard and P. Zapol. Predicting the energetics, phase stability, and morphology evolution of faceted and spherical anatase nanocrystals. *The Journal of Physical Chemistry B*, 108(48):18435–18440, 2004. doi: 10.1021/jp0472459, ►.

[213] Jiří Komrska. Algebraic expressions of shape amplitudes of polygons and polyhedra. *Optik - International Journal for Light and Electron Optics*, 80: 171 – 183, 1988. ISSN 0030-4026. (reprint in Czech kindly provided by the author).

[214] J. Komrska and W. Neumann. Crystal shape amplitudes of platonic polyhedra. i. general aspects and the shape amplitudes of the tetrahedron, cube, and octahedron. *physica status solidi (a)*, 150(1):89–111, 1995. ISSN 1521-396X. doi: 10.1002/pssa.2211500109, ►.

[215] Jiří Komrska. Matematické základy kinematickeé teorie difrakce. Institute of Physical Engineering, VUT Brno, (in Czech), ►.

[216] Paolo Scardi, Matteo Leoni, Diego G. Lamas, and Edgardo D. Cabanillas. Grain size distribution of nanocrystalline systems. *Powder Diffraction*, 20 (4):353–358, 2005. doi: 10.1154/1.2135309, ►.

[217] Jorge Martinez-Garcia, Matteo Leoni, and Paolo Scardi. Analytical expression for the dislocation contrast factor of the ?001?100 cubic slip-system: Application to *cu2o*. *Phys. Rev. B*, 76(17):174117, Nov 2007. doi: 10.1103/PhysRevB.76.174117.

[218] W.I.F. David, Matteo Leoni, and Paolo Scardi. Domain size analysis in the rietveld method. *Materials Science Forum*, 651:187–200, 2010. doi: 10.4028/www.scientific.net/MSF.651.187, ►.

[219] William H. Press, William T. Vetterling, Saul A. Teukolsky, and Brian P. Flannery. *Numerical Recipes in C++: the art of scientific computing*. Cambridge University Press, New York, NY, USA, 2nd edition, 2002. ISBN 0-521-75033-4.

[220] Gene Howard Golub and Charles F. Van Loan. *Matrix Computations*. JHU Press, Baltimore, Maryland, USA, 3rd edition, 1996. ISBN 0-8018-5413-X.

[221] Carl Inge Colombo Nilsen. Constrained Least Squares. `http://folk.uio.no/inf9540/CLS.pdf`, May 2005, ►.

[222] Kai Borre. 11.9 Least Squares With Equality Constraints. `http://kom.aau.dk/~borre/kalman/lecture2/p403.pdf`, October 2004, ►.

[223] Charles F. Van Loan. Generalizing the singular value decomposition. *SIAM Journal on Numerical Analysis*, 13(1):pp. 76–83, 1976. ISSN 00361429, ►.

[224] Susan Blackford. Generalized Singular Value Decomposition (GSVD) . `http://www.netlib.org/lapack/lug/node36.html`, October 1999, ►.

[225] Zdeněk Matěj and Radomír Kužel. MStruct - program/library for MicroStructure analysis by powder diffraction. `http://xray.cz/mstruct/`, May 2011, ►.

[226] Marek Andrzej Kojdecki. Deconvolution by Example - Computational Test of Effective Algorithms. *Materials Science Forum*, 378–381:12–17, 2001. doi: 10.4028/www.scientific.net/MSF.378-381.12, ►.

[227] R. Kužel, L. Nichtová, D. Heřman, J. Šícha, and J. Musil. Growth of magnetron sputtered TiO_2 thin films studied by X-ray scattering. *Zeitschrift für Kristallographie Supplements*, 26:241–246, 2007. doi: 10.1524/zksu.2007.2007.suppl_26.241, ►.

[228] R. Cerny, V. Favre-Nicolin, J. Rohlicek, M. Husak, Z. Matej, and R. Kuzel. Expanding fox: Auto-indexing, grid computing, profile fitting. *IUCr: Commission on Powder Diffraction*, (35):16–19, jun 2007, ►.

[229] R. Kužel, L. Nichtová, Z. Matěj, J. Šícha, and J. Musil. Magnetron deposited TiO_2 thin films — crystallization and temperature dependence of microstructure and phase composition. *Zeitschrift für Kristallographie Supplements*, 27:287–294, 2008. doi: 10.1524/zksu.2008.0035, ►.

[230] R. Kuzžel, L. Nichtová, Z. Matěj, J. Šícha, and J. Musil. Complex XRD studies of crystallisation of amorphous and nanocrystalline magnetron deposited TiO_2 films with different thickness. In *Proceedings of ICTF14&RSD2008*, pages 143–146, 2008. ISBN 978-90-334-7347-0, ►.

[231] Z. Matěj, L. Nichtová, and R. Kužel. Expanding FOX for microstructural analysis. *Materials Structure in Chemistry, Biology, Physics and Technology*, 15(1):46–49, 2008. ISSN 1211-5894, ►.

[232] Olga Šolcová, Lenka Matějová, Simona Krejčíková, Zdeněk Matěj, Radomír Kužel, Zdeněk Strýhal, and Oldřich Benada. Structural Study of Tailored Titania Thin Layers. *Collection of Czechoslovak Chemical Communications*, 73(8–9):1222–1230, 2008. ISSN 0010-0765. doi: 10.1135/cccc20081222, ►.

[233] Olga Šolcová, Lenka Matějová, Petr Klusoň, Zdeněk Matěj, Zdeněk Strýhal, Jaroslav Pavlík, and Tomáš Cajthaml. Preparation and Characterization of Thin Nanocrystalline TiO_2 Layers. In Plinio Innocenzi, Yuriy L. Zub, and Vadim G. Kessler, editors, *Sol-Gel Methods for Materials Processing*, NATO Science for Peace and Security Series C: Environmental Security, pages 441–446. Springer Netherlands, 2008. ISBN 978-1-4020-8514-7. doi: 10.1007/978-1-4020-8514-7_40, ►.

[234] L. Nichtová, R. Kužel, Z. Matěj, J. Šícha, and J. Musil. Time and thickness dependence of crystallization of amorphous magnetron deposited TiO_2 thin films. *Zeitschrift für Kristallographie Supplements*, 30:235–240, 2009. doi: 10.1524/zksu.2009.0034, ►.

[235] Z. Matěj, L. Nichtová, and R. Kužel. Coplanar grazing exit X-ray diffraction on thin polycrystalline films. *Zeitschrift für Kristallographie Supplements*, 30:157–162, 2009. doi: 10.1524/zksu.2009.0022, ►.

[236] Z. Matěj, R. Kužel, and L. Nichtová. XRD total pattern fitting applied to study of microstructure of TiO_2 films. *Powder Diffraction*, 25(2):125–131, 2010. doi: 10.1154/1.3392371, ►.

[237] Radomír Kužel, Lea Nichtová, Zdeněk Matěj, and Tereza Brunátová. Temperature evolution of microstructure of TiO_2 thin films and powders studied by X-ray diffraction. In *Nanocon 2010*, pages 346–351. Tanger, Ltd, 2010. ISBN 978-80-87294-19-2, ►.

[238] R. Kužel, L. Nichtová, Z. Matěj, and J. Musil. In-situ X-ray diffraction studies of time and thickness dependence of crystallization of amorphous TiO2 thin films and stress evolution. *Thin Solid Films*, 519(5):1649 – 1654, 2010. ISSN 0040-6090. doi: DOI:10.1016/j.tsf.2010.08.122, ►. 37th International Conference on Metallurgical Coatings and Thin Films (ICMCTF).

[239] A. C. Larson, R. B. Von Dreele, and B. H. Toby. GSAS homepage. `http://www.ccp14.ac.uk/solution/gsas/`, jul 2011, ►.

[240] Bruker AXS. DIFFRAC^{plus} TOPAS. `http://www.bruker-axs.com/topas.html`, jul 2011, ►.

[241] Johannes Birkenstock, Thomas Messner, Reinhard Fischer, Michael Wendschuh, and Christoph Vogt. BRASS — Bremen Rietveld Analysis and Structure Suite. `http://www.brass.uni-bremen.de/`, jul 2011, ►.

[242] Václav Petříček, Michal Dušek, and Lukáš Palatinus. JANA — Crystallographic Computing System for Standard and Modulated Structures. `http://jana.fzu.cz/`, jul 2011, ►.

[243] Vincent Favre-Nicolin and Radovan Černý. Fox, Free Objects for Crystallography. `http://vincefn.net/Fox/`, jul 2011, ►.

[244] Vincent Favre-Nicolin and Radovan Černý. *FOX*, 'free objects for crystallography': a modular approach to *ab initio* structure determination from powder diffraction. *Journal of Applied Crystallography*, 35(6):734–743, Dec 2002. doi: 10.1107/S0021889802015236, ►.

[245] Vincent Favre-Nicolin and Radovan Černý. A better FOX: using flexible modelling and maximum likelihood to improve direct-space ab initio structure determination from powder diffraction. *Zeitschrift für Kristallographie*, 219:847–856, 2004. doi: 10.1524/zkri.219.12.847.55869, ►.

[246] Radovan Černý and Vincent Favre-Nicolin. FOX: A friendly tool to solve nonmolecular structures from powder diffraction. *Powder Diffraction*, 20 (4):359–365, 2005. ISSN 08857156. doi: 10.1154/1.2135314, ►.

[247] Free Software Foundation. GNU General Public License. `http://www.gnu.org/copyleft/gpl.html`, jul 2011, ►.

[248] Ralf W. Grosse-Kunstleve, Nicholas K. Sauter, Nigel W. Moriarty, and Paul D. Adams. Computational Crystallography Toolbox. `http://cctbx.sourceforge.net/`, jul 2011, ►.

[249] Ralf W. Grosse-Kunstleve, Nicholas K. Sauter, Nigel W. Moriarty, and Paul D. Adams. The *Computational Crystallography Toolbox*: crystallographic algorithms in a reusable software framework. *Journal of Applied Crystallography*, 35(1):126–136, Feb 2002. doi: 10.1107/S0021889801017824, ►.

[250] G. Lim, W. Parrish, C. Ortiz, M. Bellotto, and M. Hart. Grazing incidence synchrotron x-ray diffraction method for analyzing thin films. *Journal of Materials Research*, 2(04):471–477, 1987. doi: 10.1557/JMR.1987.0471, ►.

[251] M. Hart, W. Parrish, M. Bellotto, and G. S. Lim. The refractive-index correction in powder diffraction. *Acta Crystallographica Section A*, 44(2): 193–197, Mar 1988. doi: 10.1107/S010876738701050X, ►.

[252] Michael F. Toney and Sean Brennan. Observation of the effect of refraction on x rays diffracted in a grazing-incidence asymmetric Bragg geometry. *Phys. Rev. B*, 39(11):7963–7966, Apr 1989. doi: 10.1103/PhysRevB.39.7963, ►.

[253] T. Noma, K. Takada, and A. Iida. Surface-sensitive x-ray fluorescence and diffraction analysis with grazing-exit geometry. *X-Ray Spectrometry*, 28(6): 433–439, 1999. ISSN 1097-4539. doi: 10.1002/(SICI)1097-4539(199911/12)28:6<433::AID-XRS386>3.0.CO;2-C, ►.

[254] Paolo Colombi, Paolo Zanola, Elza Bontempi, Roberto Roberti, Marcello Gelfi, and Laura E. Depero. Glancing-incidence X-ray diffraction for depth profiling of polycrystalline layers. *Journal of Applied Crystallography*, 39 (2):176–179, Apr 2006. doi: 10.1107/S0021889805042779, ►.

[255] Paolo Colombi, Paolo Zanola, Elza Bontempi, and Laura E. Depero. Modeling of glancing incidence X-ray for depth profiling of thin layers. *Spectrochimica Acta Part B: Atomic Spectroscopy*, 62(6-7):554 – 557, 2007. ISSN 0584-8547. doi: 10.1016/j.sab.2007.02.012, ►. A Collection of Papers Presented at the 18th International Congress on X-Ray Optics and Microanalysis (ICXOM 2005).

[256] Z. Matěj. MStruct course. *Materials Structure in Chemistry, Biology, Physics and Technology*, 17(2a):k99–k102, 2010. ISSN 1211-5894, ►.

[257] R. Kužel, L. Nichtová, Z. Matěj, D. Heřman, J. Šícha, and J. Musil. Study of crystallization of magnetron sputtered TiO_2 thin films by X-ray scattering. *Zeitschrift für Kristallographie Supplements*, 26:247–252, 2007. doi: 10.1524/zksu.2007.2007.suppl_26.247, ►.

[258] Hisako Sato, Kanta Ono, Takayoshi Sasaki, and Akihiko Yamagishi. First-Principles Study of Two-Dimensional Titanium Dioxides. *The Journal of Physical Chemistry B*, 107(36):9824–9828, 2003. doi: 10.1021/jp035017t, ►.

[259] M. Iuga, G. Steinle-Neumann, and J. Meinhardt. Ab-initio simulation of elastic constants for some ceramic materials. *The European Physical Journal B - Condensed Matter and Complex Systems*, 58:127–133, 2007. ISSN 1434-6028. doi: 10.1140/epjb/e2007-00209-1, ►.

[260] Hongzhi Yao, Lizhi Ouyang, and Wai-Yim Ching. Ab Initio Calculation of Elastic Constants of Ceramic Crystals. *Journal of the American Ceramic Society*, 90(10):3194–3204, 2007. ISSN 1551-2916. doi: 10.1111/j.1551-2916.2007.01931.x, ►.

[261] E. Shojaee and M. R. Mohammadizadeh. First-principles elastic and thermal properties of TiO_2: a phonon approach. *Journal of Physics: Condensed Matter*, 22(1):015401, 2010. doi: 10.1088/0953-8984/22/1/015401, ►.

[262] M. Dopita and D. Rafaja. X-ray residual stress measurement in titanium nitride thin films. *Zeitschrift für Kristallographie Supplements*, 23:67–72, 2006. doi: 10.1524/zksu.2006.suppl_23.67, ►.

[263] N. C. Popa. Diffraction-line shift caused by residual stress in polycrystal for all Laue groups in classical approximations. *Journal of Applied Crystallography*, 33(1):103–107, Feb 2000. doi: 10.1107/S002188989901345X, ►.

[264] Herfried Behnken and Viktor Hauk. Calculation of the x-ray elasticity constants (XEC) of the polycrystals from the single-crystal elastic data for arbitrary crystal symmetry. *Zeitschrift für Metallkunde (Int. J. Mater. Res.)*, 77(9):620–626, 1986. ISSN 0044-3093.

[265] J. F. Nye. *Physical Properties of Crystals: Their Representation by Tensors and Matrices*. Clarendon Press, Oxford, 2008. ISBN 978-0-19-851165-6. (first published in 1957).

[266] Daniel Šimek, Radomír Kužel, and David Rafaja. Reciprocal-space mapping for simultaneous determination of texture and stress in thin films. *Journal of Applied Crystallography*, 39(4):487–501, Aug 2006. doi: 10.1107/S0021889806015500, ►.

[267] H. Dosch. Evanescent absorption in kinematic surface Bragg diffraction. *Phys. Rev. B*, 35(5):2137–2143, Feb 1987. doi: 10.1103/PhysRevB.35.2137, ►.

[268] K.Al Usta, H. Dosch, A. Lied, and J. Peisl. Depth controlled grazing angle neutron diffraction. *Physica B: Condensed Matter*, 173(1-2):65 – 70, 1991. ISSN 0921-4526. doi: DOI:10.1016/0921-4526(91)90035-D, ►.

[269] Arthur James Cochran Wilson. *X-ray optics: the diffraction of X-rays by finite and imperfect crystals*. Methuen's monographs on physical subjects. Methuen, 1949, ►.

List of Figures

List of Tables

List of Abbreviations

BET ..... Brunauer, Emmett, Teller
CSD ..... Crystallite Size Distribution
EBSD ..... Electron Backscatter Diffraction
ECAP ..... Equal Channel Angular Pressing
FE-SEM ..... Field Emission Scanning Electron Microscopy
LPA ..... Line Profile Analysis
mW-H ..... modified Williamson-Hall (plot)
SchE ..... Scherrer Equation
SEM ..... Scanning Electron Microscopy
SPD ..... Severe Plastic Deformation
TEM ..... Transmission Electron Microscopy
TPF ..... Total Pattern Fitting
WA ..... Warren-Averbach (analysis)
W-H ..... Williamson-Hall (plot)
WPPM ..... Whole Powder Pattern Modelling
XRD ..... X-Ray Diffraction